Reservoir Characterization and Steam Monitoring in Heavy Oil Reservoirs

---

A Dissertation

Presented to

the Faculty of the Department of Earth and Atmospheric Sciences

University of Houston

In Partial Fulfillment

of the Requirements for the Degree

Doctor of Philosophy

By

Ayato Kato

December 2010

Reservoir Characterization and Steam Monitoring in Heavy Oil Reservoirs

Ayato Kato

APPROVED:

Dr. Robert R. Stewart, Supervisor
Department of Earth and Atmospheric Sciences

Dr. De-hua Han, Co-supervisor
Department of Earth and Atmospheric Sciences

Dr. Christopher L. Liner, Committee member
Department of Earth and Atmospheric Sciences

Dr. Azra N. Tutuncu, Committee member
Petroleum Engineering Department
Colorado School of Mines

Dean, College of Natural Sciences and Mathematics

ACKNOWLEDGEMENTS

Dr. Rob Stewart, my dissertation supervisor, has provided guidance and contributed many useful suggestions to this dissertation. I appreciate his patient proofreading of this dissertation. I want to thank Dr. De-hua Han, my dissertation co-advisor, for his advice and guidance while I did my graduate study at University of Houston. I also want to thank Dr. Christopher Liner and Dr. Azra Tutuncu for their useful comments, suggestions, and encouragement in my study. I wish to extend my gratitude to Dr. Evgeny Chesnokov and Dr. Gennady Goloshubin for their valuable technical suggestions.

I thank JACOS, JAPEX, and JOGMEC for allowing me to use very valuable data in the Hangingstone heavy oilfield and publish the result. Furthermore, JOMGEC allowed to me to enroll in the Ph.D. program at the University of Houston, and has provided me all financial support for my research. All my colleagues in JOGMEC have given me many useful comments for my research and assistance for my life. I specially thank Mr. Ono and Dr. Tsuji for their suggestions and continuous encouragement. Dr. Takahashi stimulated me to be interested in rock physics and gave me useful suggestions for study abroad. I also thank Mr. Nakayama. He has provided me many technical suggestions for the case study as well as encouragement.

I thank all members in rock physics and AGL groups at the University of Houston for useful suggestions and support. Daniel Morgan, Fang Li, Min Sun, Julian Yao, and Fuyong Yan proofread my manuscripts and gave me valuable suggestions. I thank them for their patience. Nebojsa Pralica and Li Chang helped me with data loading from LTO

tape and manuscript binding of this dissertation, respectively. I thank them for their kindness. I also thank the FLUID/DHI and AGL sponsors for supporting this research.

Finally, and the most importantly, I thank my wife Mayuko and my parents for their encouragement, support, and confidence in me during my Ph.D. study. Without their encouragement, the completion of my dissertation would not be possible.

Reservoir Characterization and Steam Monitoring in Heavy Oil Reservoirs

---

An Abstract of a Dissertation

Presented to

the Faculty of the Department of Earth and Atmospheric Sciences

University of Houston

In Partial Fulfillment

of the Requirements for the Degree

Doctor of Philosophy

By

Ayato Kato

December 2010

ABSTRACT

I first explore viscoelastic features of heavy oil by using ultrasonic velocity measurement data collected over a wide temperature range. I found that bulk modulus is significantly increased compared to conventional oil, which is caused by bulk viscosity. The relation between bulk and shear viscosities is obtained by comparing the viscosity-induced bulk and shear moduli. Furthermore, by using the viscoelastic model of Havriliak and Negami (1967), temperature and frequency dependences of the bulk and shear moduli are predicted.

I establish a rock physics model of poorly-consolidated, heavy-oil saturated sands. For the case of inclusions in a matrix, a generalized singular approximation method is used to obtain the effective properties. Furthermore, the model incorporates the viscoelastic features of heavy oil. Thus, velocity dispersion and attenuation associated with the viscosities can be estimated. Moreover, the elastic property changes caused by steam injection are estimated by changing the fluid properties. The predictions are consistent with different actual measurements, including laboratory, well log, and time-lapse seismic data.

Density has a large contrast between reservoir and shale and is a desired property for reservoir delineation in the Hangingstone oilfield. A P-P and P-S joint AVO inversion method is developed by extending an Bayesian inversion technique to multicomponent data. The synthetic tests show that the joint method gives us superior results in density estimation compared to P-P only inversion. I applied the developed method to the

Hangingstone oilfield to estimate density volume. From the inversion result, a reservoir sand thickness map was successfully obtained.

In addition, a time-lapse AVO inversion method is developed, based on the Bayesian technique, in which all available seismic data are used to obtain initial elastic properties (V_p, V_s, and ρ) and the changes between two surveys. The method is applicable to incomplete time-lapse multicomponent data sets. After synthetic tests, the method was applied to the Hangingstone oilfield. As a result, estimation of initial elastic properties was improved by using the repeat data. Also, the P-wave velocity change was successfully estimated. The method provides a quantitative description of the reservoir and estimate of the steam distribution.

CONTENTS

LIST of TABLES

LIST of FIGURES

Chapter 1 - Introduction

1.1 Motivation

Heavy oil has become a tremendously important resource for us in this decade. Heavy-oil reserves account for more than 6 trillion barrels in place, which approximately corresponds to triple the total global reserve of conventional oil and gas (Curtis et al., 2002). Although there are several definitions, heavy oil is usually defined as having high density (less than 20º API gravity) and high viscosity (more than 10 cP) at in-situ conditions (Batzle et al., 2006).

Because heavy oil does not flow easily due to its high viscosity, it is usually produced by thermal recovery or cold production methods. The Steam Assisted Gravity Drainage (SAGD) method is one of the most common methods for producing heavy oil in Canada (Butler, 1991). It makes heavy oil flowable by heating it with injected steam and thus reducing its viscosity. The injected steam movement within reservoirs is highly influenced by geological heterogeneities. In the Athabasca oil sands, which is a large deposit of heavy oil located in northeast Alberta, Canada, it is common that impermeable shale intricately exists within the reservoirs and can potentially act as permeability baffles (e.g., Roy et al., 2008). For reservoir management, it is important to both precisely delineate the intrareservoir shale before production and monitor steam front movement during production. Three-dimensional seismic data, which can provide broad lateral coverage, are valuable for the reservoir delineation and steam front monitoring. Numerous studies in heavy-oil reservoirs by using 3D seismic data have been reported

(e.g., Isaac, 1996; Sun, 1999; Nakayama et al., 2008; Roy et al., 2008). Despite these efforts, quantitative reservoir delineation and steam front monitoring by 3D seismic data is still challenging.

One of the main reasons is the lack of an adequate rock physics model, which can calculate the effective elastic properties of heavy-oil saturated rock under changing conditions of pressure, temperature, and saturation. Heavy oil has a shear modulus associated with shear viscosity - unlike conventional oil (e.g., Han et al., 2008). Moreover, the shear modulus is frequency-dependent and significantly changes with temperature (Behura et al., 2007). Thus, conventional rock physics models, including Gassmann's equation (Gassmann, 1951), might be inapplicable for heavy-oil saturated rock. Although some attempts to model heavy-oil saturated rock have been made (e.g., Leurer and Dvorkin, 2006; Gurevich et al., 2008), they are not conclusive. The classical paper of Stokes (1845) tells us that compressive fluids have not only shear viscosity but also bulk viscosity. However, the bulk viscosity has been often neglected or assumed to be zero in theoretical calculation because there is very limited experimental data due to difficulty of the direct measurement (e.g., Litovitz and Davis, 1964). There is a recently published paper concerning bulk viscosity of heavy oil (Kato and Han, 2009). Kato and Han (2009) analyzed ultrasonic velocity measurement data collected over a wide temperature range and reported that bulk modulus of heavy oil is substantially reinforced by its bulk viscosity, as shear viscosity acting on shear modulus. Thus, we need to establish an adequate rock physics model of heavy-oil saturated rock, taking into account the two kinds of viscosity.

Another challenge to the use of 3D seismic data for better reservoir management is the difficulty of discriminating between reservoir and shale. Since the contrast of P- and S-wave velocities between shale and reservoir at in-situ conditions is commonly small in the Athabasca oil sands, it is difficult to distinguish them by only conventional seismic attributes associated with the velocities (e.g., Roy et al., 2008; Figure 1.1). On the other hand, bulk density has a larger contrast between reservoir and shale and might be a more desired property for the reservoir delineation. A three-term AVO inversion is one of techniques extracting density reflectivity from seismic AVO response. Since seismic AVO response is commonly insensitive to density contrast at small incident angles (Aki and Richards, 1998), density estimation is highly influenced by noise and normally less reliable. Moreover, if we use long offset data in order to reduce the noise effects, we are faced with new problems requiring additional data pre-conditioning. Thus, the three-term AVO inversion for density estimation is a challenge.

Furthermore, as seismic interpretation techniques have become mature, emphasis on more quantitative interpretation using all available seismic data has increased. Multicomponent seismic and time-lapse seismic surveys have remarkable benefits, giving us more valuable information than the single survey. For example, additionally using P-S wave data yields more accurate Vp/Vs estimation, which is a good lithology discriminator (e.g., Soubotcheva and Stewart, 2006; Xu and Stewart, 2006b; Dumitrescu and Lines, 2007). Also, time-lapse seismic data clearly delineate steam front distribution (e.g., Eastwood et al., 1994; Issac, 1996; Sun, 1999; Nakayama et al., 2008). However, it is a challenging task to integrate multiple survey data, such as the time-lapse and

multicomponent seismic data, to make quantitative interpretation. The joint inversion using multiple survey data is one of the integration techniques. Furthermore, rock physics knowledge can be used for constraints to obtain a more realistic and stable inversion solution. Thus, it is obvious that we need to develop a new workflow of integrating all available seismic data along with rock physics knowledge to make quantitative interpretation.

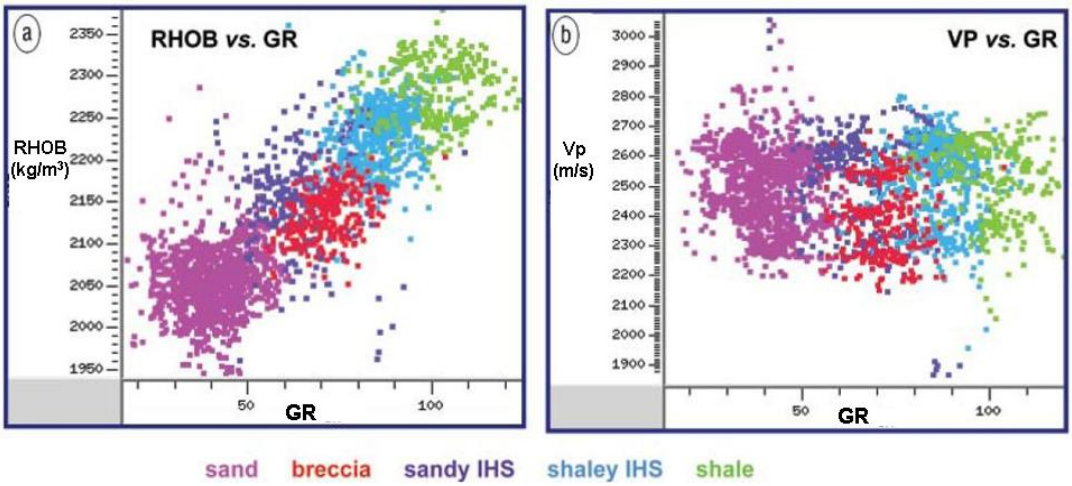

Figure 1.1. Typical relationship of P-wave velocity and density with gamma ray in the Athabasca oil sands (After Roy et al., 2008).

1.2 Hangingstone Oilfield Overview

I use the comprehensive dataset, which consists of time-lapse and multicomponent seismic data, well logs, and laboratory measurement data along with geological information. The data were acquired in the Hangingstone oilfield, located approximately 50 km south-southwest of Fort McMurray, Alberta, Canada (Figure 1.2). There, Japan Canada Oil Sands Limited (JACOS) has operated and developed heavy-oil resources.

1.2.1 Geology and Field Development

The reservoirs in the Hangingstone oilfield correspond to the Lower Cretaceous McMurray Formation, which is overlies the Devonian-Cretaceous Unconformity. The Lower Cretaceous McMurray Formation is one of the main formations with heavy-oil deposits in the Athabasca area and contains in total about 900 billion barrels of heavy oil in place (Alberta Energy and Utilities Board, 2007). In the study area, the McMurray Formation is about 300 m in depth and the sedimentary environment is interpreted to consist of fluvial to upper estuarine channel-fill deposits (Takahashi, 2010; Figure 1.3). The reservoirs correspond to vertically stacked, incised valley-fill sands with very complex vertical and horizontal distributions. Figure 1.4 is typical well logs acquired in the field. The McMurray Formation is overlain by Wabiskaw shale and underlain by massive Devonian limestone (Takahashi, 2010). The reservoir, from about 280 m to 306 m in depth, shows excellent reservoir quality with high porosity and high resistivity.

Heavy oil with 8.5 °API gravity does not move easily due to high viscosity at in-situ condition. Thus, JACOS has used the Steam-Assisted Gravity Drainage (SAGD) method to produce the heavy oil (Figure 1.5). The SAGD method is one of the thermal in situ recovery techniques (Butler, 1982) which has been widely used for heavy-oil production in Canada. In the SAGD method, two horizontal wells are drilled in a reservoir and hot steam is continuously injected from the upper well into the reservoir. Vertical distance between the two horizontal wells is typically 5 m and horizontal length is 750 m. At the vicinity of the injected well, since viscosity of heavy oil is dramatically reduced with heat of the injected steam, the heavy oil becomes flowable and moves downward by gravity.

Then, the lower well produces the drained heavy oil along with the injected steam. The area where heavy oil is sufficiently heated and drained by the injected steam is called steam chamber (Butler, 1982). Development of the steam chamber is strongly influenced by local geological heterogenities, because the SAGD process relies on gravity drainage. Interbedded shale within the reservoirs potentially acts as a barrier or baffle to the steam movement. Thus, for efficient production and field development, it is extremely important to precisely predict the reservoir distributions and monitor steam movement.

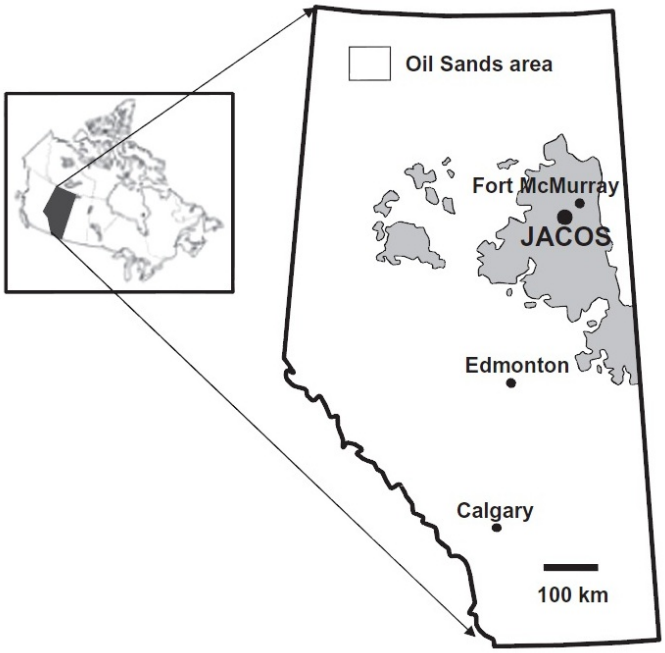

Figure 1.2. The Hangingstone oilfield and heavy-oil sands reservoirs in Alberta, Canada (After Takahashi, 2010).

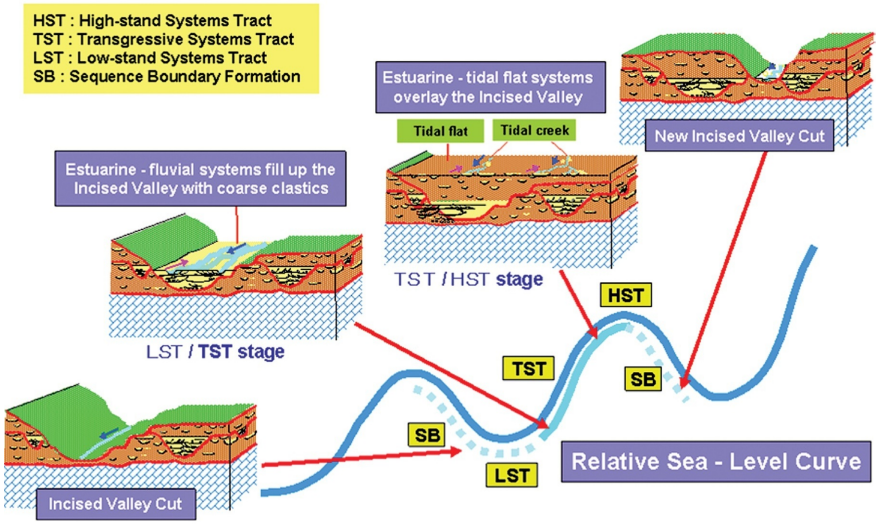

Figure 1.3. Sequence stratigraphic framework of the McMurray formation (Takahashi, 2010).

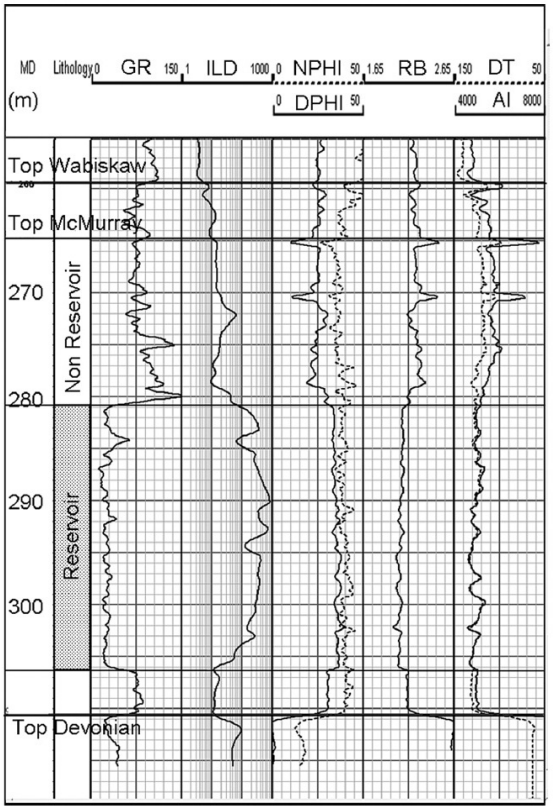

Figure 1.4. Example of the well log data in the Hangingstone oilfield (After Takahashi, 2010).

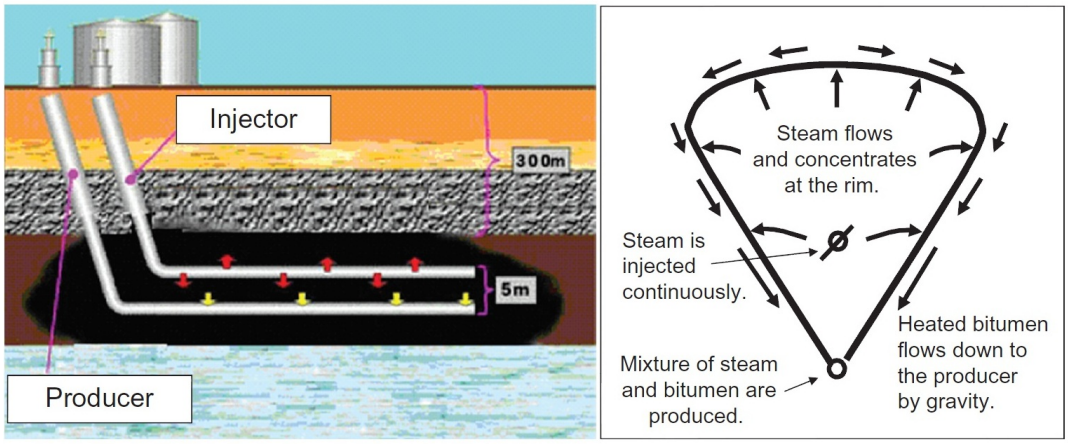

Figure 1.5. The SAGD method (After Takahashi, 2010).

1.2.2 Previous Geophysical Studies

For the reservoir delineation and steam monitoring, a time-lapse seismic survey was conducted in the field (Nakayama et al., 2008). The baseline survey (5.4 km^2) and repeat survey (4.3 km^2) were acquired in February 2002 and March 2006, respectively, as shown by Figure 1.6. The field acquisition parameters are almost the same. The only major difference is the receiver type; three-component digital sensors were used in the repeat survey while analog geophone arrays were used in the baseline survey. Thus, P-P and P-S wave data are available in the repeat survey, while P-P wave data are only available in the baseline survey.

There is considerable literature using the seismic data to conduct reservoir characterization in the field (e.g., Kashihara et al., 2010; Nakayama et al., 2008; Takahashi, 2009). Takahashi (2010) used the baseline P-P wave data to perform seismic-guided reservoir characterization, based on acoustic impedance inversion and multi

attribute analysis, and successfully constructed the three-dimensional geological model. Kashihara et al. (2010) used the same data to perform geostatistical reservoir property mapping. In addition, Nakayama et al. (2008) carried out the time-lapse cross-equalization analysis (Figure 1.7) to obtain several attribute maps which clearly show substantial differences between the two surveys. For example, Figure 1.8 is the time difference of the Top Devonian horizon. One observes that there are large differences around the SAGD wells. The time differences were interpreted to be caused by P-wave velocity decrease due to the steam injection. Also, they conducted multicomponent data analysis and obtained the reservoir Vp/Vs map. Furthermore, Tanaka et al. (2009) integrated the analysis of the time-lapse seismic data with the empirical rock physics model (Kato et al., 2008) to estimate the volume of the steam chamber.

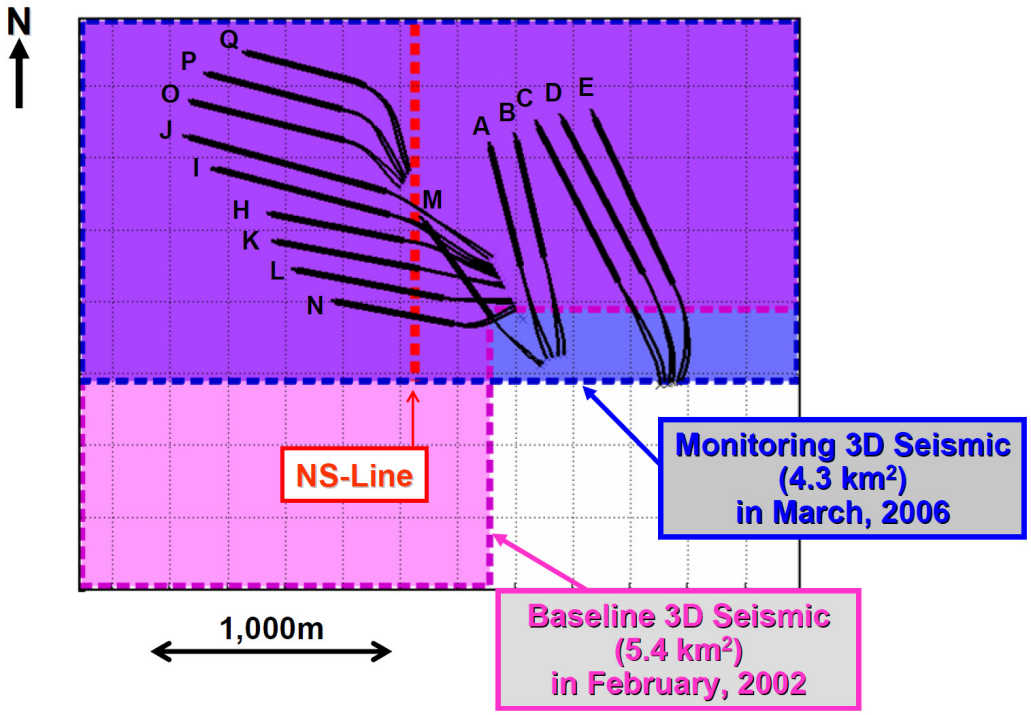

Figure 1.6. Map of the time-lapse 3D seismic survey with the SAGD well locations. Black solid lines represent the SAGD well paths (from Nakayama et al., 2008).

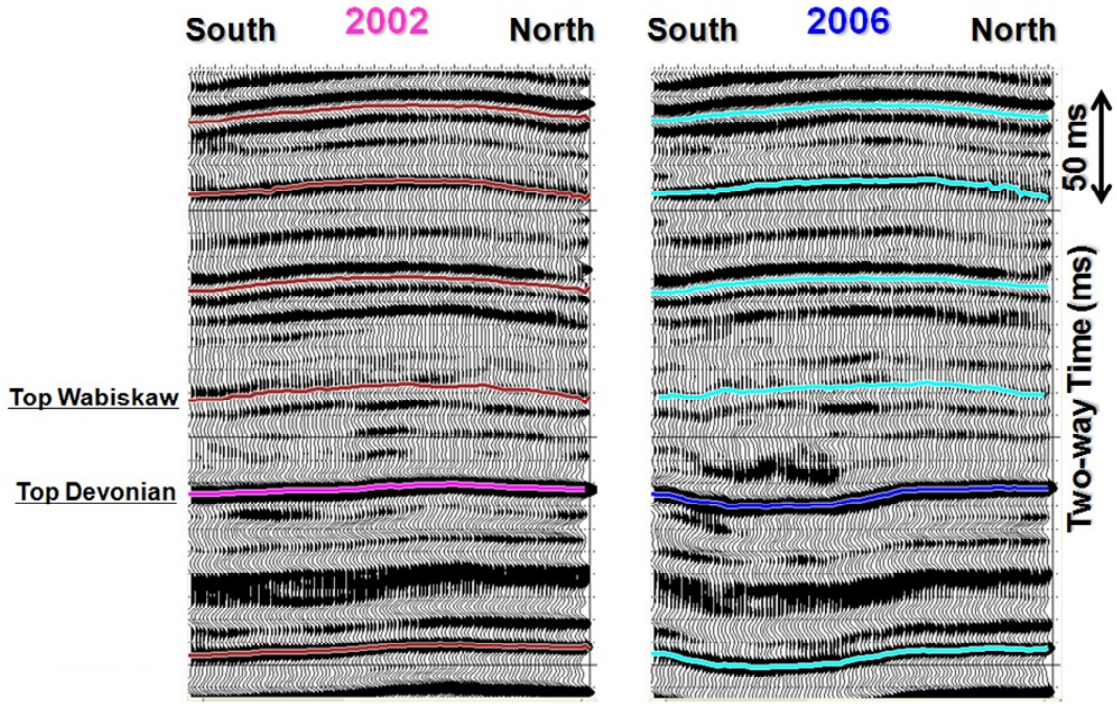

Figure 1.7. The baseline and repeat P-P wave time section with the interpreted horizons (After Nakayama et al., 2008).

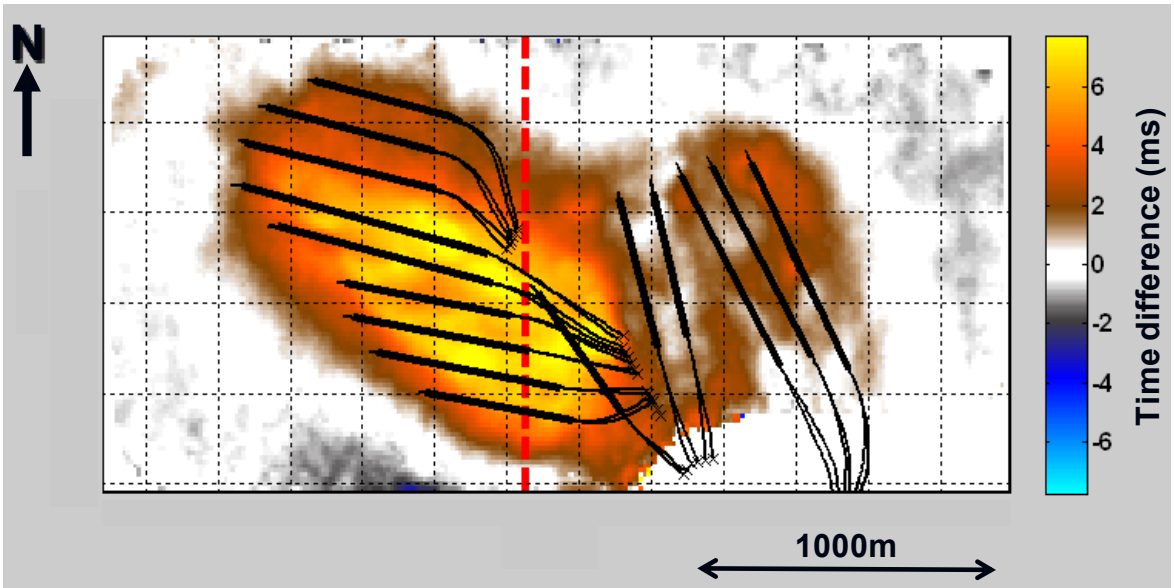

Figure 1.8. Time differences of the Top Devonian horizon between 2002 and 2006. The positive value shows that the horizon at 2006 is deeper than that at 2002 (After Nakayama et al., 2008).

1.3 Dissertation Objectives and Organization

The main objectives of this dissertation are to establish a rock physics model of poorly consolidated, heavy-oil saturated sands and to develop new methods of quantitative reservoir characterization and steam monitoring in heavy-oil reservoirs.

The first objective is to obtain temperature and frequency dependences of elastic properties of heavy oil. I will use the ultrasonic velocity measurement data collected over a wide temperature range to investigate bulk viscosity and its related bulk modulus of heavy oil. I will compare the viscosity-induced bulk modulus with the corresponding shear modulus to obtain the relation between bulk and shear viscosities. Furthermore, using the viscoelastic model along with the relationship, temperature and frequency dependences of bulk and shear moduli of heavy oil will be predicted. These tasks will be discussed in Chapter 2. The predicted moduli will be used in the following chapters.

The second objective is to establish an adequate rock physics model for poorly consolidated, heavy-oil saturated sands. Generalized Singular Approximation method will be used in the computation of effective elastic properties. Also, the bulk and shear viscosities will be taken into account in the model. The model will be validated with actual measurement data; the laboratory, well logs, and time-lapse seismic data. Furthermore, S-wave velocity prediction will be carried out by using the model. Also, I will compute the velocity dispersion and attenuation associated with the viscosities. These tasks will be discussed in Chapter 3.

The third objective of this dissertation is to develop a method of quantitatively discriminating between reservoir and shale by using multicomponent seismic data along with the rock physics knowledge. I first investigate the relationship between lithology and the corresponding elastic properties in the Hangingstone oilfield. I will extend the Bayesian inversion technique to multicomponent seismic data. The method will be validated with synthetic data. Furthermore, the developed method will be applied to the Hangingstone oilfield. In the implementation, seismic data conditioning and correlation between the P-P and P-S waves will be discussed. From the inversion results, the reservoir sand thickness map will be obtained. The methodology along with the synthetic test will be discussed in Chapter 4, while implementation of the method with the field data will be discussed in Chapter 5.

The fourth objective of the dissertation is to develop a workflow of the time-lapse AVO inversion method. The method will simultaneously obtain elastic properties and the changes between two surveys, which are consistent with all the available seismic data with the rock physics knowledge. Furthermore, the method is extended to multicomponent time-lapse seismic data. After testing with synthetic data, the method will be applied to the Hangingstone oilfield. The temperature map will be obtained from the inversion result along with the rock physics analysis. The methodology along with the synthetic test will be discussed in Chapter 6, while the implementation of the method with the field data will be discussed in Chapter 7.

Chapter 2 – Viscoelastic Properties of Heavy Oils

2.1 Introduction

For quantitative seismic interpretation, we need an adequate rock physics model, which can compute effective elastic properties of heavy-oil saturated rock under various conditions of pressure, temperature, and saturation caused by steam injection. In addition, for the rock physics modeling, it is essential to accurately know temperature and pressure dependences of elastic properties of heavy oil itself.

Han et al. (2008) described the temperature dependence of P- and S-wave velocities of heavy oil by using the liquid and glass points, which are defined as temperature at shear viscosity of 10^3 cP and 10^{15} cP (Figure 2.1). According to Han et al. (2008), at temperatures lower than the glass point, heavy oil acts as a solid material due to its extremely high viscosity. At temperatures higher than the liquid point, viscosity is low enough so that its effect on the velocities can be neglected; it acts as an elastic material like a standard liquid. In between these two regions, it acts as a viscoelastic material (so-called quasi-solid state), where wave propagation is strongly dispersive with high attenuation.

Heavy oil in the quasi-solid state has a finite shear modulus induced by the shear viscosity. Furthermore, the corresponding bulk modulus also significantly increases compared to that of conventional oil, which results from additionally induced bulk modulus by the bulk viscosity (e.g., Graves and Argrow, 1999).

There is considerable literature reporting laboratory measurement of shear viscosity. For example, dynamic rheometrical measurement provides us with frequency- and temperature-dependent data on shear viscosity (e.g., Behura et al., 2007; Rojas, 2010). However, there is a very limited work reporting bulk viscosity measurement (e.g., Litoviz and Davis, 1964; Malbrunot et al., 1983; Dukhin and Goetz, 2009), although it has been known to have a fundamental role in a fluid dynamic. The classic paper of Litoviz and Davis (1964) reviewed bulk viscosity measurements for several Newtonian liquids. In their review, bulk viscosity of water at 15 ˚C is 3.9 cP, which is about three times larger than the corresponding shear viscosity. A more recent study by Dukihin and Goetz (2009) used the acoustic spectroscopy apparatus (Dukhin and Goetz, 2002) to estimate bulk viscosity of Newtonian liquids.

Moreover, it is more difficult to find information concerning measurement of bulk viscosity of heavy oil. The remarkable exception is an old paper of Tasköprülü et al. (1961). They conducted ultrasonic P-wave attenuation measurement at different temperatures on viscous heavy oil. Using the shear viscosity data from the dynamic rheometrical measurement on the same sample (Barlow and Lamb, 1959), they found that the measured P-wave attenuation is much higher than the attenuation due to the shear viscosity. They concluded that the bulk viscosity is approximately four thirds higher than the shear viscosity in the measured temperature range. In accordance with the limited laboratory measurements along with the theory, it can be considered that bulk viscosity has substantial influence on P-wave propagation through a viscoelastic material.

However, although shear viscosity is commonly taken into account in the rock physics modeling for heavy-oil saturated rock, bulk viscosity has been often neglected or simple assumed to be zero (e.g., Das and Batzle, 2009). One of the main reasons is that we do not have enough data on bulk viscosity of heavy oils. Therefore, it is obvious that we need to improve our understanding on bulk viscosity and its related bulk modulus.

In this study, I focus on bulk viscosity of heavy oil. The bulk viscosity may be indirectly estimated by the ultrasound attenuation method through the viscoelastic theory (e.g., Tasköprülü et al., 1961; Dukhin and Goetz, 2009). However, the measurement of attenuation with high accuracy is difficult, if not impossible. In contrast, ultrasonic velocity measurement data are relatively more obtainable. Thus, using the complete ultrasonic velocity measurement data on several heavy-oil samples, I aim to estimate the relationship between the shear and bulk viscosities and obtain temperature dependences of them.

The workflow of this study is presented in Figure 2.2. From the ultrasonic velocity measurement data along with the static bulk modulus and density, the viscosity-induced bulk and shear moduli are obtained. For the viscosity-induced shear modulus, an adequate viscoelastic model is selected using the temperature-dependent model of the shear viscosity. It is noted that the shear viscosity model is calibrated with the S-wave velocity measurement data. Furthermore, by applying the viscoelastic model to the viscosity-induced bulk modulus, a relation between the shear and bulk viscosities is obtained. Using this result along with the shear viscosity model and the viscoelastic

model, I obtain the temperature- and frequency-dependent models of the moduli and velocities.

In the following sections, I will first review the background theories which is associated with the viscoelastic modeling. Next, after presenting the ultrasonic velocity measurement data, I will describe the shear viscosity model along with the calibration method. Then, the analyzed results of the velocity measurement data based on the shear viscosity model will be described. They mainly consist of three parts; viscoelastic modeling of shear modulus, the relationship between shear and bulk viscosities, and viscoelastic modeling of bulk modulus and velocities. Finally, I will describe the summary and proposal for the further work.

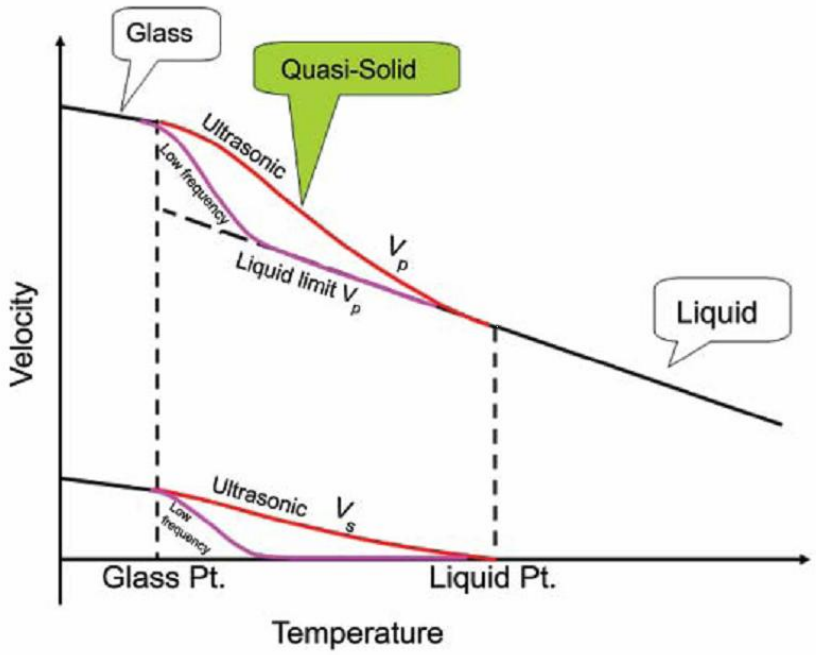

Figure 2.1. Concept of temperature dependence of P- and S-wave velocities of heavy oil at two different frequencies; ultrasonic and low frequencies. The temperature dependence can be approximately described by three main stages; liquid, quasi-solid, and solid states (after Han et al., 2008).

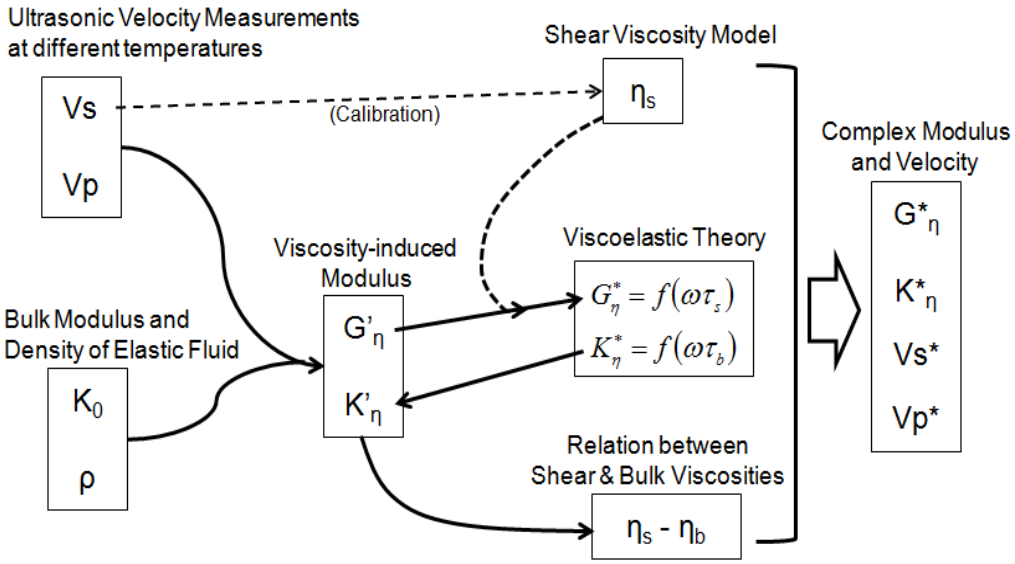

Figure 2.2. Workflow of viscoelastic modeling of heavy oil. From the ultrasonic velocity measurement data (V_s and V_p) along with bulk modulus (K_0) and density (ρ) of the elastic fluid, the viscosity-induced shear and bulk moduli (G'_η and K'_η) are obtained. Using the viscoelastic theory with shear viscosity model, the relation between shear and bulk viscosities is derived. Finally, using these results, the complex moduli and velocities ($G^*_\eta, K^*_\eta, V^*_s$, and V^*_p) are modeled.

2.2 Background Theory

First I will review the constitutive equations for elastic and viscous fluids in the isotropic case and describe two kinds of moduli and viscosities; bulk and shear moduli for the elastic solid and bulk and shear viscosities for the viscous fluid. Next, I will briefly describe the viscoelastic theory which can incorporate both the elastic and viscous features. The viscoelastic theory mainly consists of two models; single-phase relaxation model and multi-phase relaxation model.

2.2.1 Elastic Solid and Viscous Fluid

For a linear elastic solid, the relationship between the stress and strain can be expressed by Hooke's law:

$$\sigma_{ij} = C_{ijkl}\varepsilon_{kl}, \tag{2.1}$$

where σ_{ij} and ε_{kl} are the stress and strain tensors, and C_{ijkl} is the elastic stiffness tensor. For an isotropic solid, (2.1) can be simplified to the following form:

$$\sigma_{ij} = \lambda\varepsilon_{kk}\delta_{ij} + 2\mu\varepsilon_{ij}, \tag{2.2}$$

where λ and μ are the Lame's constants, and δ_{ij} is the Kroeneker delta tensor. From (2.2), the shear modulus μ is defined as the ratio of shear stress to shear strain as follows:

$$\sigma_{ij} = 2\mu\varepsilon_{ij} \qquad i \neq j. \tag{2.3}$$

Also, the bulk modulus K is defined as the ratio of hydrostatic stress to volumetric strain:

$$\frac{1}{3}\sigma_{ii} = K\varepsilon_{ii}. \tag{2.4}$$

The bulk modulus K is mutually related with the other two constants:

$$K = \lambda + 2\mu/3. \tag{2.5}$$

In contrast, for a linear Newtonian viscous fluid, the viscous stress tensor τ_{ij} is proportional to rate of the deformation tensor as (e.g., Mase, 1970; Lai et al., 1974):

$$\tau_{ij} = K_{ijpq}D_{pq}, \tag{2.6}$$

where K_{ijpq} is the viscosity coefficient and $D_{pq} = \frac{1}{2}\left(\frac{\partial v_p}{\partial x_q} + \frac{\partial v_q}{\partial x_p}\right)$ is the deformation rate tensor. Following the similar procedures as Hooke's law, the constitutive equation for an isotropic Newtonian viscous fluid is expressed as:

$$\tau_{ij} = \eta_\lambda \delta_{ij} D_{kk} + 2\eta_s D_{ij}, \tag{2.7}$$

where η_λ and η_s are the viscosity coefficients of the fluid. Particularly, η_s is called shear viscosity. From (2.7), the shear viscosity can be defined as the ratio of shear viscous stress to shear deformation rate:

$$\tau_{ij} = 2\eta_s D_{ij}, \qquad i \neq j. \tag{2.8}$$

By taking into account the effect of hydrostatic pressure *p*, the mean normal stress σ_{ii} is expressed from (2.7):

$$\frac{1}{3}\sigma_{ii} = -p + \eta_b D_{ii}, \tag{2.9}$$

where $\eta_b = \eta_\lambda + \frac{2}{3}\eta_s$ is the bulk viscosity. The bulk viscosity is the proportionality constant relating the viscous mean normal stress to the rate of volume change. The bulk viscosity is sometimes referred to as "volume viscosity", "second viscosity coefficient", "expansion coefficient of viscosity", or "coefficient of bulk viscosity" by various authors working in different fields, as Dukhin and Goetz (2009) described.

The bulk and shear viscosities are considered to be associated with individual molecular motions. Following Temkin (2001), molecules in liquids and gases have translational, rotational, and vibrational degrees of freedom. Shear viscosity is associated only with the translational motion of the molecules. In contrast, bulk viscosity is associated with both

the rotational and vibrational motions. Thus, it can be suggested that the relationship between shear and bulk viscosities reflects the molecular structure in the medium.

2.2.2 Single-phase Relaxation Model

A viscoelastic material like a viscous oil shows both elastic and viscous behaviors, depending on the wave frequency. The viscoelastic theory can incorporate both elastic and viscous features. I will consider the single-phase relaxation model of the viscoelastic theory (e.g., Debye, 1929). If a static shear modulus is zero, the complex adiabatic shear modulus, G_η^*, is expressed as:

$$G_\eta^* = \frac{i\omega\tau_s}{1+i\omega\tau_s} = \frac{G_\infty\omega^2\tau_s^2}{1+\omega^2\tau_s^2} + i\frac{G_\infty\omega\tau_s}{1+\omega^2\tau_s^2}, \tag{2.10}$$

where G_∞ is the high frequency-limiting shear modulus, and ω is the angular frequency. τ_s is a relaxation time of the shear motion expressed as:

$$\tau_s = \frac{\eta_s}{G_\infty}. \tag{2.11}$$

Equation (2.10) corresponds to the well-known Maxwell model which connects an elastic spring and a viscous dashpot together in series as a mechanical analog (e.g., Christensen, 1982).

When considering a sinusoidal, damped shear plane wave, a solution has the form:

$$A_0 \exp\left[i\omega\left(t - \frac{d}{C_s^*} \right) \right], \tag{2.12}$$

where d is the distance and C_s^* is the complex shear velocity expressed as:

$$\frac{1}{C_s^*} = \frac{1}{V_s} - i\frac{\alpha_s}{\omega}, \tag{2.13}$$

where V_s and α_s are the S-wave phase velocity and absorption coefficient, respectively. The following relationship can be defined as:

$$\rho C_s^{*2} = G_\eta^*, \tag{2.14}$$

where ρ is the density. By substituting (2.10) into (2.14) with (2.13), the following formulas are obtained:

$$\begin{aligned} G'_\eta &= \frac{\rho V_s^2\left[1-(\alpha_s V_s/\omega)^2\right]}{\left[1+(\alpha_s V_s/\omega)^2\right]^2}, \\ G''_\eta &= \frac{\rho V_s^2(2\alpha_s V_s/\omega)}{\left[1+(\alpha_s V_s/\omega)^2\right]^2}, \end{aligned} \tag{2.15}$$

where G'_η and G''_η are the real and imaginary parts of the complex shear modulus, and correspond to the storage and loss moduli, respectively (Ferry, 1980). When the condition $(\alpha_s V_s/\omega)^2 << 1$ is satisfied (Litovitz et al., 1954), one obtains from (2.15):

$$\begin{aligned} G'_\eta &= \rho V_s^2, \\ G''_\eta &= 2\rho V_s^3 \alpha_s/\omega. \end{aligned} \tag{2.16}$$

Hence, from (2.13) and (2.16), the phase velocity and attenuation can be expressed as:

$$\begin{aligned} V_s &= \sqrt{\frac{G'_\eta}{\rho}} = \sqrt{\frac{G_\infty \omega^2 \tau_s^2}{\rho(1+\omega^2\tau_s^2)}}, \\ \frac{1}{Q_s} &= \frac{G''_\eta}{G'_\eta} = \frac{1}{\omega\tau_s}, \end{aligned} \tag{2.17}$$

where $Q_s = \pi f / V_s \alpha_s$ is the shear wave quality factor.

In a similar way, the complex adiabatic bulk modulus is expressed as:

$$K^* = K_0 + K_\eta^* = K_0 + \frac{K_2 \omega^2 \tau_b^2}{1+\omega^2 \tau_b^2} + i \frac{K_2 \omega \tau_b}{1+\omega^2 \tau_b^2}, \tag{2.18}$$

where $K_2 = K_\infty - K_0$; K_2, K_0, and K_∞ are the relaxational bulk modulus, the static bulk modulus, and the high frequency-limiting bulk modulus, respectively. K_0 corresponds to the bulk modulus of an idealized elastic fluid and is independent of the wave frequency. τ_b is the relaxation time of compressive movement and is expressed as:

$$\tau_b = \frac{\eta_b}{K_2}. \tag{2.19}$$

Furthermore, the complex P-wave modulus can be defined as:

$$M^* = M' + iM'' = K^* + \frac{4}{3} G^*. \tag{2.20}$$

For the P-wave, one follows the same procedures as the S-wave. The solution has the form:

$$\rho C_p^{*2} = M^*, \tag{2.21}$$

where

$$\frac{1}{C_p^*} = \frac{1}{V_p} - i \frac{\alpha_p}{\omega}. \tag{2.22}$$

In addition, C_p^*, V_p, and α_p are, respectively, the complex P-wave velocity, the P-wave phase velocity, and the absorption coefficient for the P-wave. When $\left(\alpha_p V_p / \omega\right)^2 << 1$, one obtains:

$$\begin{aligned} M' &= \rho V_p^2, \\ M'' &= 2\rho V_p^3 \alpha_p / \omega. \end{aligned} \tag{2.23}$$

Thus, the phase velocity and attenuation of P-wave are expressed as:

$$V_p = \sqrt{\frac{M'}{\rho}}, \qquad \frac{1}{Q_p} = \frac{M''}{M'}, \tag{2.24}$$

where $Q_p = \pi f / V_p \alpha_p$ is the P-wave quality factor.

2.2.3 Multi-phase Relaxation Model

Although some rock physics modeling studies concerning heavy oil assumed the single-phase relaxation model (e.g., Wolf et al. 2006), it has been known that the model does not correctly describe the frequency dispersion behavior of experimental data in many cases (e.g., Sharkov, 2003). One of the possible reasons is that liquids and solid substances, consisting of composite clusters of molecules, have multiple relaxation times instead of single relaxation time because each molecular type has an individual relaxation time.

For the multi-phase relaxation models, some empirical formulas have been proposed based on the single-phase relaxation model (e.g., Cole and Cole, 1941; Davidson and Cole, 1950; Havriliak and Negami, 1967). Cole and Cole (1941) introduced an empirical parameter in the complex shear modulus model as:

$$G_\eta^* = G_\infty \left[\frac{(i\omega\tau_s)^{1-\alpha}}{1+(i\omega\tau_s)^{1-\alpha}} \right], \tag{2.25}$$

where α is the empirical parameter which varies from 0 to 1. The Cole and Cole model has been used in rock physics modeling by several authors. Behura et al.

(2007) suggested that the model has a good fit with their frequency-dependent measurement data on the Uvalde heavy oil. Furthermore, Gurevich et al. (2008) and Makarynska et al. (2010) used the Cole and Cole model in their rock physics modeling on heavy-oil saturated rock. Figure 2.3 shows the real and imaginary parts of the complex shear modulus. Although the Cole and Cole model has a wider transition zone (quasi-solid state) than the Maxwell model, depending on the empirical parameter, α, it still has symmetric distribution with $\omega\tau_s = 1$.

Davidson and Cole (1951) modified the Cole and Cole model as:

$$G_\eta^* = G_\infty \left[1 - \frac{1}{\left[1 + (i\omega\tau_s)\right]^\gamma} \right], \tag{2.26}$$

where γ is an another constant parameter, which also varies from 0 to 1. The Davidson and Cole model has asymmetric distribution with $\omega\tau_s = 1$ (Figure 2.3). In contrast, Havriliak and Negami (1967) generalized the above two models to propose the following formula:

$$G_\eta^* = G_\infty \left[1 - \frac{1}{\left[1 + (i\omega\tau_s)^{1-\alpha}\right]^\gamma} \right], \tag{2.27}$$

where two constant empirical parameters, α and γ, are introduced; α and γ also vary from 0 to 1. The Havriliak and Negami model has an asymmetric distribution with $\omega\tau_s = 1$ like the Davidson and Cole model (Figure 2.3), but the real part shows a more gentle rising as $\omega\tau_s$ increases. Han et al. (2007a) compared the ultrasonic S-wave velocity measurement data with the empirical models and reported that the Havriliak and Negami model has the best fit with them.

The bulk modulus in the multi-phase relaxation models can be formulated as well as the shear modulus, as followed by:

$$K^* = K_0 + K_\eta^* = K_0 + K_2\left[\frac{(i\omega\tau_b)^{1-\alpha}}{1+(i\omega\tau_b)^{1-\alpha}}\right], \tag{2.28}$$

for the Cole and Cole model,

$$K^* = K_0 + K_\eta^* = K_0 + K_2\left[1-\frac{1}{[1+(i\omega\tau_b)]^{\gamma}}\right], \tag{2.29}$$

for the Davidson and Cole model,

$$K^* = K_0 + K_\eta^* = K_0 + K_2\left[1-\frac{1}{\left[1+(i\omega\tau_b)^{1-\alpha}\right]^{\gamma}}\right], \tag{2.30}$$

for the Havriliak and Negami model, respectively. It is noted that K_η^* and G_η^* in the models are the complex bulk and shear moduli induced by the corresponding viscosities. Moreover, the viscosity-induced complex bulk and shear moduli are decomposed into the real and imaginary parts; the real parts are expressed by K_η' and G_η' while the imaginary parts are expressed by K_η'' and G_η'', respectively.

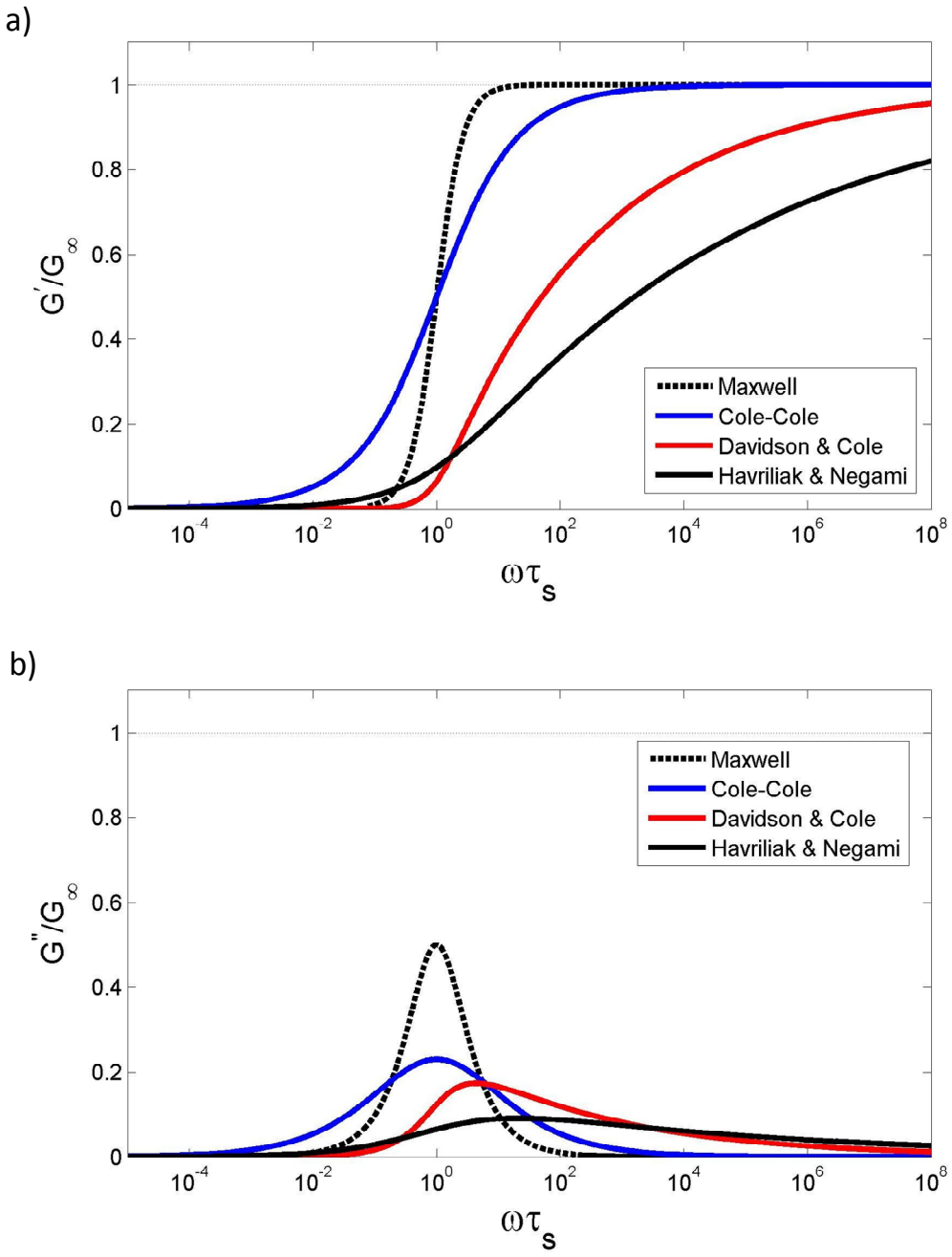

Figure 2.3. Normalized complex shear modulus of the Maxwell, Cole-Cole, Davidson and Cole, and Havriliak and Negami models; (a) real and (b) imaginary parts. The constant parameters in the models are $\alpha = 0.45$ and $\gamma = 0.17$.

2.3 Ultrasonic Velocity Measurement Data

I used the ultrasonic velocity measurement data on heavy oils from Liu et al. (2007) to investigate the relationship between the bulk and shear moduli at high frequency. Liu et al. (2007) measured ultrasonic P-and S-wave velocities over a wide temperature range for several heavy-oil samples by using acoustic reflection and transmission methods (Han et al., 2008). Table 2.1 shows the summary of the samples used and Figure 2.4 shows the P- and S-wave velocities as a function of temperatures for all the samples. It is noted that the measurements have been conducted at the atmospheric pressure and frequency of 1.0 MHz and that most of the samples have been taken from heavy-oil fields in Canada. Also, note that results for sample #5 will be mainly presented in the latter analysis because the measurements were the most densely performed.

Table 2.1. Summary of the ultrasonic velocity measurement data on heavy-oil samples (After Liu et al. 2007).

Sample ID	Specific Gravity	API Density (°API)	Minimum Temperature (˚C)	Maximum Temperature (˚C)	Number of Measurement	Sampling Place
1	0.897	26.25	3.1	32.8	4	China
2	0.943	18.52	2.6	23.9	4	Unknown
3	0.970	14.36	-40.7	-6.8	10	Unknown
4	0.993	10.97	3.7	45.4	4	Venezuela
5	1.004	9.38	-47.5	67.1	20	Canada
6	1.006	9.23	-44	-6.3	9	Unknown
7	1.006	9.20	2.5	86.4	9	Canada
8	1.010	8.61	-40.5	54.8	18	Unknown
9	1.010	8.60	-31.5	80	20	Unknown
10	1.014	8.05	-5.4	40.3	13	Canada

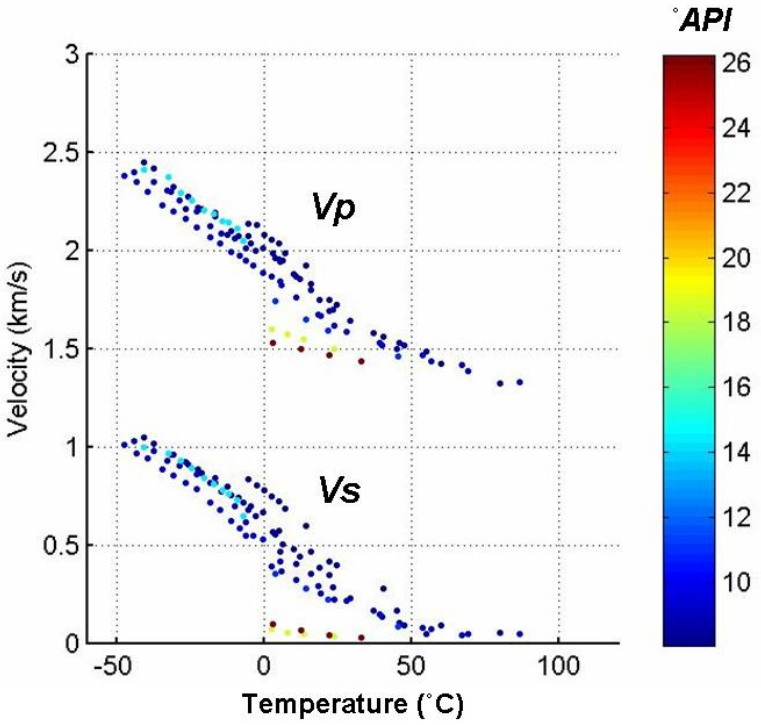

Figure 2.4. Ultrasonic P- and S-wave velocities of the heavy oils as a function of temperature. The color corresponds to the API gravity.

2.4 Shear Viscosity Model

To model elastic properties of heavy oil as a function of temperatures with the viscoelastic model, a relationship between temperature and viscosity is required. Beggs and Robinson (1975) developed a relationship between dead oil shear viscosity and temperature as follows:

$$\eta_s = 10^X, \tag{2.31}$$

where

$$\begin{aligned} X &= yT^{-1.163}, \\ y &= 10^Z, \\ Z &= 3.0324 - 0.02023\gamma. \end{aligned} \tag{2.32}$$

In addition, γ is the API gravity degrees; T is temperature degrees in Fahrenheit. Furthermore, De Ghetto et al. (1995) published a set of modified model for dead oil shear viscosity as follows:

$$\mathrm{Log}_{10}\left(\mathrm{Log}_{10}\left(\eta_s+1\right)\right)=1.90296-0.012619\gamma-0.61748\,\mathrm{Log}_{10}\left(T\right), \quad (2.33)$$

for extra heavy oil (˚API <10), and

$$\mathrm{Log}_{10}\left(\mathrm{Log}_{10}\left(\eta_s+1\right)\right)=2.06492-0.0179\gamma-0.70226\,\mathrm{Log}_{10}\left(T\right), \quad (2.34)$$

for heavy oil (10 to 22.3 ˚API).

Figure 2.5 shows temperature dependence of the Beggs and Robinson model and the De Ghetto model. Although the models have been widely used in the industry, their estimation at lower temperatures than room temperature may be less reliable (e.g., Batzle et al., 2006). Hossain et al. (2005) compared several empirical viscosity models with the measurement data on heavy oils and concluded that the existing models cannot reasonably predict shear viscosity at the lower temperatures. In addition, Han et al. (2009) compared the existing models with each other at different temperatures and reported that there are significant differences at temperatures lower than 20 ˚C. They pointed out three potential problems for the existing models. The first one is that the models have been constructed mostly based on the measurements at temperatures higher than room temperature. The second one is that all the existing models are a function of API gravity. Hinkle et al. (2007) conducted the dynamic rheometrical measurements on heavy oils. They reported that shear viscosity does not correlate well to the API gravity and suggested that heavy oils may have a shear viscosity specially constituted with its composition. The last one is the temperature unit. The models which contain temperature

in a logarithm cannot work in the minus degree range of temperatures. Thus, Han et al. (2009) proposed a modified formula of the shear viscosity based on the De Gheutto model to overcome the problems as:

$$\eta_s = 10^x - 1, \tag{2.35}$$

where

$$\begin{aligned} x &= 10^y, \\ y &= a + b\,\mathrm{Log}_{10}(T_K) + c(\mathrm{Log}_{10}(T_K))^2. \end{aligned} \tag{2.36}$$

In addition, T_K is the absolute temperature (°K) and *a*, *b*, and *c* are empirical parameters. If the shear viscosity measurement data over wide temperature range are available, the empirical parameters can be determined by correlating the measurement data. However, the data are not available in most cases. Han et al. (2009) suggested that the parameters may be determined by calibration with the ultrasonic S-wave velocity data with the glass and liquid points. As I previously discussed, the glass and liquid points are defined by the specified shear viscosities; 10^3 cP for the liquid point and 10^{15} cP for the glass point. Furthermore, shear velocities at the glass and liquid points are practically defined by individual criteria (Han et al., 2008). Thus, if one has an S-wave velocity curve in the wide temperature range from the glass to liquid points, it is possible to find the temperature at the points. From the relationship between the temperature and viscosity, the parameters can be determined.

In this study, I use the Equation (2.35) and (2.36) as the shear viscosity model. For the heavy-oil samples of Liu and Han (2007), direct measurements of the shear viscosity are not available. Thus, I use the S-wave velocity correction method to determine the

parameters for each sample. Figure 2.5 shows the estimated shear viscosity of sample #5, in which the determined parameters are $a = 62.9$, $b = -44.9$, and $c = 8.1$. The estimated shear viscosity shows a more gentle temperature dependence in the lower temperature range and good agreement with the existing models in the higher temperature range.

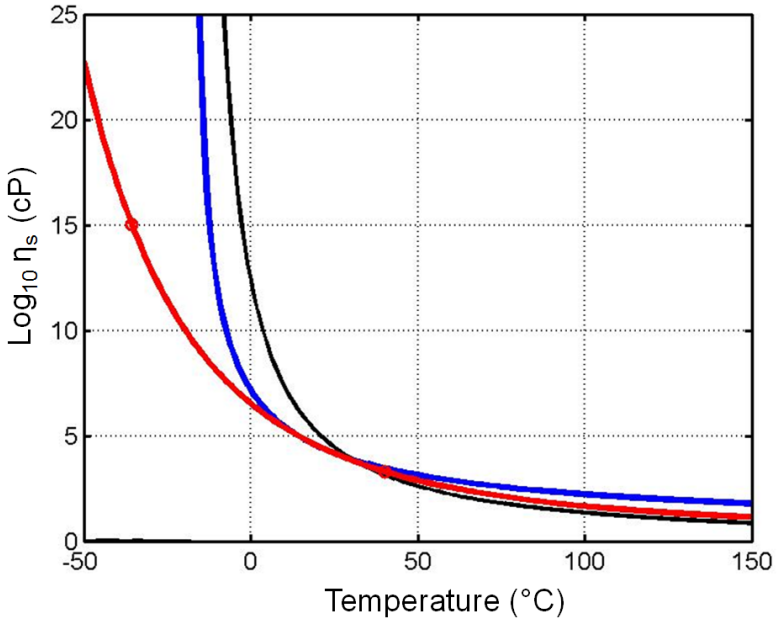

Figure 2.5. The estimated shear viscosity of sample #5 (9.38 ˚API). The black and blue curves represent the Beggs and Robinson model and De Ghetto model, respectively. The red curve corresponds to the estimated values by the Equation (2.38) and (2.39) with the S-wave velocity calibration.

2.5 Analysis of Velocity Measurement Data

I will describe the analyzed results of the velocity measurement data based on the shear viscosity model. They mainly consist of three parts; viscoelastic modeling of shear modulus, the relationship between shear and bulk viscosities, and viscoelastic modeling of bulk modulus and velocities.

2.5.1 Viscoelastic Modeling of Shear Modulus

To compute the bulk and shear moduli from the P- and S-wave velocities in the case of an isotropic medium, the density is required. In the database of Liu and Han (2007), density measurements are not available. Thus, assuming that temperature dependences of the density are the same as that of conventional oil, they are calculated by the Fluid Application of Geophysics (FLAG) software package (e.g., Liu, 2006), that the FLUID/DHI consortium has developed based on laboratory measurements along with the theories. However, the FLAG program has the allowable temperatures from 15.6 °C to 180 °C for calculating oil density, whereas I need the values at lower temperatures. Thus, by making the additional assumption that the trend of the oil density does not significantly change above and below the temperature limitations, the formulas in the FLAG program are used for calculating the values over the temperature limitations. Figure 2.6 presents the oil densities calculated by the FLAG program along with the extrapolation, showing the estimated density simply decreases with the temperature. Furthermore, the static bulk modulus (K_0) is also required for evaluating the bulk viscosity. Similarly, the values are estimated by the FLAG program with the extrapolation (Figure 2.6).

Figure 2.7 shows temperature dependence of the measured P- and S-wave velocities, in which the solid curve represents the P-wave velocity of conventional oil, showing an almost linear trend with temperature (Han et al., 2008). As temperature decreases, the S-wave velocity starts to have a finite value at around 60 ˚C. Shear viscosity at the temperature is nearly 10^3 cP, which corresponds to the liquid point by the definition. Similarly, the P-wave starts to deviate from the conventional oil's trend at around the temperature, suggesting that the heavy oil becomes a quasi-solid state under the temperature. The velocities are converted to moduli by using the estimated density (Figure 2.8). The shear modulus has a finite value at lower temperatures than the liquid point. The shear modulus at the glass point (10^{15} cP) has a value of 0.83 GPa. This is a consequence of the fact that the shear viscosity is calibrated with the S-wave velocity. The bulk modulus starts to deviate from the static bulk modulus (K_0) at around the liquid point.

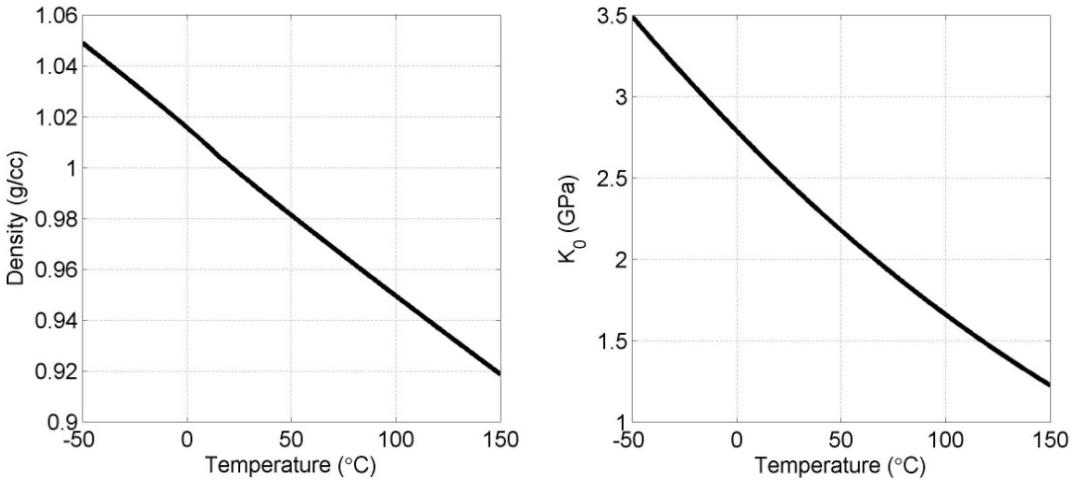

Figure 2.6. Density and static bulk modulus (K_0) of heavy oil (9.38 °API) as a function of temperature.

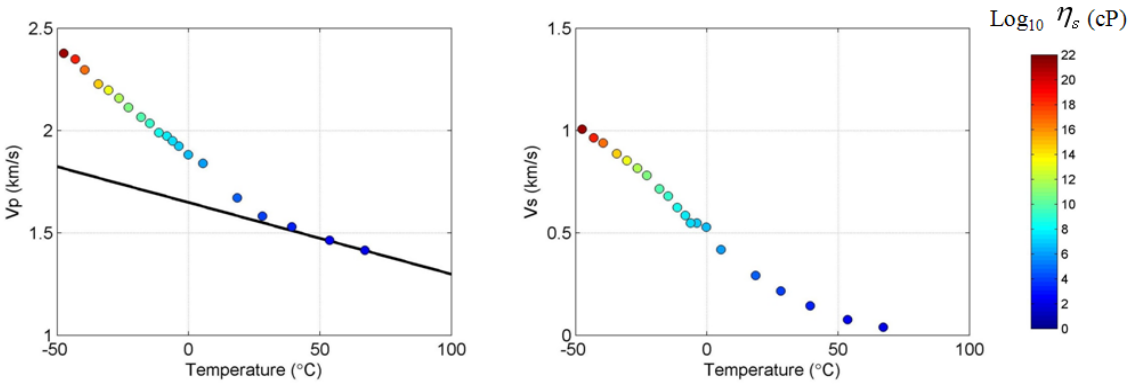

Figure 2.7. P- and S-wave velocities of sample #5. The colors correspond to the estimated shear viscosity. The solid curve represents the corresponding values for the conventional oil.

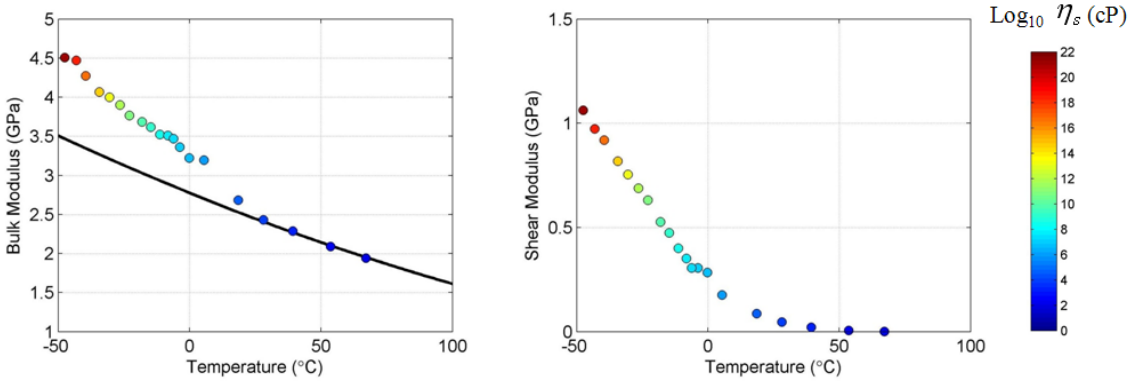

Figure 2.8. Bulk and shear moduli of sample #5. The colors correspond to the estimated shear viscosity. The solid curve represents the static bulk modulus (K_0).

As I mentioned before, Han et al. (2007a) reported that the Havriliak and Negami model has the best fit with the ultrasonic velocity measurement data. However, in their analysis, the De Ghetto's extra heavy-oil model was applied as the shear viscosity model. Since the De Ghetto model may be less reliable at lower temperatures, we need to reevaluate the viscoelastic model by using the calibrated shear viscosity model.

Figure 2.9 shows the four different viscoelastic models of the shear modulus with the measurement data, where G_∞ is set to be 0.83 GPa. The constant parameters required in the model are determined by the best fit in least-square fashion; $\alpha = 0.81$ for the Cole and Cole model, $\gamma = 0.11$ for the Davidson and Cole model, and $\alpha = 0.50$ and $\gamma = 0.21$ for the Havriliak and Negami model. One can see that the Maxwell and the Cole and Cole models do not fit with the measurement data because the models have a symmetric distribution with $\mathrm{Log}_{10}\omega\tau_s = 0$. In contrast, the Davidson and Cole and Havriliak and Negami models, showing the asymmetric distribution, have much better agreement with the data. Although both the models have almost the same curves at high $\omega\tau_s$, they have substantial differences at lower $\omega\tau_s$. The Davidson and Cole model shows shaper rising in the range while the Havriliak and Negami model more correctly follows the data trend in the range. Therefore, the Havriliak and Negami model is used for the latter analysis. These results are consistent with the previous study (Liu and Han, 2006).

The Havriliak and Negami model is used to predict the temperature and frequency dependences of the complex shear modulus (G_η^*) of sample #5. Figure 2.10 shows the temperature dependence of the real, imaginary parts, and the attenuation at 100 Hz, 10 kHz, and 1 MHz. The attenuation is calculated by Equation (2.17). As temperature decreases, the real part G_η' starts to rise. However, the temperature where the real part G_η' starts to rise is different with the wave frequency. At lower frequencies, the temperature is lower and the rising curve is steeper. Figure 2.11 shows the frequency dependence of them at 10 °C, 30 °C, and 100 °C. Similarly, as the frequency increases, the real part G_η'

starts to rise. At lower temperatures, the frequency where the substantial rising occurs is lower.

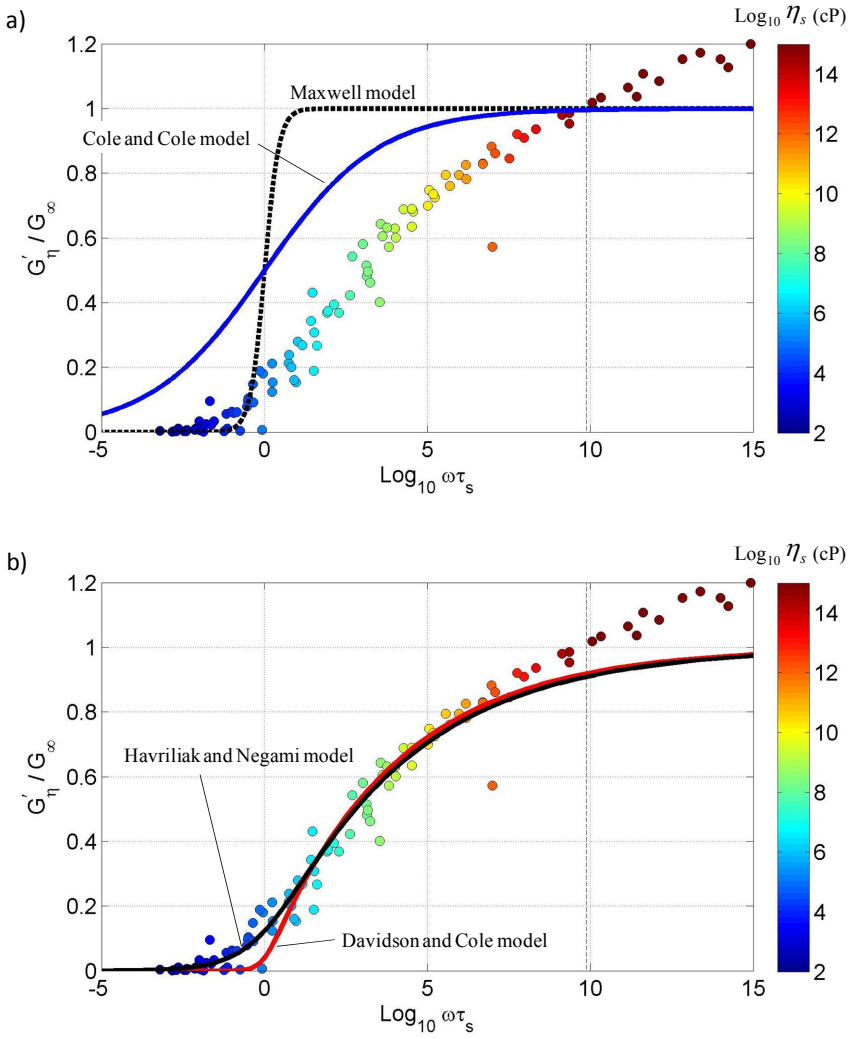

Figure 2.9. Relative shear modulus (G'_η / G_∞) vs. $\mathrm{Log}_{10}\, \varpi\tau_s$. The circles represent the measurement data. The color represents the estimated shear viscosity. The black dot, blue, red, and black solid curves represent the Maxwell, Cole and Cole, Davidson and Cole, and Havriliak and Negami models, respectively.

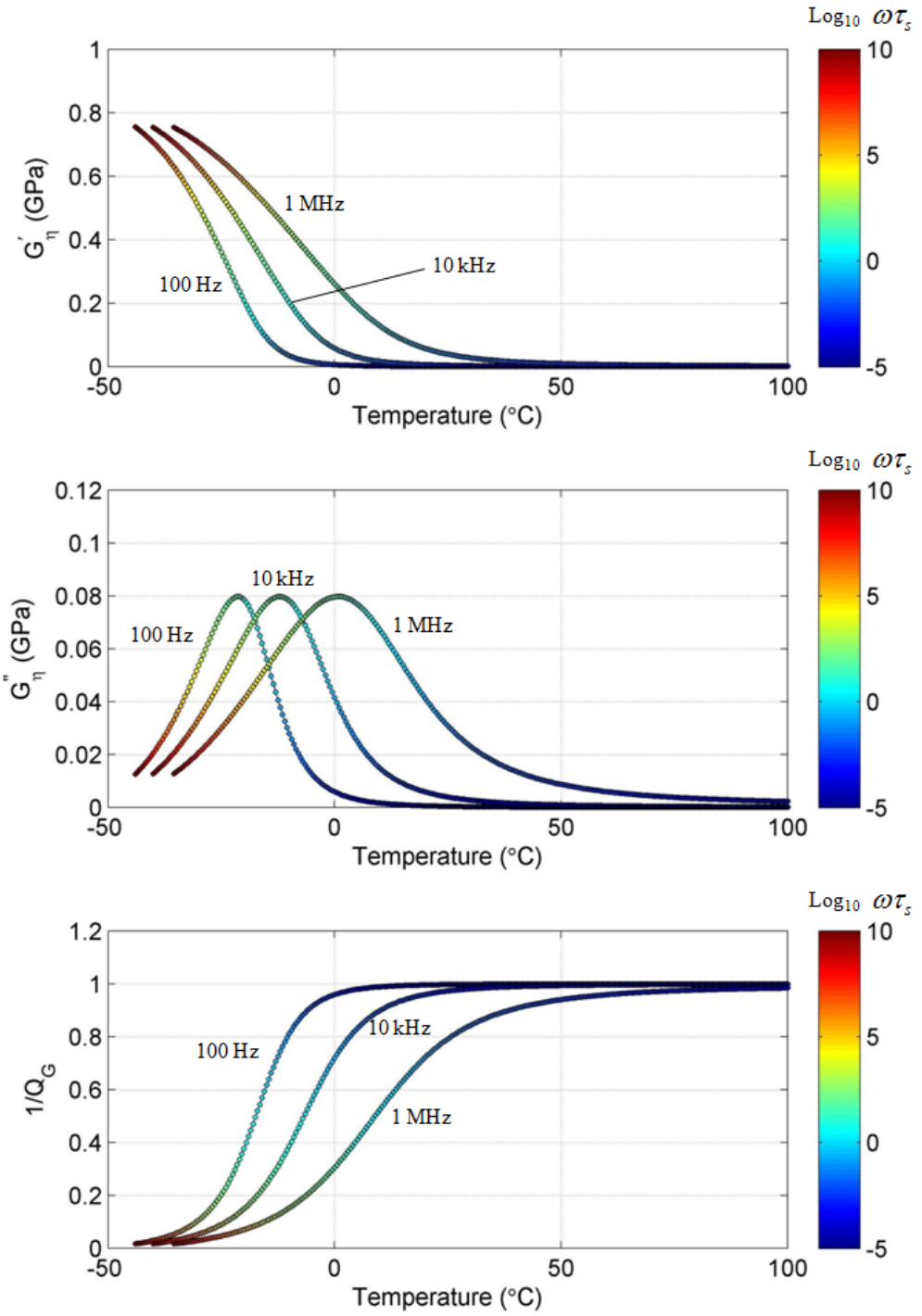

Figure 2.10. Temperature dependence of real part, imaginary part, and attenuation (1/Q) of shear modulus at 10 Hz, 10 kHz, and 1 MHz for sample #5 (9.38 °API). The color represents the $\omega\tau_s$ in logarithmic scale.

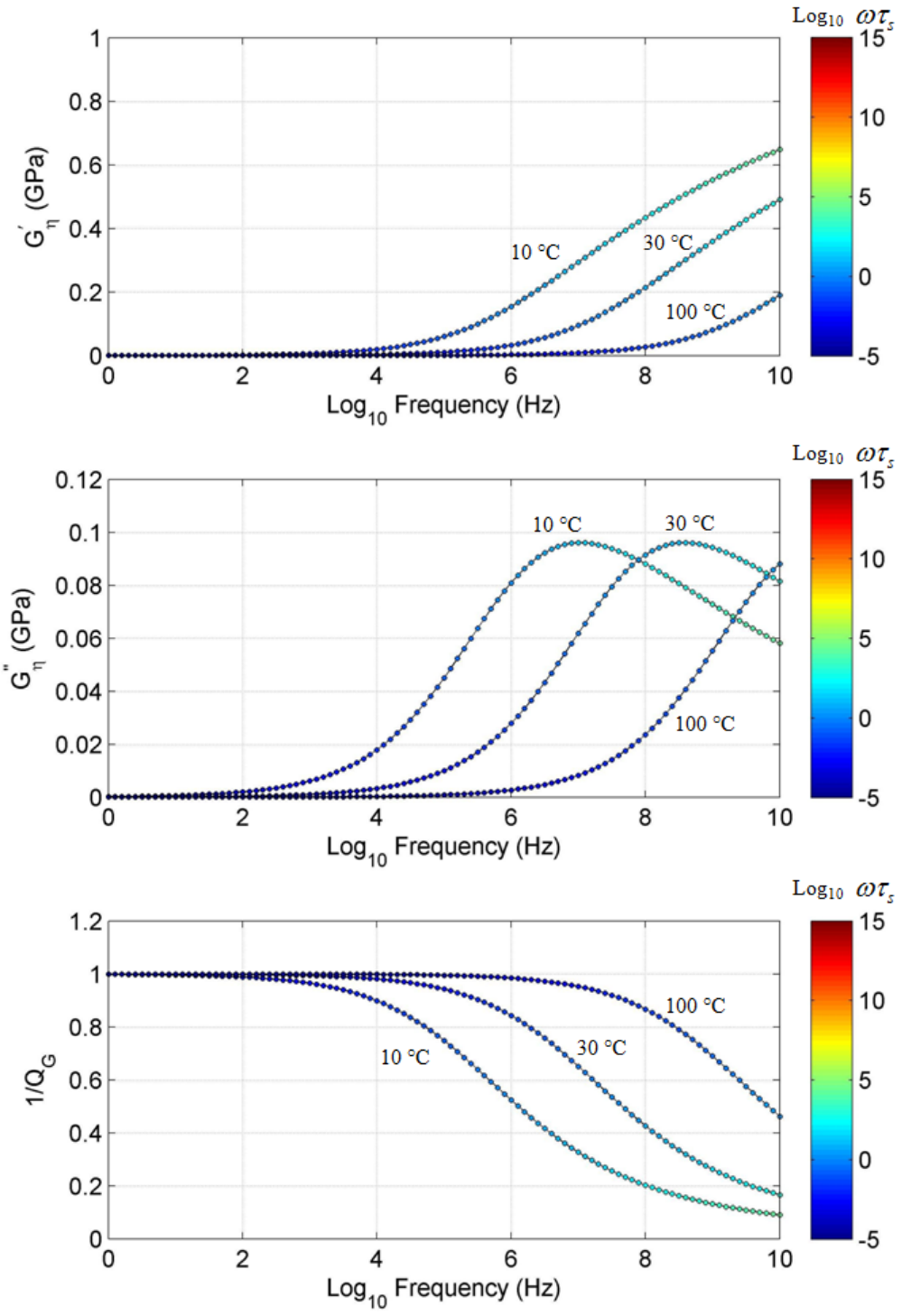

Figure 2.11. Frequency dependence of real part, imaginary part, and attenuation (1/Q) of shear modulus at 10 °C, 30 °C, and 100 °C for sample #5 (9.39 °API). The color represents the $\omega\tau_s$ in logarithmic scale.

2.5.2 Relationship between Shear and Bulk Viscosities

The bulk modulus (K'_η) induced by the bulk viscosity will be evaluated by calculating the amount of the deviation of the bulk modulus from the K_0 (Figure 2.8). Figure 2.12 shows the relationship between the viscosity-induced shear modus (G'_η) and bulk modulus (K'_η) for the same sample as in Figure 2.8. With increasing shear viscosity from the liquid point, K'_η increases more rapidly than G'_η. At around 10^8 cP in the shear viscosity, K'_η increases at a reduced rate and G'_η starts to increase significantly. When the shear viscosity comes closer to the glass point, G'_η and K'_η have similar magnitudes.

Figure 2.13 shows the same cross plot as the Figure 2.12 but for all the samples. Although they are more scattered, they still show a similar trend as that of sample #5. The data scatter could be caused by a variety of basic oil properties such as compositions, density, and molecular structure. However, since there are not sufficient data for evaluating their dependences on the relationship, I assume a simple single relationship to obtain the fitting curve for all the samples. After careful tests, the fitting curve is determined to be cubic below the glass point and linear above the glass point as:

$$K'_\eta = 2.81G'^3_\eta - 5.34G'^2_\eta + 3.67G'_\eta, \tag{2.37}$$

for the quasi - solid state (from 10^3 cP to 10^{15} cP in shear viscosity), and

$$K'_\eta = 1.17G'_\eta, \tag{2.38}$$

for the elastic - solid state (above 10^{15} cP in shear viscosity). The solid curves in Figure 2.13 represent the fitting curve. The correlation coefficient is 0.906 for all the samples.

Based on the definition of the glass point (η_s = 10^{15} cP), K_2 can be determined to be 0.97 GPa by the fitting curves.

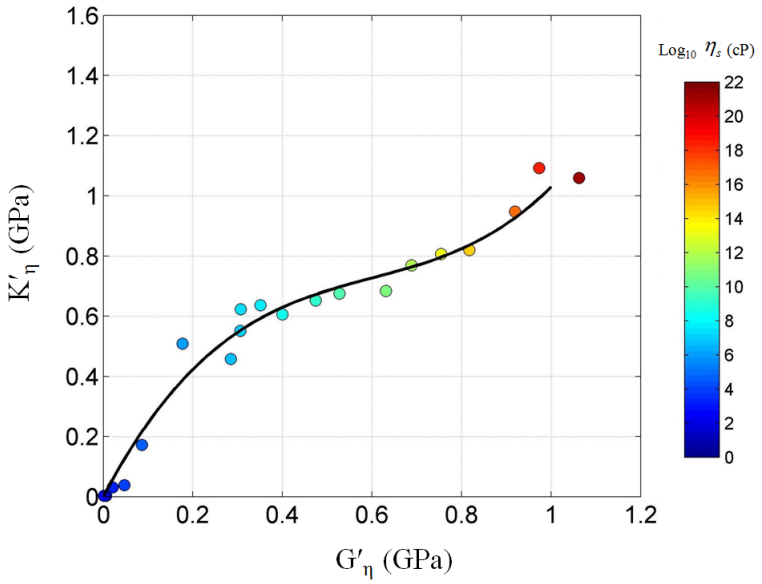

Figure 2.12. K'_η vs. G'_η for sample #5. The solid curve represents the fitting line. The color represents the shear viscosity.

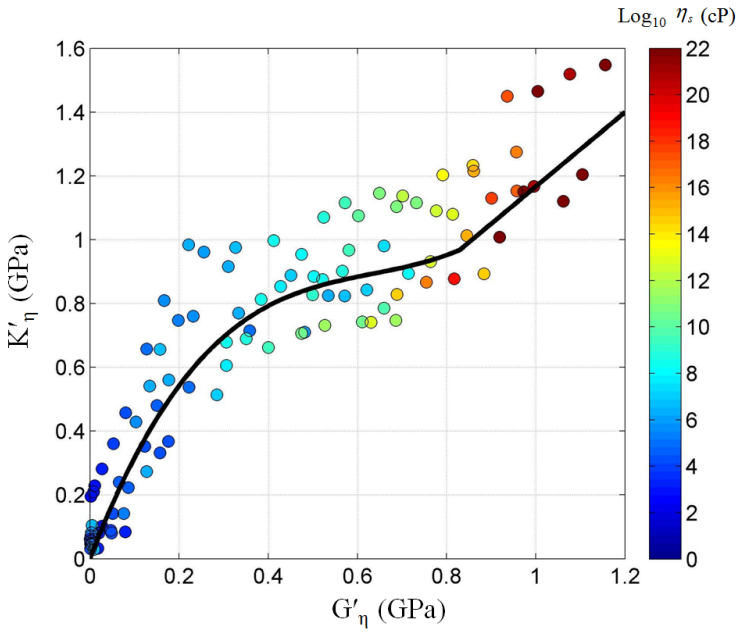

Figure 2.13. K'_η vs. G'_η for all the samples. The solid curve represents the fitting line. The color represents the shear viscosity.

Next, I derive the relationship between the shear and bulk viscosities for the heavy oils. In the derivation, I assume that the viscoelastic model, which is fitted with the shear modulus, is applicable to the bulk modulus. Furthermore, the empirical relationship between G'_η and K'_η (Equation (2.37)) is assumed to be reasonably valid. Procedures of the derivation are as follows;

(1) K_2 is set to be 0.97 GPa based on the relationship between shear and bulk modulus with the shear viscosity (Figure 2.13).

(2) The complex shear modulus G^*_η at high frequency (1 MHz) is computed by the Havriliak and Negami model with the constant parameters.

(3) By using the empirical relationship between K'_η and G'_η as Equation (2.37), K'_η at the quasi-solid state is calculated from the real part of the G^*_η.

(4) The calculated K'_η is fitted by the Havriliak and Negami model with the same constant parameters to obtain optimum τ_b at each temperature.

(5) By comparing the τ_b with the corresponding τ_s, the relationship between shear and bulk viscosities at each temperature is derived.

Figure 2.14 shows the resulting relationship between the shear and bulk viscosities for sample #5. The bulk viscosity has a parallel relationship with the shear viscosity at lower than around 10^3 cP and higher than around 10^9 cP in the shear viscosity. A transition region exists between the two regions, where bulk viscosity gradually deviates from the parallel relationship with the shear viscosity. Moreover, using the shear viscosity model,

one can obtain the temperature dependence of the bulk viscosity. Figure 2.15 shows the shear and bulk viscosities as a function of temperature for sample #5.

The bulk viscosity has a similar magnitude as the shear viscosity at around the liquid point (60 °C), where the difference is less than one order of magnitude. As temperature decreases from the liquid point, the bulk viscosity increases at a higher rate than that of the shear viscosity. At around 0 °C, the bulk and shear viscosities are nearly 10^{10} cP and 10^{7} cP, respectively. The difference of temperature dependence between the bulk and shear viscosities may be related with molecular structures of the heavy oil. As I described, the shear viscosity is associated with the translational molecular motion while the bulk viscosity is associated with the rotational and vibrational molecular motions (Temkin, 2001). It is suggested that the molecular motions of the heavy oil have individual temperature dependence. Furthermore, the bulk viscosity is larger than the shear viscosity in the all temperature ranges. It is suggested that the viscosity-induced bulk modulus (K_η') is larger than the viscosity-induced shear modulus (G_η') in the case of satisfying $K_2 > G_\infty$. Thus, it can be emphasized that we should take into account effects of the bulk viscosity, as well as the shear viscosity, for rock physics modeling of heavy-oil saturated rock.

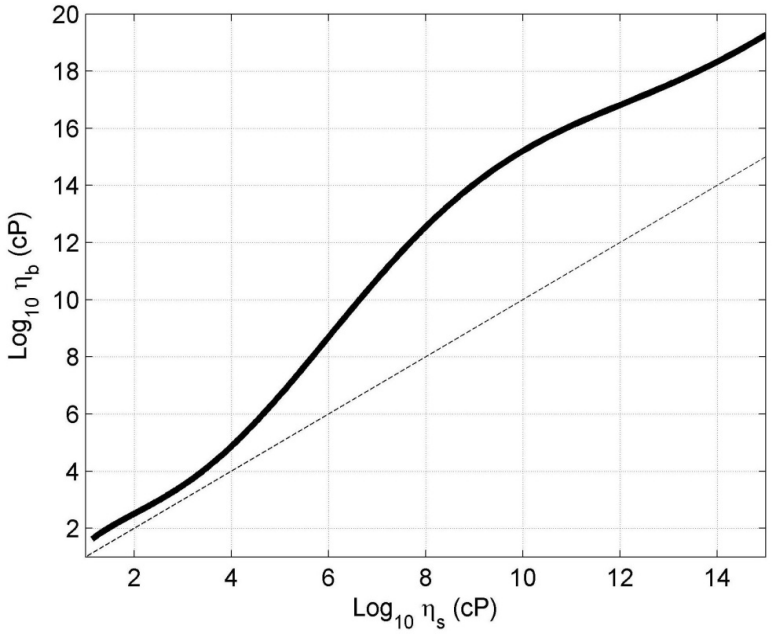

Figure 2.14. Shear viscosity and bulk viscosity.

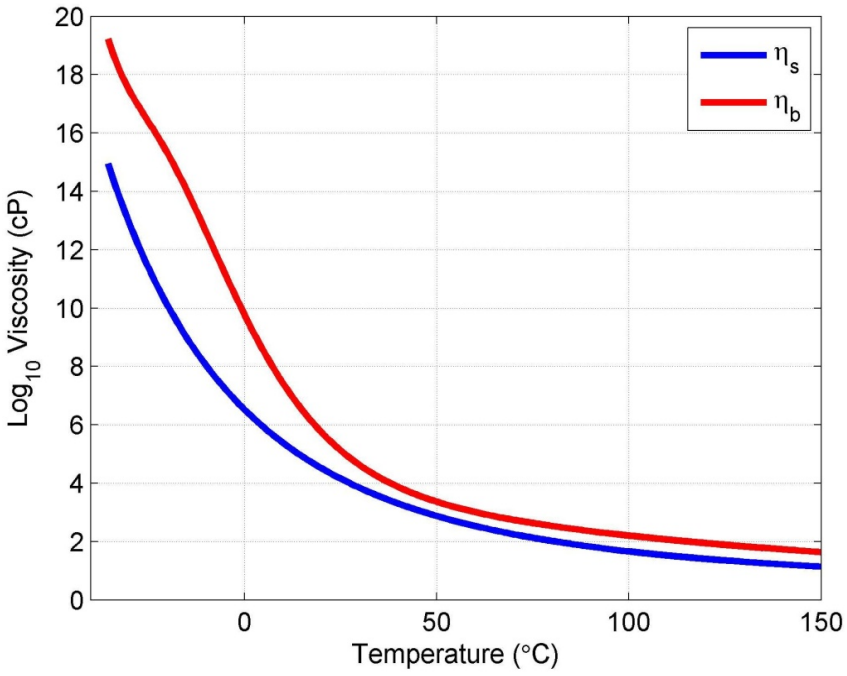

Figure 2.15. Temperature dependence of shear and bulk viscosities for heavy oil with 9.38 ˚API.

2.5.3 Viscoelastic Modeling of Bulk Modulus and Velocities

For a Newtonian liquid, the viscosities are frequency-independent parameters, leading to the relationship between shear and bulk viscosities that is also frequency independent. Assuming that heavy oil is a Newtonian liquid (e.g., Song, 1986), the temperature and frequency dependences of the bulk modulus are predicted by using the relationship.

In the same way as the complex shear modulus (Figures 2.10 and 2.11), Figure 2.16 and 2.17 show the temperature and frequency dependences of the bulk modulus (K_η^*) for the same sample #5. It is obvious that the viscosity-induced bulk modulus (K_η^*) has significant frequency dependence and substantial attenuation. Although the real parts (K_η') have the similar behavior with temperature as the corresponding shear modulus (G_η'), K_η' at lower temperatures than around 40 °C shows steeper rising as temperature decreases. Furthermore, adding to K_η^* the static bulk modulus (K_0), the quantity $K_0 + K_\eta^*$ are obtained (Figures 2.18 and 2.19). The total bulk modulus ($K_0 + K_\eta^*$) also shows significant frequency dependence and substantial attenuation.

Next, using the estimated density (Figure 2.6), the moduli are converted to the complex P- and S-wave velocities by using the Equations (2.17), (2.20), and (2.24). Figures 2.20 and 2.21 show the temperature and frequency dependences of the complex S-wave velocity while Figures 2.22 and 2.23 show the temperature and frequency dependences of the complex P-wave velocity. Like the corresponding shear modulus, the S-wave velocity shows significant velocity dispersion and substantial attenuation. Also, the P-wave

velocity shows the viscoelastic features. It is important that the frequency dependence and attenuation of the P-wave velocity are caused by not only the shear viscosity but also the bulk viscosity, and that the contribution from the bulk viscosity is larger than that of the shear viscosity.

The predicted moduli and velocities are compared to the ultrasonic laboratory measurement data. Figure 2.24 shows the comparison of the real parts of the complex shear and bulk moduli and P- and S-wave velocities for all the samples. Although, in the elastic-solid state (shear viscosity > 10^{15} cP), the predictions tend to underestimate the value, they are virtually consistent with the measurement data in the quasi-solid state. The discrepancy in the elastic-solid state is a consequence of the fact that my model is based on the viscoelastic theory so that it cannot describe the behavior in the elastic-solid state.

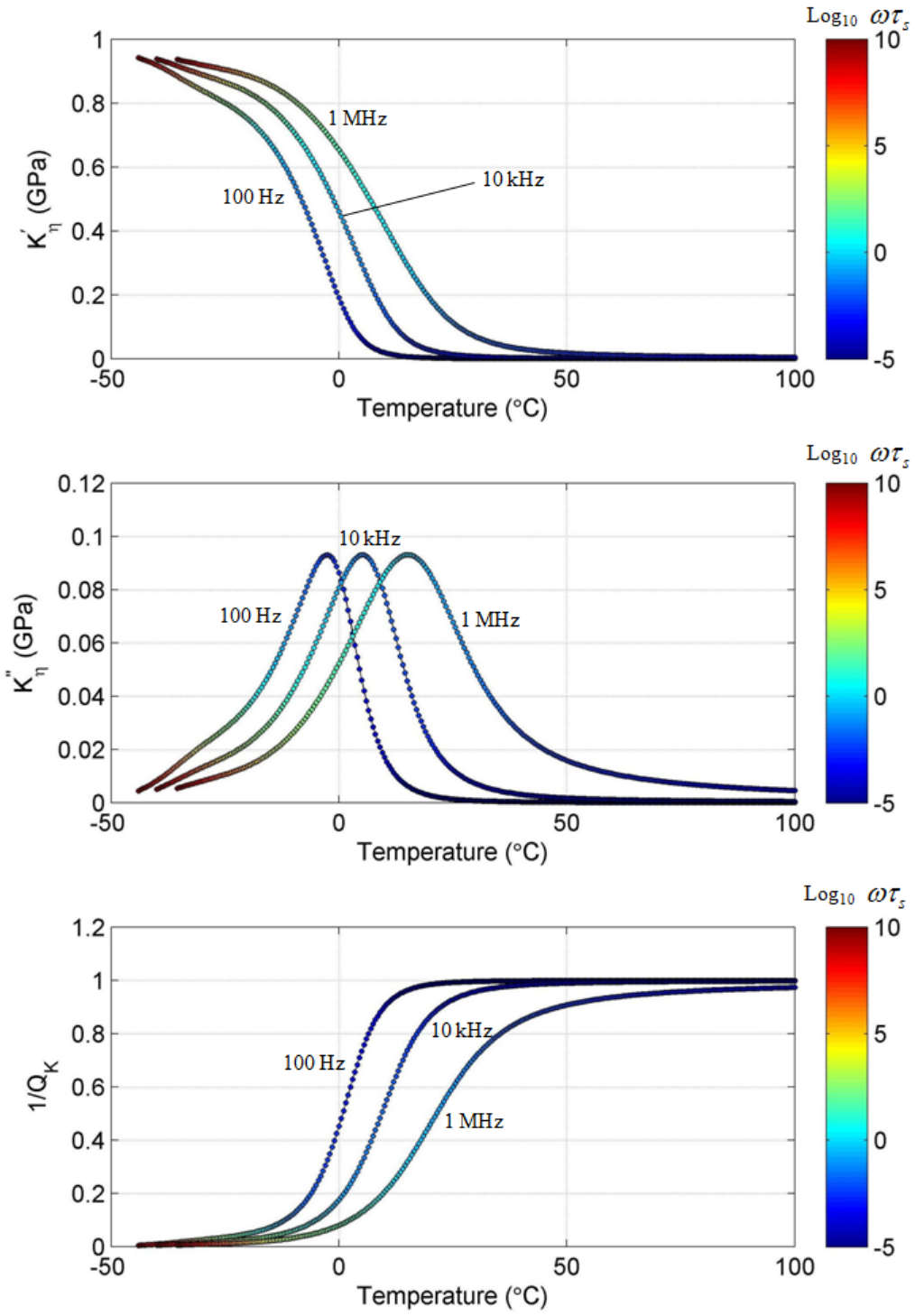

Figure 2.16. Temperature dependence of real part, imaginary part, and attenuation (1/Q) of K_η^* at 10 Hz, 10 kHz, and 1 MHz for sample #5 (9.38 °API). The color represents the $\omega\tau_s$ in logarithmic scale.

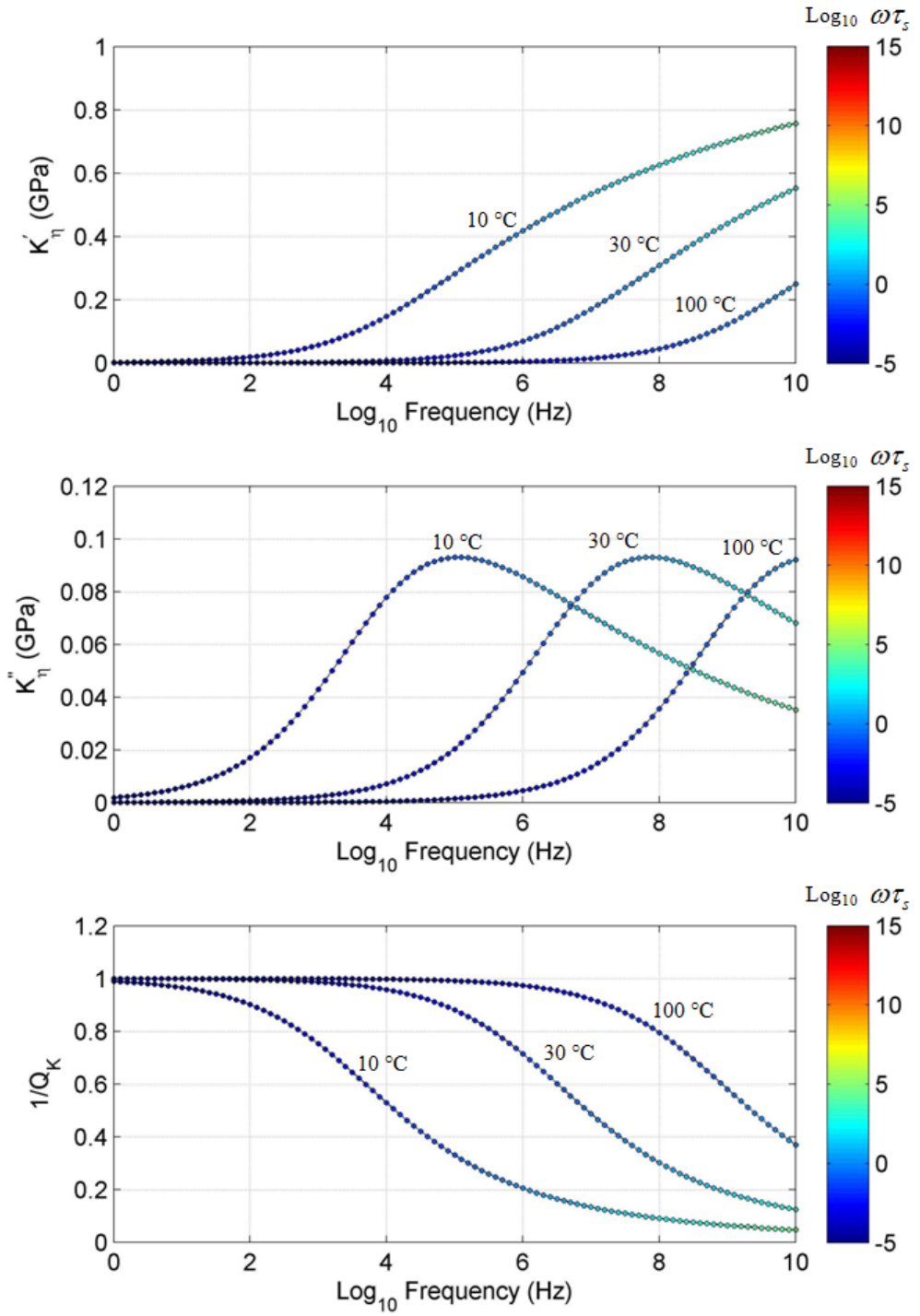

Figure 2.17. Frequency dependence of real part, imaginary part, and attenuation (1/Q) of K_η^* at 10 °C, 30 °C, and 100 °C for sample #5 (9.39 °API). The color represents the $\omega\tau_s$ in logarithmic scale.

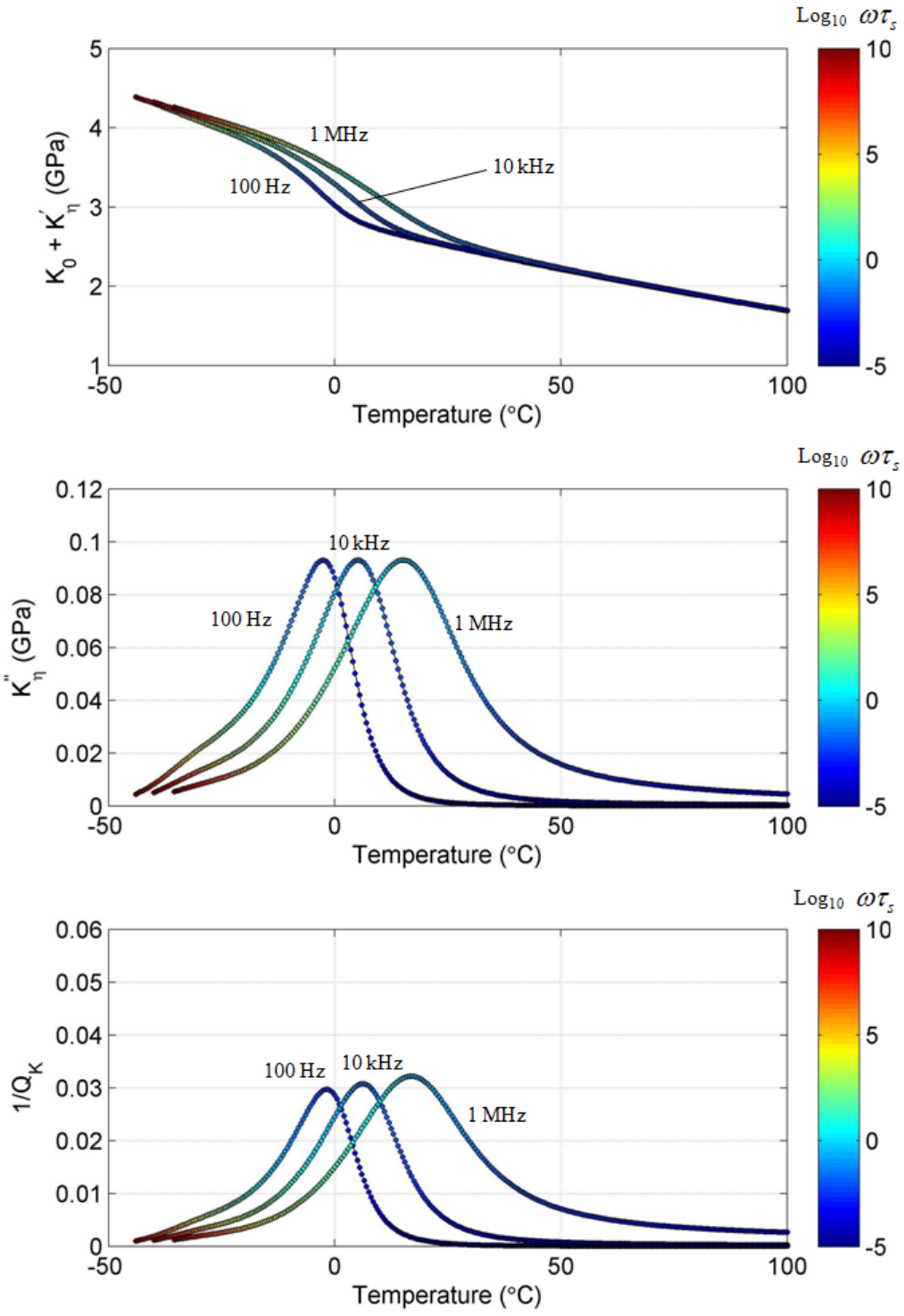

Figure 2.18. Temperature dependence of real part, imaginary part, and attenuation (1/Q) of $K_0 + K_\eta^*$ at 10 Hz, 10 kHz, and 1 MHz for sample #5 (9.38 °API). The color represents the $\omega\tau_s$ in logarithmic scale.

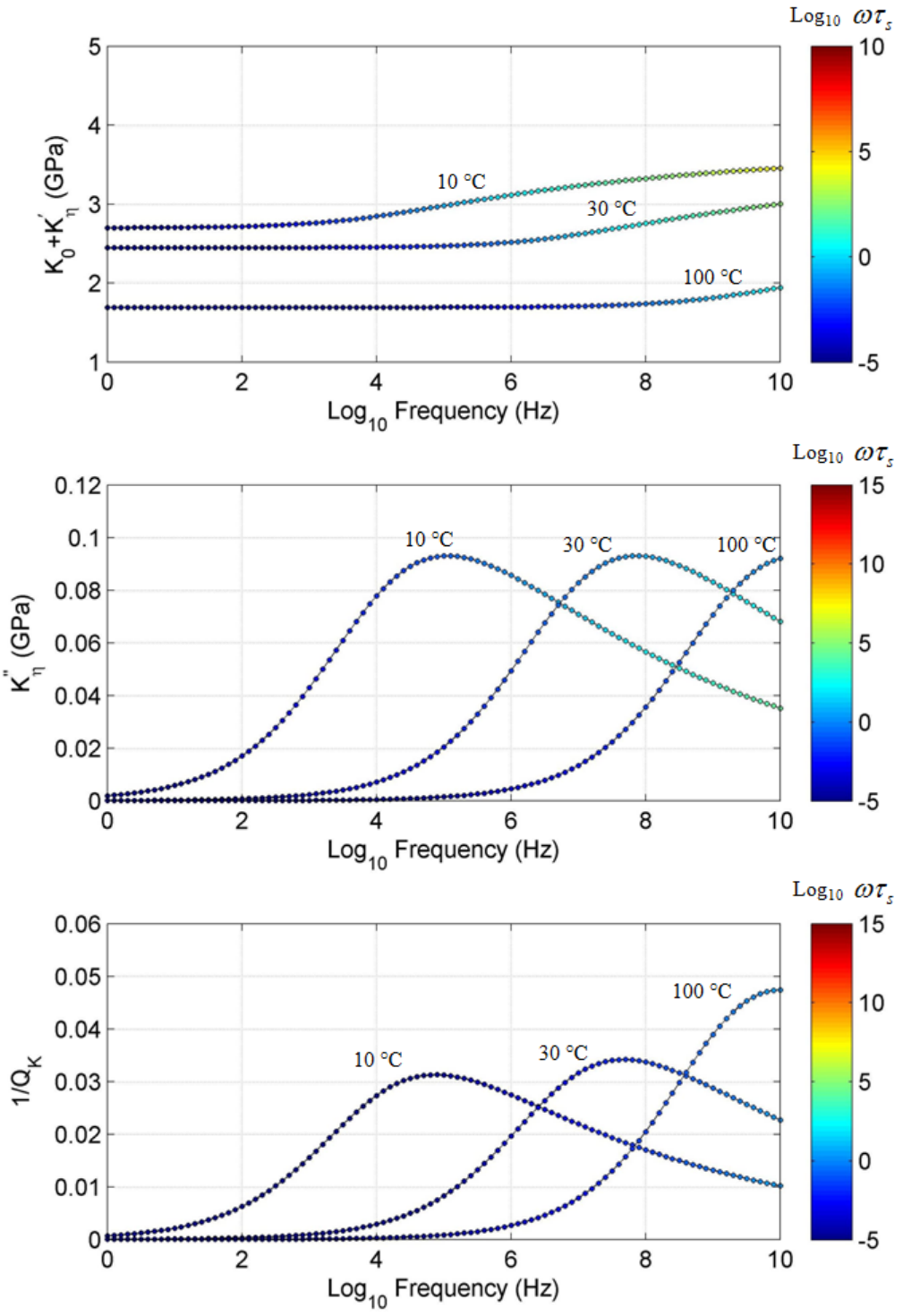

Figure 2.19. Frequency dependence of real part, imaginary part, and attenuation (1/Q) of $K_0 + K_\eta^*$ at 10 °C, 30 °C, and 100 °C for sample #5 (9.39 °API). The color represents the $\omega\tau_s$ in logarithmic scale.

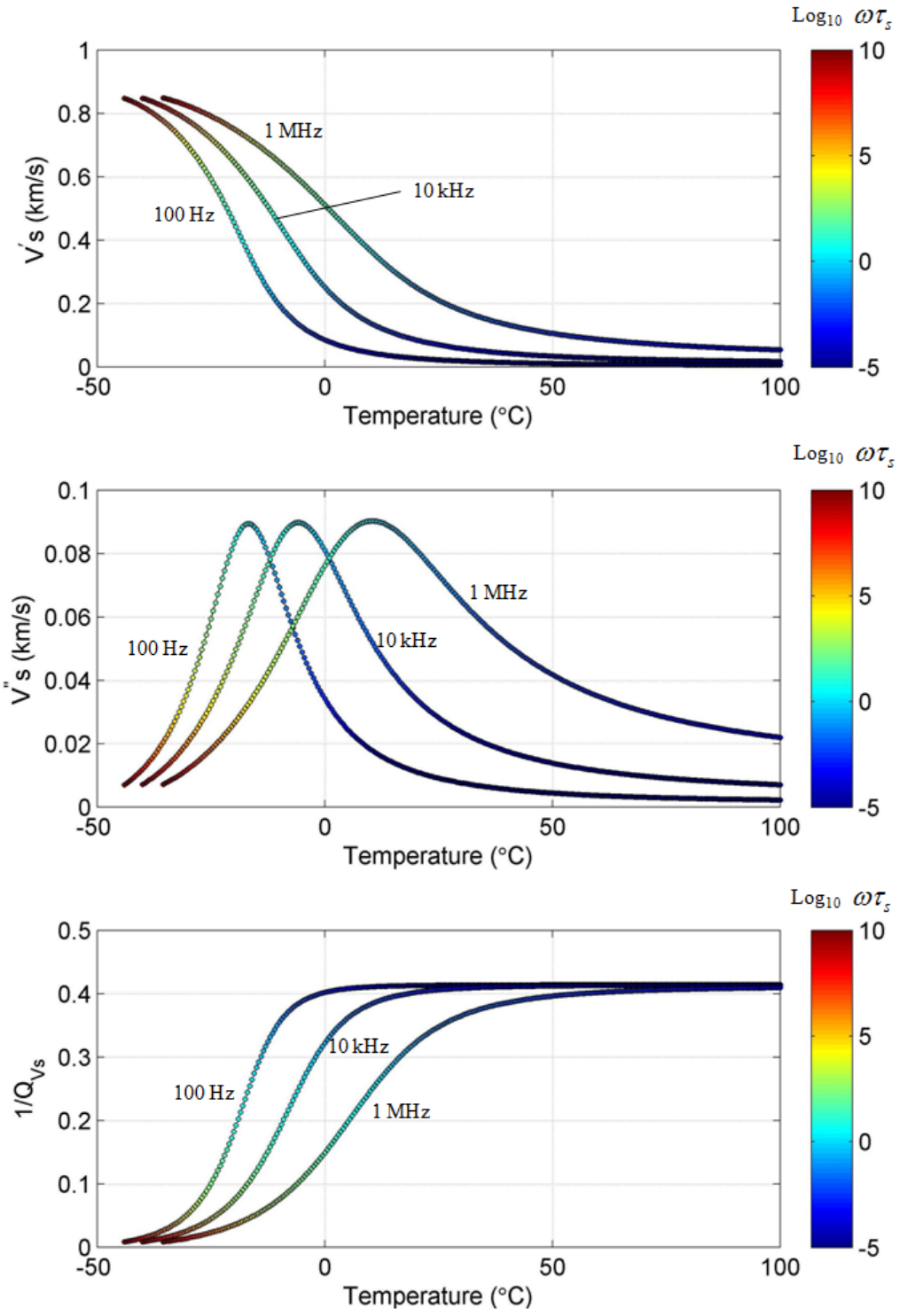

Figure 2.20. Temperature dependence of real part, imaginary part, and attenuation (1/Q) of V_s^* at 10 Hz, 10 kHz, and 1 MHz for sample #5 (9.38 °API). The color represents the $\omega\tau_s$ in logarithmic scale.

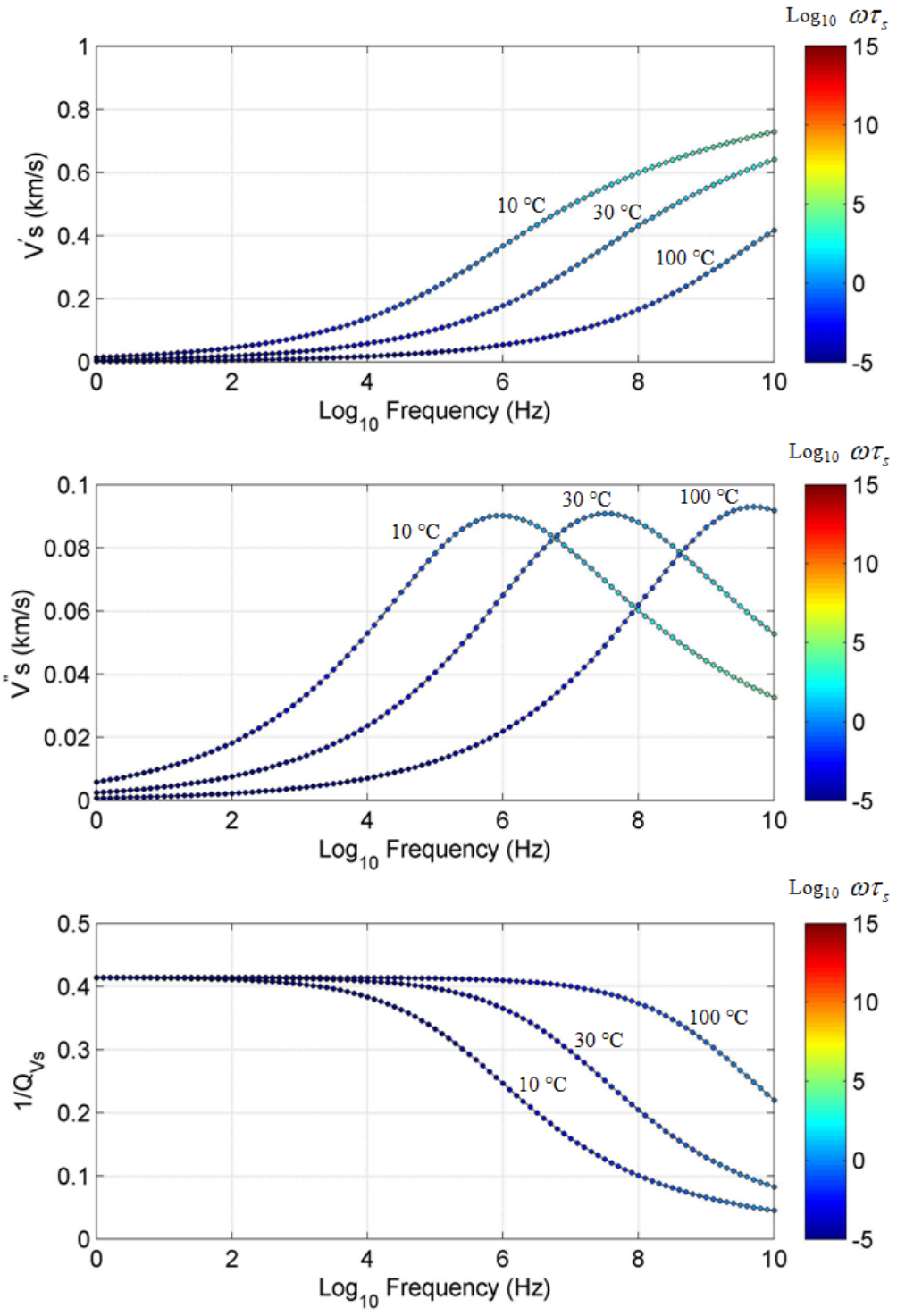

Figure 2.21. Frequency dependence of real part, imaginary part, and attenuation (1/Q) of V_s^* at 10 °C, 30 °C, and 100 °C for sample #5 (9.39 °API). The color represents the $\omega\tau_s$ in logarithmic scale.

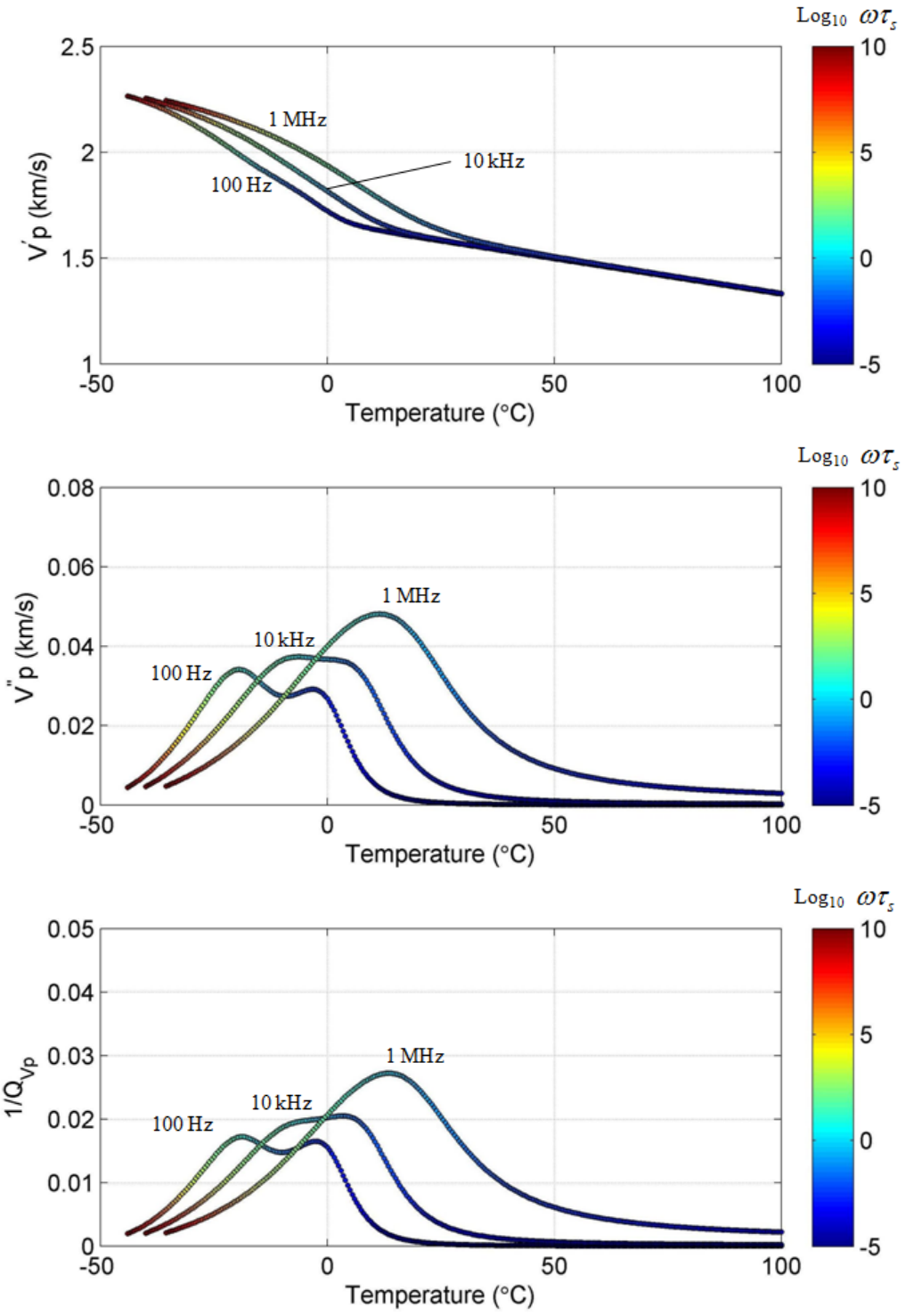

Figure 2.22. Temperature dependence of real part, imaginary part, and attenuation (1/Q) of V_p^* at 10 Hz, 10 kHz, and 1 MHz for sample #5 (9.38 °API). The color represents the $\omega\tau_s$ in logarithmic scale.

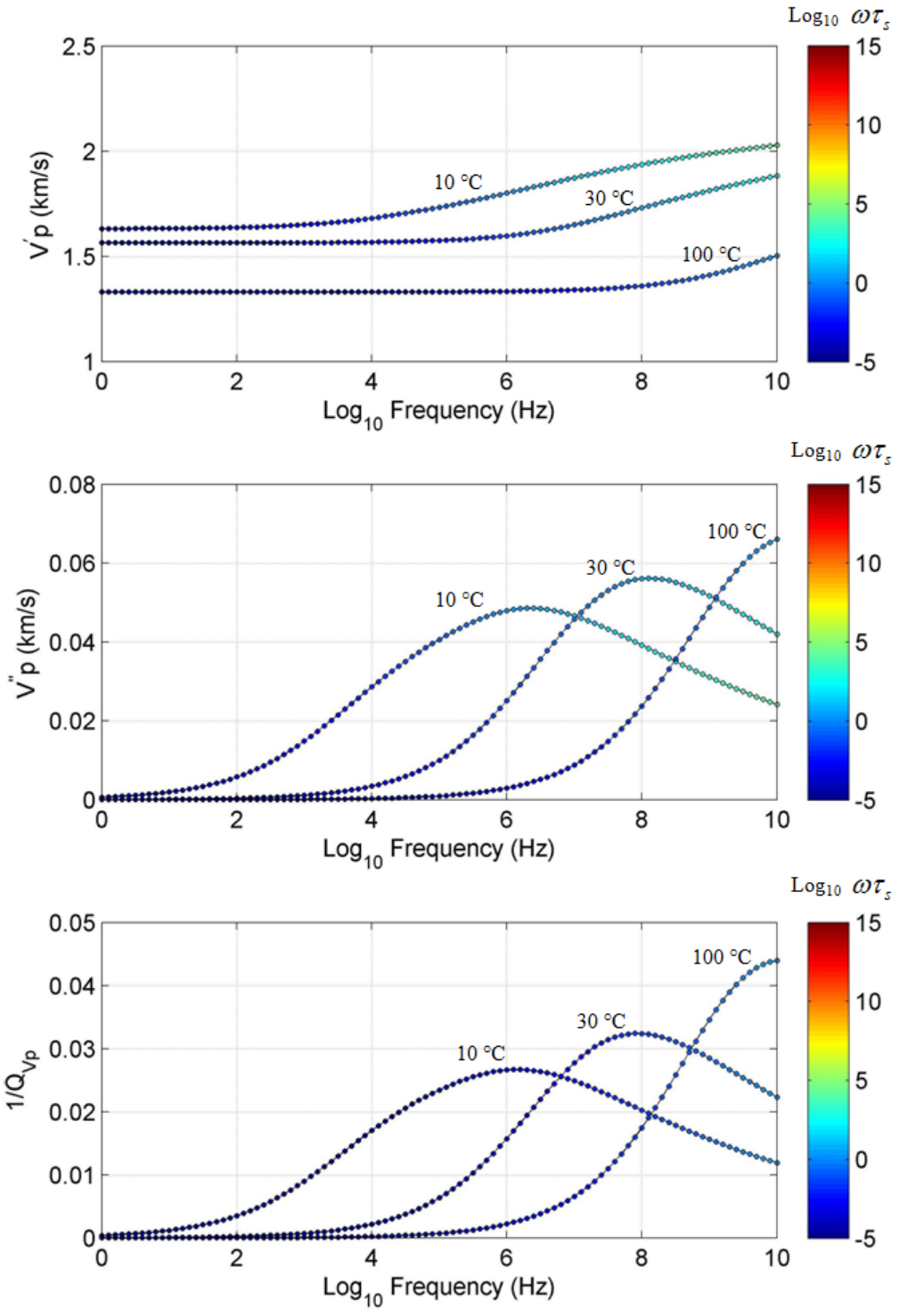

Figure 2.23. Frequency dependence of real part, imaginary part, and attenuation (1/Q) of V_p^* at 10 °C, 30 °C, and 100 °C for sample #5 (9.39 °API). The color represents the $\omega\tau_s$ in logarithmic scale.

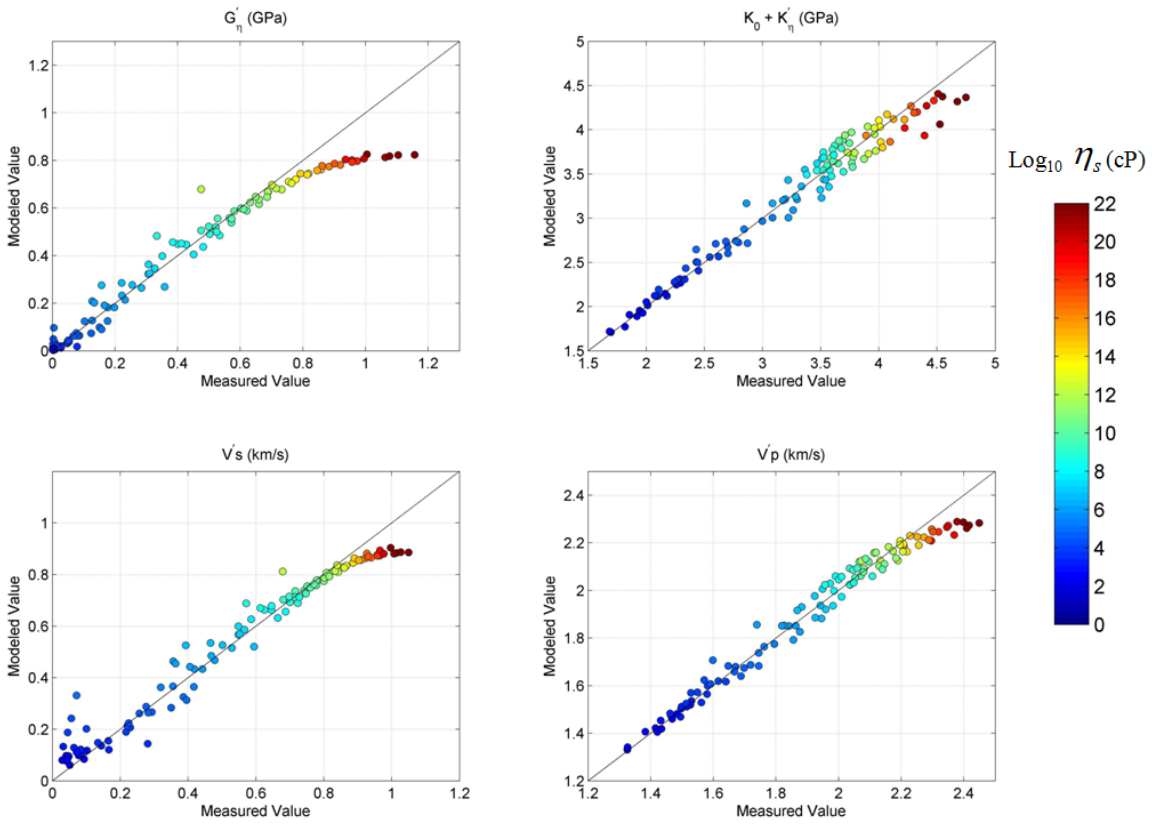

Figure 2.24. Comparison between the prediction and the ultrasonic measurement data for the shear and bulk moduli, and P- and S-wave velocities. The X- and Y-axes represent the measurement and prediction, respectively. The color represents the shear viscosity.

2.6 Summary

The bulk viscosity of heavy oil has often been neglected or simply assumed to be zero in theoretical calculations and rock physics modeling studies. One of the possible reasons is that we do not have enough data on the bulk viscosity of heavy oils. However, the ultrasonic acoustic measurements clearly show the existence of the bulk viscosity. Thus, I use the ultrasonic velocity measurement data to investigate the bulk viscosity and its related bulk modulus of heavy oil.

The ultrasonic measurement data over a wide temperature range shows that heavy oils in the quasi-solid state have additional bulk modulus induced by the bulk viscosity as well as shear modulus induced by shear viscosity. Using the calibrated empirical model of the shear viscosity, I compare several viscoelastic models with the measured shear modulus. Then, I conclude that the Havriak and Negami model has the best fit. Furthermore, I compare the viscosity-induced bulk modulus with the corresponding shear modulus. The relation between the bulk and shear viscosities is successfully derived with help of the Havriak and Negami model. Using the relationship along with the shear viscosity model and the Havriak and Negami model, the temperature and frequency dependences of the moduli and velocities of the heavy oil are predicted. The predicted moduli and the velocities are virtually consistent with the temperature-dependent data at high frequency. These analyses clearly show that the bulk viscosity of the heavy oil is larger than the corresponding shear viscosity. Thus, it is obvious that we should take into account effects of the bulk viscosity, as well as the shear viscosity, in the rock physics modeling of heavy-oil saturated rock.

2.7 Proposal for Future Work

It is important that the relationship between shear and bulk viscosities is obtained using the ultrasonic velocity measurement data over a wide temperature range on several heavy-oil samples. However, we may need to make continuous efforts for investigating the bulk viscosity and it-induced bulk modulus for heavy oils. Because, in the viscoelastic model, the imaginary part plays an important role for frequency dependence with attenuation, as well as the real part. The real part can be evaluated by the ultrasonic

velocity measurement data acquired at different temperatures, whereas the imaginary part cannot be directly validated by the single-frequency data. The evaluation may be performed by the direct measurement of the bulk viscosity or the acoustic attenuation measurement. Thus, the laboratory measurements could be one of the remaining tasks for improving our understanding on the bulk viscosity and its related bulk modulus.

Furthermore, the shear viscosity model is a key element in the viscoleastic modeling. In this study, I used the calibrated empirical model of shear viscosity by assuming that heavy oil is a linear Newtonian fluid. However, there are recent studies (e.g., Wang et al., 2006; Rojas, 2010) reporting that shear viscosity of heavy oil is frequency dependent. If heavy oil was a non-Newtonian fluid, the relationship between shear and bulk viscosities became more complicated. The shear viscosity may be directly measured by the dynamic rheometrical measurements. Thus, the integrated analysis using the direct measurements on shear viscosity, along with the ultrasonic velocity measurement, is also one of the possible future tasks.

Chapter 3 – Rock Physics Modeling of Heavy-oil Saturated Sands

3.1 Introduction

For quantitative interpretation of seismic data acquired in heavy-oil reservoirs, it is essential to precisely understand the relationship between seismic properties of the heavy-oil saturated rock (such as velocity and attenuation) and reservoir properties (such as temperature, pressure, and fluid saturation). The most distinguished characteristic of heavy-oil saturated rock from a seismic point of view is the viscoelastic behavior which is due to extremely high viscosity of the heavy oil. Heavy oil has frequency-dependent shear modulus induced by the shear viscosity. Thus, Gassmann's equation (Gassmann, 1951), which has been the most commonly used in the industry, is not applicable for fluid substitution in the heavy-oil saturated rock (e.g., Makarynska et al., 2010). Moreover, since the shear viscosity dramatically changes with temperature, the induced shear modulus significantly varies with temperature. Thus, the relationship between the seismic properties and reservoir properties under various conditions becomes much more complicated than that of conventional oil. It is obvious that we need to establish a rock physics model which can compute effective elastic properties of the heavy-oil saturated rock.

The heavy-oil deposits in Canada are mainly located in northern Alberta and range in age from Upper Devonian to Lower Cretaceous. The Lower Cretaceous McMurray Formation is one of the main deposits. Because heavy-oil reservoirs in the McMurray

Formation at shallow depth generally have not been sufficiently compacted, the reservoir sands are poorly consolidated and have high porosity, from 30 to 40 % (Hein and Cotterill, 2006). If we aim to model elastic properties of the heavy-oil saturated sands in the McMurray Formation, we may face with additional difficulties. Because the grain-grain contacts are loose and the pores have high connectivity, we should choose an adequate rock physics modeling method, which may differ from that of a well-consolidated rock.

Some attempts concerning the rock physics model of heavy-oil saturated rock have been reported in the literature (e.g., Ciz ans Shapiro, 2007; Leurer and Dvorkin, 2006, Gurevich et al., 2008; Kato et al., 2008; Das and Batzle, 2009; Makarynska et al., 2010). Ciz and Shapiro (2007) extended the Brown and Korringa (1975) anisotropic version of Gassmann's equation to a case with an elastic solid filling the pore space. The authors computed effective properties of the heavy-oil saturated rock. Leurer and Dvorkin (2006) combined the Hertz-Mindlin contact model (Mindlin, 1949) with the viscoelastic theory to formulate elastic properties of a system consisting of identical spherical grain packing and viscous fluid filling the pore. In their model, heavy oil acts as a contact cement to reinforce the intergranular contact.

The effective medium theories, which allow one to compute equivalent elastic properties of a mixture of two or more elastic constituents, have been utilized for the modeling of heavy-oil saturated rocks. Makarynska et al. (2010) used the self-consistent approach (Berryman 1980; Berryman 1992) to model elastic properties of the Uvalde heavy-oil rock. The rock is a well-consolidated carbonate and saturated with an extremely viscous

heavy oil with an API density of five (Batzle et al., 2006; Behura et al., 2007). They introduced two kinds of pores which have different aspect ratios with each other; one is a stiff pore with high aspect ratio, while the other is a compliant pore with low aspect ratio. By adjusting the two aspect ratios, they achieved good agreement with the laboratory data. However, there have been no report that their method is applicable for the poorly consolidated sands, like the heavy-oil reservoirs in the McMurray Formation.

Das and Batzle (2009) used the combined method (e.g., Sheng, 1990) of the self-consistent approach (SCA) and the differential effective medium (DEM) theory to reproduce biconnectivities of fluid and solid phases. They estimated elastic properties of the poorly consolidated sands and compared them to the laboratory data. In their findings, the shear modulus was highly over-predicted by the SCA-DEM combined method, although the bulk modulus had a good agreement.

In addition, Kato et al. (2008) conducted laboratory ultrasonic velocity measurements on the poorly consolidated sands, which had been taken from the Hangingstone oilfield. It is noted that the measurements will be presented in detail in a later section (3.3.2). They established the empirical rock physics model based on the measurements along with Gassmann's theory and predicted elastic property changes induced by the steam injection. Figure 3.1 shows the P- and S-wave velocities and Vp/Vs changes. The X-axis from left to right represents the reservoir condition changes from in-situ condition (before steam injection) to condition of the steam chamber developed by the steam injection. Since their model is mainly based on the measurements of highly porous clean sands, it is useful in

this circumstance. However, since the model does not have the capability for lithological change, it may be inapplicable for shaly sands with low porosity.

In this study, I aim to establish a rock physics model which can compute effective elastic properties of the heavy-oil reservoirs at various reservoir conditions. The model should be applicable for various lithologies; not only for clean sands with high porosity but also shaly sands with low porosity. Next, S-wave velocity prediction will be performed by using the model with the well log data. I will also compute the velocity dispersion and attenuation associated with the viscoelastic theory. Finally, changes of the properties caused by the steam injection will be predicted. It is noted that bulk viscosity of heavy oil, as I discussed in Chapter 2, is incorporated in the modeling.

In the following sections, I will first describe the Generalized Singular Approximation (GSA) method, which is used in my modeling method. Next, the temperature and pressure dependences of the fluid properties, along with the laboratory measurement data, will be discussed. Furthermore, modeling of the effective elastic properties of heavy-oil saturated rocks will be described. The modeling consists of two parts; clean sands with high porosity and shaly sands with low porosity. Moreover, elastic property changes induced by the steam injection will be discussed. Finally, I will conclude with a summary.

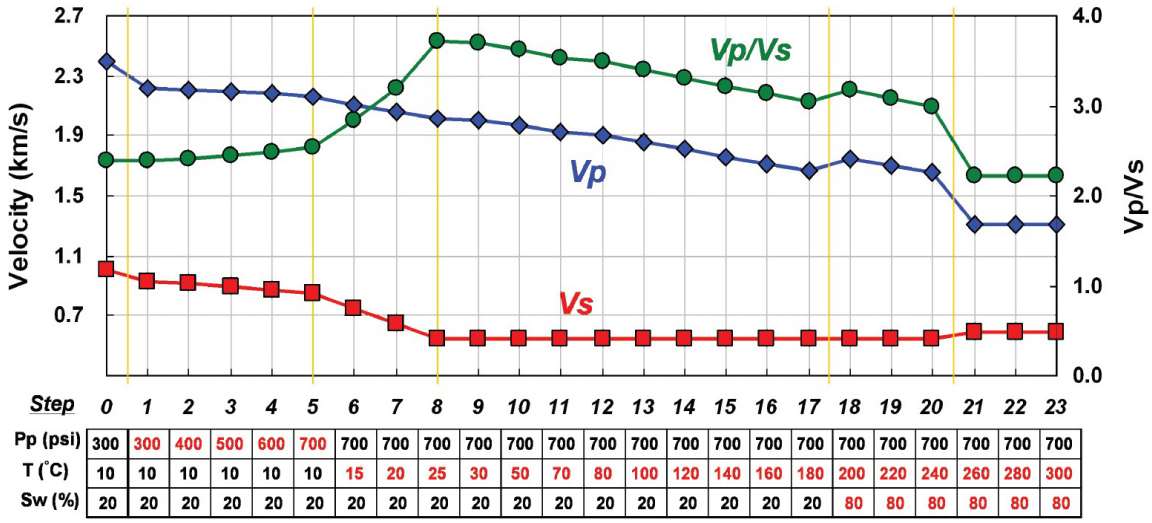

Figure 3.1. P- and S-wave velocities and Vp/Vs changes caused by the steam injection in heavy-oil reservoir (After Kato et al., 2008).

3.2 Effective Medium Modeling

The Generalized Singular Approximation (GSA) method will be mainly used to model elastic properties of heavy-oil saturated rock. I will now briefly describe the method and report the model validation for highly porous rocks.

3.2.1 Generalized Singular Approximation Method

The GSA method was first developed by Shermergor (1977) and was studied in detail and furthermore developed by Bayuk and Chesnokov (1998) and their coworkers. According to Kalinin and Bayuk (1990), the GSA method is based on analysis of the differences between the strain fields in a nonuniform body with unknown macroscopic elastic properties, and in a uniform comparison body with given properties under identical boundary conditions. By introducing a special differential operator and Green's

tensor operator of the comparison body, the strain field in the nonuniform body can be expressed as:

$$\varepsilon = \left(\mathbf{I} - \mathbf{QC}'\right)^{-1} \left\langle \left(\mathbf{I} - \mathbf{QC}'\right)^{-1} \right\rangle^{-1} \left\langle \varepsilon \right\rangle, \tag{3.1}$$

where $\mathbf{C}' = \mathbf{C} - \mathbf{C}^{\mathbf{C}}$; $\mathbf{C}$ and $\mathbf{C}^{\mathbf{C}}$ are the elastic tensors of the nonuniform and the comparison bodies, respectively, and $\mathbf{Q}$ is the integral operator containing the second derivative of Green's tensor. The angular brackets $\langle\ \rangle$ indicates a volume averaging. ε and *I* are the strain and fourth rank unit tensor, respectively.

By using Hooke's law along with the volume averaging, an expression of the effective stiffness tensor, $\mathbf{C}^*$, in the nonuniform body is obtained in an operator form, as follows (e.g., Bayuk et al., 2008):

$$\mathbf{C}^* = \left\langle \mathbf{C}\left(\mathbf{I} - \mathbf{QC}'\right)^{-1} \right\rangle \left\langle \left(\mathbf{I} - \mathbf{QC}'\right)^{-1} \right\rangle^{-1}. \tag{3.2}$$

Since the second derivative of Green's tensor, which is a part of the integrand in the operator $\mathbf{Q}$, is a generalized function, it consists of two components; formal and singular components. The formal component is dependent on the position while the singular part is controlled by elastic properties of the comparison body and shape of the inclusions and independent of the position. The GSA method neglects the formal component and keeps only the singular component. Since the singular component is a product of the local operator **g** and the delta function $\delta(x)$, the local operator can be considered to represent local interactions of the inclusions. Neglecting the formal component is equivalent to making an assumption that the effect of all interactions between the heterogeneities can be described only by the local interactions. Furthermore, Bayuk and Chesnokov (1998)

suggested that neglecting the formal component can be justified by comparing the magnitude of the formal component with that of singular component for isotropic and transversely isotropic mediums in which an analytical solution of the second derivative Green's tensor is available (Appendix A). Thus, following the assumption, the integral operator $\mathbf{Q}(\mathbf{x}-\mathbf{x}')$ can be expressed as:

$$Q_{ijkl}(\mathbf{x}-\mathbf{x}') = g_{ijkl}\delta(\mathbf{x}-\mathbf{x}'). \tag{3.3}$$

By substituting (3.3) into (3.2), the effective stiffness tensor is expressed by:

$$\mathbf{C}^{*} = \left\langle \mathbf{C}(\mathbf{I}-\mathbf{g}\mathbf{C}')^{-1} \right\rangle \left\langle (\mathbf{I}-\mathbf{g}\mathbf{C}')^{-1} \right\rangle^{-1}. \tag{3.4}$$

It is noted that (3.4) has a similar form as the self-consistent method which was first developed by Willis (1977) who used a different approach for the formula derivation.

For an ellipsoidal inclusion, the tensor g_{ijkl} has the form (e.g., Bayuk and Rodkin, 1999):

$$g_{ijkl}(x) = -\frac{1}{16\pi}\int\int\left(\Lambda^{-1}_{ik}n_{ij} + \Lambda^{-1}_{il}n_{kj} + \Lambda^{-1}_{jk}n_{li} + \Lambda^{-1}_{ji}n_{kl}\right)\sin\theta d\theta d\varphi, \tag{3.5}$$

where

$$\begin{aligned}
&\Lambda_{ij} = C^{c}_{imjn}n_{mn},\\
&n_{mn} = n_m n_n,\\
&n_1 = \sin\theta\cos\varphi / a_1,\\
&n_2 = \sin\theta\sin\varphi / a_2,\\
&n_3 = \cos\theta / a_3,
\end{aligned} \tag{3.6}$$

where a_1, a_2 and a_3 are the semi-axes of the inclusion; θ and φ are the polar and azimuthal angles, respectively. It is noted that the semi-axes can have independent value with each other.

If one considers a medium with single phase inclusion, the expression of the effective stiffness tensor has the form (Bayuk and Rodkin, 1999):

$$\mathbf{C}^{*} = \left[(1-v_i)\mathbf{S_m} + v_i\mathbf{S_i}\right]^{-1} + \mathbf{C}^{\mathbf{C}} + \mathbf{g}^{-\mathbf{1}}, \tag{3.7}$$

where v_i is the volume concentration of the inclusion and the tensor $\mathbf{S_m}$ and $\mathbf{S_i}$ are defined by:

$$\begin{aligned} \mathbf{S_m} &= \left(\mathbf{C_m} - \mathbf{C}^{\mathbf{C}} - \mathbf{g}^{-\mathbf{1}}\right), \\ \mathbf{S_i} &= \left(\mathbf{C_i} - \mathbf{C}^{\mathbf{C}} - \mathbf{g}^{-\mathbf{1}}\right). \end{aligned} \tag{3.8}$$

Furthermore, assuming that the volume averaging can be replaced by statistical averaging, (3.4) can be extended to that for a heterogeneous body with multi-phase inclusions. As Chesnokov et al. (2009), the formula is expressed as:

$$\begin{aligned} \mathbf{C}^{*} = &\left\{\sum_i v_i \mathbf{C_i} \int P_i(\chi_i;\theta,\varphi,\psi)\left[\mathbf{I} - \mathbf{g_i}\left(\mathbf{C_i} - \mathbf{C}^{\mathbf{C}}\right)\right]^{-1} \sin\theta d\chi_i d\theta d\varphi d\psi\right\} \\ &\times \left\{\sum_i v_i \int P_i(\chi_i;\theta,\varphi,\psi)\left[\mathbf{I} - \mathbf{g_i}\left(\mathbf{C_i} - \mathbf{C}^{\mathbf{C}}\right)\right]^{-1} \sin\theta d\chi_i d\theta d\varphi d\psi\right\}^{-1}, \end{aligned} \tag{3.8}$$

where χ_i is the aspect ratio of the inclusions, and θ, φ, and ψ are the three Euler angles. P_i is the distribution function of the inclusion.

In the GSA method, selection of the comparison body is arbitrary. Bayuk and Chesnokov (1998) and Bayuk et al. (2008) introduced an empirical parameter, f, which is called friability, to define the properties of the comparison body in the case of a single-phase inclusion as follows:

$$\mathbf{C}^{\mathbf{C}} = (1-f)\mathbf{C}^{\mathbf{m}} + f\mathbf{C}^{\mathbf{i}}. \tag{3.9}$$

The friability f varies from 0 to 1. By setting $f = 0$ and 1, the GSA formula is equivalent to the upper and lower Hashin-Shtrikman bounds (Hashin and Shtrikman, 1963; Willis,

1977), respectively; they are called the HS bounds hereafter. The effective stiffness tensor calculated by the GSA method with different friabilities falls within the upper and lower HS bounds. Thus, it can be considered that the friability f is a representative parameter for inner-structure like the pore connectivity. It is noted that, if setting $\mathbf{C}^{\mathbf{C}} = \mathbf{C}^{*}$, the formula is equivalent with the self-consistent method (Willis, 1977).

3.2.2 Model Validation for Highly Porous Rock

The majority of the effective medium theory is based on Eshelby (1957) solution. Since the Eshelby method does not take into account interactions of the inclusions, the original Eshelby method is only applicable at dilute inclusion's concentration. The limitation is a critical problem when one intends to model elastic properties of highly porous rock. Thus, to overcome the limitation, many studies have been made to extend the original Eshelby method to higher volume concentration. The self-consistent method (e.g., Berryman, 1980) and differential effective medium model (e.g., Norris, 1985) are two of them. The methods approximate the interactions by using individual way. Likewise, the GSA method assumes that the integral operator $\mathbf{Q}$ can be replaced with the local operator $\mathbf{g}$. If the assumption is satisfied (Bayuk and Chesnokov, 1998), the GSA method takes into account all the interactions of the inclusions, suggesting that the GSA method has no limitation on the volume concentration. This is one of the significant advantages when one models effective elastic properties of highly porous, poorly consolidated sands. Also, the GSA method has a flexible parameter of the friability. By adjusting the parameter, one can predict almost all values within the HS bounds. Thus, it enables one to relate the effective elastic properties of the system to the volume concentration.

In order to investigate the GSA method's abilities, I compute the effective elastic properties of a matrix-inclusion system, in which the matrix is quartz and the inclusion is air, and compare them with Walton's rough model (Walton, 1987) at high porosities. It is noted that Kato et al. (2008) reported that Walton's rough model can successfully predict the dry frame's moduli of the poorly consolidated sands. Thus, Walton's rough model is used as a reference. Furthermore, for the comparison, predictions by the DEM model based on Norris (1985) are presented.

Figure 3.2 shows the bulk and shear moduli predicted by the DEM model with different aspect ratios. In the calculations, quartz mineral and dry pore are regarded as the matrix and inclusion, respectively. The black solid curve with circles represents Walton's rough model at porosities from 0.38 to 0.44. In Walton's calculation, pressure is set to be 300 psi, and the coordination number changes with porosity, following the relationship reported by Murphy (1982).

When carefully looking at the moduli at high porosity, although the bulk modulus predicted by the DEM model with aspect ratio of 0.07 has good agreement with Walton's prediction over all, the shear modulus predicted with the same aspect ratio is slightly overestimated. On the other hand, Figure 3.3 shows the prediction by the GSA method with different friabilities. In the calculation, a constant aspect ratio (0.08) is used. The GSA predictions can cover the whole area below the HS upper bound by changing the friability as well as porosity, which is similar to the DEM model with different aspect ratios. However, it shows remarkable improvement of the data agreement. One can see that Walton's prediction fits well with the GSA prediction with friability of 0.9985 for

both bulk and shear moduli. For rock physics modeling, it is important to use a consistent parameter (such as aspect ratio or friability) for both bulk and shear moduli.

Furthermore, I investigated the prediction in bulk modulus vs. shear modulus domain. When keeping constant porosity, the bulk and shear moduli by the DEM varies with the aspect ratio, but the ratio of the bulk modulus to shear modulus (*K/G*) follows the specified curve in the domain. In the case of the GSA model, the moduli vary with the friability (constant aspect ratio). Figure 3.4 shows the bulk and shear moduli predicted by the models with a constant porosity of 0.42. In the DEM model, the predictions cannot reach Walton's rough model. In contrast, Walton's rough model virtually falls on the GSA prediction curve. Thus, it can be suggested that the GSA method is a better predictor for poorly consolidated sands, compared to the DEM model.

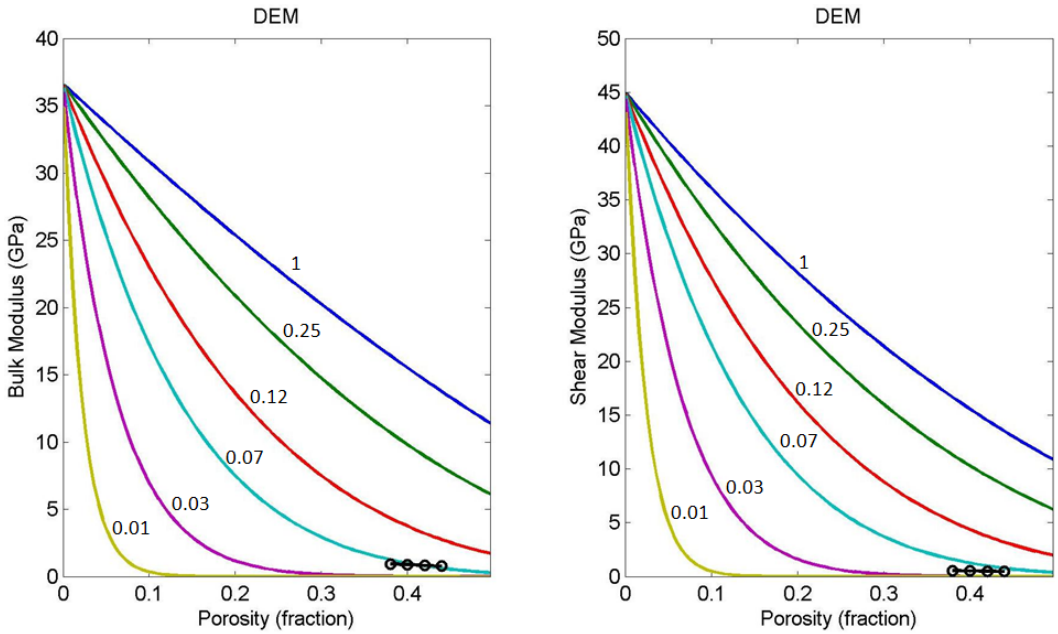

Figure 3.2. Bulk and shear moduli vs. porosity as predicted by the DEM model with different aspect ratios. The circles represent the value predicted by Walton's rough model at porosities from 0.38 to 0.44.

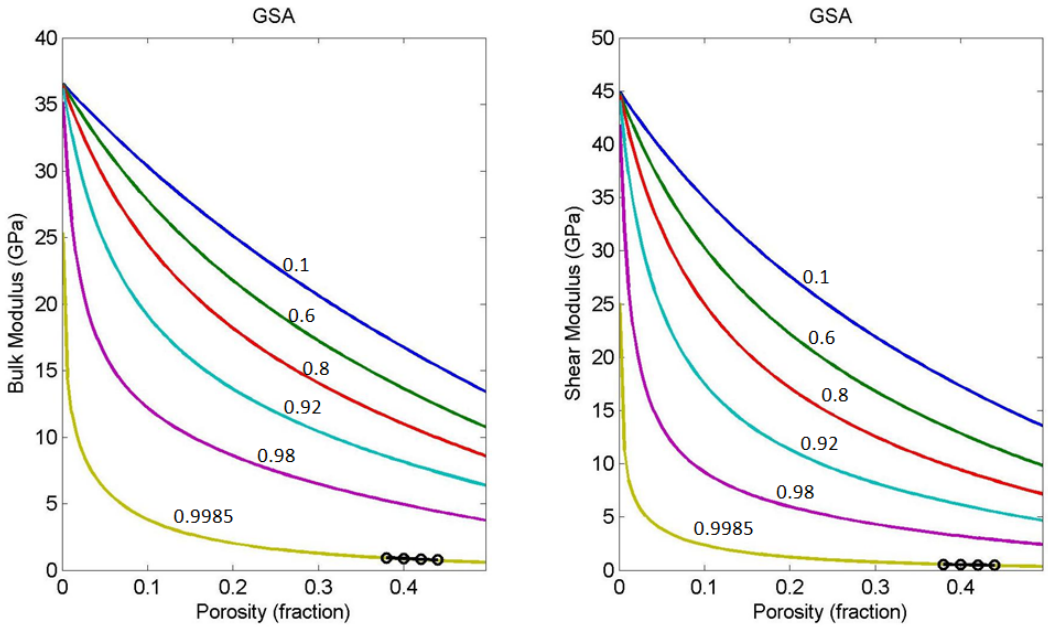

Figure 3.3. Bulk and shear moduli vs. porosity as predicted by the GSA method with different friabilities. The circles represent the value predicted by Walton's rough model at porosities from 0.38 to 0.44.

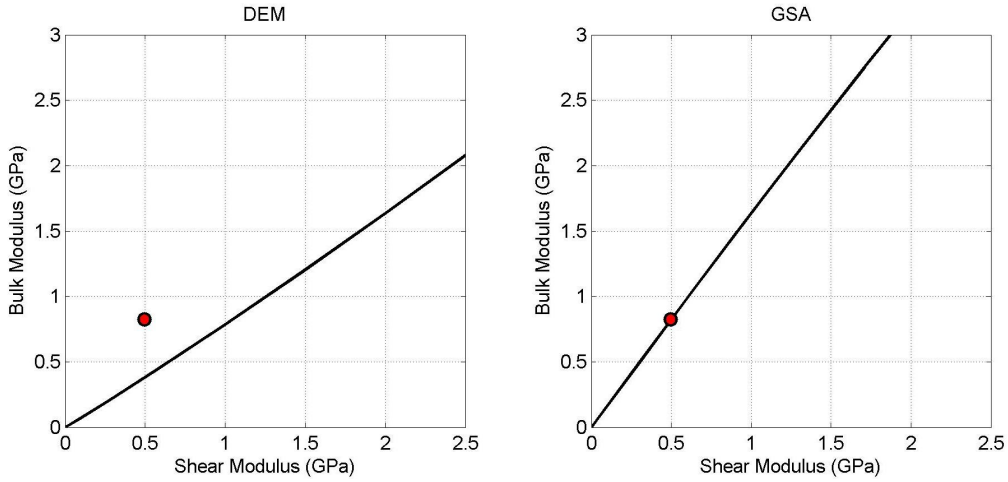

Figure 3.4. Bulk modulus vs. shear modulus as predicted by the DEM and GSA methods. The red circle represents the value predicted by Walton's rough model with a porosity of 0.42.

3.3 Laboratory Measurement Data

To establish a rock physics model of heavy-oil saturated rock, it is essential to calibrate the model with actual measurement data, such as laboratory or field data. In this study, I used the laboratory ultrasonic velocity measurement data which had been acquired by the joint study (Kato et al., 2008; Nakayama et al., 2008) between Japan Oil, Gas and Metals National Corporation (JOGMEC) and Japan Canada Oil Sands Limited (JACOS). The joint study performed the ultrasonic velocity measurement on both heavy oil and heavy-oil saturated sands, which had been taken from the Hangingstone oilfield. The heavy oil has 8.35 °API density. In the following sections, I show results of the measurements on the heavy oil and heavy-oil saturated sands.

3.3.1 Ultrasonic Velocity Measurement Data of Heavy Oil

Figure 3.5 shows the waveshapes recorded by the P- and S-wave transducers for the heavy oil at different temperatures, in which a frequency of 0.5 MHz was used. At - 20 ˚C, first break of both P- and S-wave is clearly observed in the waveshapes, as indicated by the red arrows in the figure; at around 11 μs and 28 μs for P-wave and S-wave, respectively. As temperature increases, the traveltime of the first break tends to increase without significant amplitude decay for the P-wave. In contrast, the amplitude of the S-wave significantly becomes weaker and the traveltime becomes longer as temperature increases. Finally, it is difficult to detect the first break of the S-wave at 0 °C. Figure 3.6 shows the calculated P- and S-wave velocities at different temperatures for the heavy oil. It is noted that there is a lack of data for the S-wave velocity at higher temperatures than 0 °C.

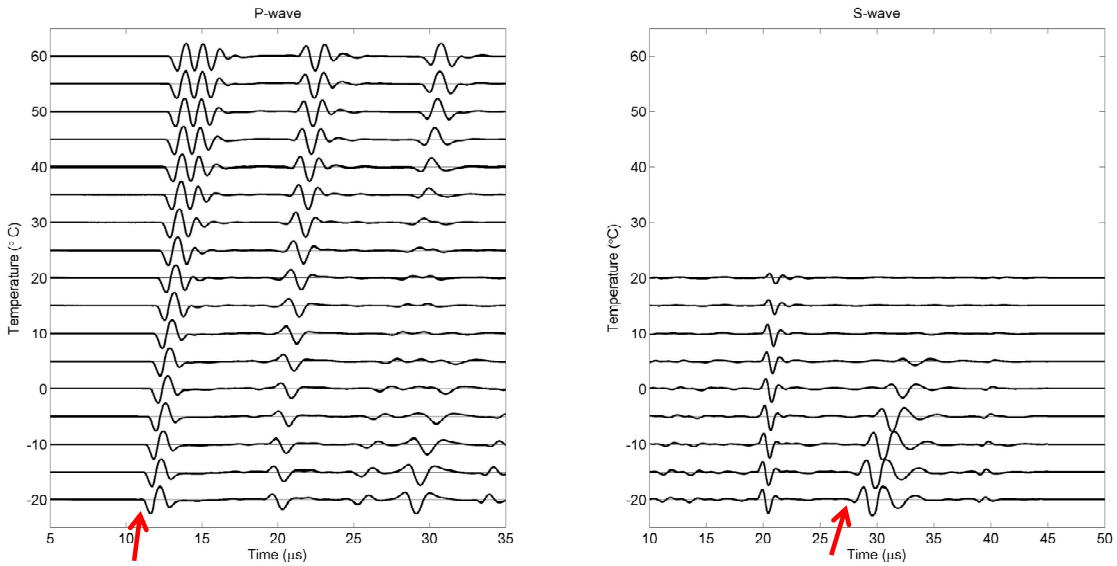

Figure 3.5. Waveshapes recorded by P- and S-wave transducers at different temperatures for the heavy oil (After Kato and Onozuka, 2007). The X-axis represents the travel time while the Y-axis represents the temperature. The red arrows represent the first break at -20 °C.

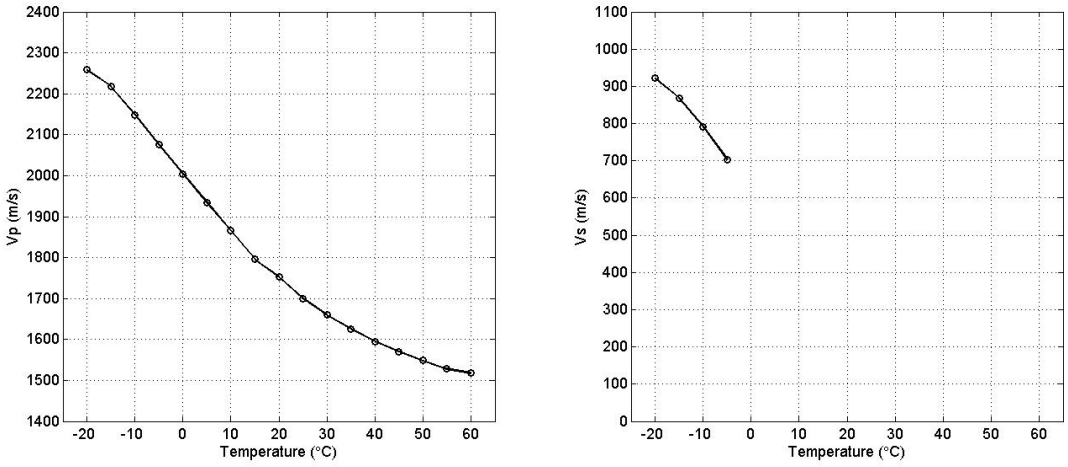

Figure 3.6. P- and S-wave velocities at different temperatures for the heavy oil (After Kato and Onozuka, 2007). It is noted that the first break of the S-wave cannot be detected due to high attenuation at higher temperatures than 0 °C.

3.3.2 Ultrasonic Velocity Measurement Data of Heavy-oil Saturated Sands

Kato et al. (2008) reported the ultrasonic velocity measurement for the heavy-oil saturated sands to establish the empirical rock physics model (Figure 3.1). For the ultrasonic velocity measurement, four plug samples were obtained from a whole core, which had been sampled in the Hangingstone oilfield. Figure 3.7 shows the four plug core samples (#2, #3, #7, and #10, respectively), which are 1.5 inch in diameter and more or less 1 inch in length. Although porosity of the samples was not measured, the value can be approximately estimated from the bulk volume and weight reported by Kato et al. (2008). The estimated porosity is 0.42 in volume fraction.

Figure 3.8 shows pressure dependence of the ultrasonic velocities for the samples. In the Hangingstone oilfield, it is considered that confining and pore pressures in the reservoirs are 900 psi and 300 psi, respectively, at in-situ condition, resulting in a differential pressure of 600 psi (Kato et al., 2008). In the field, the heavy oils are produced by the SAGD method. In the SAGD method, hot steam is injected into the reservoirs at a hydraulic pressure of 700 psi, resulting in differential pressure of 200 psi. The ultrasonic velocity measurement shows a slight decrease of both P- and S-wave velocities as the differential pressure decreases due to the pore pressure increase. Kato et al. (2008) established the empirical formulas for the pressure dependence based on the measurements as follows:

$$\begin{aligned} V_P &= 0.0593 \ln\left(900 - P_{pore}\right) - 0.375 + V_{P0}, \\ V_S &= 0.0780 \ln\left(900 - P_{pore}\right) - 0.495 + V_{S0}, \end{aligned} \tag{3.10}$$

where V_{P0} and V_{S0} are the P- and S-wave velocities (km/s) at the in-situ condition; P_{pore} is pore pressure (psi); V_P and V_S are P- and S-wave velocities (km/s) at the pore pressure of P_{pore}. The solid curves in Figure 3.8 represent the pressure dependences of the formula (3.10), suggesting a good match with the measurement data.

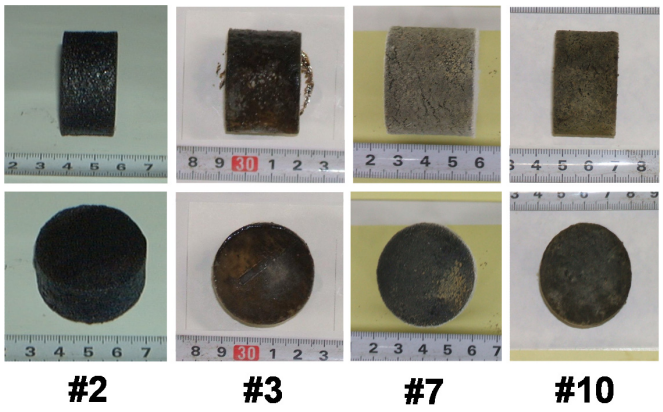

Figure 3.7. The core samples used in the ultrasonic velocity measurements (After Kato et al., 2007).

Kato et al. (2008) also reported the temperature dependence of the ultrasonic velocities for the same samples (Figure 3.9). The temperature dependence significantly varies at around 40 ˚C for both the P- and S-wave velocities. As temperature increases, the P- and S-wave velocities significantly decrease in the lower temperature range. In contrast, in the higher temperature range, the P-wave velocity more gently decreases with temperature and the S-wave velocity virtually remains constant. As previously discussed in Chapter 2, the behavior in the lower temperature range is associated with the viscoelastic feature that bulk and shear moduli of the heavy oil are enforced by the corresponding viscosities. Other literature (e.g., Nur et al., 1984; Eastwood, 1993;

Schmitt, 1999; Batzle et al., 2006; Behura et al., 2007; Han et al., 2007b) also reported the similar temperature dependence of ultrasonic velocities for the heavy-oil saturated rock.

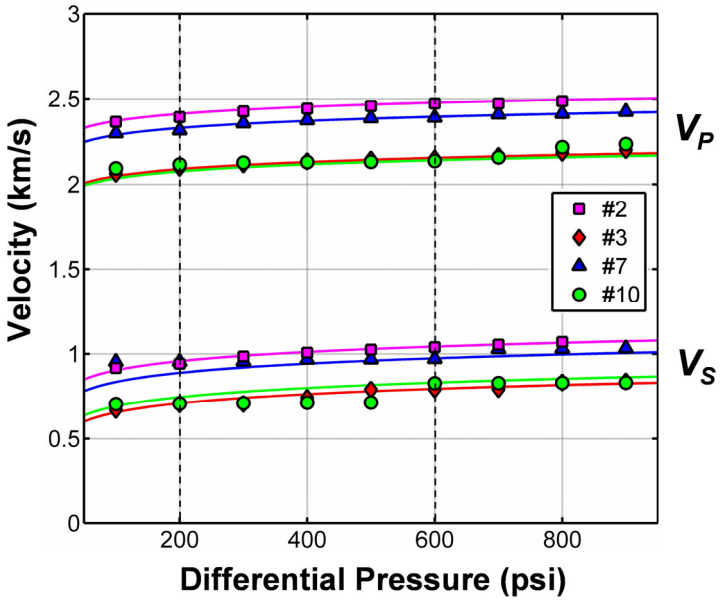

Figure 3.8. P- and S-wave velocities of the heavy-oil saturated sands as a function of differential pressure (After Kato et al., 2008).

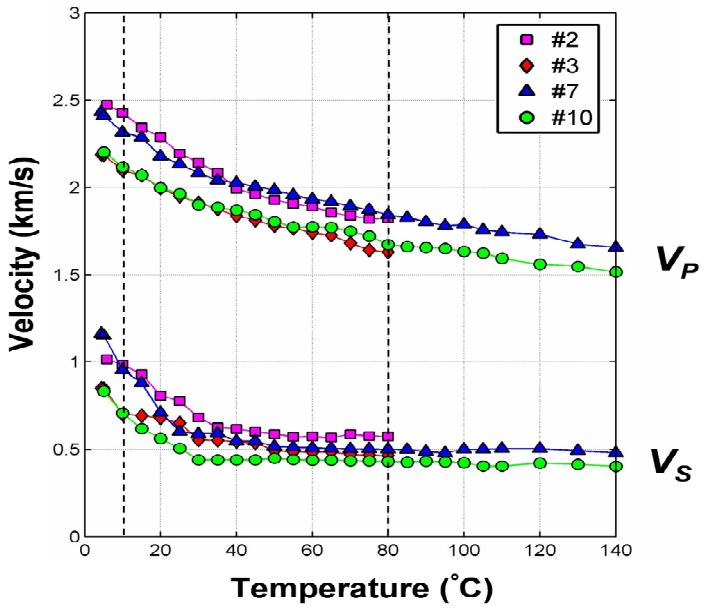

Figure 3.9. P- and S-wave velocities of the heavy-oil saturated sands at differential pressure of 200 psi as a function of temperature (After Kato et al., 2008).

3.4 Modeling of Fluid Properties

To model elastic property changes of the heavy-oil reservoirs, it is essential to know temperature and pressure dependences of fluids filling pore spaces. Heavy oil and brine are included in the fluids. Furthermore, since steam has been used for the heavy-oil production, it is included. For each fluid, different methods are used for calculating the moduli and density. Table 3.1 shows the summary of the methods.

Table 3.1. Methods for calculating fluids properties.

	Temperature Dependence (10 °C to 300 °C)	**Pressure Dependence (300 - 700 psi)**
Bulk & Shear Moduli of Heavy Oil	Viscoelastic theory	FLAG program (conventional oil)
Density of Heavy Oil	FLAG program (conventional oil) + extraploation	FLAG program (conventional oil)
Bulk Modulus and Density of Brine	FLAG program (brine)	FLAG program (brine)
Bulk modulus and Density of Steam	IAPWS-IF97	IAPWS-IF97

For the bulk and shear moduli of the heavy oil, temperature dependence is modeled by the viscoelastic theory, as I discussed in Chapter 2. For the heavy-oil sample of Kato and Onozuka (2007), the S-wave velocity measurement is only available from -20 °C to -5 °C. Thus, in addition to their measurement data, the measurement data of the sample #10 in Liu et al. (2007) are used for calibrating the shear viscosity model. It is noted that the sample #5, which had been taken from the Athabasca area, shows similar temperature dependence as the sample of Kato and Onozuka (2007). The shear viscosity model is formulated by the Equation (2.35) and (2.36), and the constant parameters are determined as $a = 124.0$, $b = -92.1$, and $c = 17.1$. Furthermore, following the results in the Chapter 2, the maximum moduli enforced by the corresponding viscosities, G_∞ and K_2, are set to be 0.83 GPa and 0.96 GPa, respectively. The constant parameters, α and γ, in the Havriliak and Negami model are assumed to be 0.50 and 0.21, respectively. Moreover, the relationship between shear and bulk viscosities in Figure 2.14 is used to obtain temperature dependence of the bulk viscosity. Figures 3.10 and 3.11 show the modeled

bulk and shear moduli and P- and S-wave velocties of the heavy oil from -30 ˚C to 150 ˚C. The modeled values have a good agreement with the measurement data of Kato et al. (2008) although only value at temperatures lower than 0 ˚C is available for the S-wave velocity.

Han et al. (2008) showed ultrasonic velocity measurement data for several heavy-oil samples. They reported that pressure dependences of the heavy-oil samples are virtually insensitive to temperature in the measured temperature range from 10 °C to 80 °C. Furthermore, they concluded that the pressure dependence of heavy oils can be approximated by that of the conventional oils. By following their conclusions, I use the pressure dependence of the corresponding conventional oil as that of the heavy oil. The properties of conventional oil are calculated by the FLAG program.

Density of the heavy oil is calculated by the FLAG program, assuming that the temperature and pressure dependences are the same as that of the corresponding conventional oil. However, as I previously discussed in Chapter 2 (see Figure 2.6), the FLAG program has the allowable temperature. Thus, by making an additional assumption that the trend of oil density does not significantly change above and below the temperature limitations, the formulas in the FLAG program are used for calculating the property over the temperature limitations.

For calculating temperature and pressure dependences of brine properties, I use the FLAG program. In the calculation, salinity solution is assumed to be 50,000 ppm. Also, temperature and pressure dependences of the steam are calculated by the IAPWS-IF97 (Wagner and Kruse, 1998).

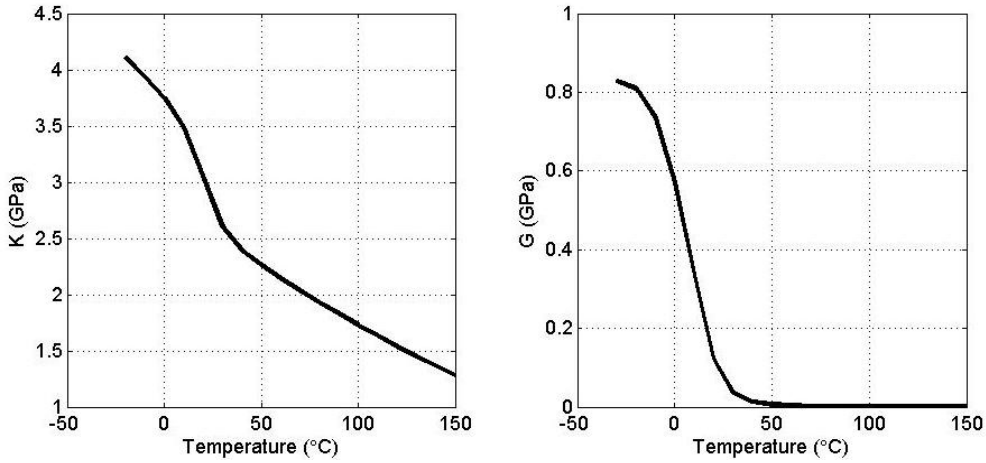

Figure 3.10. Modeled bulk and Shear moduli of the heavy oil at a frequency of 0.5 MHz.

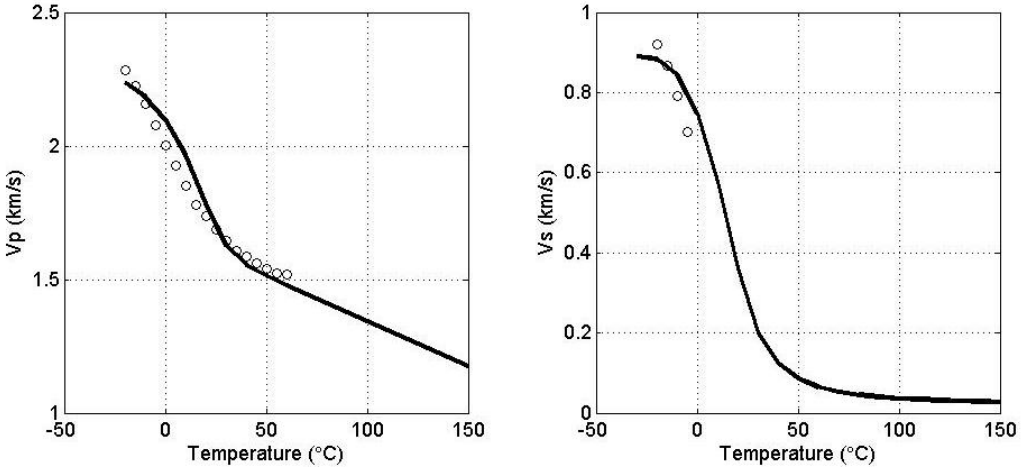

Figure 3.11. Modeled P- and S-wave velocities of the heavy oil at a frequency of 0.5 MHz. The circles represent the laboratory measurement data (Figure 3.9).

3.5 Modeling of Heavy-oil Saturated Clean Sands

For establishing a rock physics model, it is important to calibrate the model with the actual measurement data. I use the laboratory data of Kato et al. (2008) as the calibration data. The core samples of Kato et al. (2008) are clean sands. Thus, my first aim is to model effective elastic properties of the clean sands saturated with heavy oil. The effects of clay is discussed in a later section (3.6).

3.5.1 Temperature Dependence

Figure 3.12 shows thin section of the core sample which the JOGMEC-JACOS joint study acquired (Tsuji 2008, personal communication). It is noted that heavy oil had been removed by toluene solvent. It can be observed that the rock is formed by silt-size grains, which mainly consists of quartz with a small amount of feldspar. Also, the rock has high porosity and the grains have loose contact with each other. It is noted that the existence of clay minerals is not clearly observed.

I took the following steps for modeling the heavy-oil saturated clean sands (Figure 3.13):

1. Form a solid rock cube consisting of a quartz mineral.
2. Form an ellipsoidal pore which is filled with brine and heavy-oil mixture. The pore has a needle-type shape with specified aspect ratio ($a_1 > a_2 = a_3$; where a_1, a_2, and a_3 are semi-axes of the ellipsoid).

3. The pores are embedded into the rock cube to be randomly distributed until the total pore volume becomes the estimated porosity (0.42). The GSA method is used to compute the effective elastic properties.

The bulk and shear moduli and density of the quartz mineral are assumed to be 36.6 GPa, 45.0 GPa, and 2.65 g/cc, respectively. It is noted that bulk density of the rock is simply determined by the volume fraction along with density of each component.

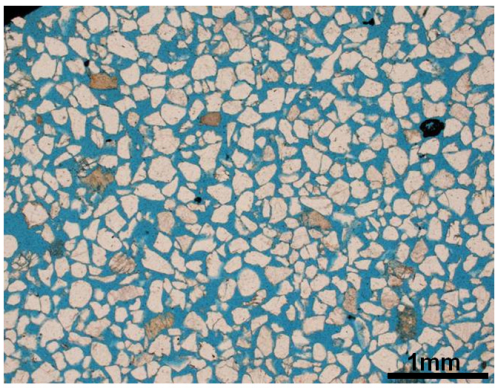

Figure 3.12. Thin section of the heavy-oil saturated sands (from Tsuji 2008; personal communication).

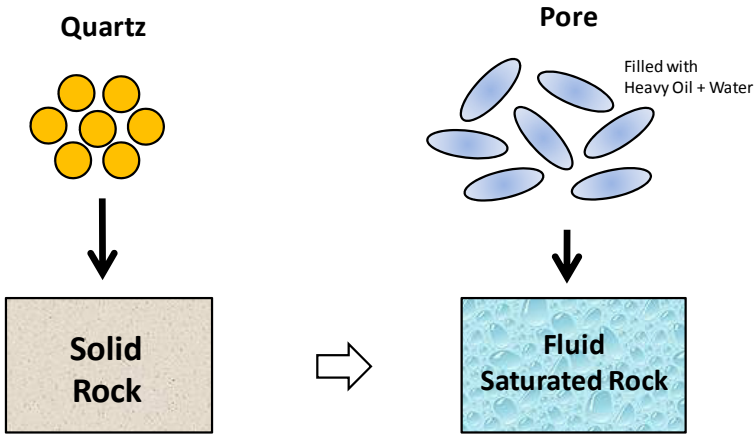

Figure 3.13. Diagram of rock physics modeling for the heavy-oil saturated clean sands.

The volume fraction ratio between heavy oil and brine in the pore space is assumed to be 0.80, in accordance with the petrophysical analysis based on the well log data. Effective elastic moduli of heavy oil and brine mixture depend on scales of mixing of the components. Mavko et al. (1998) reported that the Reuss and Voigt averages can model the upper and lower bounds for the effective elastic properties. I use the same concept, but since heavy oils have shear modulus unlike elastic fluids, I use the HS bounds instead of the Reuss and Voigt averages. The HS bounds are expressed by:

$$
\begin{aligned}
K^{\pm} &= K_1 + \frac{f_2}{(K_2 - K_1)^{-1} + f_1\left(K_1 + \frac{4}{3}\mu_1\right)^{-1}}, \\
\mu^{\pm} &= \mu_1 + \frac{f_2}{(\mu_2 - \mu_1)^{-1} + \frac{2f_1(K_1 + 2\mu_1)}{5\mu_1\left(K_1 + \frac{4}{3}\mu_1\right)}},
\end{aligned}
\tag{3.11}
$$

where K_1 and K_2 are bulk moduli of individual phases; μ_1 and μ_2 are the shear moduli; f_1 and f_2 are the volume fraction. The HS upper and lower bounds are computed by interchanging which phase is termed 1 and which is termed 2. If the mixture is intimately mixed in the finest scales, the HS lower bound may be used by setting the termed 1 and 2 for heavy oil and brine, respectively. On the other hand, in the case of the mixture forming patchy saturation in which the two phases are largely separated, the HS upper bound may be used by setting the termed 1 and 2 for brine and heavy oil, respectively. The two cases are the highest and lowest cases, and all actual cases may fall within the bounds. After careful tests, I choose an averaged value of the HS bounds for effective properties of the heavy-oil and brine mixture, which makes the best fit with the laboratory data.

In the GSA modeling, I need to determine two parameters; aspect ratio and friability of the pore. They are also determined by the best fit with the laboratory data of the ultrasonic P- and S-wave velocities at a differential pressure of 600 psi. I use 0.42 as the volume concentration of the inclusion, which corresponds to the estimated porosity of the core samples. The determined values of the aspect ratio and friability are 0.998 and 0.08, respectively. The modeled velocities show the temperature dependence which significantly changes at around 40 °C (Figure 3.14). The results are consistent with the laboratory data. Figure 3.15 shows the bulk and shear moduli which are used for calculating the velocities in Figure 3.14.

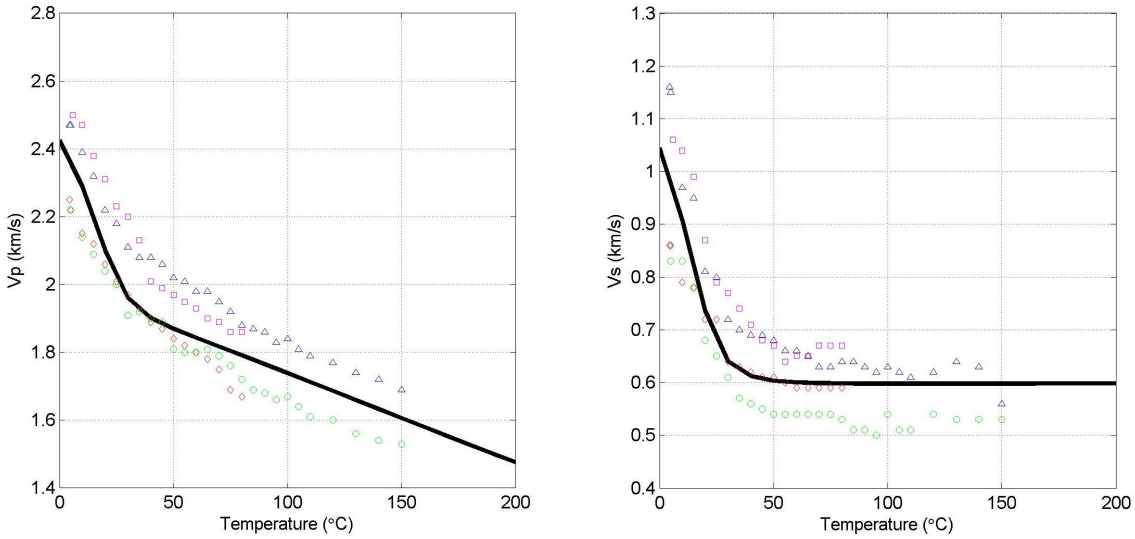

Figure 3.14. Modeled P- and S-wave velocities of the heavy-oil saturated clean sands at a frequency of 0.5 MHz. The square, diamond, triangle, and circle represent the laboratory data for the sample 2, 3, 7, and 10, respectively, at differential pressure of 600 psi.

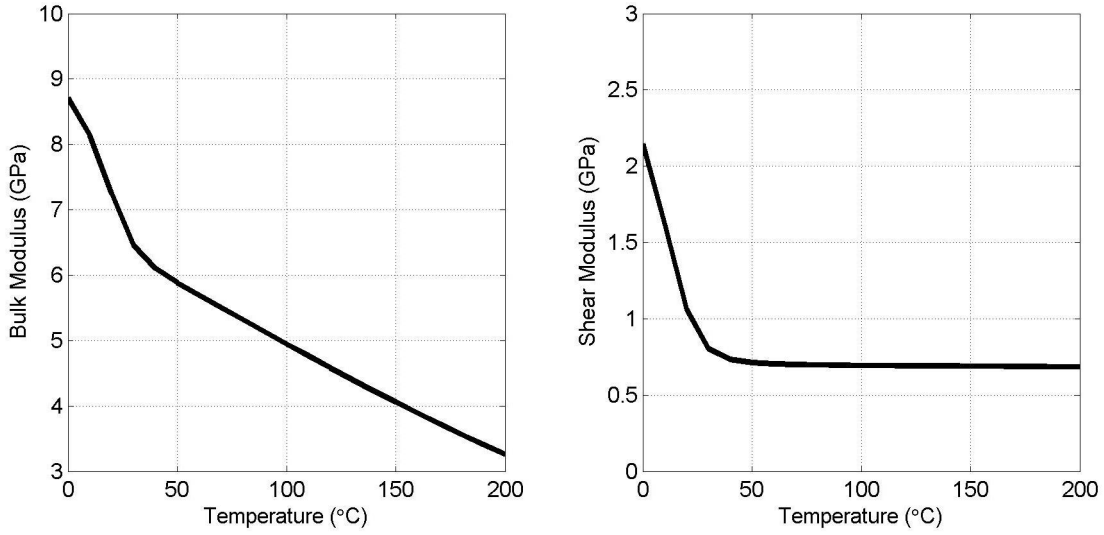

Figure 3.15. Modeled bulk and shear moduli of the heavy-oil saturated clean sands at a frequency of 0.5 MHz.

3.5.2 Pressure Dependence

The formula of the GSA method does not have an explicit pressure-dependent parameter. However, if pore pressure increases, leading to differential pressure decrease, it is natural that the grain-grain contacts become looser and that the pore connectivity increases. According to Bayuk and Chesnokov (1998), the friability in the GSA method represents pore connectivity. Thus, pressure dependence of the velocities may be able to be expressed by the friability change. It is noted that aspect ratio of the pore can also vary with pore pressure variations. However, it may be considered that the change is practically small enough to be ignored in the circumstance of pore pressure changes from 300 psi to 700 psi with constant confining pressure of 900 psi.

At each 100 psi in the pore pressure from 0 to 800 psi, the friability is determined by the best fit with the laboratory data (Figure 3.8) along with the empirical formula (3.10). Thus, the relationship between the friability and pore pressure are obtained by fitting a quadratic expression as follows:

$$f = 2.777 \times 10^{-4} \times P_p^{\,2} + 6.0598 \times 10^{-7} \times P_p + 0.99744, \tag{3.12}$$

where P_p is the pore pressure (psi) and f is the friability. Figure 3.16 shows the normalized friability as a function of differential pressure, in which the confining pressure is 900 psi. One can see that the friability increases as differential pressure decreases, leading to a decrease in velocity.

Figures 3.17 and 3.18 show the modeled pressure dependence of the P- and S-wave velocities and the bulk and shear moduli, respectively, in accordance with Equation (3.12). The modeled velocities have a good agreement with the pressure dependence of the laboratory data over all. It should be noted that the friability is not a quantitative parameter, but an empirical parameter. Thus, magnitude of the friability variation caused by the pore pressure may change at different conditions, such as rock minerals, porosity, texture, reservoir condition, wave frequency and so on. However, because there is not enough data for evaluating them, I assume that the pressure dependence is practically constant change at different conditions.

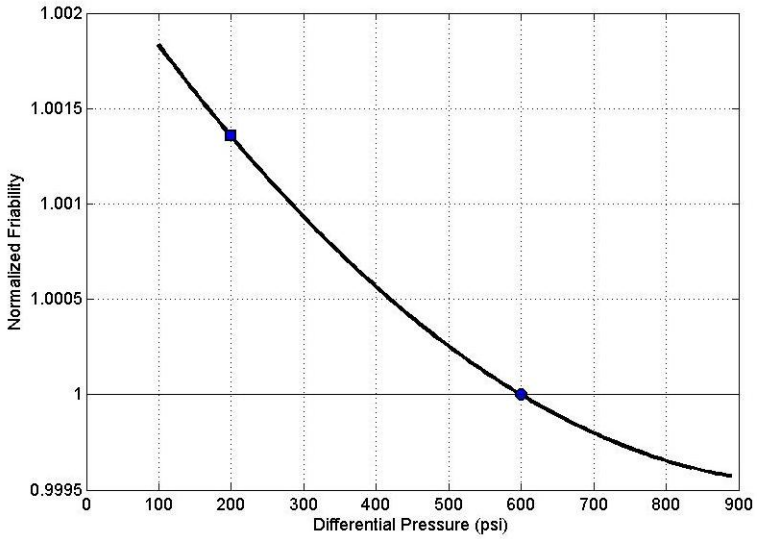

Figure 3.16. Normalized friability as a function of differential pressure.

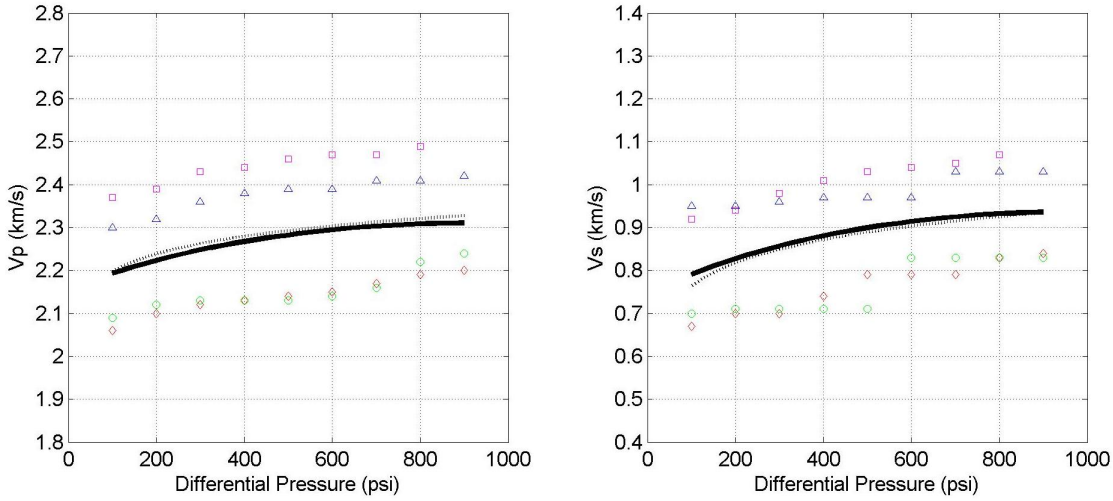

Figure 3.17. Modeled P- and S-wave velocities of the heavy-oil saturated sands (solid curve) as a function of differential pressure. The frequency is 0.5 MHz and the temperature is 10 °C, respectively. The dotted line represents the pressure dependence of Kato et al. (2008).

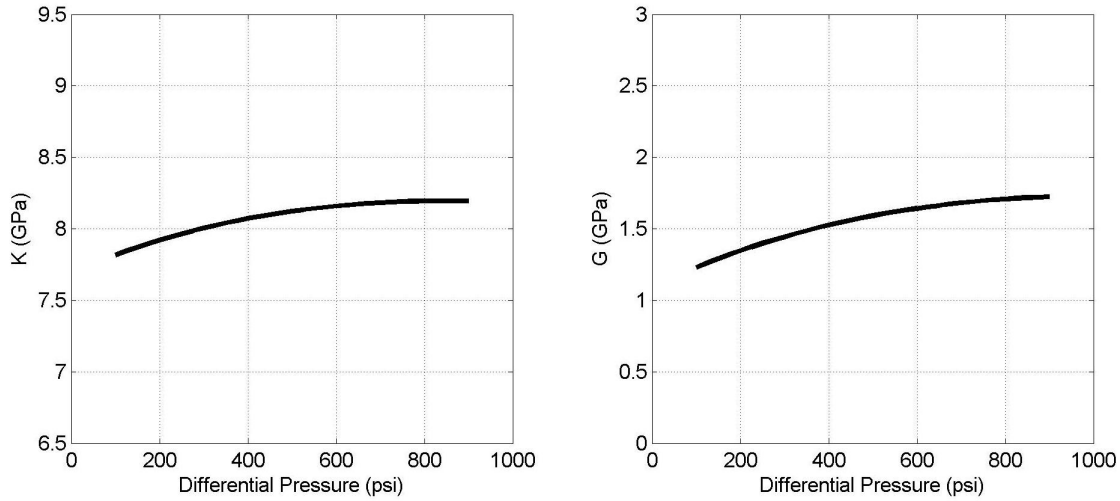

Figure 3.18. Modeled bulk and shear moduli of the heavy-oil saturated clean sands as a function of differential pressure. The frequency is 0.5 MHz and the temperature is 10 °C, respectively.

3.6 Modeling of Heavy Oil-saturated Shaly Sands

The modeling method for heavy-oil saturated clean sands is extended to a system of sand-clay mixture, which is also saturated with heavy oil. Since the laboratory data on the sand-clay mixture is not available in the study area, I use the well log data along with the petrophysical data for calibrating the model. Table 3.2 shows summary of the wells used in this chapter. In well A, the DSI log was acquired so that S-wave velocity data are available as well as the P-wave velocity. However, the temperature data are not available. In contrast, in wells B and C, the temperature data are available while the S-wave velocity data are not. Thus, well A is mainly used for the model calibration while wells B and C are used for predicting the steam injection effects. It is noted that since wells B and C have similar steam injection effects, I will present only the results of well B. The

results of well C will be presented only in the analysis of the traveltime delay based on the Backus average (Backus, 1962).

Table 3.2. Wells used in this study.

	Logging Data Availability	
	Shear-wave	Temperature
Well A	yes	no
Well B	no	yes
Well C	no	yes

3.6.1 Modeling Steps

Figure 3.19 shows the well log data along with the petrophysical data for well A. One finds massive clean sands below about 288 m in depth, which are indicated by the petrophyiscal data, such as high porosity, low density, low Sw, and low Vshale. At and below 300 m, several interbedded shale is observed. Furthermore, a boundary with strong property changes at around 317 m corresponds to the Top Devonian, which is a boundary between the reservoirs and consolidated carbonate rock. I take the reservoir layer from 267 m to the Top Devonian to be modeled.

For the modeling for a system of clay and sand mixture, clay properties are required. As Bayuk et al. (2007) described, clay is made up of blocks consisting of subparallel, very thin phyllosilicate monocrystals. Their surfaces are separated by sheets of bound water, and much of the water may be bound to the surface due to the small distance between the clay plates. Thus, as Homby et al. (1994) and Sayers (1994) pointed out, the clay-water

composites, instead of pure clay mineral, should be used as basic elements in the calculation of effective elastic properties.

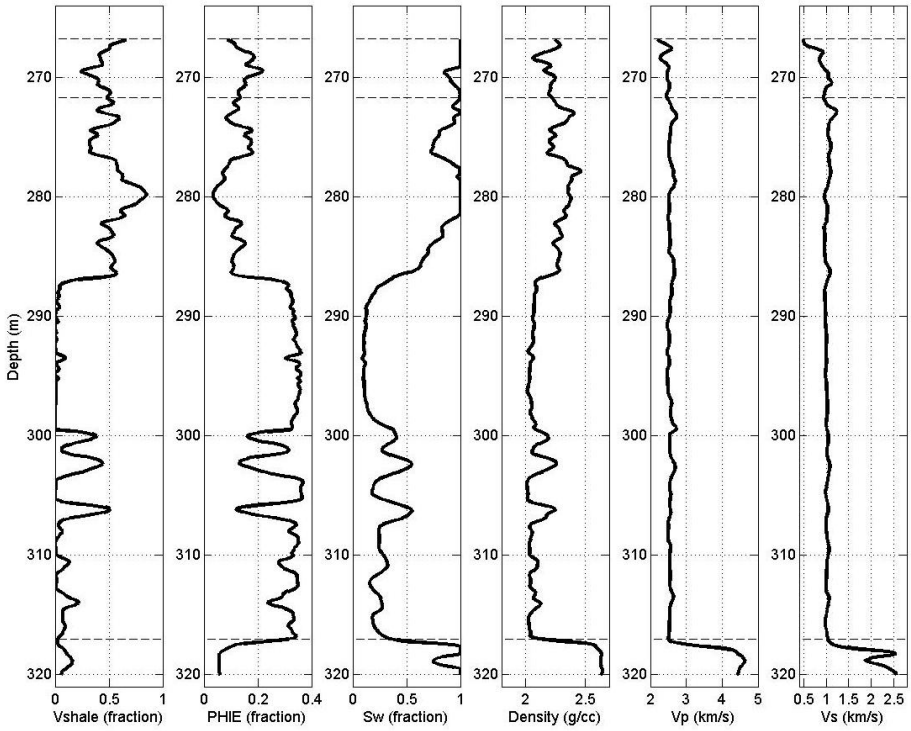

Figure 3.19. The well log data along with the petrophysical data for well A.

Elastic properties of the clay-water composite have been estimated by many authors. Table 3.3 shows the review conducted by Bayuk et al. (2007). The estimations are not consistent with each other and show wide variety. Castagna et al. (1985) estimated P- and S-wave velocities for a montmorillonite-illite mixture by extrapolating the well log data to pure clay point; 3.60 km/s and 1.85 km/s for P- and S-wave velocities, respectively. Han et al. (1986) used laboratory data to estimate the values for mixed clay by the similar method; 3.41 km/s and 1.63 km/s for P- and S-wave velocities. Vanorio et al. (2003) conducted acoustic measurements on water-clay suspensions and estimated elastic

properties of the kaolinite-water mixture; bulk and shear modulus are 12.0 and 6.0 GPa, respectively. The results are consistent with measurements of Prasad et al. (2002). Sayers (2005) and Bayuk et al. (2007) estimated the anisotropic elastic properties of the clay-water mixtures from the laboratory measurement data on shale (Jones and Wang, 1981) by an inversion technique with the effective medium theory.

As Katahara (1996) and other authors pointed out, elastic properties of the clay-water mixture depend not only on the dry clay properties, but on the shape and size of particles and pore, and the extent of particle and pore alignment. Such textural variables can differ from one rock to another. Thus, it can be suggested that elastic properties of the clay-water composite should be individually determined in each field.

Table 3.3. Elastic properties of clays (After Bayuk et al., 2007).

Clay	K (GPa)	μ (GPa)	ρ (g/cm^3)	V_p (km/s)	V_s (km/s)	V_p/V_s	Method used	Reference
Illite	52.3	31.7	2.79	5.82	3.37	1.73	VRH averaging	Katahara, 1996
Chlorite	54.3	30.2	2.69	5.93	3.35	1.77	- - - - -"- - - - -	- - - - -"- - - - -
Kaolinite	55.5	31.8	2.52	6.23	3.55	1.75	- - - - -"- - - - -	- - - - -"- - - - -
Motmorillonite-illite mixture				3.60	1.85	1.95	Extrapolation of empirical dependences to pure clay	Castagna et al., 1985
Mixed clays				3.40	1.60	2.13	- - - - -"- - - - -	Tosaya, 1982
Mixed clays	21.4	6.7	2.62	3.41	1.63	2.09	- - - - -"- - - - -	Han et al., 1986; Berge and Berryman, 1995
Illite				4.2	2.5	1.68	- - - - -"- - - - -	Eastwood and Castagna, 1986
Smectite	7.0	3.9	2.29	2.30	1.30	1.77	Measurements on cold-pressed sample	Vanorio et al., 2003
Kaolinite	12.0	6.0	2.59	2.78	1.52	1.83	Measurements on clay-water suspension, AFAM	Vanorio et al., 2003 Prasad et al., 2002
Illite	60.2	25.4	2.71	5.89	3.06	1.92	Inverted from clay-epoxy mixture properties	Wang et al., 2001
Smectite	9.3	6.9	2.40	2.78	1.70	1.63	- - - - -"- -- - -	Wang et al., 2001
Illite-smectite mixture (60/40)	37.0	18.2	2.55	4.90	2.67	1.84	- - - - -"- - - - -	Wang et al., 2001
Kaolinite	44.3	22.1	2.44	5.50	3.01	1.83	- - - - -"- - - - -	Wang et al., 2001
Kaolin (rock or mineral?)	1.4	1.4	1.58	1.44	0.93	1.55	Measurements on cubic sample	Woeber et al., 1963
Illite-smectite-kaolinite-chlorite mixture	8.1	2.8	2.17	2.33	1.13	2.06	Inversion from Jones and Wang data (1981) and calculations with the self-consistent method	This study
Illite-Smectite-Kaolinite-Chlorite mixture	16.0	6.4	2.17	3.36	1.76	1.91	Inversion from Jones and Wang data (1981) and calculations with the self-consistent method	Sayers, 2005

In this study, I determine the value of the clay-water mixture by applying the extrapolation method in the same way as Castagna (1985) and Han et al. (1986). As shown in Figure 3.20, by extrapolating the data trend toward zero porosity (equivalent to 1.0 in Vshale), the moduli of the clay-water composite are empirically estimated; 14.5 GPa and 3.5 GPa for bulk and shear moduli, respectively. The estimated values are close to the estimation made by Vanorio et al. (2003) and Sayers (2005). It is noted that the clay-water composite is expected to have anisotropic properties (e.g., Sayer, 2005; Bayuk et al., 2007). But, since sufficient data for evaluating them is not available, I assume that it can practically be regarded as isotropic.

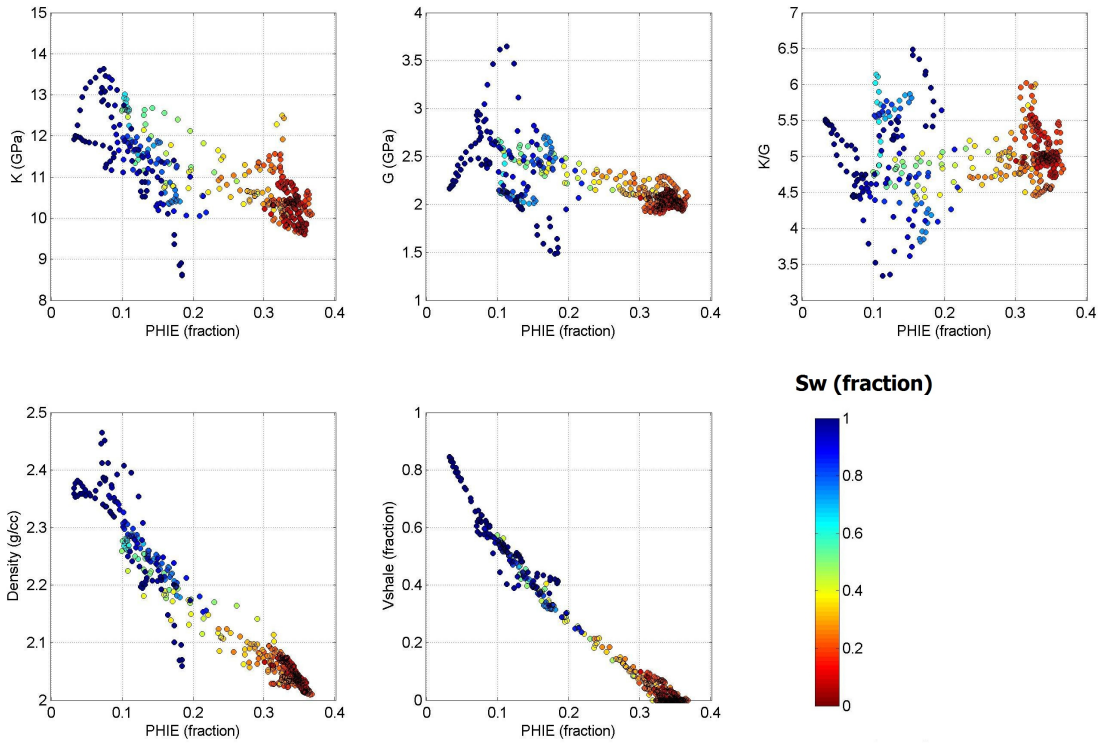

Figure 3.20. Relationship of bulk modulus, shear modulus, K/G, density and Vshale with porosity (PHIE). The color represents the water saturation (fraction).

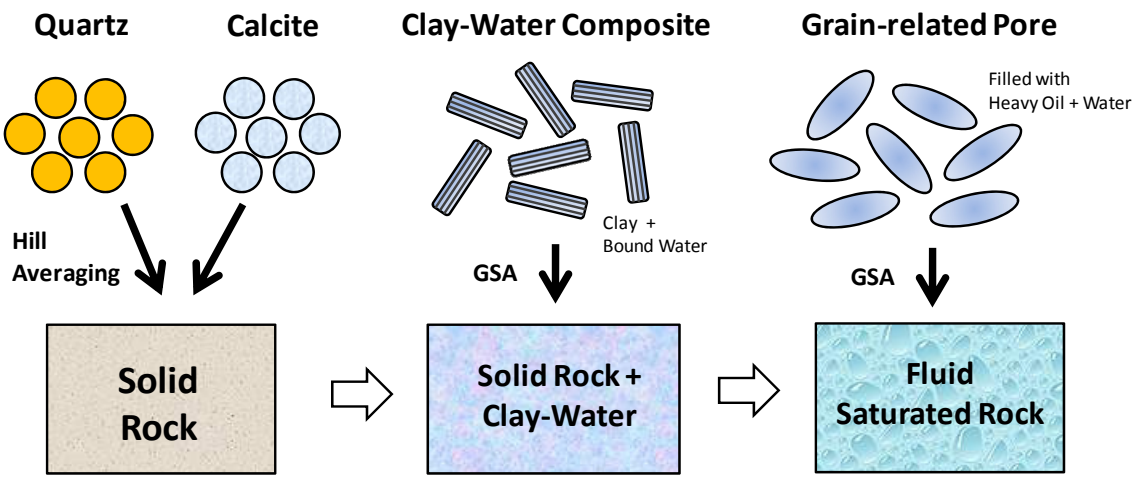

Figure 3.21. Diagram of the rock physics modeling for the poorly consolidated shaly sands saturated with heavy oil.

I took the following steps for modeling the heavy-oil saturated shaly sands (Figure 3.21).

(1) Form a solid rock cube consisting of quartz and calcite minerals. The Voigt-Ruess-Hill average is used for calculating the elastic properties.

(2) The clay-water composites are embedded into the solid rock cube. The clay-water composites are randomly distributed. The GSA method is used to calculate the effective elastic properties. The resulting cube, consisting of the quartz-calcite grains and clay-water mixtures, is regarded as a homogeneous matrix with the effective stiffness in the next step.

(3) Fill the pores with heavy-oil and brine mixture, as discussed in the case of clean sands. Then, the pores are embedded into the cube until the total pore volume becomes the measured porosity. The effective properties are calculated by the GSA method.

Since mixing of calcite minerals within the reservoir are observed by the petrophysical analysis, the Voigt-Reuss-Hill average is used to estimate the elastic properties of the rock cube which consists of quart and calcite minerals. When applying the GSA method in the second step, aspect ratio and friability of the clay-water composite is set to be 0.85 and 1.00, respectively. Furthermore, when applying the GSA method in the last step, the friability of the pores is determined at each depth point of the well log data by using the following objective function:

$$\psi(f) = \left(K_e^* - K_t^*\right)^2 + \left(G_e^* - G_t^*\right)^2, \tag{3.12}$$

where K_e^* and G_e^* are the modeled bulk and shear moduli; K_t^* and G_t^* are the corresponding values based on the well logs. Because aspect ratio of grain is assumed to be practically invariant between the clean sands and shaly sands, I use the same aspect ratio (0.08). The volume fractions of the clay-water composite and grain-related pore are assumed to be equivalent to Vshale and PHIE, which are provided from the petrophysical analysis.

Figure 3.22 shows the modeled bulk and shear moduli and the P- and S-wave velocities, respectively. The modeled moduli and velocities show good agreement with the well log data over all; for not only clean sands but also shaly sands, the properties are predicted very well. But, if one looks carefully at bulk and shear moduli, some discrepancies between the model and well log data show up. For example, at about 288 m in depth, the bulk modulus is overestimated while the shear modulus is underestimated. Furthermore, below about 298 m, the bulk modulus tends to be slightly underestimated while the shear modulus tends to be slightly overestimated. The discrepancies are also observed in the

crossplot between the modeled and the well log values, as presented by Figure 3.23. Despite these visible discrepancies, it can be emphasized that both bulk and shear moduli, as well as P- and S-wave velocities, are well estimated for not only clean sands but also shaly sands.

Figure 3.24 shows the determined friability along with the petrophysical data. The friability tends to vary with the other properties such as Vshale and porosity, which is consistent with Bayuk et al. (2008). In order to obtain a relationship between the friability and porosity, the crossplot is presented by Figure 3.25, showing high correlation; the correlation coefficient is 0.851. At higher porosities than 0.30, the friability is more than 0.99 at almost all points. As the porosity decreases, the friability also tends to decrease. The relationship may help us determine the friability in the other locations unless geological setting does not largely change.

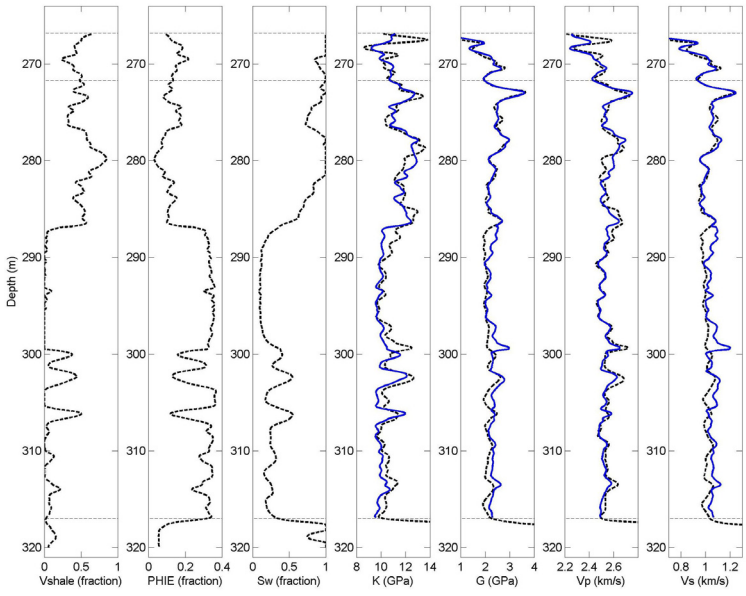

Figure 3.22. Modeling results at a frequency of 10 kHz for well A. The blue solid curves represent the modeled values and the dash black curves represent the well log values.

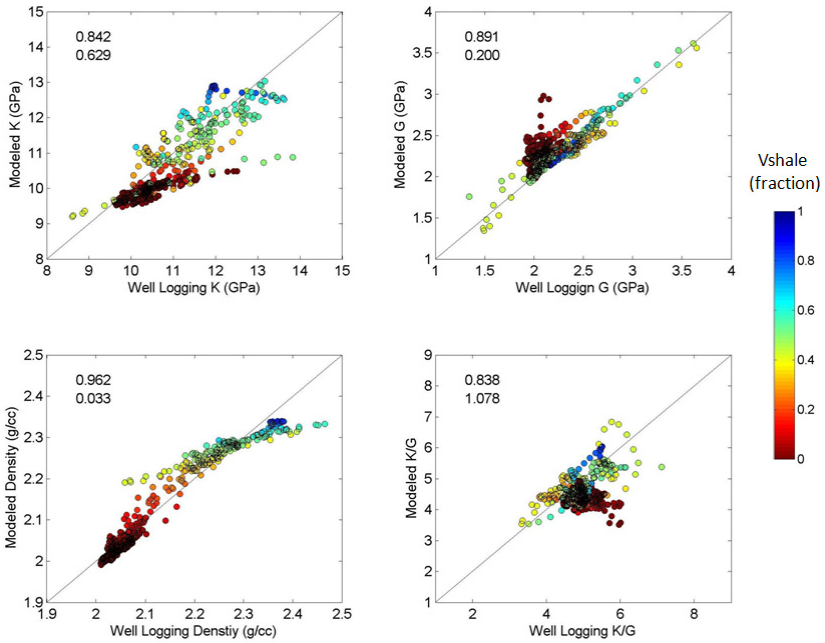

Figure 3.23. Relationship between the modeled values and the well log value for bulk and shear moduli, density, and K/G for well A. The color represents Vshale (fraction). The first and second values at the upper left are the correlation coefficient and RMS error, respectively.

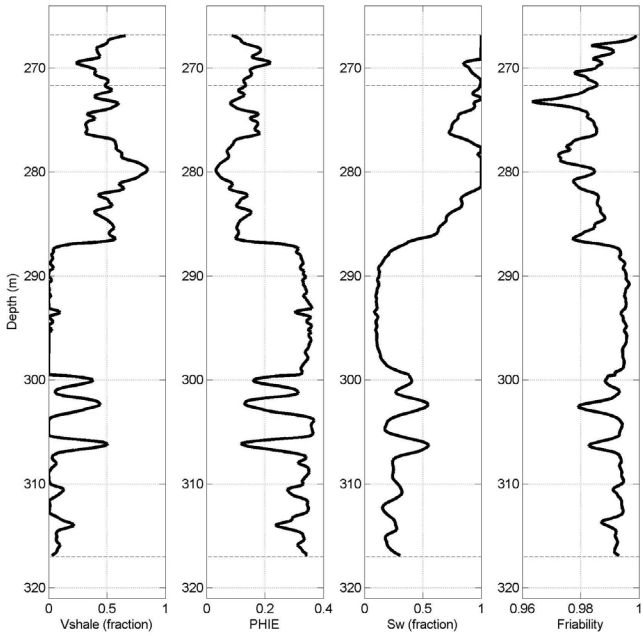

Figure 3.24. Estimated friability with the petrophysical data for well A.

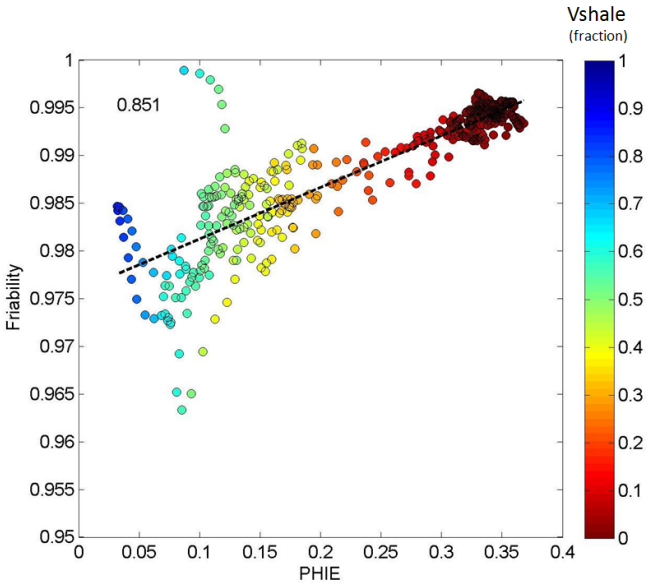

Figure 3.25. Relationship between the friability and porosity (PHIE) for well A. The color represents the Vshale (fraction).

3.6.2 S-wave Velocity Prediction

Next, I model the elastic properties in wells B and C. It is noted that only results of well B are presented. Because the wells do not have shear velocity data, the objective function of determination of the friability is defined by the P-wave velocity instead of the moduli:

$$\psi(f) = \left(V_{pe}^{*} - V_{pt}^{*}\right)^2, \tag{3.13}$$

where V_{pe}^{*} and V_{pt}^{*} are the modeled and well log P-wave velocities, respectively. In the similar way as well A, the friability is determined at each depth point. Figure 3.26 shows the modeling results along with the petrophysical data. These results demonstrate that the method may enable one to estimate S-wave velocity from other well log data.

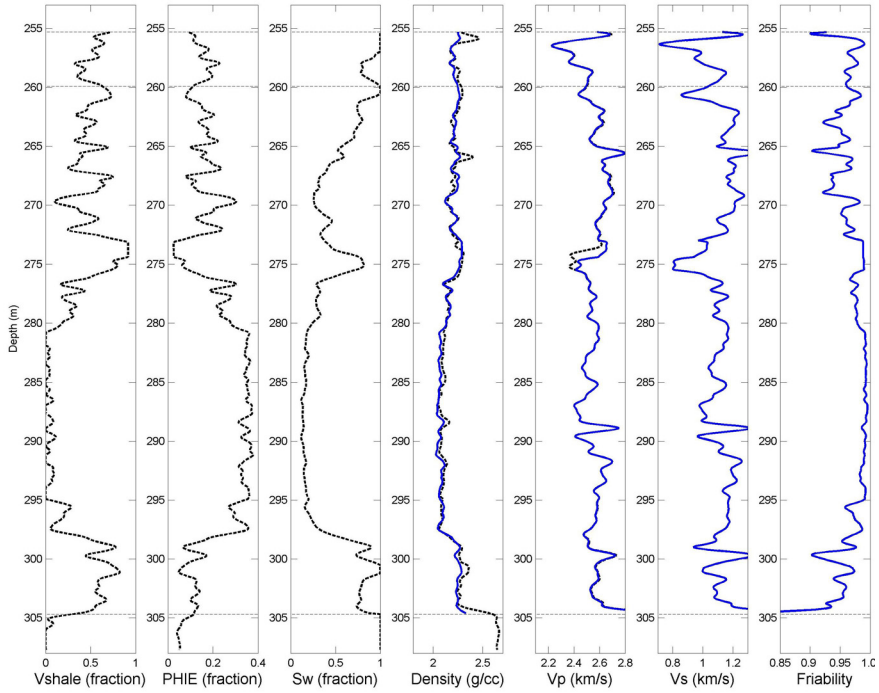

Figure 3.26. Modeling results at a frequency of 10 kHz for well B. The blue solid curves represent the modeled values and the dash black curves represent the well log values.

3.7 Elastic Property Changes caused by Steam Injection

In the study area, heavy oil has been produced by the SAGD method, in which hot steam is injected into the reservoirs. The steam injection dramatically makes the reservoir condition change. The reservoir conditions include pore pressure, temperature, fluid saturation, and steam phase. Furthermore, the reservoir condition changes lead to elastic property changes in the reservoirs. I aim to model the elastic property changes.

3.7.1. Prediction of Elastic Property Changes

Figure 3.27 shows the workflow of modeling the elastic property changes. It is assumed that the parameters associated with elastic properties of dry rock frame, such as the porosity, volume concentration of minerals, and aspect ratio of inclusion, are not affected

by the steam injection, implying that the parameters are constant between the baseline and repeat surveys. In contrast, the friability of the grain-related pore is not included in the constant parameters because it changes with the pore pressure due to the steam injection, as previously discussed.

Because the well log data for estimating pore pressure and water saturation in the reservoirs at the repeat survey are not available, they are determined by the following criteria:

Pore pressure: since it can be considered that the pore pressure changes due to the steam injection can suddenly propagate through the permeable interval, the pore pressure at the repeat survey is assumed to rise from 300 to 700 psi in the whole reservoirs layer at the locations of wells B and C. In contrast, it is assumed that there is no pressure change above and below the reservoir because the overburden shale and carbonate rocks underneath the reservoir have low permeability so that they prevent the pore pressure variation for propagating efficiently.

Fluid saturation: Kato et al., (2008) described the reservoir condition changes caused by the steam injection by the representative 23 steps (Figure 3.1). According to their model, heavy oil is replaced by the injected steam at temperature of 200 °C. After the replacement, the steam and irreducible heavy oil coexist in the invariant pore space. The volume fraction is 80 % and 20 % for the steam and heavy oil, respectively. I follow their model for fluid saturation at the repeat survey.

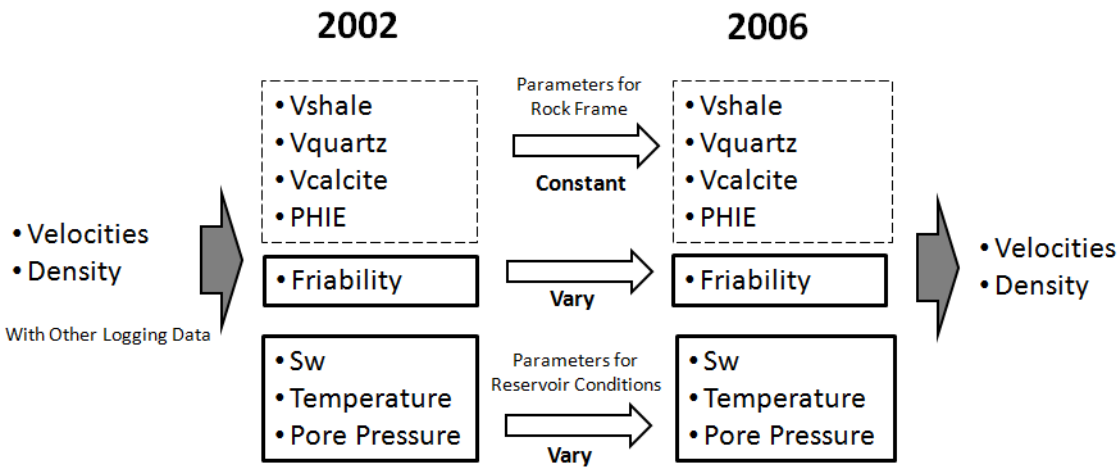

Figure 3.27. Workflow of the time-lapse modeling.

Figure 3.28 shows the modeled P- and S-wave velocities and density at the baseline and repeat surveys for well B. The temperature in the depth interval from about 275 to 300 m significantly increased from 2002 to 2006, implying the steam chamber has been largely developed. In the same interval, the P- and S-wave velocities substantially decreased. The P-wave velocity drop is particularly significant. It is noted that heavy oils in the interval from about 277 to 295 m are assumed to be replaced by the injected steam because the temperature is over 200 °C, leading to the irreducible oil saturation condition; 20 % for the heavy oil and 80 % for the injected steam. Furthermore, in the interval from about 281 to 287 m, the steam phase changes from liquid to vapor because the temperature is over about 260 °C (Wagner and Kruse, 1998). The density drop in the interval is significant as well as the P-wave velocity. The maximum decrease from 2002 to 2006 is approximately 0.30 g/cc, 910 m/s, and 140 m/s for the density, P- and S-wave velocities, respectively. These changes correspond to the relative change with 14.4 % (density), 36.4 % (V_p), and 13.6 % (V_s), respectively. Also it is noted that small velocity changes are

observed above about 270 m, where a raise in temperature was not observed. The velocity changes were caused only by the pore pressure change instead of both the pressure and temperature changes.

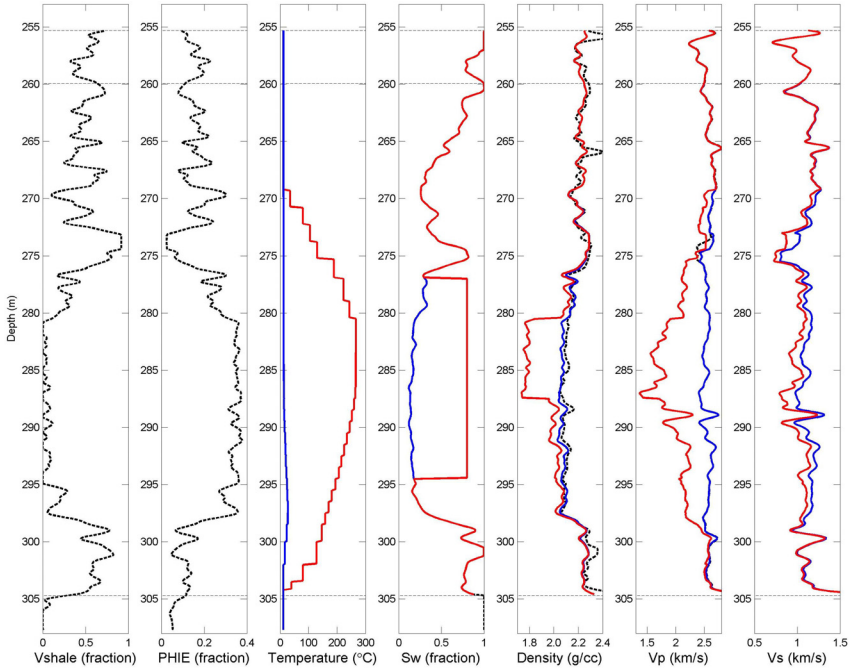

Figure 3.28. Modeled density and P- and S-wave velocity changes for well B. The frequency is 10 kHz. The blue and red solid curves represent the modeled values at 2002 and 2006, respectively. The black dash curves represent the well log data at 2002.

As I previously discussed, the elastic properties of heavy oil are dependent on the wave frequency, as well as temperature and pressure. Heavy-oil saturated rock also has the frequency dependent elastic properties, as observed by the laboratory measurements (e.g., Behura et al., 2007). In accordance with the viscoelastic theory, the velocity dispersion and the associated attenuation can be estimated. Of course, the velocity dispersion is caused not only by the viscoelastic characteristics. Many other mechanisms have been proposed. For example, Biot inertial coupling (Biot, 1956), squirt flow between pores

(Mavko and Jizba, 1991), volatile/mineral interaction (Clark, et al., 1980; Vo-Thanh, 1995), and scattering attenuation associated with geometry are some of them. However, the various mechanisms are outside the scope of this study. I only focus on the viscosity-induced velocity dispersion and associated attenuation.

Figures 3.29 and 3.30 show the velocity dispersion between the surface seismic and the well log frequencies at the baseline survey for wells A and B, respectively. It is noted that 100 Hz and 10 kHz are regarded as the representative frequency of the surface seismic and well log data, respectively. One observes there are substantial velocity dispersions in the whole reservoir layer, which show good correlation with the water saturation (Sw) curve. This is a consequence of the fact that this velocity dispersion is caused by the viscoleastic characteristics of heavy oil. In the reservoir interval, magnitude of the velocity dispersion for P- and S-wave velocities is approximately 92 m/s and 70 m/s, respectively. These correspond to the relative change with 3.9 % (V_p) and 7.1 % (V_s), respectively.

In contrast, at the repeat survey, the velocity dispersion cannot be distinguished in the whole reservoir layer except shallower interval from about 265 to 270 m (Figure 3.31). Because the steam chamber has been largely developed, viscosities of the heavy oil are either significantly reduced with the heat, or the heavy oil is replaced by elastic fluid of the injected steam. Thus, the velocity dispersion in the reservoir almost disappears. The shallower interval, showing the small velocity dispersion, still contains substantial not-yet heated heavy oil (low Sw and low temperature).

In the viscoelastic theory, attenuation is coupled with the velocity dispersion. Figures 3.32 and 3.33 show the modeled attenuation (1/Q) at the baseline survey for wells A and B, respectively. The attenuation can be observed in the whole reservoir layer. For the shear and bulk moduli, the well log frequency has larger attenuation than the surface seismic frequency. But, the difference between the two frequencies is more significant in the shear modulus than that of the bulk modulus. As presented in Figures 2.10 and 2.18, the bulk modulus has peak attenuation at individual temperature with each frequency, although the attenuation of the shear modulus shows monotonic decrease with frequency in some temperature ranges. Because the reservoir temperature is between peak attenuations of the bulk modulus with the surface seismic and well log frequencies, $1/Q_k$ with the frequencies have similar magnitude with each other. But, substantial differences are observed in the interval from about 290 to 300 m in well B, where the temperature was already slightly raised (from 11 °C to 27 °C) at 2002, as shown by Figure 3.28. It is suggested that the slight rise in a temperature can significantly affect the attenuation.

The heavy-oil reservoirs at the baseline survey approximately have the following magnitude of the quality factor (Q):

Q_{Vp} : 100 and 50 at 100 Hz and 10 kHz, respectively,

Q_{Vs} : 70 and 20 at 100 Hz and 10 kHz, respectively.

These results are expected to help us interpret attenuation estimated using field data (e.g., Macrides and Kanasewich, 1987; Schmitt, 1999; Xu and Stewart, 2006a; Reine et al., 2009).

It is important to validate the predicted values with the actual measurement data. Unfortunately, since the acoustic log data at the repeat survey are not available, the modeled values at the well log frequency cannot be evaluated. However, we can utilize the surface seismic data for the validation, although the vertical resolution is much poorer than the well log data. Nakayama et al. (2008) performed the time-lapse analysis using the seismic data and showed that the Top Devonian horizon, nearly corresponding to the reservoir bottom, has significant time-delay at the repeat survey (see Figure 1.8). The time-delay has been interpreted to be caused by the P-wave velocity decrease in the reservoir due to the steam injection.

The modeled values at 100 Hz are applied by the Backus average (Backus, 1962), where the wavelength is set to be 25 m, which approximately corresponds to 100 Hz in the P-wave case. Figures 3.34 and 3.35 show the results of the Backus average for wells B and C, respectively. It is noted that the P- and S-wave velocities represent the velocity of a vertical propagating wave. The density is obtained by the moving average, instead of the Backus average. Both wells show the P-wave velocity significantly decreases in the whole reservoir layer, but well B has more of a decrease than well C. I calculate the traveltime delay caused by the velocity decrease based on the result of the Backus average; 6.02 ms and 3.88 ms in two-way time for wells B and C, respectively. Figure 3.36 shows comparison of the time-delay between the surface seismic analysis (Nakayama et al., 2008) and my modeling results. They are very consistent, although there are only two wells available. Thus, it may be supported that the model can

reasonably predict the associated P-wave velocity changes at the corresponding frequency caused by the steam injection.

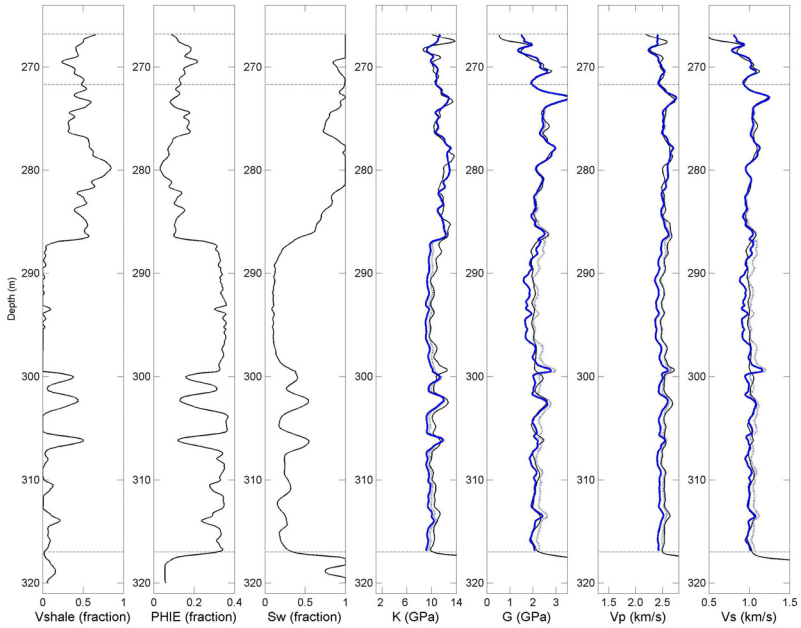

Figure 3.29. Modeled bulk and shear moduli, and P- and S-wave velocities at 2002 for well A. The blue dot and solid curves represent the modeled values at 10 kHz and 100 Hz, respectively. The black curves represent the well log data at 2002.

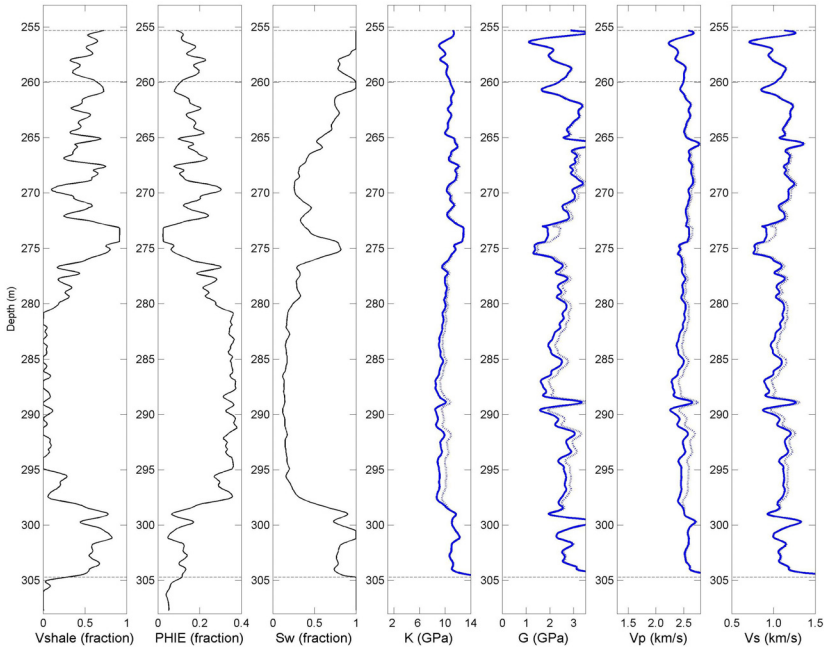

Figure 3.30. Modeled bulk and shear moduli, and P- and S-wave velocities at 2002 for well B. The blue dot and solid curves represent the modeled values at 10 kHz and 100 Hz, respectively. The black curves represent the well log data at 2002.

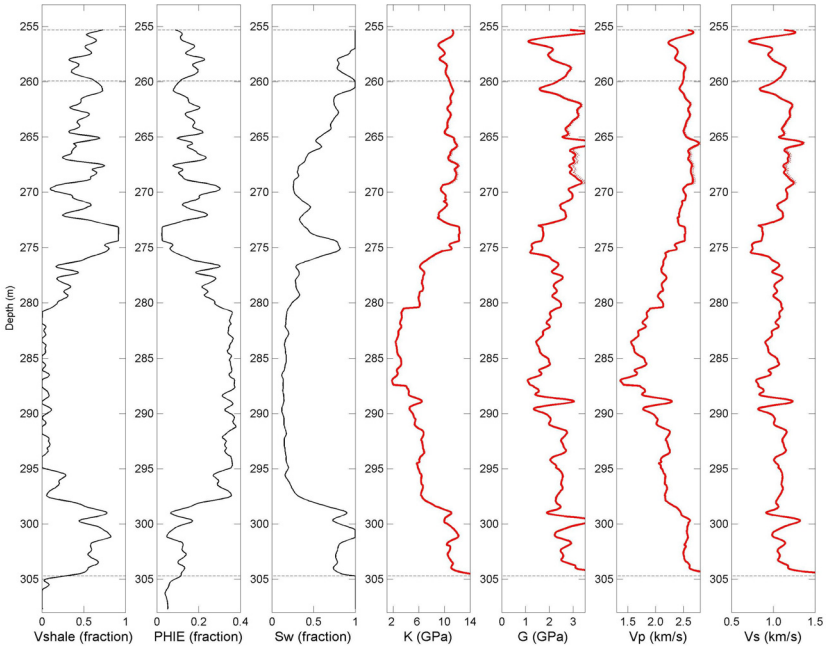

Figure 3.31. Modeled bulk and shear moduli, and P- and S-wave velocities at 2006 for well B. The red dot and solid curves represent the modeled values at 10 kHz and 100 Hz, respectively. The black curves represent the well log data at 2002.

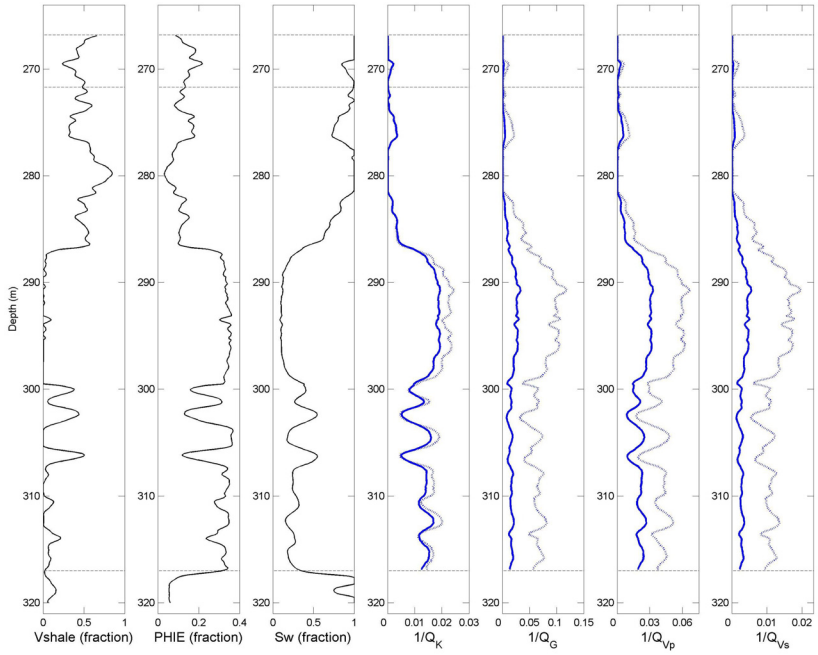

Figure 3.32. Modeled attenuation (1/Q) associated with the viscoelastic characteristics of heavy oil at 2002 for well A. The blue dot and solid curves represent the attenuation (1/Q) at frequency of 10 kHz and 100 Hz, respectively.

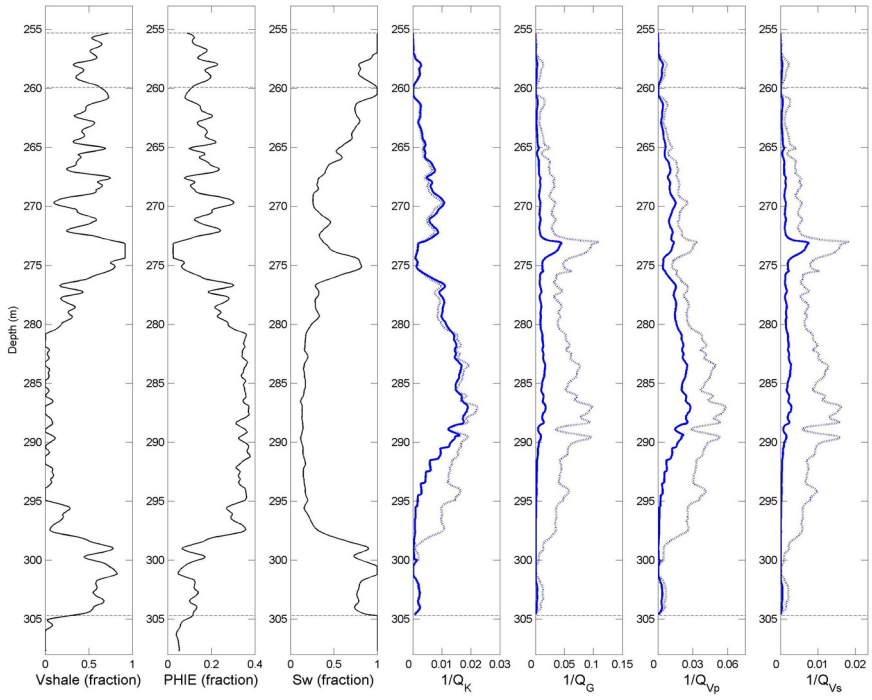

Figure 3.33. Modeled attenuation (1/Q) associated with the viscoelastic characteristics of heavy oil at 2002 for well B. The blue dot and solid curves represent the attenuation (1/Q) at frequency of 10 kHz and 100 Hz, respectively.

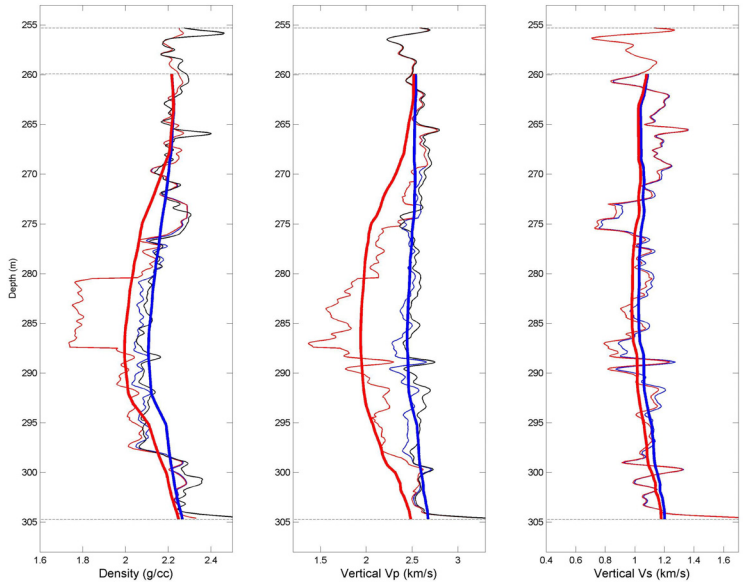

Figure 3.34. Backus averaging of the modeled P- and S-wave velocities for well B. The blue and red thin curves represent the modeled values at 2002 and 2006, respectively. The blue and red thick curves represent the Backus average at 2002 and 2006, respectively. The velocities correspond to that of a wave propagating along the vertical direction.

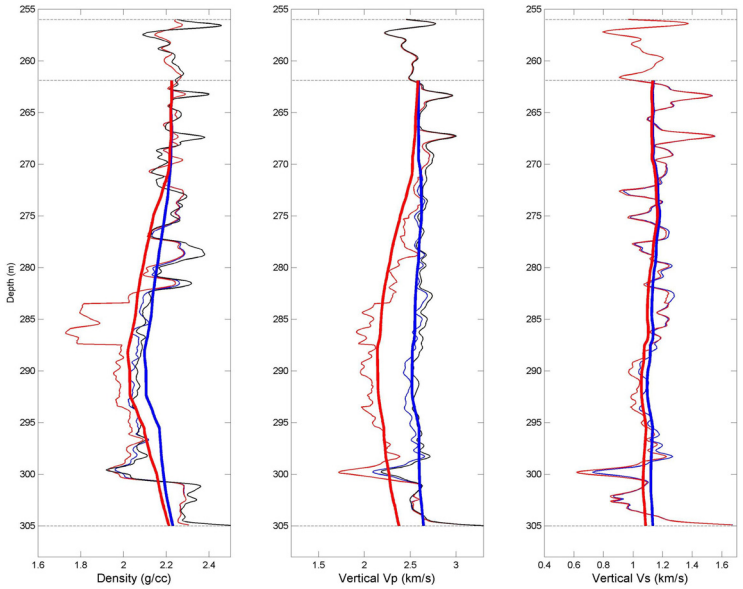

Figure 3.35. Backus averaging of the modeled P- and S-wave velocities for well C. The blue and red thin curves represent the modeled values at 2002 and 2006, respectively. The blue and red thick curves represent the Backus average at 2002 and 2006, respectively. The velocities correspond to that of a wave propagating along the vertical direction.

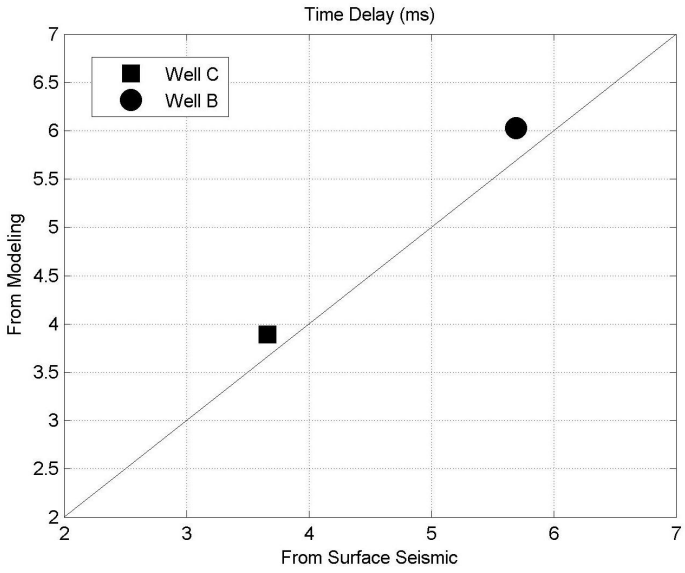

Figure 3.36. Comparison of time-delay of the reservoir layer between the modeled value and surface seismic analysis.

3.7.2 Sequential Elastic Property Changes

The elastic property changes of the heavy-oil reservoir at various reservoir conditions, which are caused by the steam injection, can be predicted by using the established model. I use the reservoir condition model of Kato et al. (2008) to predict the changes for clean sands and shaly sands. The model has 23 steps. Each step represents the specific stage of the SAGD operation, and defines the corresponding state of the reservoirs by the four parameters; pore pressure, temperature, water saturation, and steam phase. The parameter changes with step are as follows [also see Kato et al. (2008)]:

Step 1 to 5 : Pore pressure increases from 300 to 700 psi.
Temperature is constant (10 °C).

Step 5 to 23 : Temperature increases from 10 to 300 °C.
Pore pressure is constant (700 psi).

Step 18 : Heavy oils are replaced by the injected steam at 200 °C, leading to the irreducible oil saturation of 20 %.

Step 21 : Steam phase changes from liquid to vapor at 260 °C.

Figure 3.37 shows the modeled P- and S-wave velocities, Vp/Vs, and density changes at the well log frequency for the clean sands and shaly sands. The modeling parameters for the clean sand and shaly sands are assumed to be equivalent to the values at 297.0 m and 302.5 m in well A, respectively (also see Table 3.4).

The decrease in P- and S-wave velocities due to increased pore pressure is slightly larger in the clean sands than that in the shaly sands. After the pore pressure increase, the P- and S-wave velocities in the clean sands suddenly decrease as temperature slightly increases. However, since the amount of the decay in the S-wave velocity is more significant than the P-wave, Vp/Vs increases. At about 30 °C (step 9), Vp/Vs has the maximum magnitude (about 2.7). As the temperature rise continues, the P-wave velocity also continues to decrease until step 18, while the S-wave velocity is virtually constant at all the remaining steps. At step 18, where the heavy oils are replaced by the hot steam, the P-wave velocity increases because the hot steam has a higher bulk modulus than that of the heavy oil. Furthermore, at step 22, where the steam phase changes from liquid to vapor states, the P-wave velocity significantly drops and the S-wave velocity slightly increases because of the density decrease. In contrast, the shaly sands have a smaller decrease in P- and S-wave velocities due to temperature changes from 10 to 30 °C, compared to that of the clean sands. The maximum magnitude in Vp/Vs at around 30 °C is virtually same between the clean sands and shaly sands. Above 30 °C, the P-wave velocity in the shaly

sands changes with almost same rate as the clean sands until steam phase changes (step 21), and the corresponding S-wave velocity is almost constant like the clean sands.

Figure 3.38 shows the P- and S-wave velocities and Vp/Vs changes at the surface seismic frequency. They have a similar trend as that of the well log frequency. Particularly, at higher temperatures than 30 °C (after step 9), they are virtually equivalent to that at the higher frequency. With the surface seismic frequency, the heavy oil at initial condition has lower velocities than that of the well log frequency. Thus, as temperature increases from 10 °C to 30 °C, the velocity drops are smaller than the well log frequency, but still significant. The modeled elastic property changes will be used in Chapter 7 for quantitative interpretation of steam distribution.

Table 3.4. Parameters of the GSA based modeling for clean sands and shaly sands.

	Vquartz (fraction)	Vcalcite (fraction)	Vclay (fraction)	PHIE (fraction)	Aspect Ratio	Friability	Sw (fraction)
Clean Sands	0.618	0.015	0.013	0.354	0.080	0.995	0.100
Shaly Sands	0.460	0.000	0.381	0.159	0.080	0.990	0.400

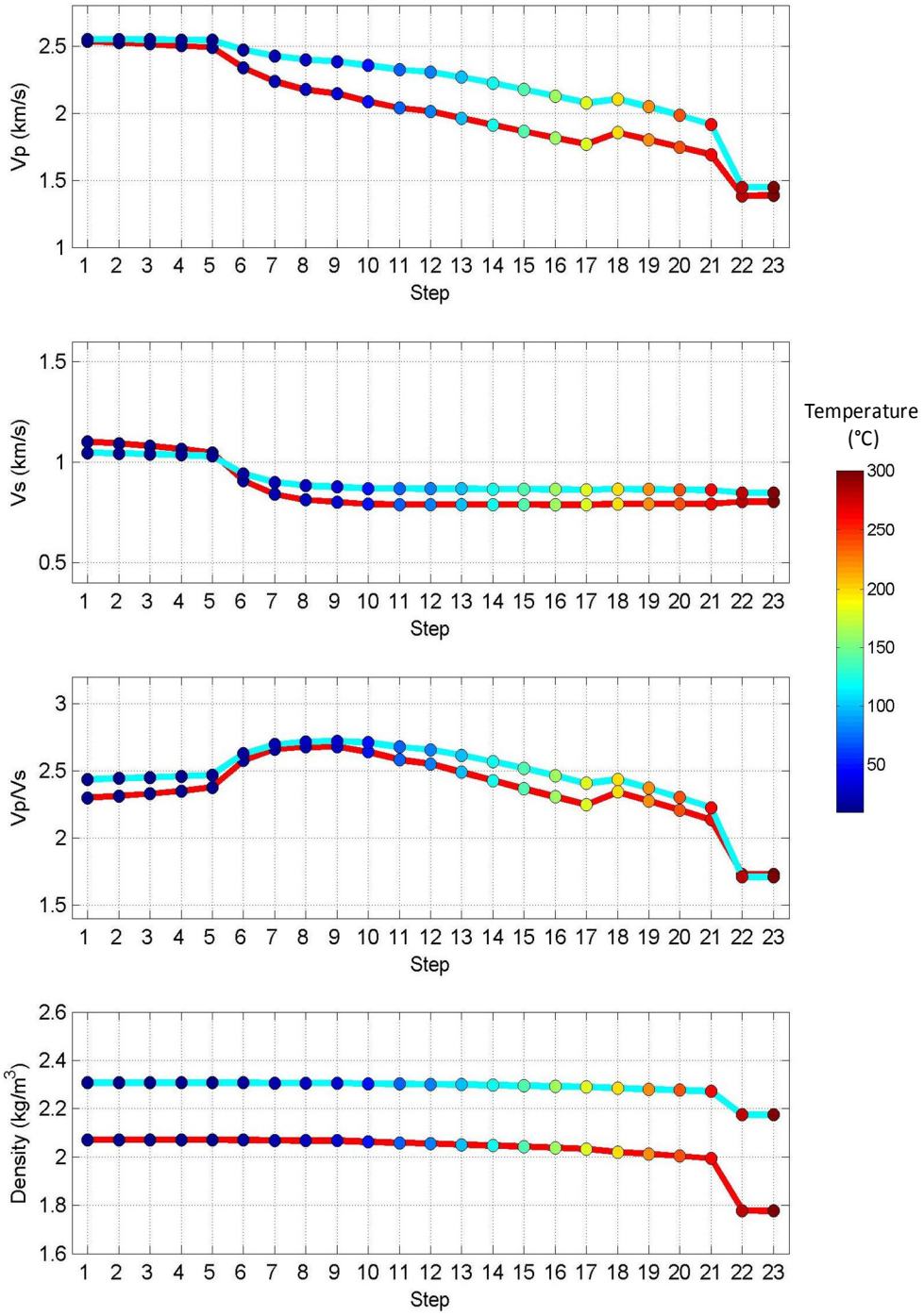

Figure 3.37. P- and S-wave velocities, Vp/Vs and density changes induced by the steam injection. The frequency is 10 kHz. The X-axis is the reservoir condition change, which is represented by 23 steps based on Figure 3.1. The red and light blue solid curves represent clean sands and shaly sands, respectively. The color of the circle represents the temperature.

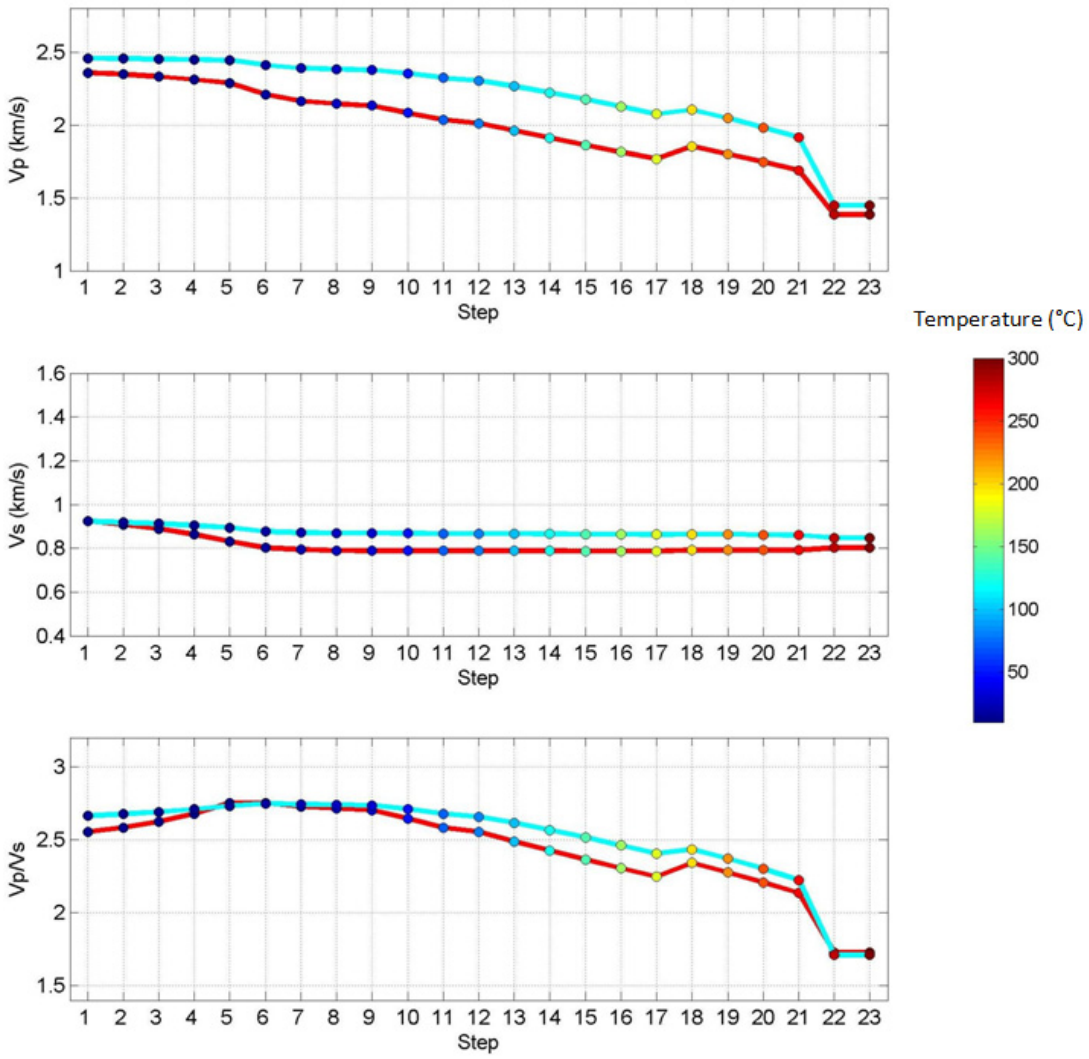

Figure 3.38. P-wave velocity, S-wave velocity, and Vp/Vs changes induced by the steam injection. The frequency is 100 Hz. The X-axis is the reservoir condition change, which is represented by 23 steps based on Figure 3.1. The red and light blue solid curves represent clean sands and shaly sands, respectively. The color of the circle represents the temperature.

3.8 Summary

In this chapter, I established the rock physics model of computing effective elastic properties of poorly consolidated, heavy-oil saturated sands at various reservoir conditions. The model can be applicable for not only clean sands with high porosity but also shaly sands with low porosity. The model is validated with the actual measurements from the laboratory, well logs, and time-lapse seismic data. Furthermore, the model precisely incorporates the complicated viscoelastic characteristics of the heavy oil. Particularly, the bulk viscosity is taken into account in the model. Thus, the model can precisely predict the elastic property change of the heavy-oil saturated sands at not only reservoir conditions (such as temperature, pressure, and water saturation) but also the wave frequency.

The GSA method is mainly used as an engine of the model. Although the GSA method has the assumption that effect of all interactions between the heterogeneities can be described only by the local interactions, the GSA method has no limitation on the volume concentration of the inclusions in the case of satisfying the assumption. This ability of the GSA method may be one of the reasons for successfully predicting effective properties of the poorly consolidated sands.

This model has very wide applications. As I presented, this model can be used for S-wave velocity prediction. Moreover, this model can predict the viscosity-induced velocity dispersion and associated attenuation.

Chapter 4 – P-P and P-S Joint AVO Inversion for Density Estimation - Methodology and Synthetic Test

4.1 Introduction

Three-dimensional seismic data which can provide broad lateral coverage are valuable for precise reservoir delineation and quantitative steam front monitoring. Numerous studies in heavy-oil reservoirs using 3D seismic data have been reported (e.g., Isaac, 1996; Sun, 1999; Nakayama et al., 2008; Roy et al., 2008). Despite these efforts, quantitative reservoir delineation by 3D seismic data is still challenging. This is partially because conventional seismic attributes are not good lithology discriminators in the Athabasca heavy-oil fields (e.g., Roy et al., 2008; Xu and Chopra, 2008). This is a result of small contrasts in P- and S-wave velocities between the reservoir and shale. On the other hand, the bulk density has a larger contrast between them and might be a more desired property for reservoir delineation.

A three-term AVO inversion is one of the techniques for extracting density reflectivity from seismic AVO responses. However, seismic AVO responses are commonly insensitive to density contrasts at small incident angles (Aki and Richards, 1998). Nevertheless, conventional P-P wave AVO analysis routinely utilizes incident angles only up to 35 - 40 degree (Roy et al., 2008). Consequently, density estimation is highly influenced by noise and the result is less reliable.

There are two possible options to improve the density estimation. The first one is to utilize larger incident angles. The large incident angle data is expected to make the inversion problem more stable. However, as Roy et al. (2008) and others discussed, when we intend to use the large incident angle data, we are faced with new problems in requiring additional data processing, including NMO stretch correction, Q compensation, and non-hyperbolic normal moveout.

The other option is to use converted P-S wave data, along with the P-P wave data. It has been common that the three-term AVO inversion for density estimation is applied to P-P wave data (e.g., Downton, 2005; Roy et al., 2008). However, it is expected that P-P and P-S joint inversion, which solves the problem by simultaneously using the two datasets, can give us more robust parameter estimation (e.g., Stewart, 1990). Papers concerning the three-term PP and PS joint inversion were recently published (Veire and Landrø, 2006). They used a least-squares method with singular value decomposition to show successful results applied on synthetic and real field data. However, the successful cases are very limited and the technique is not yet mature. Thus, it is obvious that we need continuous efforts to optimize the P-P and P-S joint inversion for density estimation.

In this chapter, I mainly focus on the second option to develop the P-P and P-S joint inversion for density estimation. I first describe the relationship between lithology and the corresponding elastic properties in Hangingstone oilfield. After the residual function map analysis, I will follow the Bayesian inversion theory and the formulas of P-P and P-S angle gathers. Furthermore, I will describe synthetic test of the developed method.

Finally I will conclude with a summary. It is noted that application of the method to the field data, along with the data conditioning, will be discussed in Chapter 5.

4.2 Reservoir Delineation

For reservoir delineation, it is important to accurately understand the relationship between lithology and the corresponding elastic properties in the study area. Figure 4.1 shows the relationship between elastic properties (P-wave velocity, Vp/Vs, and density) and Vshale in the McMurray Formation in the Hangingstone oilfield. The left column is the well log data while the right column is based on the rock physics modeling at the surface seismic frequency of 100 Hz.

The P-wave velocity at both the well log (about 10 kHz) and surface seismic frequencies shows poor correlation with Vshale, suggesting that the P-wave velocity is not a desirable parameter. There is considerable literature reporting that Vp/Vs is a good lithology discriminator (e.g., Xu and Stewart, 2006b; Dumitrescu and Lines, 2009). The well log Vp/Vs shows weak convex downward distribution with Vshale (Figure 4.1c). Thus, reservoir delineation is difficult via the well log Vp/Vs. Also, at the surface seismic frequency, Vp/Vs has better correlation with Vshale because the value of clean sands is smaller than the corresponding well log data (Figure 4.1d). However, the difference between clean sands and shale is still small. Thus, to use Vp/Vs is not encouraged in this reservoir delineation. In contrast, bulk density shows almost linear relationship with Vshale (Figure 4.1e), whose correlation coefficient is 0.944. The bulk density of clean sands and shale are about 2.05 g/cc and 2.30 g/cc, respectively, resulting in significant difference between them (about 12 %). Consequently, it is concluded that the bulk

density is the most desirable property for the reservoir delineation in this area, which is consistent with the studies made in other heavy-oil fields in Canada (e.g., Roy et al., 2008; Maria, 2009).

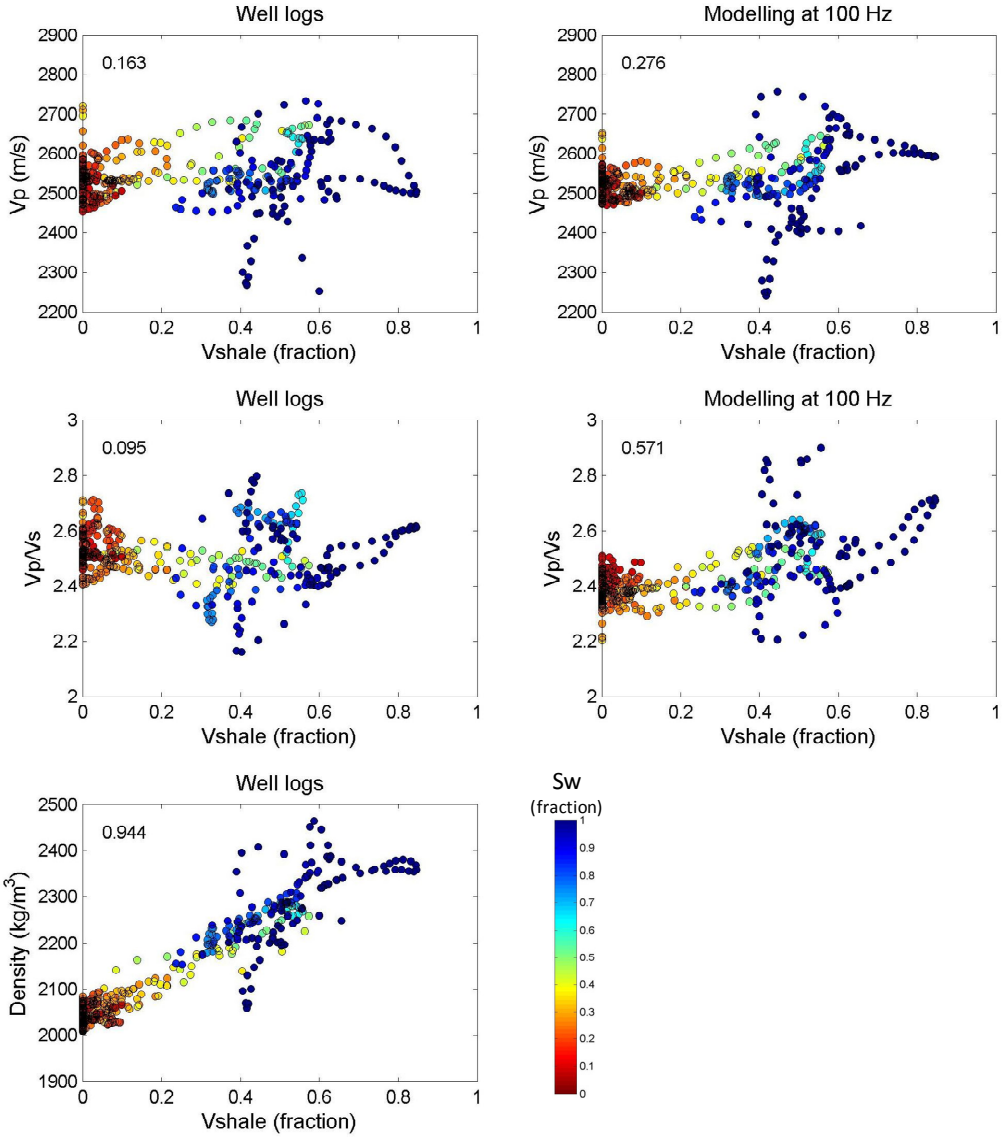

Figure 4.1. Relationship of P-wave velocity, Vp/Vs, and density with Vshale in the McMurray Formation. The left column is the well log data while the right column is based on the rock physics modeling at the surface seismic frequency (100 Hz). The number at the upper left corner is the correlation coefficient.

4.3 Residual Function Map Analysis

The use of large incident angle data, along with small incident angle data, is expected to improve the density estimation. Furthermore, P-S wave can give us additional constraints. Thus, to investigate the importance of them, I performed the Residual Function Map (RFM) analysis for the three-term AVO inversion. Following Macdonald et al. (1987), Menke (1989) and Demirbag et al. (1993), the RFM is defined for the P-P wave only, P-S wave only, and the joint inversions as:

$$\begin{aligned} E_{PP}(L_1, L_2) &= \sum \left[R_{PP} - \overline{R}_{PP}(L_1, L_2) \right]^2, \\ E_{PS}(L_1, L_2) &= \sum \left[R_{PS} - \overline{R}_{PS}(L_1, L_2) \right]^2, \\ E_{joint}(L_1, L_2) &= E_{PP}(L_1, L_2) + E_{PS}(L_1, L_2), \end{aligned} \tag{4.1}$$

where $E_{PP}(L_1, L_2)$, $E_{PS}(L_1, L_2)$, and $E_{joint}(L_1, L_2)$ are the RFM for the P-P wave, P-S wave, and the joint inversions; R_{PP} and R_{PS} are the Aki and Richards approximation for P-P and P-S wave reflection coefficients with the given reflectivities (as a reference). A full description of the AVO formulas will be provided in a later section [see Equation (4.10) and (4.11)]. Assuming a boundary between shale and clean sands as the reference, I chose the corresponding reflectivities, as shown in Table 4.1. In addition, $\overline{R}_{PP}$ and $\overline{R}_{PS}$ are the associated AVO response in which only two (L_1 and L_2) of three reflectivities (Vp, Vs, and density) change and the other is kept constant. As the difference between R_{PP} and $\overline{R}_{PP}$ (or between R_{PS} and $\overline{R}_{PS}$) is larger, the reference is more easily distinguished. In contrast, as the difference is smaller, the discrimination is more sensitive to the data noise.

Table 4.1. Properties used in the residual function analysis.

	P-wave velocity	S-wave velocity	Density
Shale	2600 m/s	1000 m/s	2300 kg/m^3
Clean Sands	2500 m/s	1050 m/s	2050 kg/m^3
Reflectivity	-0.039	0.049	-0.115

I analyze three cases with different maximum incident angles; 0 - 30°, 0 - 45°, and 0 - 60°, respectively. The Vs/Vp required in the AVO approximation is set to be 0.372 and sampling interval of the incident angle is 5 degree. Figure 4.2 shows the RFM analysis result of the P-P only inversion. The REM maps show ellipsoidal distribution, implying that the solution can be solved by a linear inversion scheme (e.g., Macdonald et al., 1987). In the combination between P-wave velocity and density reflectivities, the ellipsoid at the maximum incident angle of 30° spreads widely. As the maximum incident angle increases, the ellipsoid shrinks substantially and the reference is more easily distinguished. In the case of the combination between P-wave velocity and density reflectivities, similar results are observed. But, the ellipsoid extends more vertically. Moreover, compared to that between the P- and S-wave velocity reflectivities, the ellipsoid spreads more widely. Thus, it is suggested that the density estimation is more difficult than the estimation of P- and S-wave velocities.

In the P-S wave only inversion, as the maximum incident angle increases, the ellipsoid shrinks, like the P-P wave only inversion (Figure 4.3). But, the shrinking is smaller than that of the P-P wave only inversion. Even at the maximum incident angle of 60°, the density estimation has large uncertainties. In contrast, the joint inversion has a smaller

ellipsoid in all the cases, compared to the individual inversions (Figure 4.4). Also, as the maximum incident angle increases, the ellipsoid significantly shrinks.

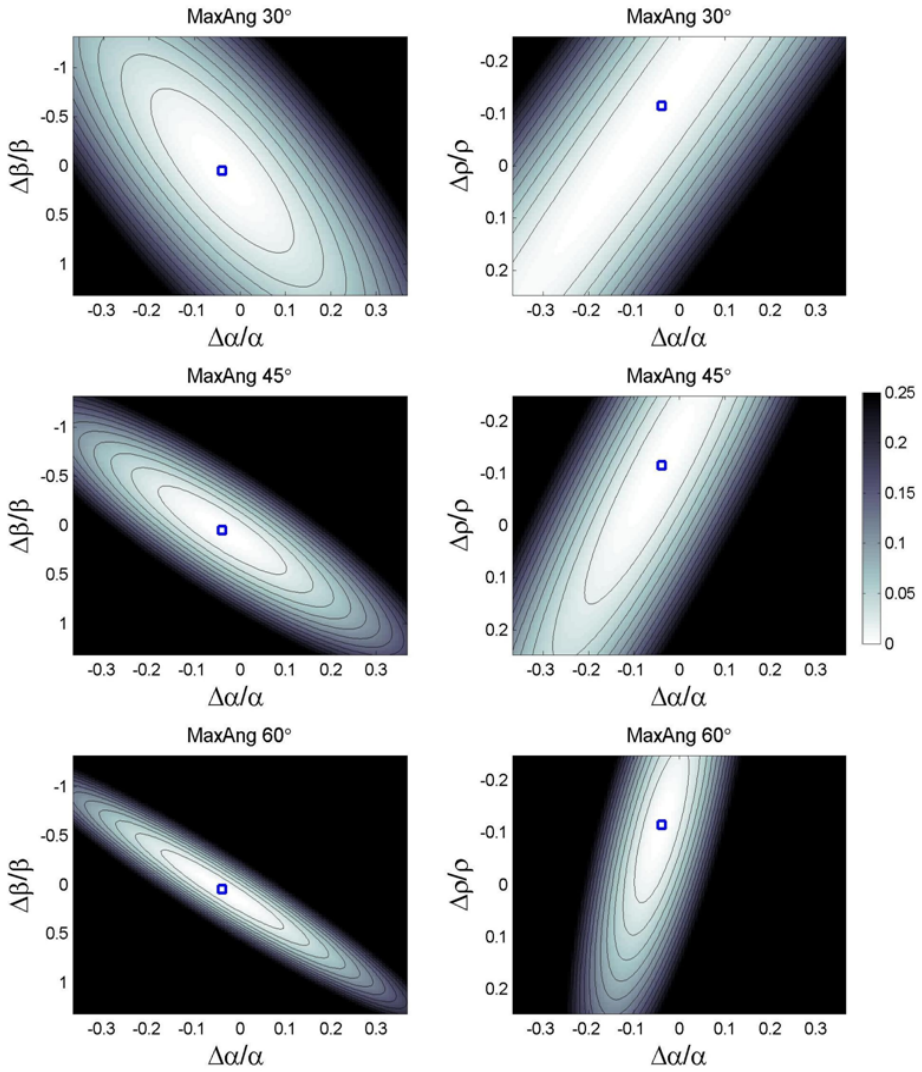

Figure 4.2. Residual function map of P-P reflection coefficient with different maximum incident angles. The maximum incident angle of the top, middle, and bottom are 30°, 45°, and 60°, respectively. The left column is between P- and S-wave velocity reflectivities while the right column is between P-wave velocity and density reflectivities. The reflectivities of the reference are shown by the blue marker. The contour interval is 0.02.

Consequently, it is concluded that the joint inversion can substantially improve the density estimation. Furthermore, large incident angle data are essential for obtaining a stable solution, particularly in the P-P only and joint inversions. However, it should be noted that the RFM analysis does not take into account the wavelet. The effect of the wavelet will be discussed in a later section.

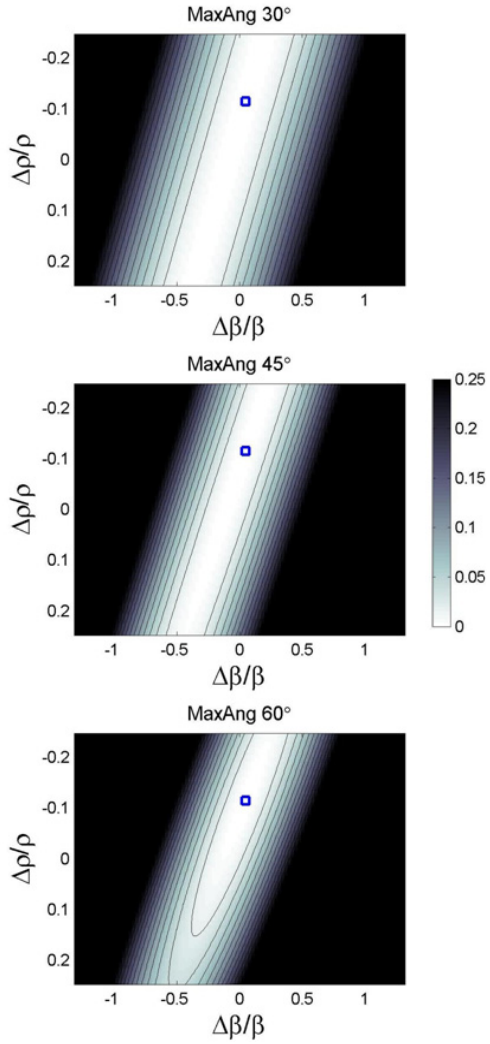

Figure 4.3. Residual function map of P-S reflection coefficient with different maximum incident angles. The maximum incident angle of the top, middle, and bottom are 30°, 45°, and 60°, respectively. The reflectivity of the reference is shown by the blue marker. The contour interval is 0.02.

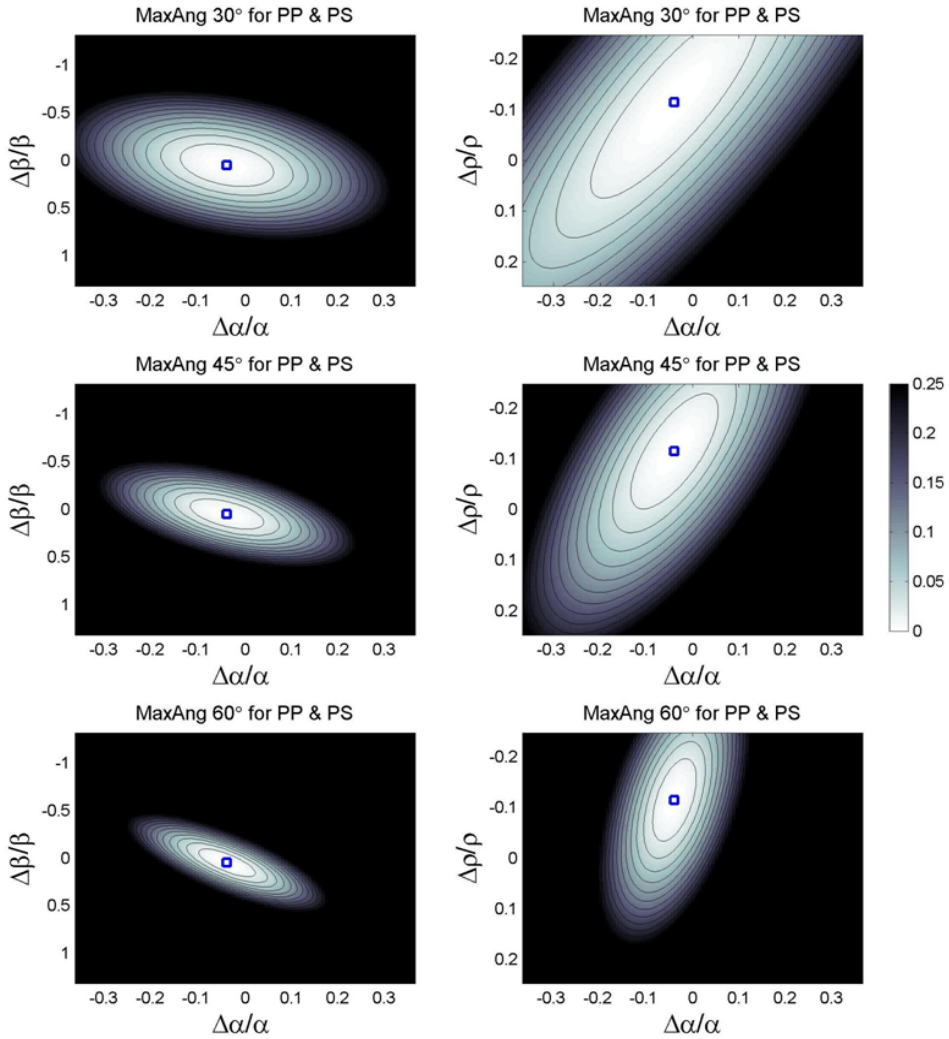

Figure 4.4. Residual function map of P-P and P-S joint inversion with different maximum incident angles. The maximum incident angle of the top, middle, and bottom are 30°, 45°, and 60°, respectively. The left column is between P- and S-wave velocity reflectivities while the right column is between P-wave velocity and density reflectivities. The reflectivities of the reference are shown by the blue marker. The contour interval is 0.02.

4.4 Bayesian Inversion Method

All field seismic data have noise to some degree. In addition, it is not unusual that subsurface elastic properties, such as velocities and density, have some correlation with each other. The mudrock line (Castagna et al., 1985) and Gardner's relation (Gardner et

al., 1974) are some of the most general relationships. Nevertheless, the most common method of the seismic AVO inversion neglects relative magnitude of the the data noise and the correlation among model parameters to get the solution in a least-square fashion.

In contrast, the stochastic method based on the Bayesian theorem can elegantly handle the data noise, together with any available information with a corresponding degree of confidence (e.g., Jackson and Matuura, 1985; Tarantola, 1987; Duijndam, 1988 a, b). Following Duijndam (1988a), the Bayes theorem is formulated as:

$$p(\mathbf{m}\,|\,\mathbf{d}) = \frac{p(\mathbf{d}\,|\,\mathbf{m})p(\mathbf{m})}{p(\mathbf{d})}, \tag{4.2}$$

where **m** and **d** are the model parameters and the observation data, respectively. The function $p(\mathbf{m}\,|\,\mathbf{d})$ is the conditional probability density function (pdf) of **m** after **d** is obtained, which corresponds to a posterior pdf. And, $p(\mathbf{d}\,|\,\mathbf{m})$ is the conditional pdf of **d** after **m** is obtained; $p(\mathbf{m})$ is a prior pdf that contains additional knowledge on **m**. The denominator $p(\mathbf{d})$ does not depend on **m** and can be considered as a constant factor.

To obtain a mathematically tractable expression, two assumptions are made. The first one is that the model parameters (**m**) have the Gaussian distribution. The other is that the data noise also has the Gaussian distribution with zero mean. With the help of these assumptions, the prior pdf can be expressed as:

$$p(\mathbf{m}) = \text{const.}\exp\left\{-\frac{1}{2}(\mathbf{m}_0 - \mathbf{m})^T \mathbf{C}_{\mathbf{m}}^{-1}(\mathbf{m}_0 - \mathbf{m})\right\}, \tag{4.3}$$

where $\mathbf{C_m}$ is the covariance matrix of $\mathbf{m}$; $\mathbf{m}_0$ is the prior mean value. When considering a general relationship between $\mathbf{d}$ and $\mathbf{m}$, as $\mathbf{d} = \mathbf{g}(\mathbf{m})$, the likelihood function is expressed as:

$$p(\mathbf{d} \mid \mathbf{m}) = \text{const.} \exp\left\{ -\frac{1}{2} \left(\mathbf{g}(\mathbf{m}) - \mathbf{d}_{\mathbf{obs}}\right)^T \mathbf{C}_n^{-1} \left(\mathbf{g}(\mathbf{m}) - \mathbf{d}_{\mathbf{obs}}\right) \right\}, \tag{4.4}$$

where $\mathbf{d_{obs}}$ is the observed data and $\mathbf{C_n}$ is the corresponding covariance matrix. To obtain the maximum likelihood function is equivalent to maximizing the product of $p(\mathbf{d} \mid \mathbf{m})$ and $p(\mathbf{m})$, which is furthermore equivalent to minimizing sum of the exponents, as given by the misfit function $F(\mathbf{m})$ as:

$$2F(\mathbf{m}) = \left(\mathbf{g}(\mathbf{m}) - \mathbf{d}_{\mathbf{obs}}\right)^T \mathbf{C}_n^{-1} \left(\mathbf{g}(\mathbf{m}) - \mathbf{d}_{\mathbf{obs}}\right) + \left(\mathbf{m}_0 - \mathbf{m}\right)^T \mathbf{C}_m^{-1} \left(\mathbf{m}_0 - \mathbf{m}\right). \tag{4.5}$$

If one considers a linear system as:

$$\mathbf{d} = \mathbf{G}\mathbf{m}, \tag{4.6}$$

the posterior probability density distribution is defined as:

$$\sigma_m(\mathbf{m}) = \text{const.} \exp\left(-\frac{1}{2} \left(\mathbf{m} - \widehat{\mathbf{m}}\right)^T \widehat{\mathbf{C}}_{\mathbf{m}}^{-1} \left(\mathbf{m} - \widehat{\mathbf{m}}\right) \right), \tag{4.7}$$

where $\widehat{\mathbf{m}}$ is the maximum of the posterior density distribution and is expressed as:

$$\widehat{\mathbf{m}} = \left(\mathbf{G}^{\mathbf{T}} \mathbf{C}_{\mathbf{n}}^{-1} \mathbf{G} + \mathbf{C}_{\mathbf{m}}^{-1}\right)^{-1} \left(\mathbf{G}^{\mathbf{T}} \mathbf{C}_{\mathbf{n}}^{-1} \mathbf{d}_{\mathbf{obs}} + \mathbf{C}_{\mathbf{m}}^{-1} \mathbf{m}_{\mathbf{0}}\right). \tag{4.8}$$

Also, $\widehat{\mathbf{C}}_{\mathbf{m}}$ is the posterior covariance matrix and is expressed as:

$$\widehat{\mathbf{C}}_{\mathbf{m}} = \left(\mathbf{G}^T \mathbf{C}_{\mathbf{n}}^{-1} \mathbf{G} + \mathbf{C}_{\mathbf{m}}^{-1}\right)^{-1}. \tag{4.9}$$

4.5 Formularization of AVO Inversion

The Zoeppritz equations fully describe the reflection and transmission coefficients at an interface for P and S plane waves in the case of an isotropic medium. The coefficients do not have a linear relationship with elastic parameters above and below the interface. Aki and Richards (1980) simplified these equations into a linear form with respect to the P- and S-wave velocities and density reflectivities, as follows:

$$\begin{aligned} R_{PP}(\theta) &= a_\alpha(\theta)\frac{\Delta\alpha}{\bar{\alpha}} + a_\beta(\theta,\gamma)\frac{\Delta\beta}{\bar{\beta}} + a_\rho(\theta,\gamma)\frac{\Delta\rho}{\bar{\rho}}, \\ R_{PS}(\theta,\varphi) &= b_\beta(\theta,\varphi,\gamma)\frac{\Delta\beta}{\bar{\beta}} + b_\rho(\theta,\varphi,\gamma)\frac{\Delta\rho}{\bar{\rho}}, \end{aligned} \tag{4.10}$$

where

$$\begin{aligned} a_\alpha(\theta) &= \frac{1}{2\cos^2\theta}, \\ a_\beta(\theta,\gamma) &= -4\gamma^2\sin^2\theta, \\ a_\rho(\theta,\gamma) &= \frac{1}{2}\left(1-4\gamma^2\sin^2\theta\right), \\ b_\beta(\theta,\varphi,\gamma) &= 2\frac{\sin\theta}{\cos\varphi}\left(\gamma^2\sin^2\theta-\gamma\cos\varphi\cos\theta\right), \\ b_\rho(\theta,\varphi,\gamma) &= -\frac{\sin\theta}{2\cos\varphi}\left(1-2\gamma^2\sin^2\theta+2\gamma\cos\theta\cos\varphi\right). \end{aligned} \tag{4.11}$$

In addition, α , β, and ρ are the P- and S-wave velocities and density; Δ and the superscript bar represent the contrast and average value across the interface for the corresponding parameter. θ is the average of P-wave incident and transmitted angles, and φ is the average of reflection and transmission angles of the associated P-S converted wave; γ is the Vs/Vp value. The Aki and Richards linear approximation is accurate for small relative changes in elastic parameters (Aki and Richards, 1980).

The Equations (4.10) and (4.11) for a single interface can be extended to time-continuous reflection coefficient by taking partial derivative of natural logarithm of the time-continuous elastic parameters with respect to time (Stolt and Weglein, 1985), as follows:

$$\begin{aligned} R_{PP}(t,\theta) &= a_{\alpha}(t,\theta)\frac{\partial}{\partial t}\ln\alpha(t) + a_{\beta}(t,\theta)\frac{\partial}{\partial t}\ln\beta(t) + a_{\rho}(t,\theta)\frac{\partial}{\partial t}\ln\rho(t), \\ R_{PS}(t,\theta,\varphi) &= b_{\beta}(t,\theta,\varphi)\frac{\partial}{\partial t}\ln\beta(t) + b_{\rho}(t,\theta,\varphi)\frac{\partial}{\partial t}\ln\rho(t), \end{aligned} \tag{4.12}$$

where $a_{\alpha}(t,\theta), a_{\beta}(t,\theta), a_{\rho}(t,\theta), b_{\beta}(t,\theta)$, and $b_{\rho}(t,\theta)$ are the corresponding coefficients defined by equation (4.11) for the time-continuous case.

Assuming that *m* different incident angles are available for both the P-P and P-S waves at each time sample, a linear relationship can be expressed in the matrix form as:

$$\begin{bmatrix} \mathbf{R_{PP}}(\theta_1) \\ \vdots \\ \mathbf{R_{PP}}(\theta_m) \\ \mathbf{R_{PS}}(\theta_1) \\ \vdots \\ \mathbf{R_{PS}}(\theta_m) \end{bmatrix} = \begin{bmatrix} \mathbf{a_{\alpha}}(\theta_1) & \mathbf{a_{\beta}}(\theta_1) & \mathbf{a_{\rho}}(\theta_1) \\ \vdots & \vdots & \vdots \\ \mathbf{a_{\alpha}}(\theta_m) & \mathbf{a_{\beta}}(\theta_m) & \mathbf{a_{\rho}}(\theta_m) \\ \mathbf{0} & \mathbf{b_{\beta}}(\theta_1) & \mathbf{b_{\rho}}(\theta_1) \\ \vdots & \vdots & \vdots \\ \mathbf{0} & \mathbf{b_{\beta}}(\theta_m) & \mathbf{b_{\rho}}(\theta_m) \end{bmatrix} \begin{bmatrix} \mathbf{dt} & \mathbf{0} & \mathbf{0} \\ \mathbf{0} & \mathbf{dt} & \mathbf{0} \\ \mathbf{0} & \mathbf{0} & \mathbf{dt} \end{bmatrix} \begin{bmatrix} \ln\boldsymbol{\alpha} \\ \ln\boldsymbol{\beta} \\ \ln\boldsymbol{\rho} \end{bmatrix}. \tag{4.13}$$

Moreover, for a simple expression, Equation (4.13) is re-expressed as follows:

$$\mathbf{R} = \mathbf{ADm}, \tag{4.14}$$

where

$$\mathbf{R} = \begin{bmatrix} \mathbf{R_{PP}}(\theta_1) \\ \vdots \\ \mathbf{R_{PP}}(\theta_m) \\ \mathbf{R_{PS}}(\theta_1) \\ \vdots \\ \mathbf{R_{PS}}(\theta_m) \end{bmatrix}, \tag{4.15}$$

$$\mathbf{A}=\begin{bmatrix} \mathbf{a}_{\alpha}(\theta_1) & \mathbf{a}_{\beta}(\theta_1) & \mathbf{a}_{\rho}(\theta_1) \\ \vdots & \vdots & \vdots \\ \mathbf{a}_{\alpha}(\theta_m) & \mathbf{a}_{\beta}(\theta_m) & \mathbf{a}_{\rho}(\theta_m) \\ \mathbf{0} & \mathbf{b}_{\beta}(\theta_1) & \mathbf{b}_{\rho}(\theta_1) \\ \vdots & \vdots & \vdots \\ \mathbf{0} & \mathbf{b}_{\beta}(\theta_m) & \mathbf{b}_{\rho}(\theta_m) \end{bmatrix}, \tag{4.16}$$

$$\mathbf{D}=\begin{bmatrix} \mathbf{dt} & \mathbf{0} & \mathbf{0} \\ \mathbf{0} & \mathbf{dt} & \mathbf{0} \\ \mathbf{0} & \mathbf{0} & \mathbf{dt} \end{bmatrix}, \tag{4.17}$$

and

$$\mathbf{m}=\begin{bmatrix} \ln\boldsymbol{\alpha} & \ln\boldsymbol{\beta} & \ln\boldsymbol{\rho} \end{bmatrix}^T. \tag{4.18}$$

The matrix **R** corresponds to the time-continuous P-P and P-S reflection coefficients. The elements $\mathbf{R}_{\mathbf{PP}}(\theta_i)$ and $\mathbf{R}_{\mathbf{PS}}(\theta_i)$ are a $n\times n$ diagonal matrix containing time continuous values of the corresponding reflection coefficient at incident angle θ_i; n is number of the time sampling. The matrix **A** corresponds to the AVO coefficients defined by (4.11), in which the elements $\mathbf{a}_{\alpha}(\theta_i)$, $\mathbf{a}_{\beta}(\theta_i)$, $\mathbf{a}_{\rho}(\theta_i)$, $\mathbf{b}_{\beta}(\theta_i)$, and $\mathbf{b}_{\rho}(\theta_i)$ are also the diagonal matrix containing the time continuous values at the incident angle θ_i. The matrix **D** represents a time-derivative operator, in which the element **dt** is expressed as:

$$\mathbf{dt}=\begin{bmatrix} -1 & 1 & 0 & \cdots & \cdots & 0 \\ 0 & -1 & 1 & 0 & \cdots & 0 \\ \vdots & & & & & \vdots \\ 0 & \cdots & \cdots & 0 & -1 & 1 \\ 0 & \cdots & \cdots & \cdots & 0 & -1 \end{bmatrix}. \tag{4.19}$$

The last matrix **m** corresponds to the model parameters. The elements, $\ln\boldsymbol{\alpha}$, $\ln\boldsymbol{\beta}$, and $\ln\boldsymbol{\rho}$, are $n\times 1$ matrix containing the time-continuous values of the corresponding parameter.

Furthermore, the time-continuous reflection coefficients are convolved with the associated wavelet, the formula is expressed as:

$$\mathbf{d}_{obs} = \mathbf{WADm}, \tag{4.20}$$

where $\mathbf{d}_{obs}$ is noise-free observation data and expressed as:

$$\mathbf{d}_{obs} = \begin{bmatrix} \mathbf{d}_{\mathbf{PP}}(\theta_1) \\ \vdots \\ \mathbf{d}_{\mathbf{PP}}(\theta_m) \\ \mathbf{d}_{\mathbf{PS}}(\theta_1) \\ \vdots \\ \mathbf{d}_{\mathbf{PS}}(\theta_m) \end{bmatrix}. \tag{4.21}$$

The elements, $\mathbf{d}_{\mathbf{PP}}(\theta_i)$ and $\mathbf{d}_{\mathbf{PP}}(\theta_i)$, are a $n \times 1$ matrix containing the time continuous observation data at incident angle θ_i for P-P and P-S waves, respectively. $\mathbf{W}$ corresponds to the wavelet matrix expressed as:

$$\mathbf{W} = \begin{bmatrix} \mathbf{W}_{\mathbf{PP}}(\theta_1) & & & & & & \\ & \ddots & & & & & \\ & & \mathbf{W}_{\mathbf{PP}}(\theta_m) & & & & \\ & & & \mathbf{W}_{\mathbf{PS}}(\theta_1) & & & \\ & & & & \ddots & & \\ & & & & & \mathbf{W}_{\mathbf{PS}}(\theta_m) \end{bmatrix}. \tag{4.22}$$

The element $\mathbf{W}_{\mathbf{PP}}(\theta_i)$ is the associated wavelet expressed as:

$$\mathbf{W}_{\mathbf{PP}}(\theta_i) = \begin{bmatrix} s_1(\theta_i) & & & & & & \\ s_2(\theta_i) & s_1(\theta_i) & & & & & \\ \vdots & & \ddots & & & & \\ s_{ns}(\theta_i) & \cdots & \cdots & s_1(\theta_i) & & & \\ & \ddots & & & \ddots & & \\ & & s_{ns}(\theta_i) & \cdots & \cdots & s_1(\theta_i) \\ & & & \ddots & & \vdots \\ & & & & \ddots & \vdots \\ & & & & & s_{ns}(\theta_i) \end{bmatrix}, \tag{4.23}$$

where $(s_1(\theta_i),...s_{ns}(\theta_i))$ are the samples of the wavelet for angle θ_i. $\mathbf{W_{PS}}(\theta_i)$ also has the similar form.

A formula of the joint AVO inversion is finally obtained as:

$$\mathbf{d_{obs}} = \mathbf{Gm}, \tag{4.24}$$

where **G** is the forward modeling operator and is expressed as:

$$\mathbf{G} = \mathbf{WAD}. \tag{4.25}$$

Thus, by combining (4.24) and (4.25) with (4.8) and (4.9), solution of the model parameters **m** can be obtained in the Bayesian framework, which is consistent with not only the seismic data but also the given additional information.

4.6 Synthetic Test

Buland and Omre (2003) conducted synthetic test on the Bayesian method for the three-term AVO inversion. But, their test was only for the P-P wave only inversion. Thus, I extend the synthetic test to the case of the P-P and P-S joint inversion. Furthermore, to investigate the feasibility of the method in the Hangingstone oilfield, I chose the test parameters that are close to the field data, such as well log data, seismic frequency bands, seismic angle range, and so on.

4.6.1 Earth Model

As I discussed in Chapter 3, heavy-oil reservoirs have the frequency-dependent moduli and velocities due to the viscosities. So, it is not proper to directly use the well log data in comparison with the surface seismic data. Thus, I model the velocities at the

corresponding frequency (100 Hz) by using the established rock physics model along with the viscoelastic theory. Then, the vertical profile of the modeled velocities along with the density are converted to time domain. Figure 4.5 shows the earth model in the two-way time domain, consisting of the P- and S-wave velocities and density. The time sampling is set to be 1 ms.

Since the Devonian Formation underling the reservoir is well-consolidated carbonate rock, resulting in a strong impedance contrast at the interface with the reservoir (see Figure 1.4), the small reflection coefficient approximation is not practically satisfied at the boundary. The time window of the synthetic test is set to end above the Top Devonian interface. The effects of the large property change at the Top Devonian interface will be discussed in Chapter 5. The heavy-oil saturated reservoir sands are mainly from about 270 ms to the end, which is indicated by the lower value of the density. The statistical values of the earth model are presented by Table 4.2.

Table 4.2. Mean and standard deviation values of the earth model.

	Mean	STD
Vp (m/s)	2336	140
Vs (m/s)	883	162
Density (kg/m^3)	2164	82

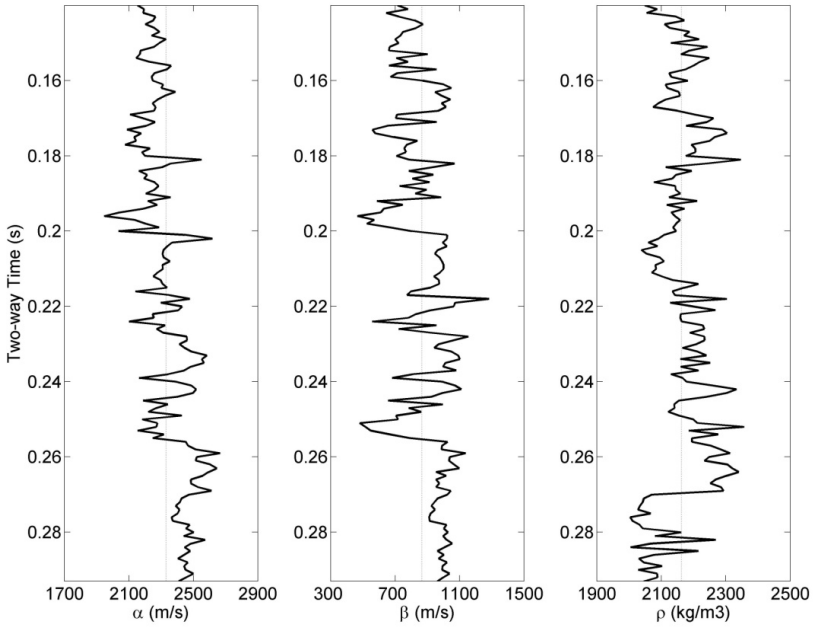

Figure 4.5. P- and S-wave velocities and density in two-way time for well A.

4.6.2 Prior Mean Model

The prior mean model $\mathbf{m}_0$ is obtained by applying a low-pass filter of 7-12 Hz to the earth model of $\ln\boldsymbol{\alpha}$, $\ln\boldsymbol{\beta}$, and $\ln\boldsymbol{\rho}$ (Figure 4.6). It can be observed that although the prior mean model follows vertical trend of the earth model, there are some deviations from them. The deviations are defined as the model parameters **m**. Figure 4.7 shows histogram of the model parameters, and Figure 4.8 shows the crossplot between them. The red curve in the histograms represents the Gaussian distribution, suggesting it is reasonable that the distribution is approximated by the Gaussian. The standard deviation and correlation coefficient are obtained by standard estimators. The estimated standard deviation for $\ln\alpha$, $\ln\beta$, and $\ln\rho$ are, respectively, $\sigma_\alpha = 0.0464$, $\sigma_\beta = 0.1848$, and $\sigma_\rho = 0.0372$. The

estimated correlation coefficient are $\upsilon_{\alpha\beta} = 0.67, \upsilon_{\alpha\rho} = 0.28$, and $\upsilon_{\beta\rho} = -0.09$. Thus, the covariance matrix of the model parameters is made based on these values as:

$$\mathbf{C_m} = \begin{bmatrix} \boldsymbol{\sigma}_\alpha^2 & \boldsymbol{\nu}_{\alpha\beta}\boldsymbol{\sigma}_\alpha\boldsymbol{\sigma}_\beta & \boldsymbol{\nu}_{\alpha\rho}\boldsymbol{\sigma}_\alpha\boldsymbol{\sigma}_\rho \\ \boldsymbol{\nu}_{\alpha\beta}\boldsymbol{\sigma}_\alpha\boldsymbol{\sigma}_\beta & \boldsymbol{\sigma}_\beta^2 & \boldsymbol{\nu}_{\beta\rho}\boldsymbol{\sigma}_\beta\boldsymbol{\sigma}_\rho \\ \boldsymbol{\nu}_{\alpha\rho}\boldsymbol{\sigma}_\alpha\boldsymbol{\sigma}_\rho & \boldsymbol{\nu}_{\beta\rho}\boldsymbol{\sigma}_\beta\boldsymbol{\sigma}_\rho & \boldsymbol{\sigma}_\rho^2 \end{bmatrix}, \tag{4.26}$$

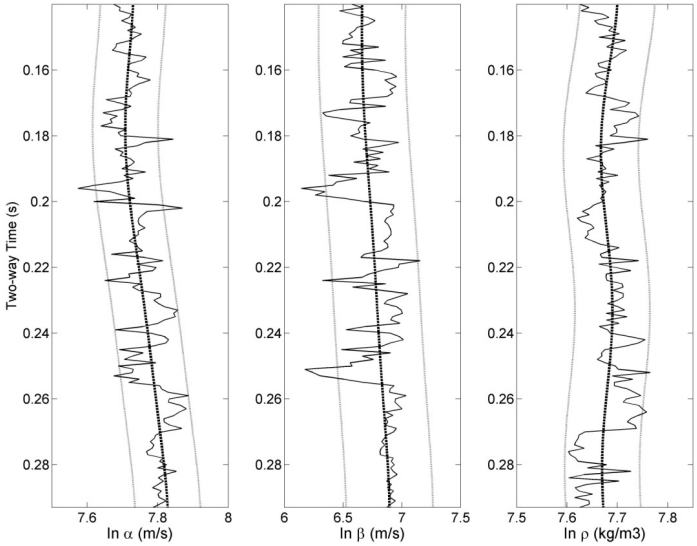

Figure 4.6. Prior mean model (thick dash) and 0.95 prediction interval (thin dot) for $\ln\alpha$, $\ln\beta$, and $\ln\rho$. The solid thin curves represent the earth model.

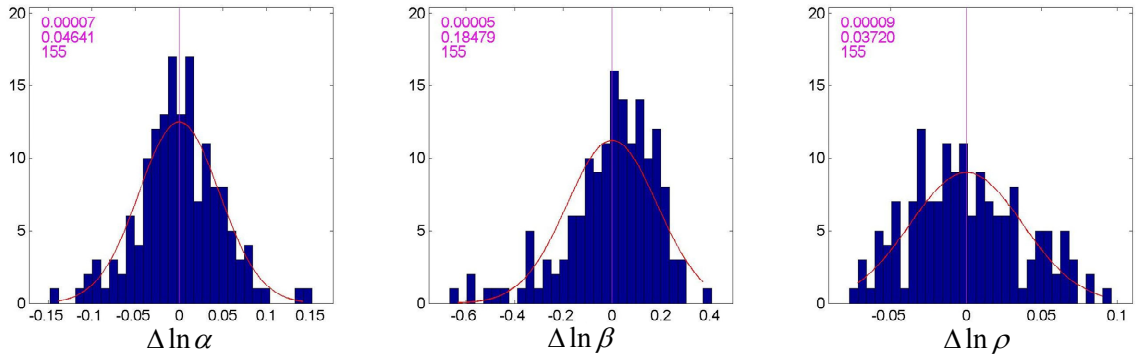

Figure 4.7. Histogram of the model parameters. The first, second and third values at the upper left corner are the mean value, standard deviation value, and number of the data, respectively.

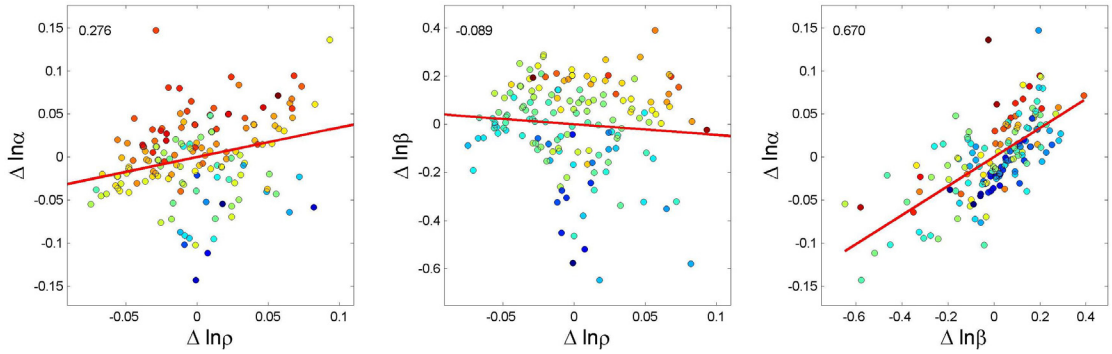

Figure 4.8. Relationship among the model parameters. The value at the upper left is the correlation coefficient. The red line represents the fitting curve determined in a least-square fashion.

4.6.3 Seismic Forward Modeling

Seismic angle gathers of P-P and P-S waves are synthesized by the convolution model along with the earth model, in which the reflection coefficient is calculated based on the Aki and Richards approximation, as Equations (4.10) and (4.11). A Vs/Vp value is required in the approximation. As Veire and Landro (2006) and others pointed out, the AVO approximation is not strongly sensitive to the background Vs/Vp value. Thus, I define a constant value of 0.372 from the mean value of the earth model. The maximum incident angle and the sampling interval are set to be 50 degree and 5 degree for both P-P and P-S waves. I use the Ricker wavelet and the dominant frequency is assumed to be 100 Hz for the P-P wave and 30 Hz for the P-S wave, respectively. Buland and Omre (2003) used two kinds of random noise in their test; one is white noise and the other is source-generated noise. The source-generated noise has a correlation among the incident angles by an exponential correlation function, $\upsilon_\theta = \exp\left[-\left|\theta_i - \theta_j\right| / d_\theta\right]$, where θ_i and θ_j are the incident angles; d_θ is the correlation range. I also use the two kinds of random

noise; but the noise magnitude differs from that of Buland and Omre (2003). I determine the standard deviations of the noise as follows; $\sigma_1 = \sigma_2 = 0.00065$, 0.0053, 0.015, and 0.028 for the P-P wave and $\sigma_1 = \sigma_2 = 0.00091$, 0.0096, 0.024, and 0.048 for the P-S wave. The noise magnitudes approximately correspond to the S/N of 50, 5, 2, and 1. Figures 4.9 and 4.10 show the synthesized P-P and P-S angle gathers with different S/N ratios.

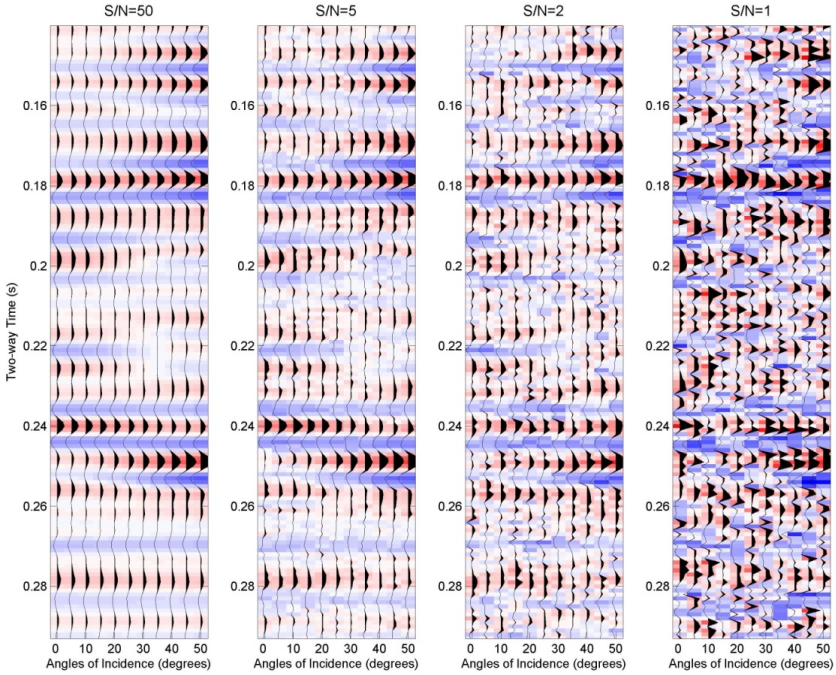

Figure 4.9. Synthetic P-P angle gather with different noise levels. The Ricker wavelet with the dominant frequency of 100 Hz is used.

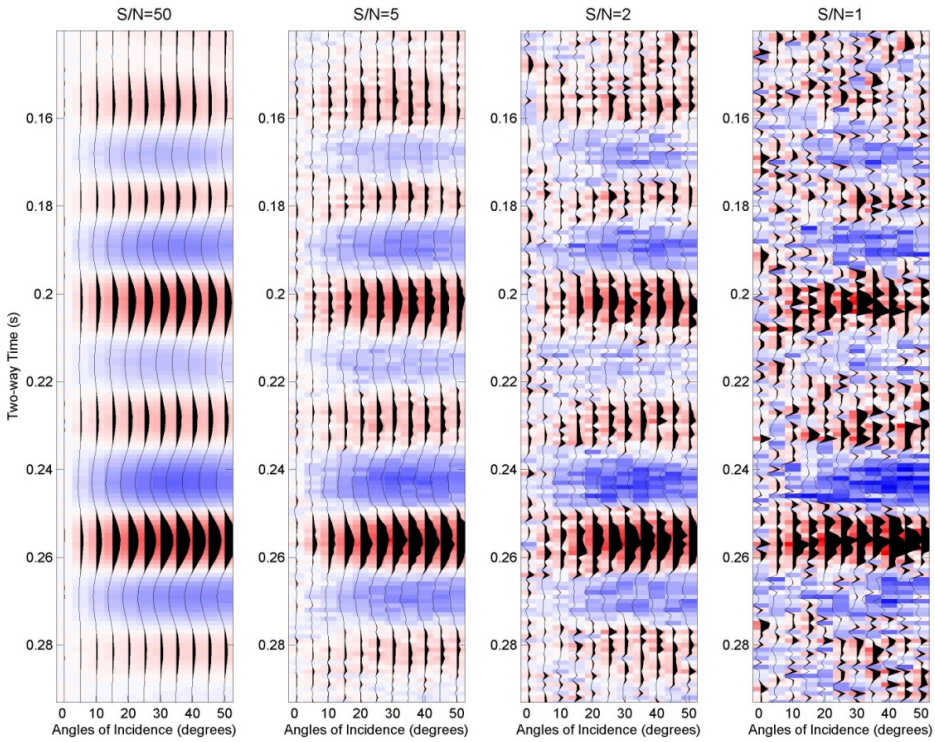

Figure 4.10. Synthetic P-S angle gather with different noise levels. The Ricker wavelet with the dominant frequency of 30 Hz is used.

4.6.4 Inversion Results

The P- and S- wave velocities and density are inverted from the synthetic data using the Bayesian method. Figures 4.11, 4.12, 4.13, and 4.14 show results of the joint inversion with the S/N of 50, 5, 2, and 1, respectively. When the seismic data quality is excellent, the P- and S-wave velocities and density are very well inverted. As the seismic data quality degrades, the inversion estimation has a poorer correlation with the earth model. The deterioration is the most significant in the density, followed by the S-wave velocity. Nevertheless, the density is still reasonably inverted even in the case of the poorest data quality (S/N of 1).

The Bayesian method provides us uncertainties of the prediction. In the figures, the black and red dot curves represent the prior and posterior prediction interval of 95 %. The difference between the prior and posterior intervals becomes smaller as the seismic data quality degrades. However, even in the case of the poorest data quality, the uncertainties of the posterior prediction become smaller than the prior prediction, suggesting that there are some contributions from seismic data in the density estimation.

Figures 4.15, 4.16, 4.17, and 4.18 show the residual analysis of the joint inversion. The first three panels from left to right represent the noise-free synthetic data, noise-added synthetic data, and synthetic data based on the inversion result, respectively. Moreover, the fourth and last panels represent the difference between the first and third panels and between the second and third panels, respectively. In the inversion implementation, we find the solution by minimizing the root-mean-square of values in the last panel, taking into account the prior information. Although the residual becomes more visible as the seismic data quality degrades, the synthetic data based on the inversion result is virtually very consistent with the synthetic data based on the earth model.

In addition to the joint inversion, synthetic tests for the P-P and P-S only inversions are performed with the same S/N conditions. Here, I only show the results with the S/N of 2 (Figures 4.19 and 4.20). The density inverted by the P-P only inversion has a poorer correlation with the earth model, compared to the joint inversion. Also, the P-S only inversion has the solution with lower frequency, compared to the joint and the P-P only inversions. This is why the lower-frequency wavelet (30 Hz) is used in the P-S wave.

Figure 4.21 shows summary of the synthetic tests for the joint, P-P only, and P-S only inversions. In the P-wave velocity estimation, the difference of the normalized RMS error between the P-P and joint inversions is smaller at a higher S/N. But, at the S/N of 1, the joint inversion has a substantially better result. Also, in the S-wave velocity estimation, the joint inversion has the best result, followed by the P-P only inversion. Why does the P-S wave inversion have the worst result in the S-wave estimation? It can be considered that the wavelet of P-S wave have significantly lower dominant frequency than that of the P-P wave.

Furthermore, in the density estimation, the joint inversion gives us substantially better result than the individual inversions although the normalized error is larger than of P- and S-wave velocity estimations. However, at a S/N of 1, the RMS error of P-S wave only inversion is close to 1. Consequently, the joint and P-P only inversions virtually have the same error magnitude. Thus, it can be concluded that the joint inversion can provide better density estimation than the individual inversions when seismic data quality is from good to fair. In contrast, when the seismic data quality is very poor, the difference between P-P only and joint inversions is not significant.

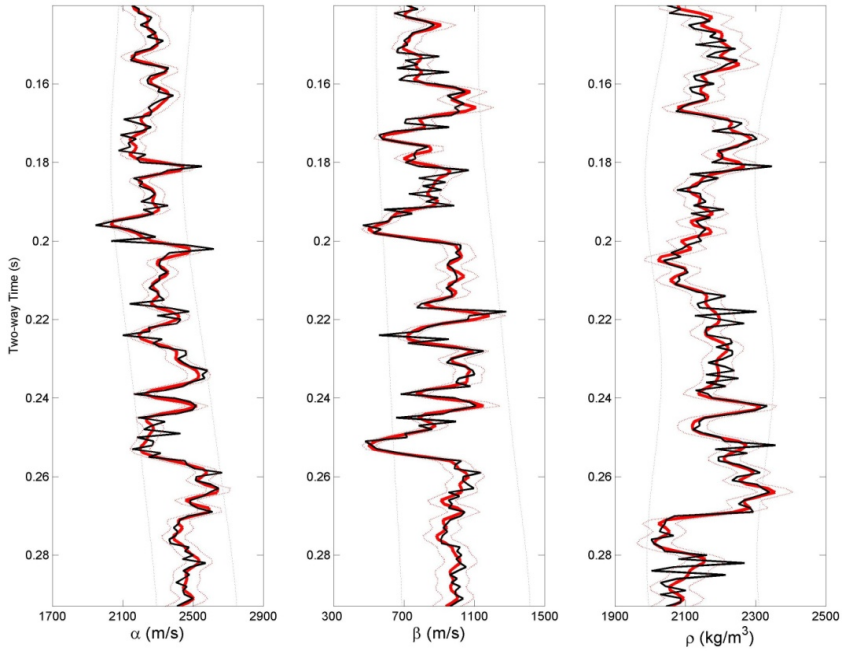

Figure 4.11. Joint inversion result with S/N of 50 (red solid curves). The black thin curves represent the true values. The red and black dot thin curves represent 0.95 prediction interval of prior and posterior models, respectively.

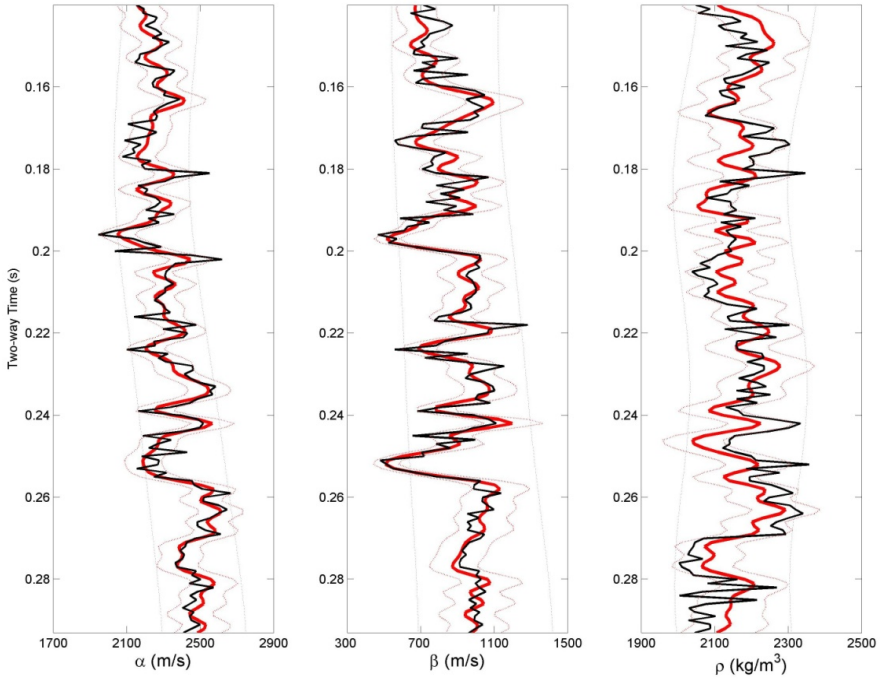

Figure 4.12. Joint inversion result with S/N of 5 (red solid curves). The black thin curves represent the true values. The red and black dot thin curves represent 0.95 prediction interval of prior and posterior models, respectively.

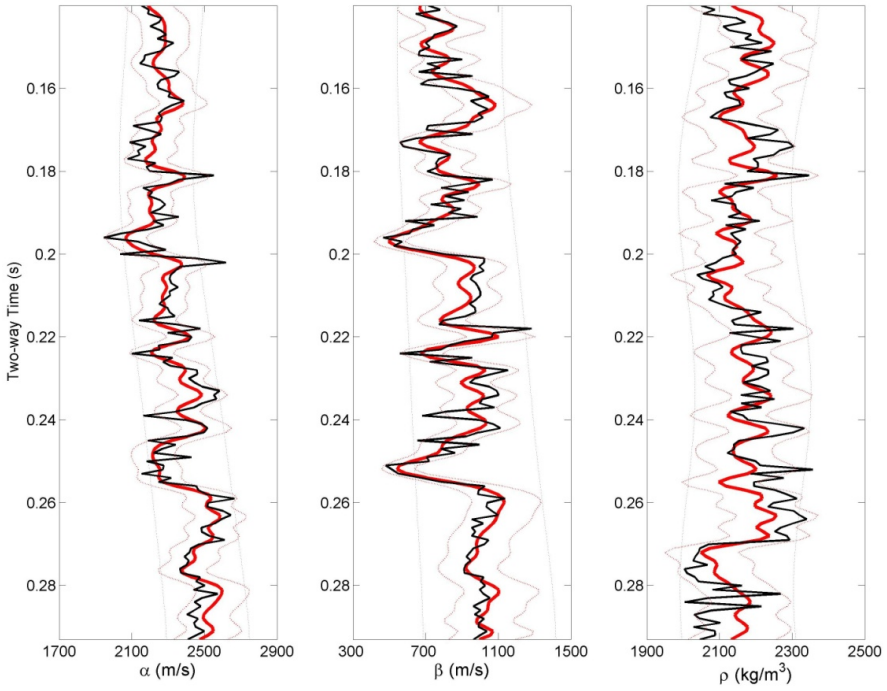

Figure 4.13. Joint inversion result with S/N of 2 (red solid curves). The black thin curves represent the true values. The red and black dot thin curves represent 0.95 prediction interval of prior and posterior models, respectively.

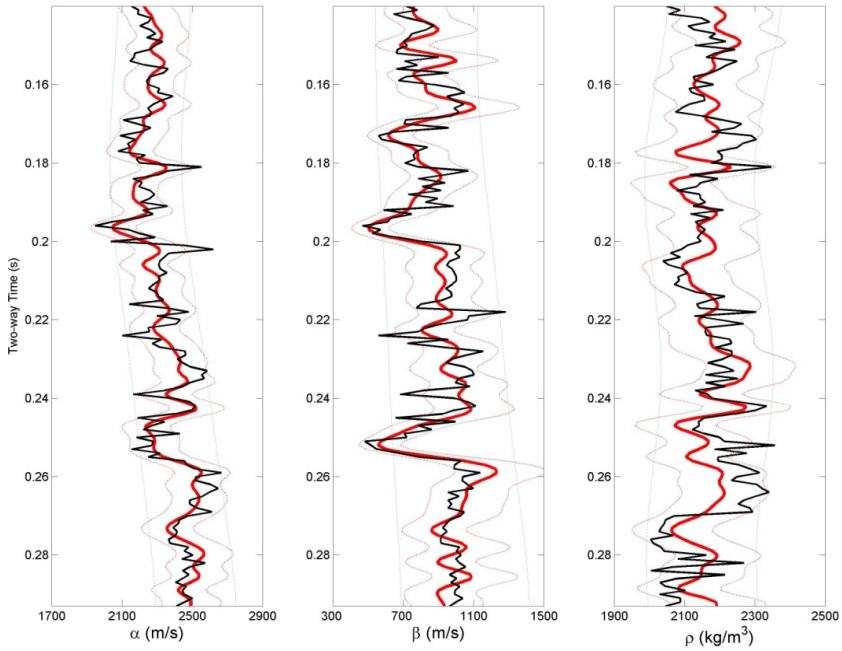

Figure 4.14. Joint inversion result with S/N of 1 (red solid curves). The black thin curves represent the true values. The red and black dot thin curves represent 0.95 prediction interval of prior and posterior models, respectively.

a)

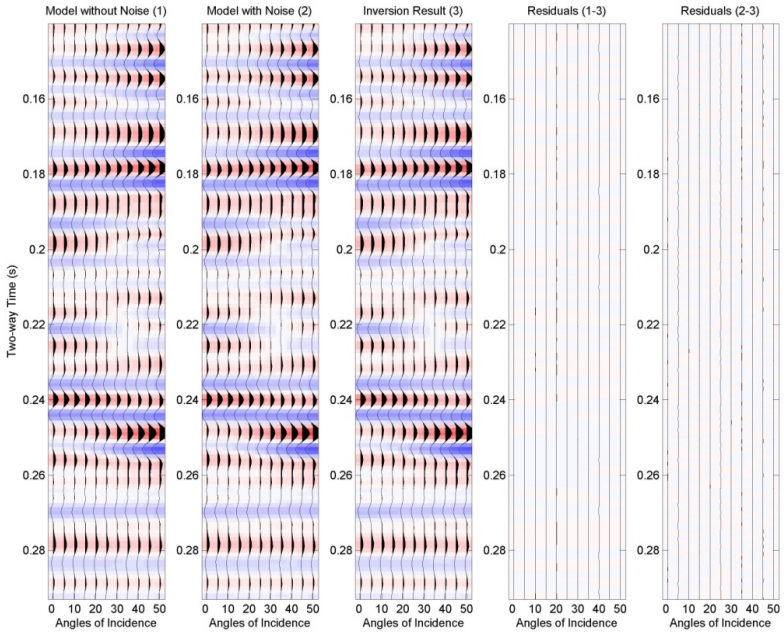

b)

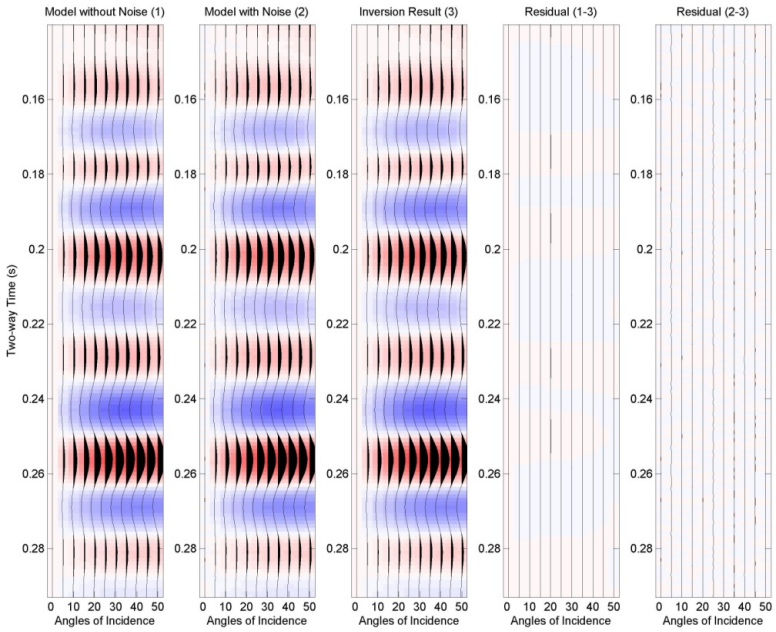

Figure 4.15. (a) P-P and (b) P-S wave residuals of the joint inversion result with S/N of 50. From left to right, (1) noise-free synthetic data, (2) noise-added synthetic data, (3) synthetic data based on the inversion result, residual between (1) and (3), and residual between (2) and (3).

a)

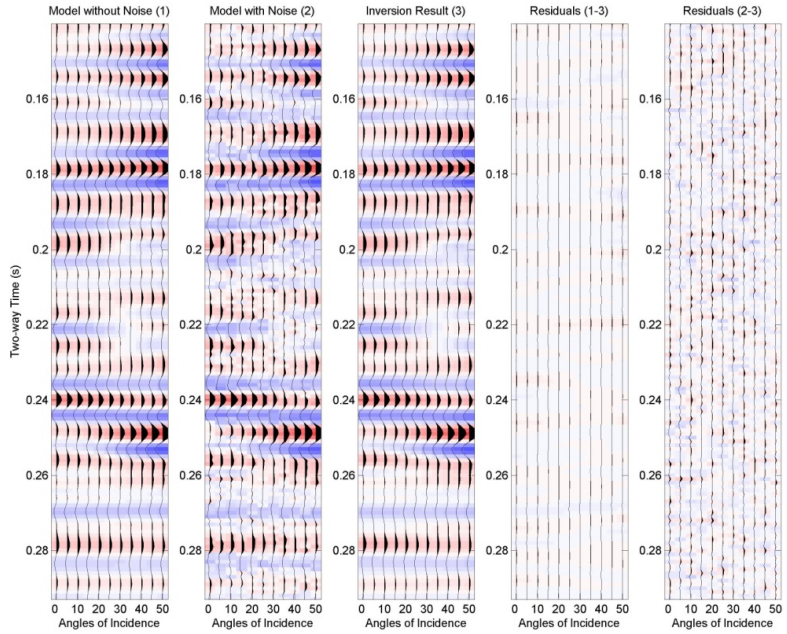

b)

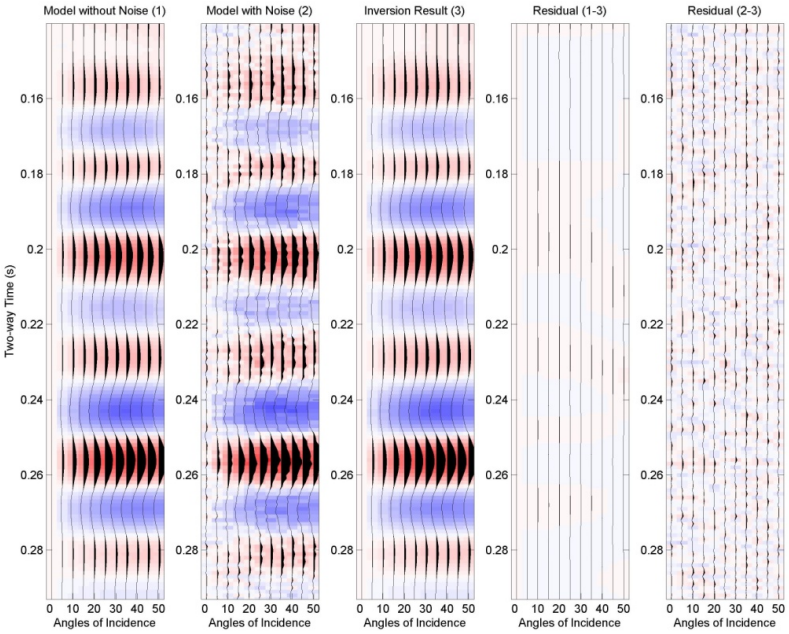

Figure 4.16. (a) P-P and (b) P-S wave residuals of the joint inversion result with S/N of 5. From left to right, (1) noise-free synthetic data, (2) noise-added synthetic data, (3) synthetic data based on the inversion result, residual between (1) and (3), and residual between (2) and (3).

a)

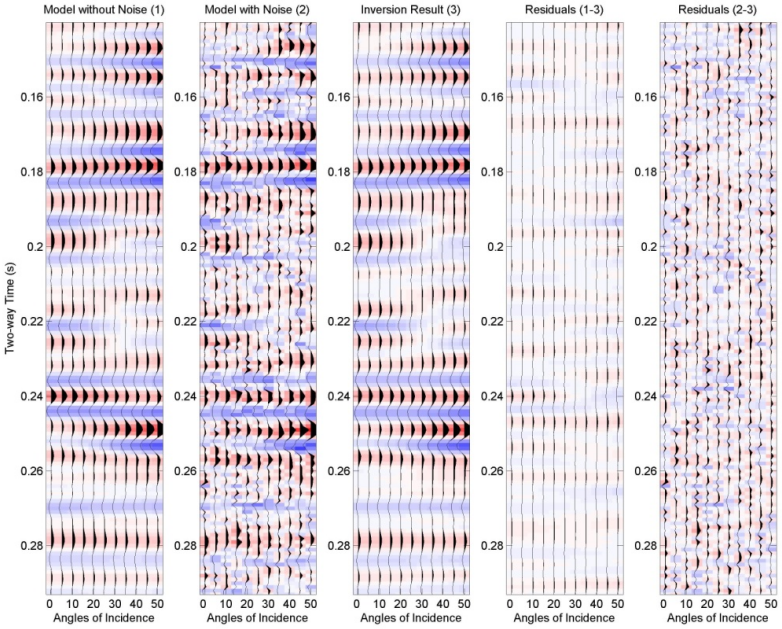

b)

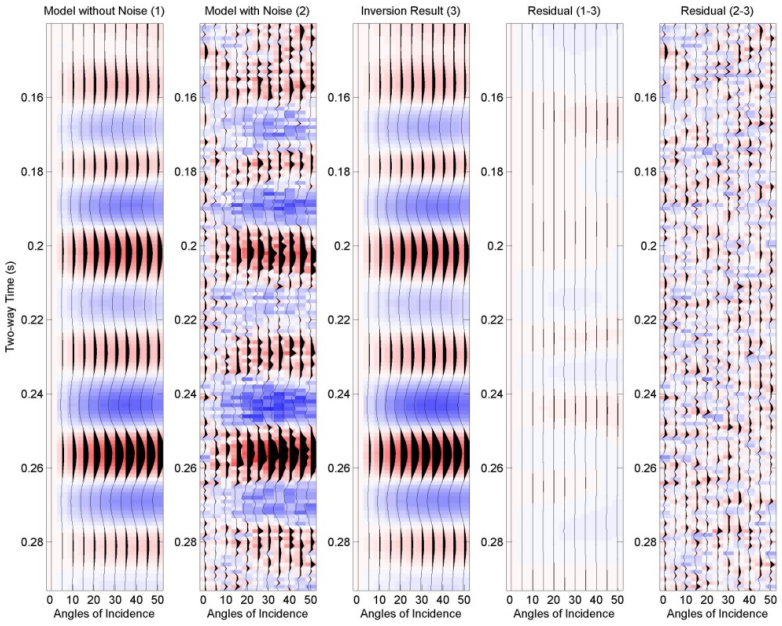

Figure 4.17. (a) P-P and (b) P-S wave residuals of the joint inversion result with S/N of 2. From left to right, (1) noise-free synthetic data, (2) noise-added synthetic data, (3) synthetic data based on the inversion result, residual between (1) and (3), and residual between (2) and (3).

a)

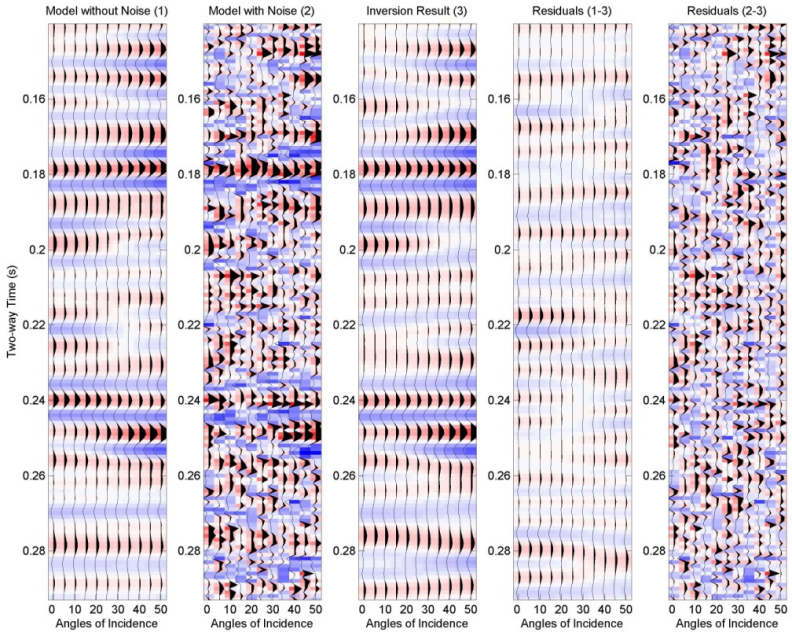

b)

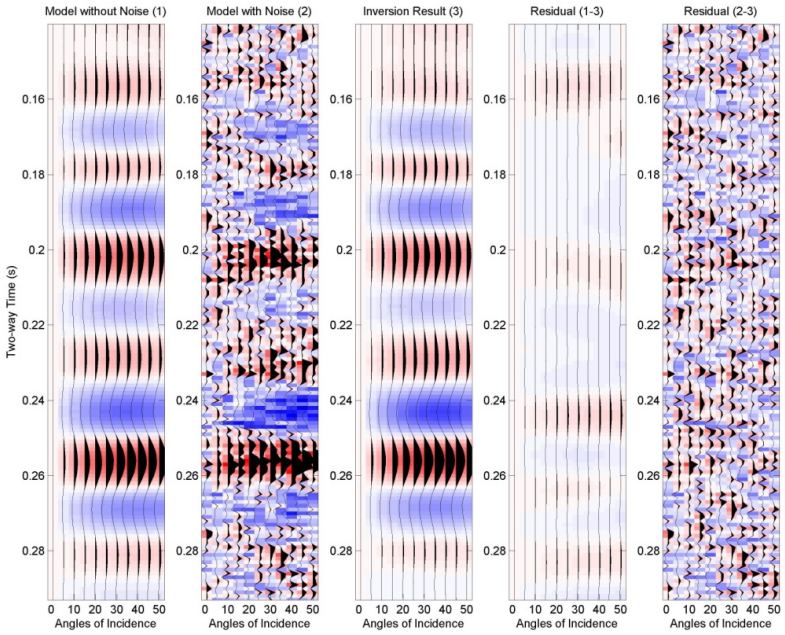

Figure 4.18. (a) P-P and (b) P-S wave residuals of the joint inversion result with S/N of 1. From left to right, (1) noise-free synthetic data, (2) noise-added synthetic data, (3) synthetic data based on the inversion result, residual between (1) and (3), and residual between (2) and (3).

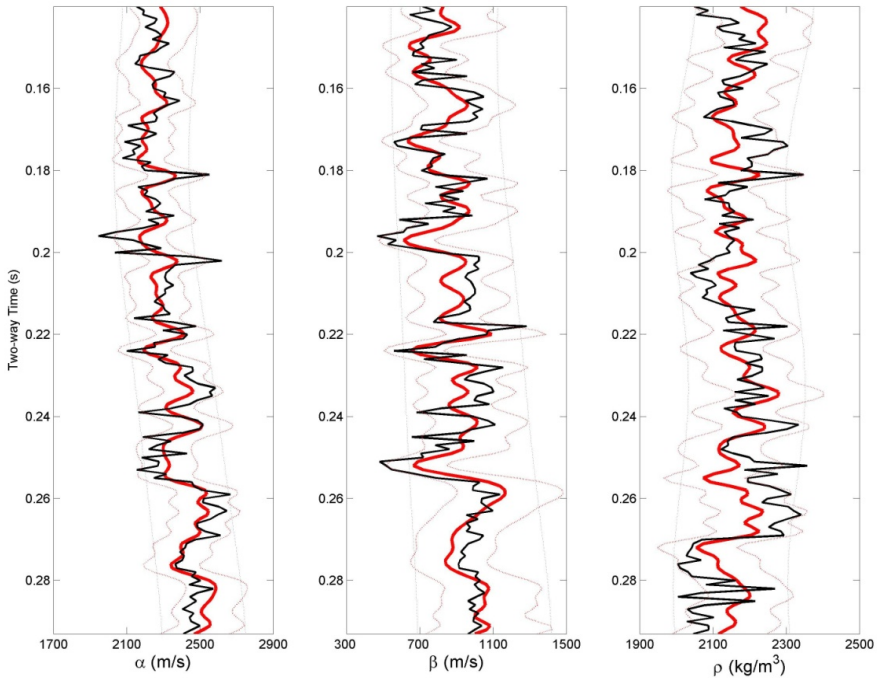

Figure 4.19. P-P only inversion result with S/N of 2 (red solid curves). The black thin curves represent the true values. The red and black dot thin curves represent 0.95 prediction interval of prior and posterior models, respectively.

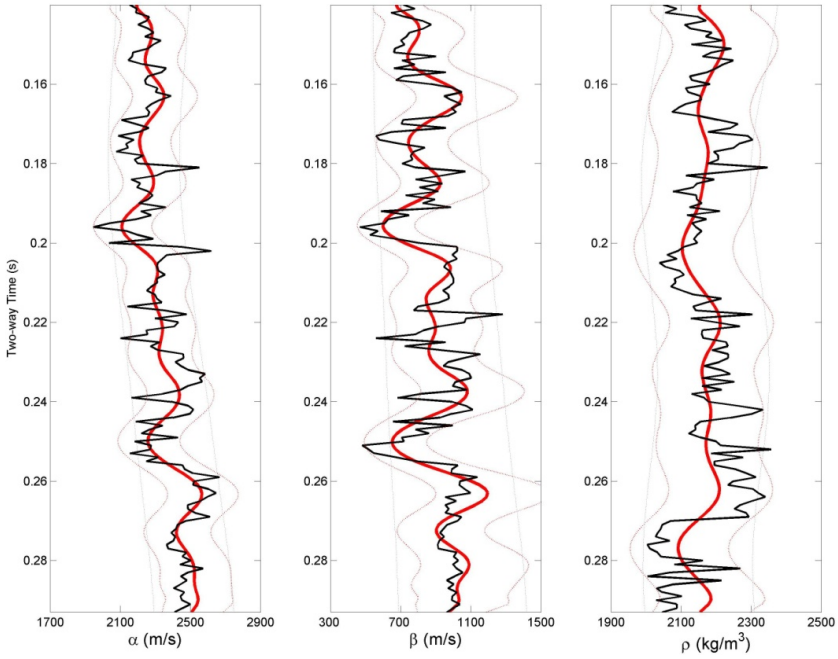

Figure 4.20. P-S only inversion result with S/N of 2 (red solid curves). The black thin curves represent the true values. The red and black dot thin curves represent 0.95 prediction interval of prior and posterior models, respectively.

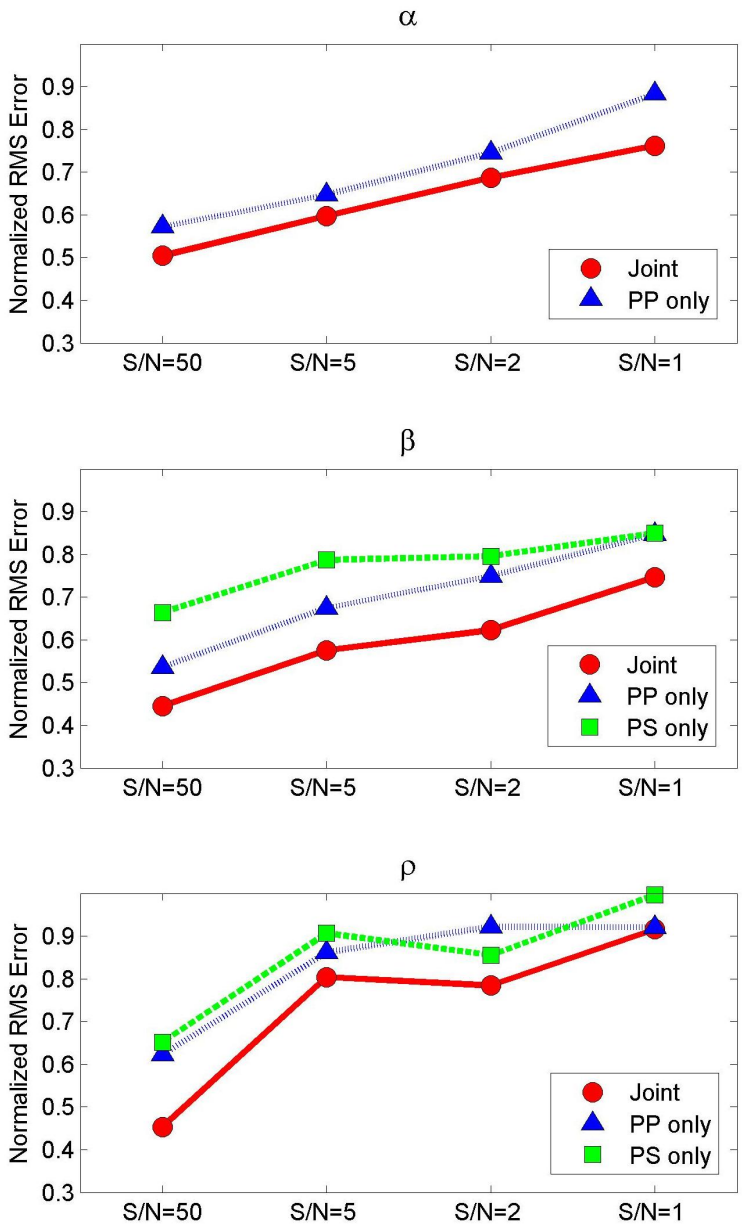

Figure 4.21. Normalized RMS error of joint (red), P-P only (blue), and P-S only (green) inversions as a function of S/N.

4.6.5 Comparison with Damped-Least Square Method

The damped least-square method is one of the most common methods in geophysical inversion problems. To compare the Bayesian method with the damped least-square method, additional synthetic tests are conducted. Figures 4.22 and 4.23 show the joint inversion results of the damped least-square method, along with the Bayesian method. It is noted that the damping factor is set to be 0.05 after careful tests. The S-wave velocity is well inverted by the damped least-square method. However, the inverted density shows severe oscillation. The comparison between the two methods (Figure 4.23) shows that the Bayesian method has better prediction at all the noise levels for all the parameters, particularly in the density estimation with poor data quality.

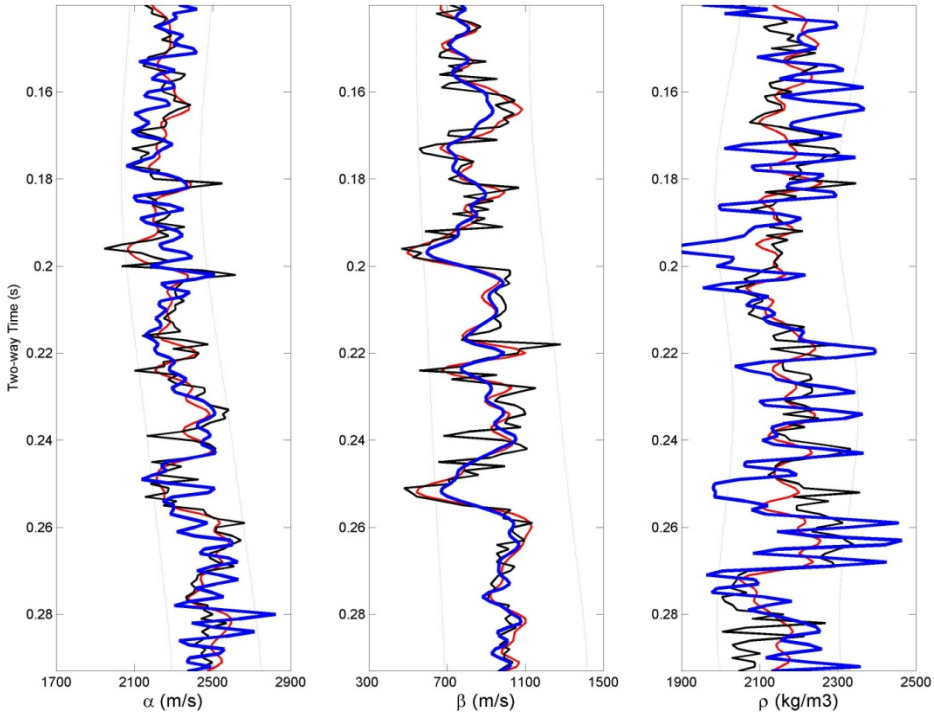

Figure 4.22. Comparison between the Bayesian (red) and the damped-least square (blue) methods for the joint inversion with S/N of 2. The black solid curves represent the earth model.

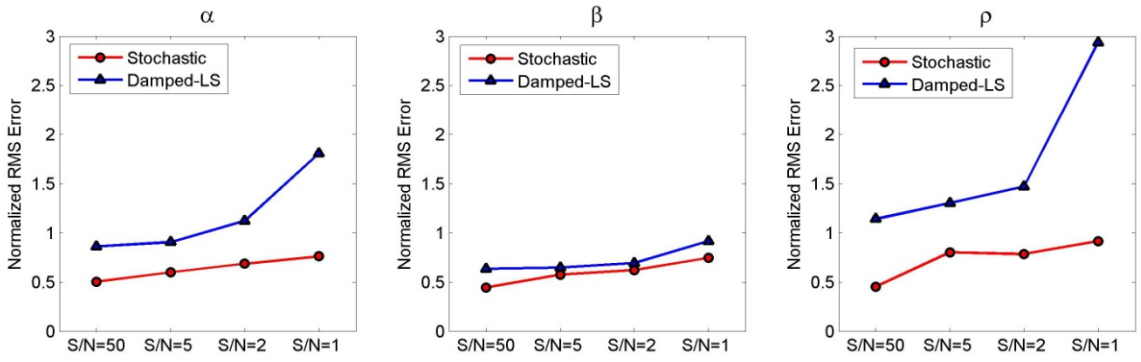

Figure 4.23. Normalized RMS error of the Bayesian (red) and damped-least square (blue) methods for the joint inversion.

4.7 Sensitivity Analysis

In the Bayesian method, the model parameters should follow the Gaussian distribution. Furthermore, the corresponding statistical parameters (correlation coefficient and variance) should be a representative of the study area. However, in the most cases, we have only a limited number well logs available, which may not be enough to define the lateral heterogeneity. Thus, when we intend to apply the Bayesian technique to field data, it is difficult to determine a proper covariance matrix of the model parameters (Buland and Omre, 2003).

Thus, to investigate the importance of the correlation coefficient in the Bayesian method, I conduct a sensitivity test. In the test, I set the correlation coefficients to be zero and perform the Bayesian joint inversion. Then, the results are compared to the case where the correlation coefficients are correctly set. Figures 4.24 shows the comparison between the zero-correlation and true-correlation results in the Bayesian joint inversion with S/N of 2. It is observed that there are substantial differences in the P-wave and density estimation. However, the no-correlation case still provides reasonable density estimation.

Figure 4-25 shows the summary of the comparisons between the no-correlation and true-correlation cases in the Bayesian joint inversion. The true-correlation case gives us better prediction in the P-wave velocity and density estimation. The improvement becomes more significant, as the seismic data quality degrades. It is suggested that setting proper correlations in the covariance matrix is important when data quality is poor. In contrast, the S-wave velocity has no significant improvement with the correlation.

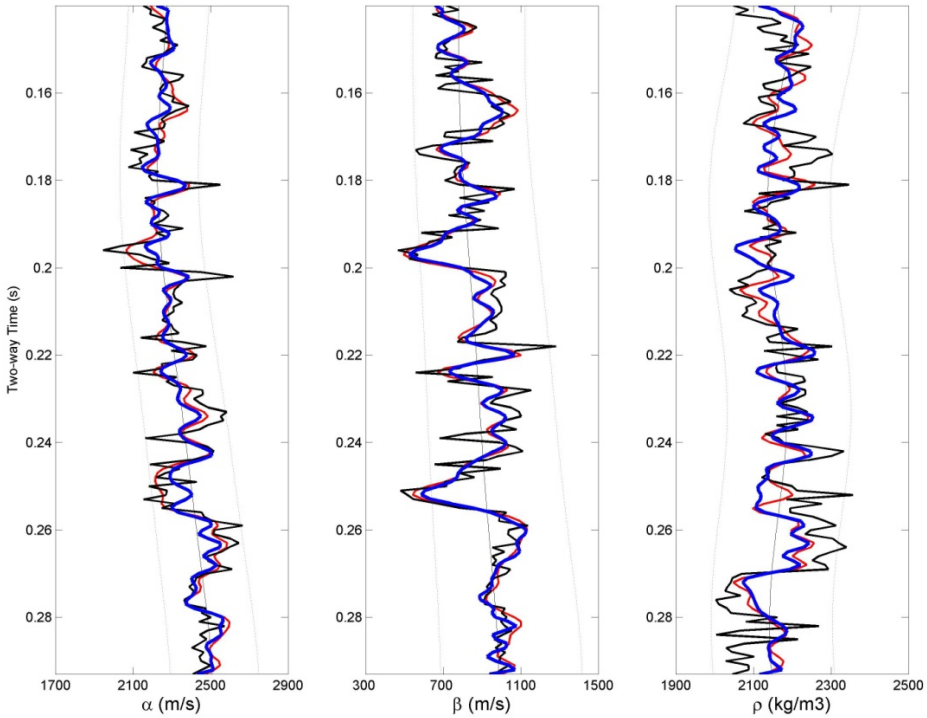

Figure 4.24. Comparison between true correlation (red) and no-correlation (blue) in the Bayesian joint inversion with S/N of 2. The black solid curves represent the earth model.

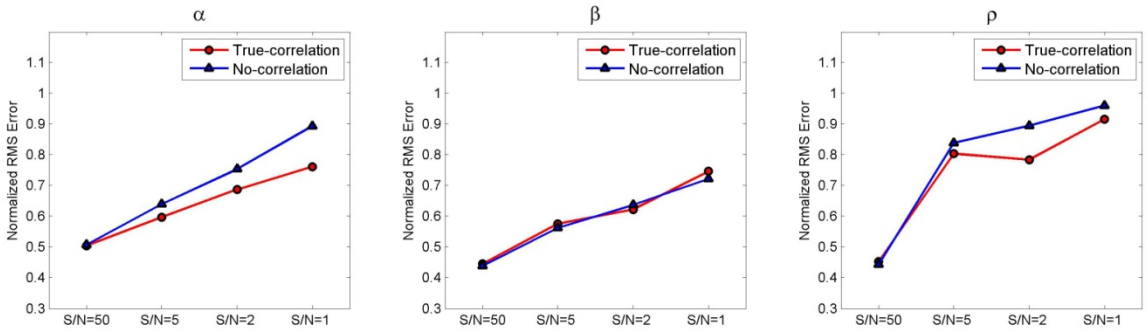

Figure 4.25. Comparison between true correlation (red) and no-correlation (blue) in the Bayesian joint inversion.

4.8 Summary

I developed the P-P and P-S joint AVO inversion based on the Bayesian method to effectively discriminate the reservoir and shale in the Hangingstone oilfield. Major findings from this study are:

1) The relationship between lithology and the corresponding elastic properties was investigated, taking into account velocity dispersion due to viscosities of the heavy oil. As a result, the P-wave velocity and Vp/Vs are not diagnostic for sand and shale. In contrast, the bulk density is an excellent discriminator.

2) The Bayesian AVO inversion technique was extended to the P-P and P-S joint inversion and the formalization was fully developed.

3) The method was tested with synthetic data based on the field data. As a result, it was confirmed that the method is effective for not only P- and S-wave velocities, but also density estimations. Moreover, compared to the P-P and P-S only inversions, the joint inversion gives us the best result over all. However, when seismic data quality is very poor, contributions from the P-S wave to the density estimation become smaller, leading to difference between P-P only and joint inversions that is not significant.

The implementation of the developed method with field data will be discussed in Chapter 5.

Chapter 5 – P-P and P-S joint AVO Inversion

- Implementation with Field Data

5.1 Introduction

In the previous chapter, the methodology and synthetic testing of the P-P and P-S joint AVO inversion for density estimation were discussed. The synthetic tests suggested that the method is feasible for use in the Hangingstone oilfield. In this chapter, I apply the method to the field data to estimate the reservoir sands distribution. For AVO analysis, data conditioning is one of the key elements to obtain a reliable result, particularly for density estimation. Furthermore, for P-P and P-S joint analysis, a correlation between them is required. In this chapter, these issues will be discussed in the implementation of the joint AVO inversion. I used Hampson-Russell, VISTA, and Seismic Un*x software to conduct parts of this analysis.

5.2 Study Area

I selected a small study area for the implementation of the P-P and P-S joint AVO inversion (Figure 5.1). There is only one well (well D) available in the area. Since the well is located far from the SAGD wells, I assume that there is no reservoir property change caused by the SAGD process. Since there is no direct measurement of the S-wave sonic log in the well, I used the established rock physics model to predict the S-wave velocity from the other well logs, as described in Chapter 3. Furthermore, taking into account the viscoelastic features of the heavy oil, the P- and S-wave velocities at the

surface seismic frequency (100Hz) are modeled. The modeled velocities are used in the inversion analysis.

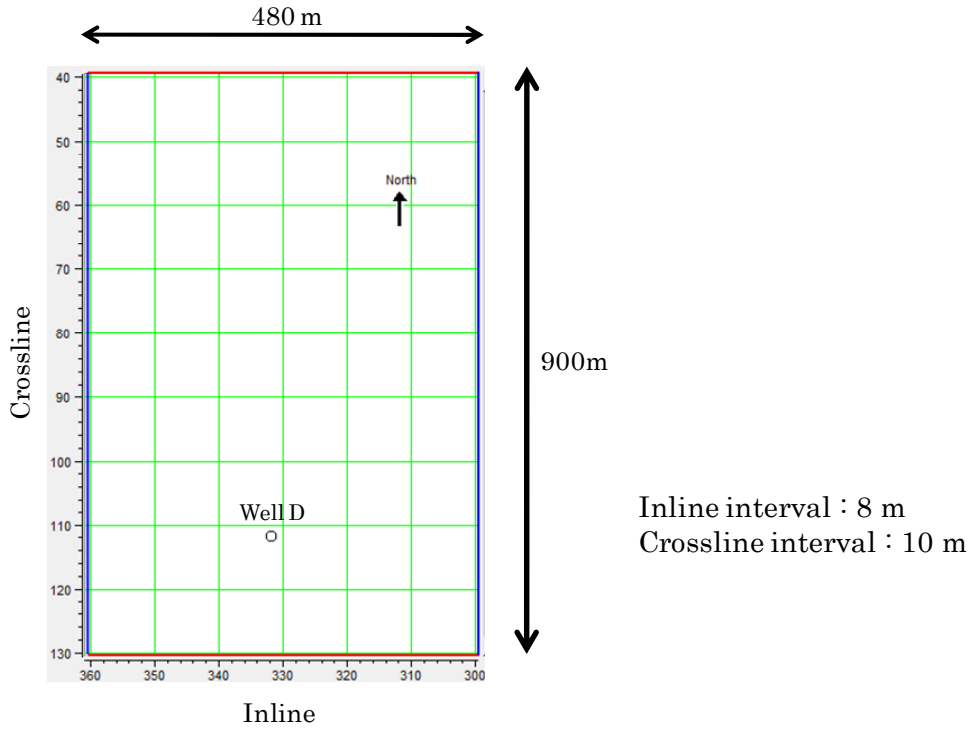

Figure 5.1. Study area for the implementation of the P-P and P-S joint AVO inversion.

5.3 Seismic Data Conditioning

It is essential to prepare fully-processed seismic data for AVO analysis (e.g., Castagna, 1993). I use the PSTM gathers as the input data for P-P and P-S waves. In both sets of data, the need for additional data processing was recognized. Thus, I took different data processing flows to solve the individual problems.

5.3.1 P-P Wave Data Conditioning

Figure 5.2 shows the P-P PSTM CMP gathers. The reservoir is at times of approximately 480 ms to 520 ms, and the strong event at the reservoir bottom corresponds to the Top Devonian interface. It can be observed that most of the reflection events in the shallow section are not flattened, but bending upward. After careful tests, I chose the following data processing flow:

1) 4th order velocity analysis and residual moveout correction
2) Noise attenuation based on parabolic Radon transform
3) Supergathers (3 x 3)
4) Transform from offset to angle gathers by ray tracing

To improve the flatness of the gathers and AVO response, I conducted 4th order velocity analysis (Alkhalifah and Tsvankin, 1995) for the PSTM CMP gather which had been removed the original NMO correction. Figure 5.3 shows the CMP gathers after the 4th order velocity analysis and residual moveout correction with the new velocity field. The determined anisotropic parameter η ranges from 0.02 to 0.04. The flatness of the reflections in the shallow section are significantly improved. However, the upward-bending in the far offset range is still visible to some degree (for example, event at 425 ms). For the bending, two possible reasons may be considered; 1) near-field effects associated with spherical waves due to shallow depth (e.g., Aki and Richards, 1980; Haase and Stewart, 2009), and 2) generation of head wave due to large velocity contrast. Nevertheless, it is emphasized that reflections in the section deeper than 450 ms, but excluding the Top Devonian interface, are almost flattened.

The reflection from the Top Devonian interface shows significant upward-bending in the far offset range. To understand this unusual feature, I created synthetic seismogram by reflectivity modeling (Kennett, 1983). Figure 5.4 shows the well log P- and S-wave velocities and density used in the modeling. There is a large velocity contrast at around 300 m, which corresponds to the Top Devonian interface. Figures 5.5a and 5.5b show the modeling result and the NMO-corrected result, respectively. A hyperbola at around 260 ms at zero-offset corresponds to a reflection event from the Top Devonian interface. At around offset of 400 m, the head wave is started to be observed. After NMO correction, although the reflections are correctly flattened, the head wave is bending upward, leading to the flattened reflections which are largely masked in the far offset range.

Since this observation in the synthetic data is consistent with the observations made in the actual CMP gathers, it is suggested that the unusual feature at around Top Devonian is caused by the corresponding head wave and the tuning effect. To attenuate the head wave, along with the upward-bending in the shallower section, the noise attenuation process based on the parabolic Radon transform is applied. Figures 5.6 and 5.7 show the noise attenuation result and the residual, respectively. It can be observed that no-flattened events including the head wave are efficiently suppressed, along with random noise. Also, there is virtually no damage in the reservoir layer.

Furthermore, to enhance the S/N, I collect the neighbor traces within 3 inlines and 3 crosslines and make the average (supergathers), presented in Figure 5.8. Random noise is further suppressed, leading to the lateral continuity of the reflection events which are slightly improved. I perform the offset-to-angle transformation by ray-tracing. In the ray-

tracing, I use the vertically smoothed P-wave velocity model (Figure 5.23). The construction of the model will be discussed in a later section. Figure 5.9 shows the transformed angle gathers from 5 to 65 degrees. In the large angle range beyond 50 degrees, the data conditioning problems are still observed; 1) data is noisy, 2) reflections are not flattened, and 3) the amplitude is not consistent with smaller angle data. Thus, I determine the mute line on 50 degrees. Finally, the angle data from 5 to 50 degrees with sampling of 5 degrees is used in the inversion.

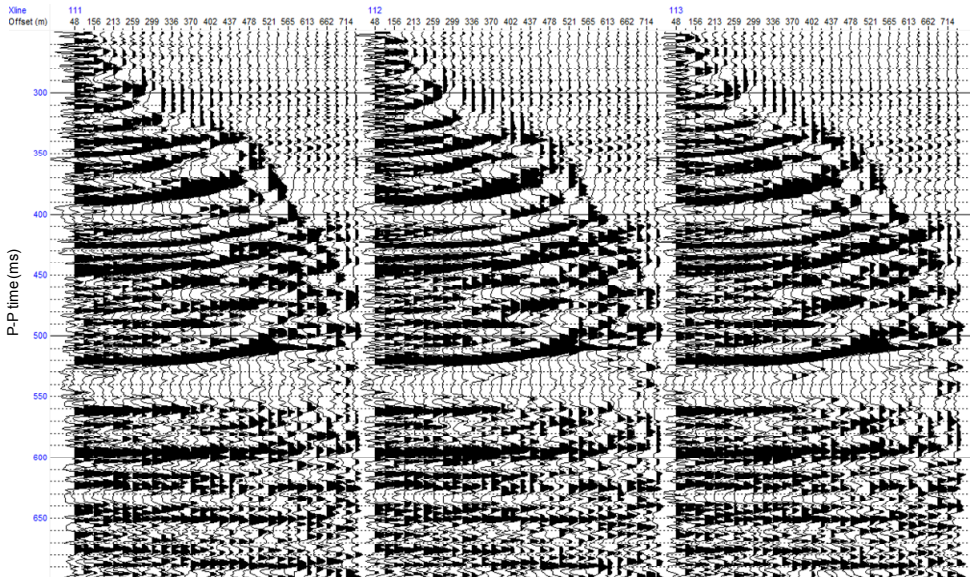

Figure 5.2. P-P wave PSTM CMP gathers.

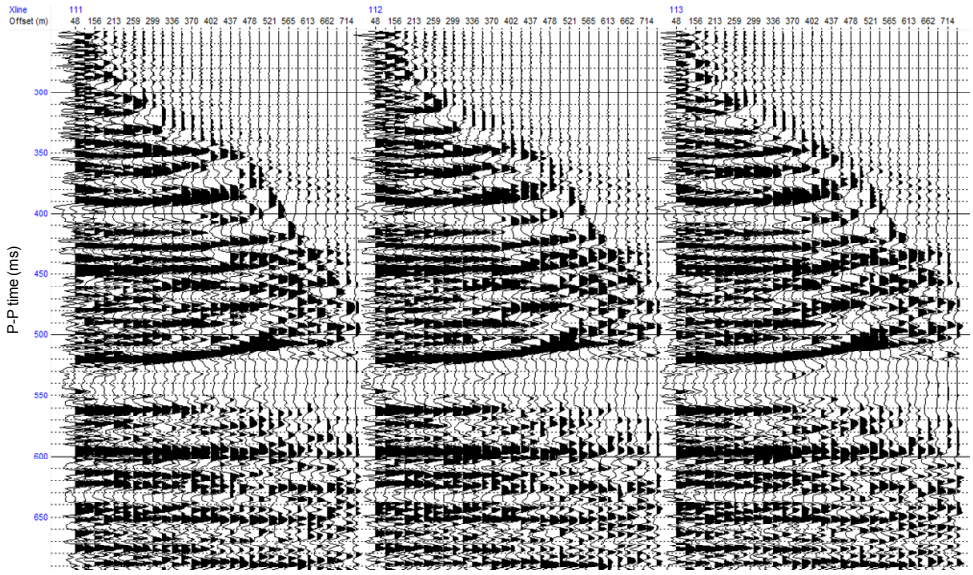

Figure 5.3. PSTM CMP gathers after 4th order velocity analysis and residual moveout correction.

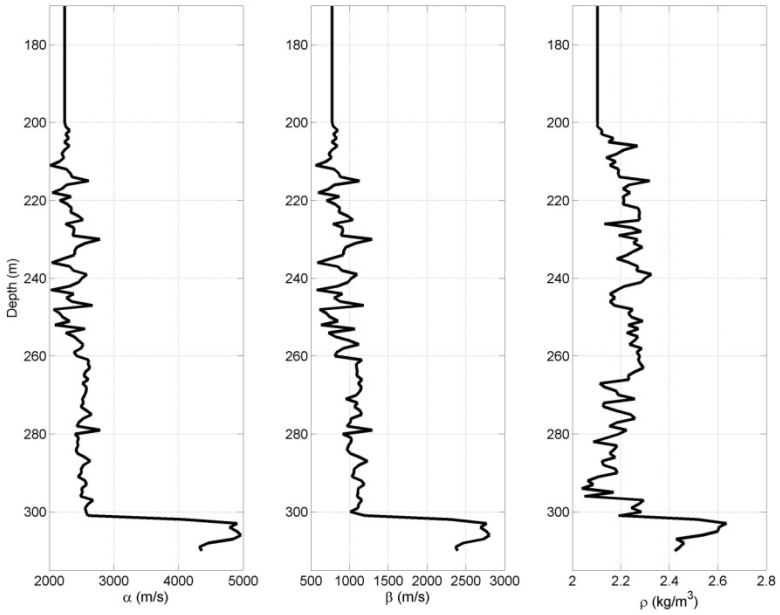

Figure 5.4. P- and S-wave velocities and density used in the reflectivity modeling.

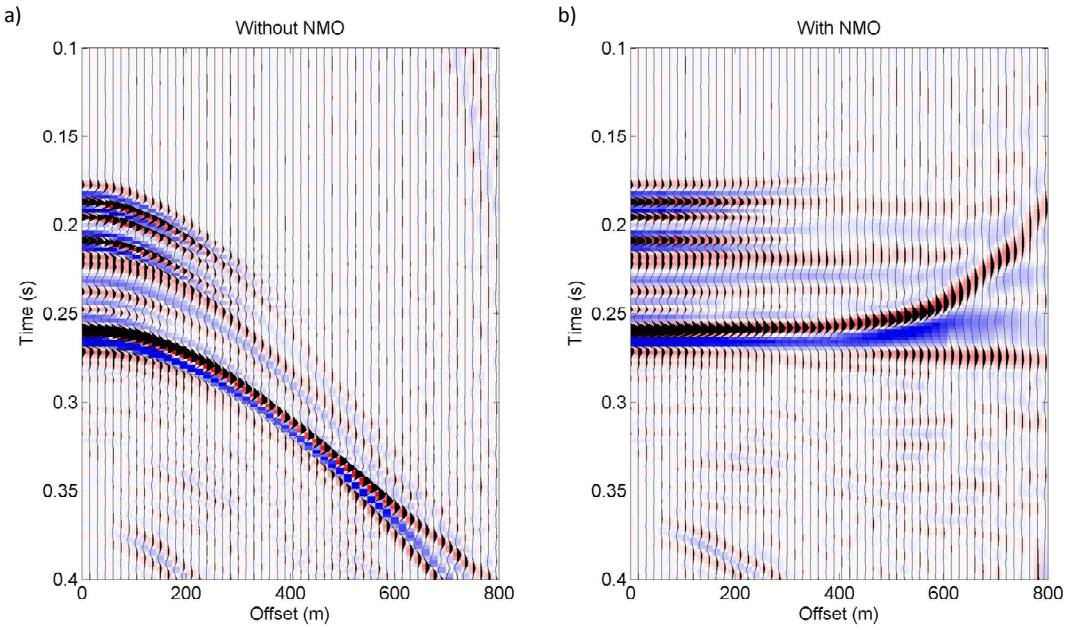

Figure 5.5. (a) Synthetic seismogram and (b) after NMO correction.

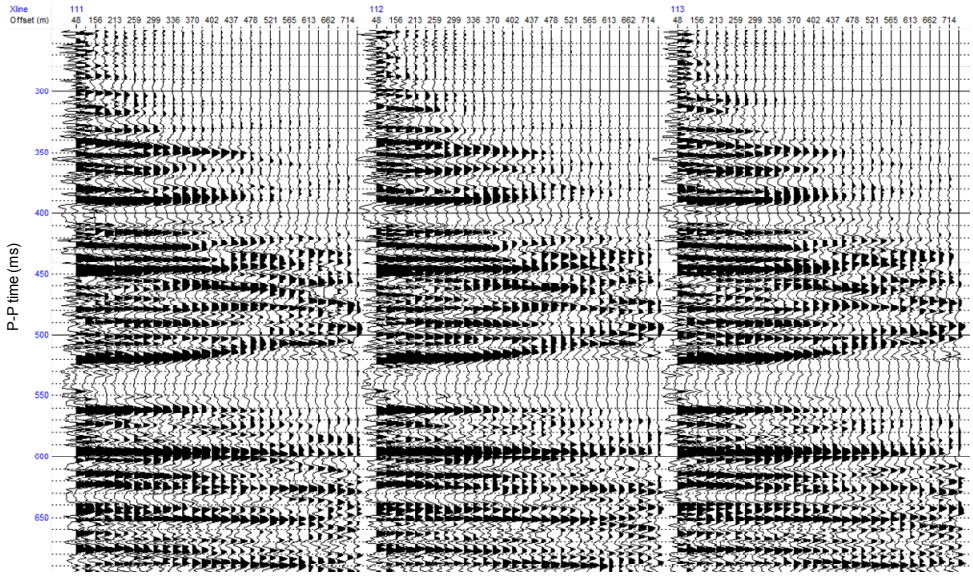

Figure 5.6. CMP gathers after the parabolic Radon transform filtering.

Figure 5.7. Suppressed noise by the parabolic Radon transform filter.

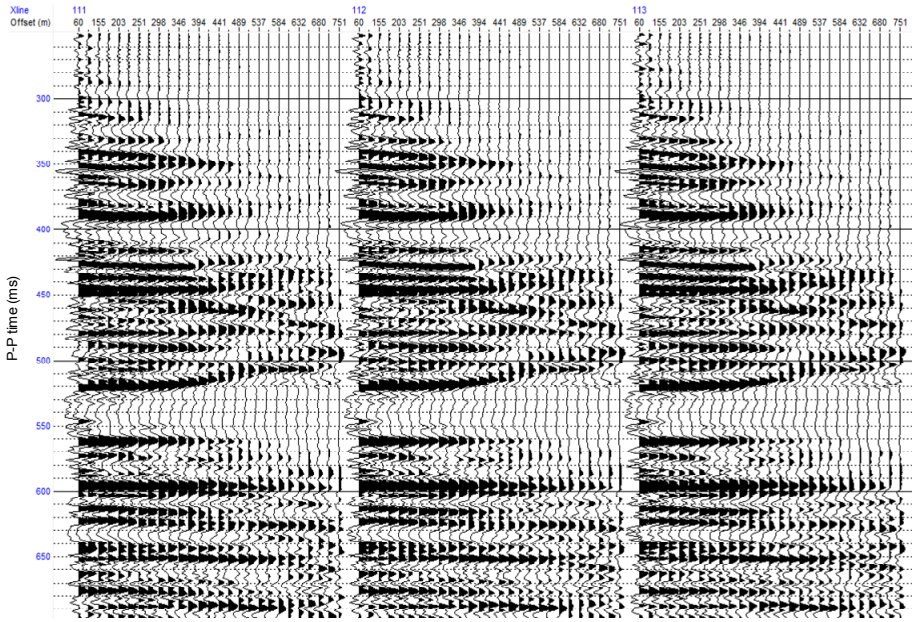

Figure 5.8. P-P wave supergathers (3 inlines and 3 crosslines).

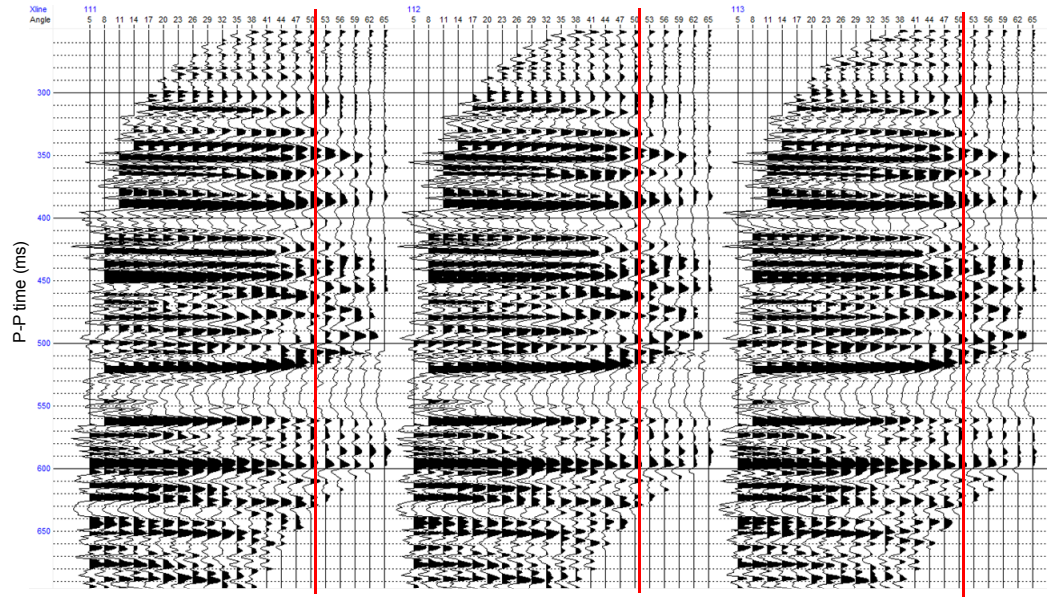

Figure 5.9. P-P wave angle gathers. The red curves represent the mute line.

5.3.2 P-S Wave Data Conditioning

Figure 5.10 shows PSTM CCP gathers of the P-S wave. It is noted that the reverse polarity is used for the P-S wave display in Chapter 5 and 7. A strong seismic event is observed at around 970 ms at near offsets, which corresponds to a reflection event from the Top Devonian interface. Parts of far offset of reflection events, including the Top Devonian, are not flattened, but bending downward. To prepare fully processed angle gathers, the data processing flow for the P-S wave was constructed as follows:

1) Residual moveout correction
2) Trim static correction
3) Regridding (from 12 × 15 m to 8 × 10 m)
4) Supergathers (5 × 5)
5) Transform from offset to angle gathers by ray tracing

The processes 1) and 2) aim to improve the flatness of the gathers. Figure 5.12 shows the CCP gathers applied by the residual moveout and trim static corrections. The reflection events including the Top Devonian are more correctly flattened even in the far offset range.

The P-S PSTM binning is 12 × 15 m, while the P-P PSTM binning is 8 × 10 m. Thus, I regrid the P-S data on the same binning. Furthermore, to enhance the S/N, I make supergathers with 5 inlines and 5 crosslines (Figure 5.13). It can be observed that random noise is suppressed, leading to greater lateral continuity of the reflection events.

In the same way as the P-P wave, I perform the offset-to-angle transformation, in which not only P-wave but also S-wave velocity models (Figure 5.23) are used in the ray tracing. Figure 5.14 shows the transformed angle gathers from 9 to 66 degrees. Finally, the angle data from 5 to 60 degrees with sampling of 5 degrees are used in the inversion analysis.

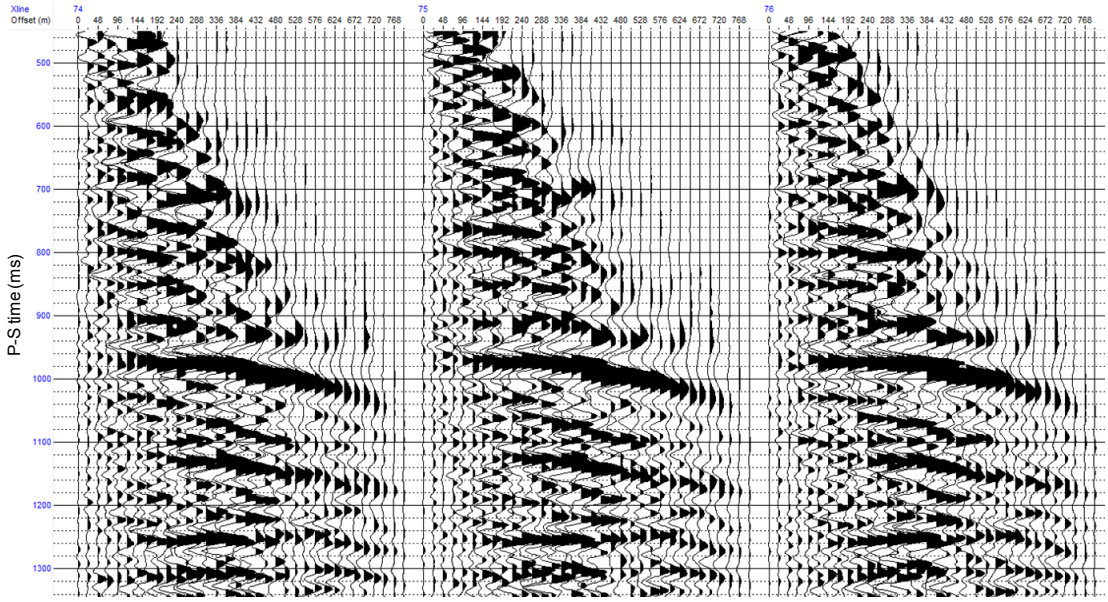

Figure 5.10. PSTM CCP gathers of P-S wave.

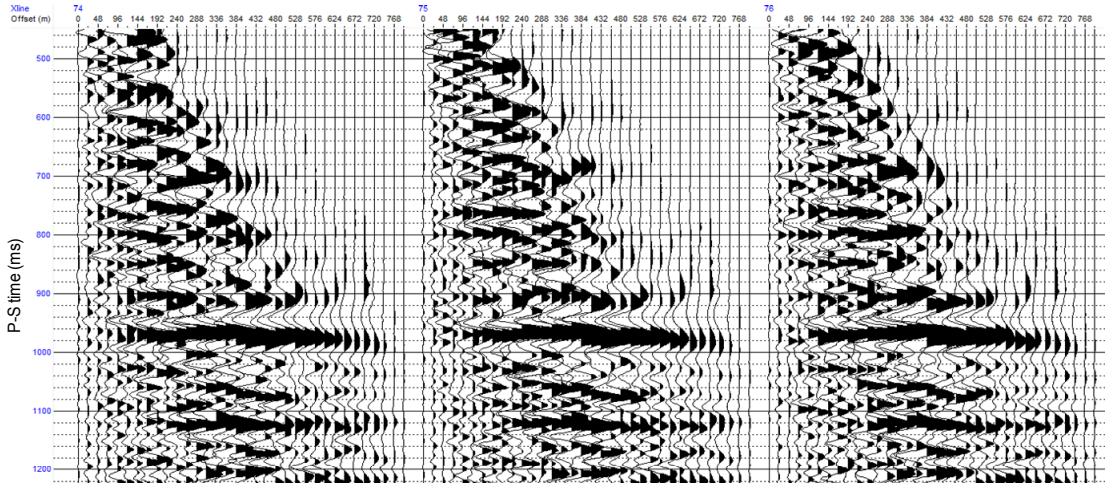

Figure 5.11. PSTM CCP gathers after the residual moveout correction.

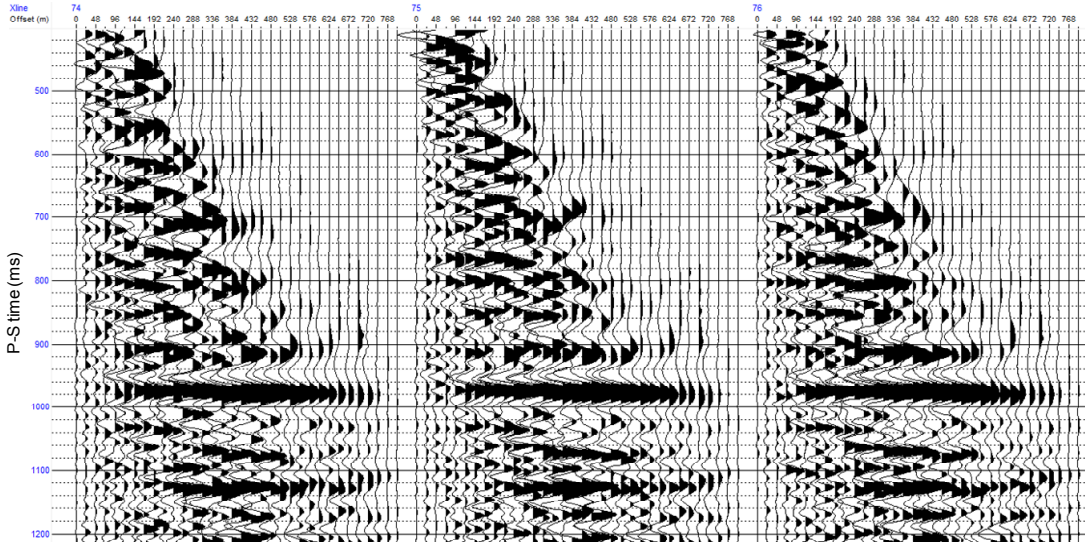

Figure 5.12. PSTM CCP gathers after the residual moveout and trim static corrections.

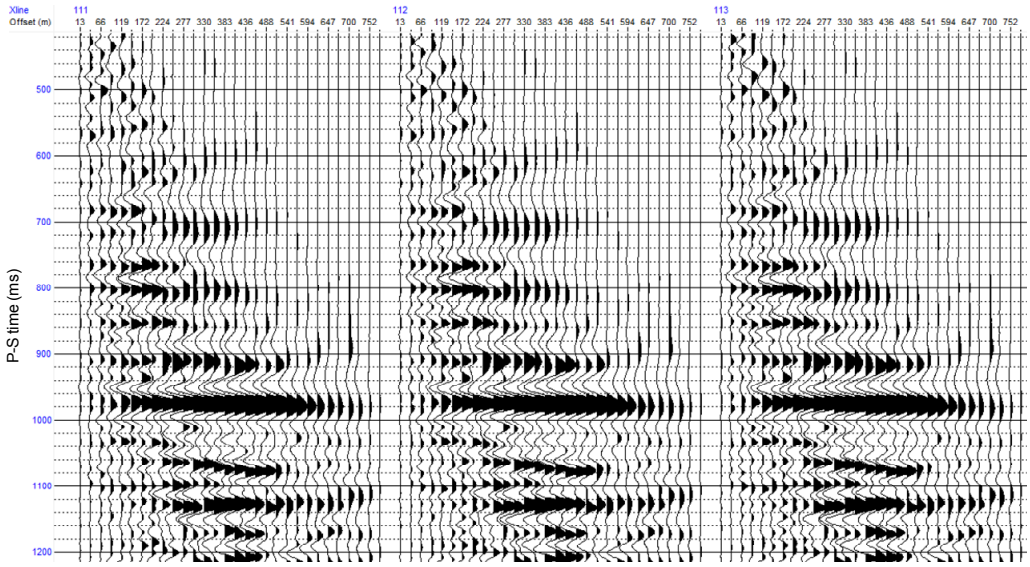

Figure 5.13. PSTM CCP gathers after averaging with 5 inlines and 5 crosslines (supergathers).

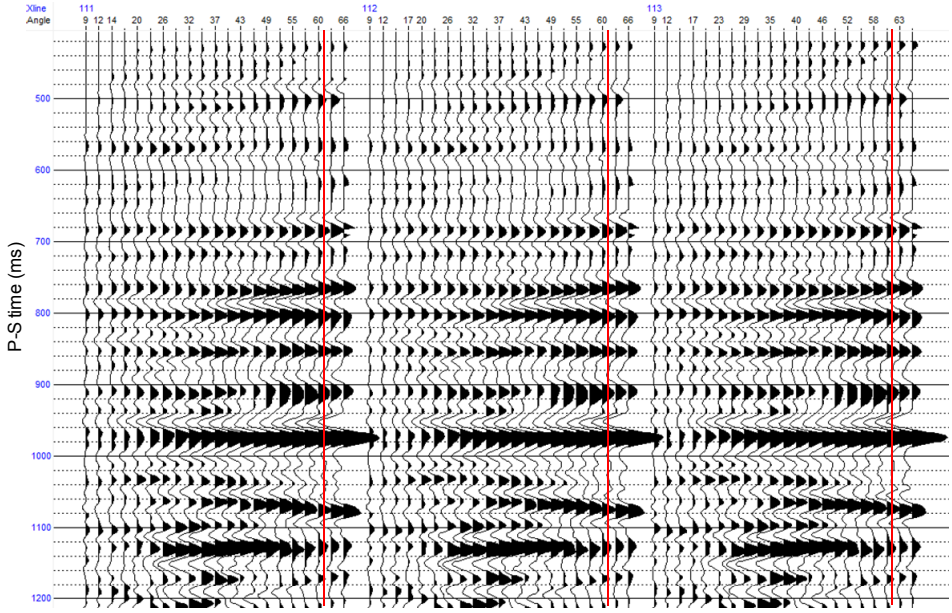

Figure 5.14. PSTM CCP gathers after the offset-to-angle transformation. The red curves represent the mute line.

5.4 Correlation between P-P and P-S Waves

Before the implementation of the P-P and P-S joint inversion, correlating the P-S wave with the P-P wave is required. For the correlation, several automatic methods have been proposed, including data correlation (e.g., Garotta, 1985; Gaiser, 1996), automatic warping (Fomel et al., 2005), and auto transferring (Nickel and Sonneland, 2004). As Zou et al. (2006) discussed, there are problems in these automatic approaches, including difference in P-P and P-S frequency bands, along with difference of P-P and P-S reflection responses from a rock physics point of view. In the study area, a significant difference of frequency band between the P-P and P-S waves is observed. I use the method based on horizon matching for the correlation. The procedures are as follows (e.g., Stewart et al., 2002; DeAngelo et al., 2003):

1) Vertical plot scale in the P-S section is squeezed to match with the corresponding P-P section over all. The process means the correlation has been made by using constant Vp/Vs. Characteristics of several key seismic events are observed, such as the similarity between the P-P and P-S sections, the lateral continuity, and so on.
2) A P-wave synthetic seismogram is created by using well logs with the associated wavelet. Then, the synthetic seismogram is tied to the P-P seismic section so that the seismic events are linked to the well logs.
3) Likewise, the P-S wave synthetic seismogram is created and tied to the P-S section. The link between the seismic events and well logs is made.

4) The seismic events in the P-P and P-S sections are linked with each other via the well logs.

I first apply the band-pass filter (10-20-105-115 Hz) to the PSTM full-stacked P-P section to match the frequency band with that of the P-S section. The filtered P-P section is used in this correlation analysis. Figure 5.15 shows the P-P and P-S sections correlated by constant Vp/Vs of 2.33. Over all, they are well correlated with each other. Furthermore, the Vp/Vs value is consistent with the well log sonic data in the reservoir (see Figure 4.1). However, vertical misalignments between the P-P and P-S sections are visible, particularly in the shallow and deep sections.

Figure 5.16 shows the synthetic seismogram of P-P and P-S waves. The synthetic seismograms are well correlated with the actual seismic data in both waves. Moreover, it is observed that the seismic events, as denoted by Marker A and B, Top Wabi, and Top Dev, are approximately correlated with same well log position for the P-P and P-S waves. Thus, I choose these seismic events to be used in the horizon matching.

In the horizon matching process, interval Vp/Vs can be calculated from the two horizons in the P-P and P-S sections as (e.g., Stewart et al., 2002; Lines et al., 2005; Nakayama et al., 2008):

$$\frac{V_P}{V_S} = 2\frac{T_{PS}}{T_{PP}} - 1, \tag{5.1}$$

where T_{PS} and T_{PP} are the corresponding P-S and P-P isochrons. Figure 5.17 shows the interval Vp/Vs maps. There are some lateral variations in each Vp/Vs map. Also, the Vp/Vs gradually decreases over all as the depth increases; the shallowest layer (from

Marker A to B) has about Vp/Vs of 2.8 and the deepest carbonate layer (Top Dev - Marker C) has about Vp/Vs of 2.0. Figure 5.17c is the corresponding map of the heavy-oil reservoir and is consistent with the previous study of Nakayama et al. (2008).

To reconstruct vertical Vp/Vs variations within the layers, I additionally used the well logs. In the standard way, I first laterally extrapolate the well log Vp/Vs along the picked horizons and obtain the Vp/Vs volume. Then, the volume is corrected by the horizon matching. Figure 5.18 shows the correlated P-P and P-S sections. The seismic events are well correlated, even at the shallow and deep sections. Also, Figure 5.19 shows the final Vp/Vs volume, which was used in the domain conversion. Figure 5.20 shows the correlated angle gathers between P-P and P-S waves, which enables one to directly compare the AVO responses between them.

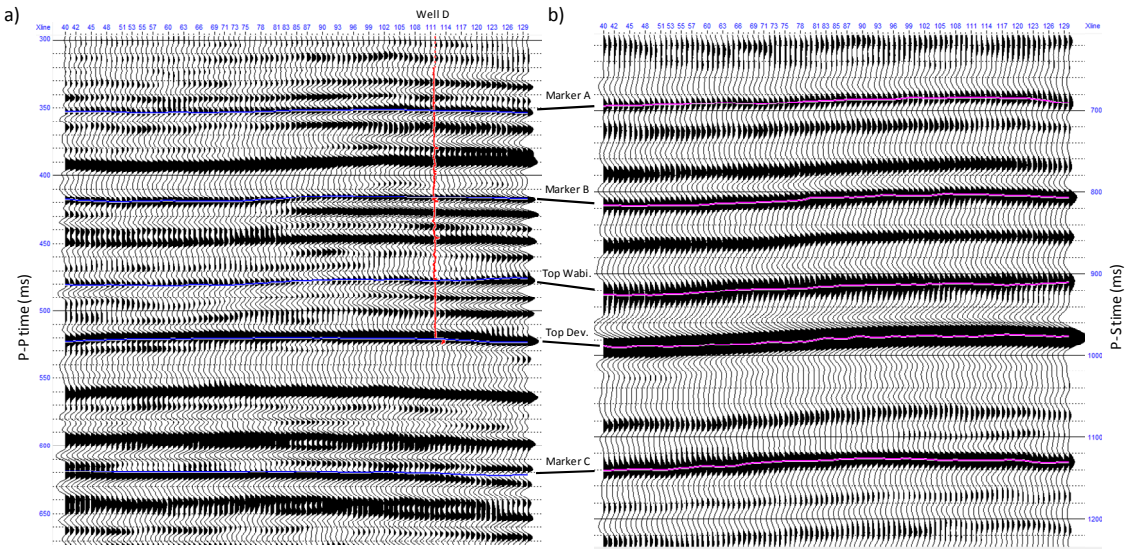

Figure 5.15. (a) P-P and (b) P-S sections with the picked seismic events. The compressing of the P-S time scale corresponds to constant Vp/Vs of 2.33.

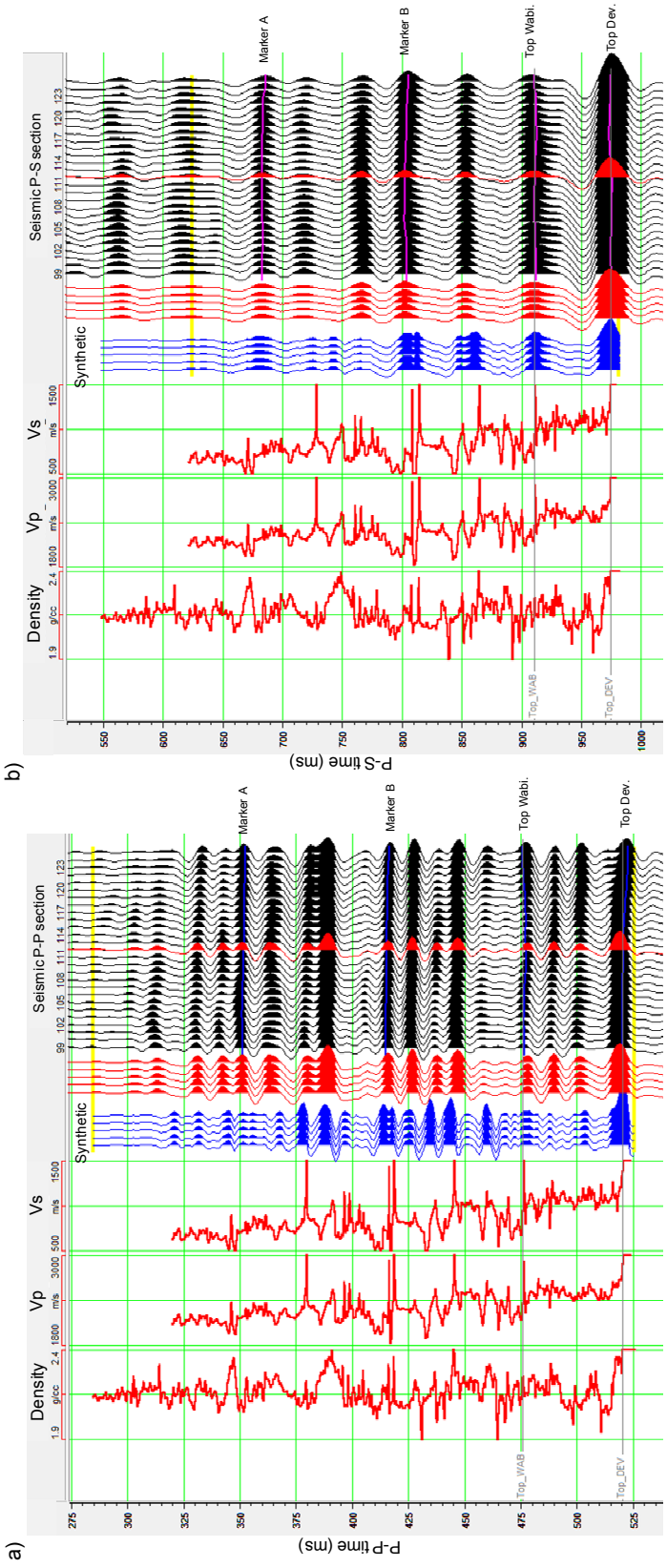

Figure 5.16. Well logs, synthetic seismogram, and surface seismic section for (a) P-P and (b) P-S wave.

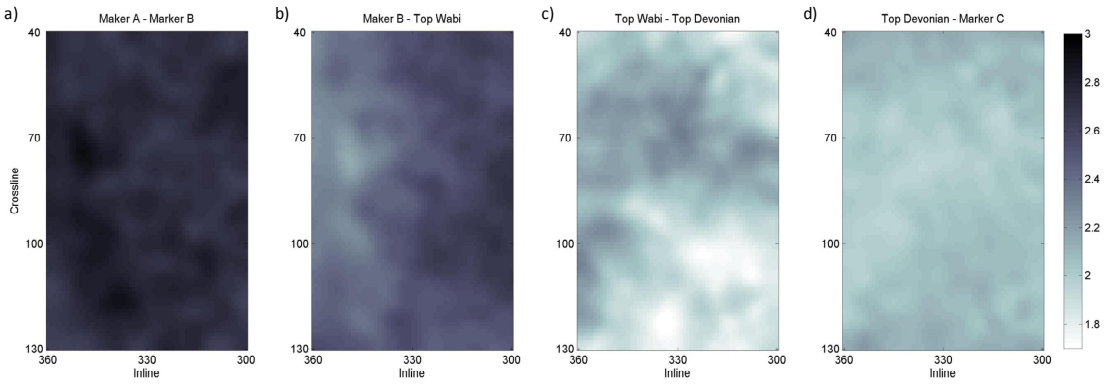

Figure 5.17. Interval Vp/Vs map for interval (a) from Marker A to Marker B, (b) from Marker B to Top Wabiskaw, (c) from Top Wabiskaw to Top Devonian, and (d) from Top Devonian to Marker C.

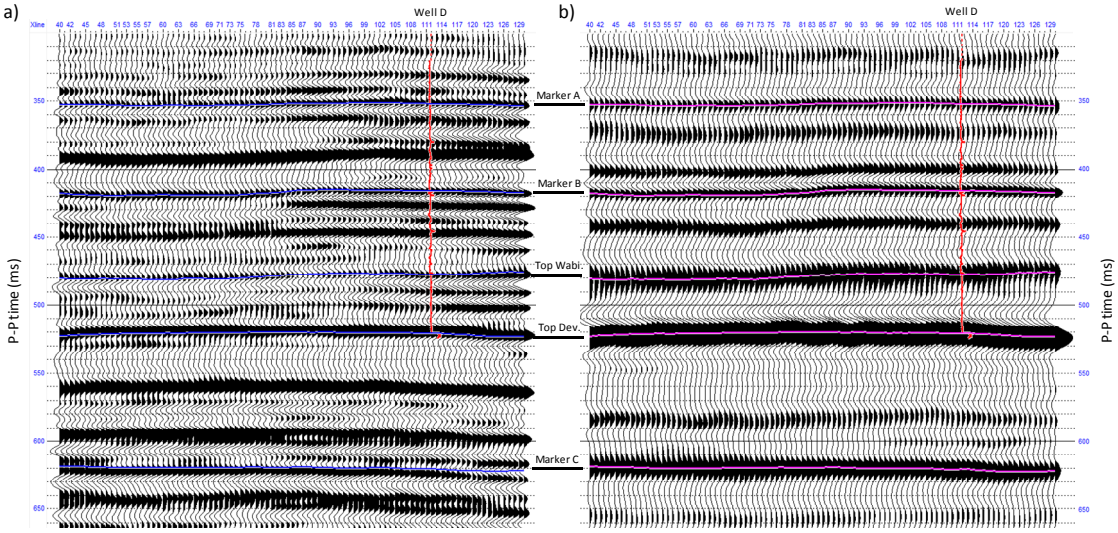

Figure 5.18. Correlated (a) P-P and (b) P-S sections. Note that the P-S section is converted to the P-P time domain.

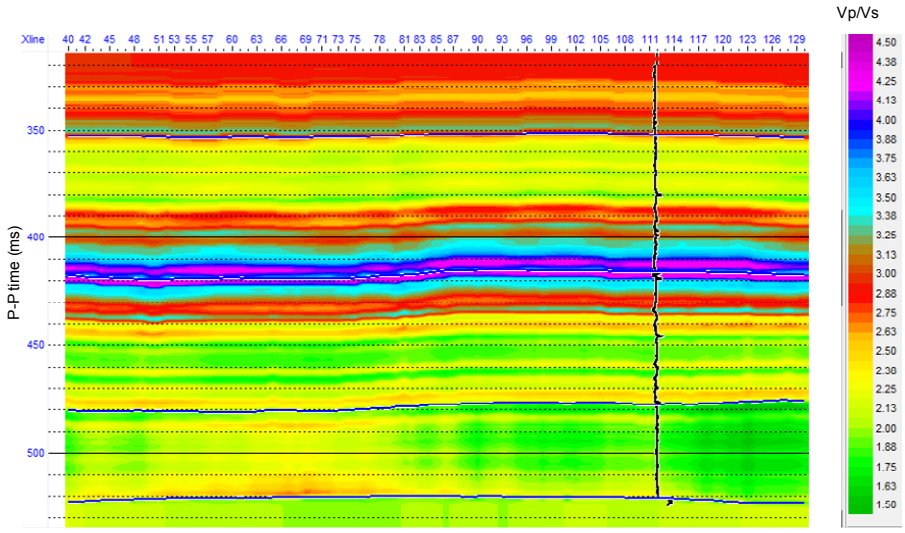

Figure 5.19. Vp/Vs section used in the domain conversion from P-S to P-P times.

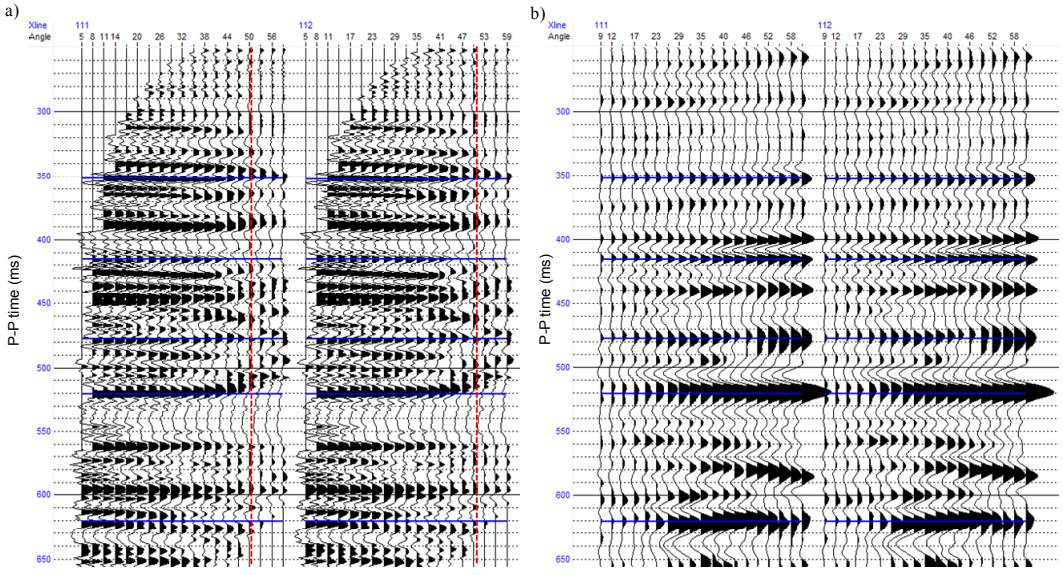

Figure 5.20. (a) P-P and (b) P-S angle gathers in the P-P domain.

5.5 Implementation of Bayesian Inversion

5.5.1 Wavelet Extraction

A key element in the seismic inversion is to extract an appropriate wavelet from seismic data, along with well logs. The angle gathers show different frequency bands as a function of the angle for the P-P and P-S waves. Thus, I determine to use angle-dependent wavelet in the inversion. I divide the gathers to three subgathers (near, mid, and far) and extract a wavelet from each sub-gathers. Angle ranges of the subgathers are as follows:

P-P wave : 5 - 20, 21 - 40, and 41 - 50 degrees for near, mid, and far subgathers

P-S wave : 5 - 20, 21 - 40, and 41 - 60 degrees for near, mid, and far subgathers

I use the statistical method to estimate the wavelet. First, the amplitude spectrum is calculated from the seismic data in the proximity of well D. Then, I assume the phase spectrum is constant with the frequency and determine the value by making the best correlation of the well-seismic tie. The wavelet length and taper are set to be 100 ms and 15 ms for the P-P wave and 200 ms and 25 ms for the P-S wave, respectively. It is noted that the P-S wavelets are extracted from the P-S data which have been converted from the P-S to the P-P time domain.

Figures 5.21 and 5.22 show the extracted wavelets for the P-P and P-S waves, respectively. All the wavelets virtually have a zero-phase. The P-P amplitude spectrums show very broad band; the maximum frequencies extend to more than 250 Hz. Also, they clearly show the angle-dependence in the frequency band; the near data have larger

amplitude spectrum than the far data in the high frequency range. In contrast, the P-S wavelets have the maximum frequency of about 100 Hz and the dominant frequency of about 30 Hz.

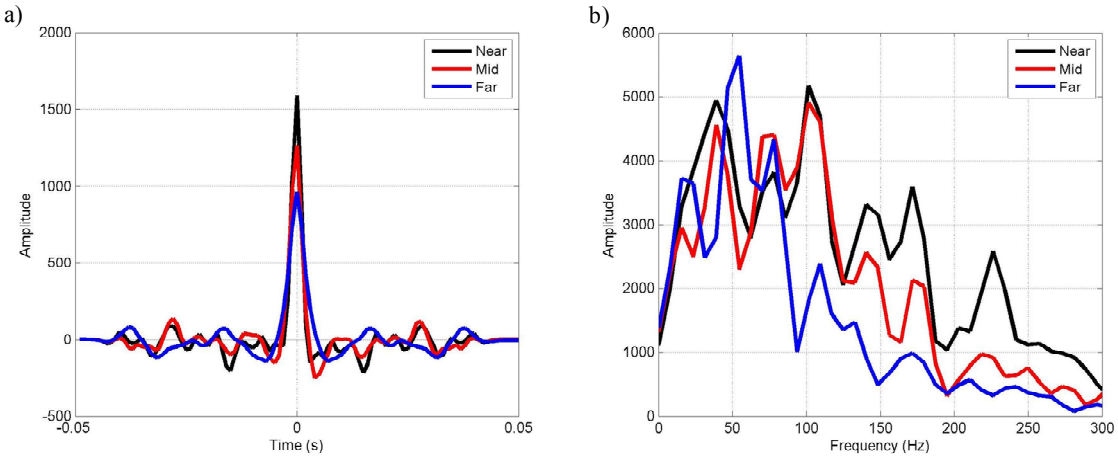

Figure 5.21. Extracted P-P wavelets.

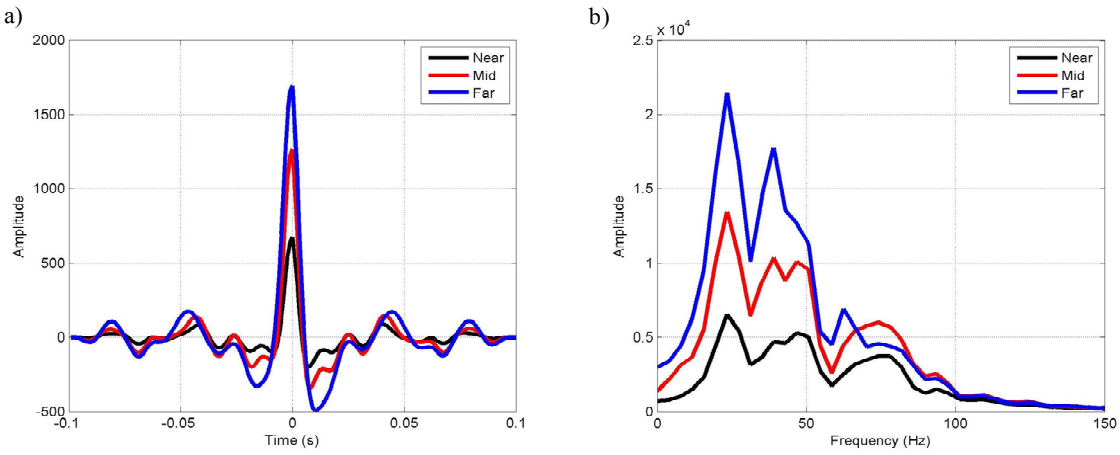

Figure 5.22. Extracted P-S wavelets.

5.5.2 Prior Model

There is a large property contrast at the Top Devonian interface. To represent the sharp contrast, I separately make prior mean model for the layers above and below the interface and obtain the final model by merging them. For the upper layer, vertically smoothed models are created by using the well logs and the picked horizons in the standard way; the well log of P- and S-wave velocities and density are applied by low-pass filter (7 - 12 Hz) and laterally extrapolated along the horizons. In contrast, for the lower carbonate layer, I assume a homogeneous medium and set α = 4,500 m/s, β = 2,550 m/s, and $\rho = 2{,}630$ kg/m^3. Figure 5.23 shows the final prior mean models. It can be observed that the upper layer has vertically smoothed variations and shape contrast with the lower layer.

In the Bayesian inversion, statistical parameters (standard deviation and correlation coefficient) of the model parameters ($\ln\alpha$, $\ln\beta$, and $\ln\rho$) work as additional constraint. For the standard deviation and correlation coefficient of the upper layer, I use the same values as the synthetic test as follows:

Standard deviation : $\sigma_\alpha = 0.0454$, $\sigma_\beta = 0.1848$, and $\sigma_\rho = 0.0372$

Correlation coefficient: $\upsilon_{\alpha\beta} = 0.67$, $\upsilon_{\alpha\rho} = 0.28$, and $\upsilon_{\beta\rho} = -0.09$

Density has poor correlation with the P- and S-wave velocities, although the velocities have high correlation with each other. For the lower carbonate layer, I assume there is no correlation among them and set the standard deviation from the well logs as:

Standard deviation : $\sigma_\alpha = 0.099$, $\sigma_\beta = 0.031$, and $\sigma_\rho = 0.034$

These values are used to make the covariance matrix of the model parameters.

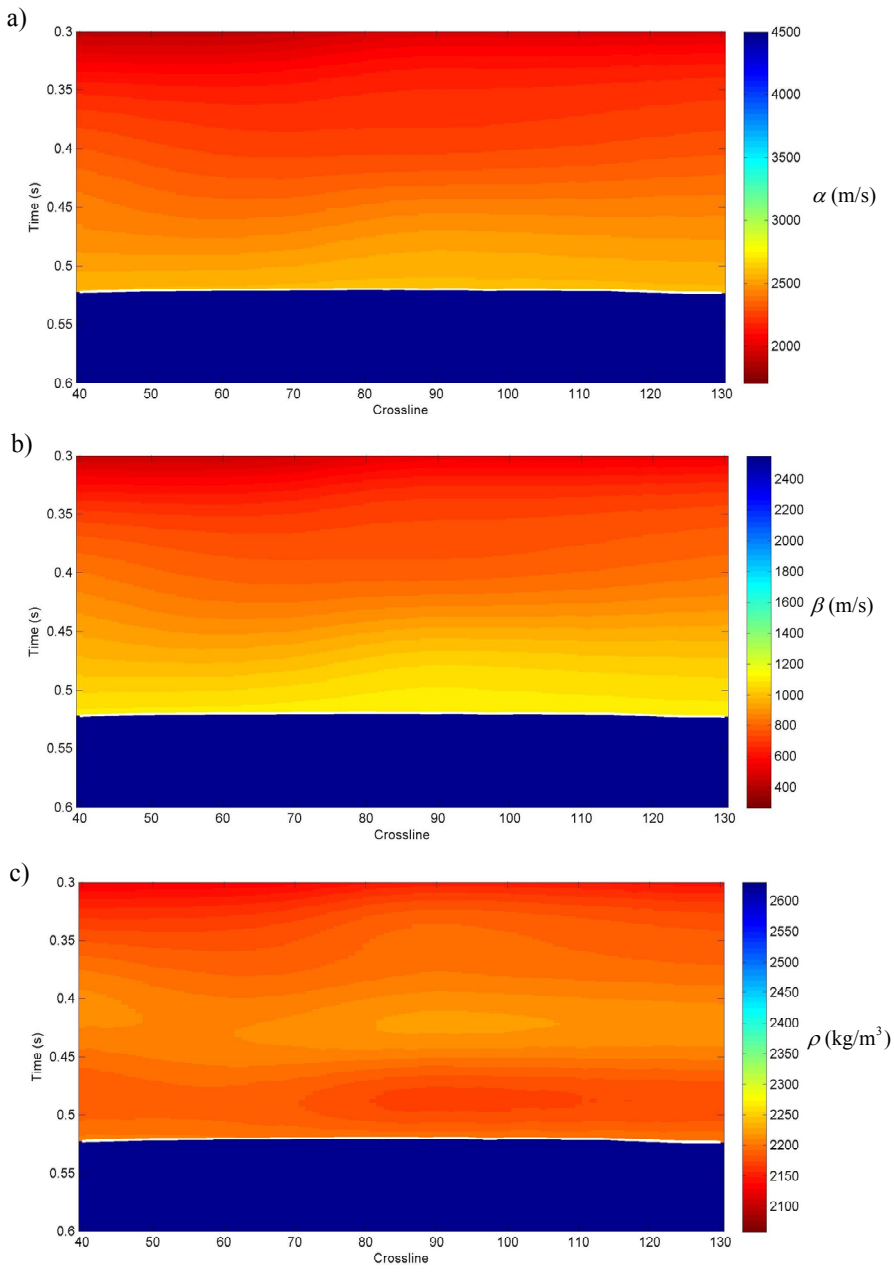

Figure 5.23. Mean value model for (a) P-wave velocity, (b) S-wave velocity, and (c) density.

5.5.3 Seismic Data Uncertainty

The Bayesian inversion can adjust the data confidence by setting the standard deviation of the corresponding covariance matrix. The standard deviation may be determined by taking into account the noise. The noise includes normal seismic noise contaminated in the data acquisition and processing. Furthermore, mis-tie between the well logs and seismic data, error of the correlation between P-P and P-S waves, and error of the forward modeling operator based on the Aki and Richards approximation should be included in the noise. After I perform a comparison between the synthetic and actual seismic data, as well as sensitivity analysis of the inversion result, the standard deviation is determined to be 75 for the both P-P and P-S waves, which approximately corresponds to S/N of 0.9 and 1.3 for P-P and P-S waves, respectively. For all the data points (times and angles), except around the Top Devonian interface, the value is used as the standard deviation of the covariance matrix.

As discussed in Chapter 5.3, because the Top Devonian interface has large velocity contrast, the incident angles exceed the critical angle in the far offset range, leading to the phase shift. Thus, we need a special treatment for the phase shift in the linearlized AVO inversion.

As expressed by Equation (4.10), the Aki and Richards formulas have the average angle as:

$$\theta = \left(\theta_i + \theta_t\right)/2, \tag{5.1}$$

where θ_i and θ_t are the incident and transmitted angles, respectively. Likewise, the P-S wave formula additionally has the P-S wave average angle as:

$$\varphi = (\varphi_r + \varphi_t)/2, \tag{5.2}$$

where φ_r and φ_t are the associated reflected and transmitted angles, respectively.

In the case of the incident angle exceeding the critical angle, we have the problem determining the transmitted angle, because there is no transmitted wave in accordance with Snell's law. However, as Downton and Ursenbach (2006) pointed out, even for angles beyond the critical angle, the Aki and Richards formulas still give us good approximation by expressing the transmitted angle as complex number as follows:

$$\theta_t = \frac{\pi}{2} - i\cosh^{-1}\left(\frac{\alpha_2}{\alpha_1}\sin\theta_r\right), \qquad \frac{\alpha_2}{\alpha_1}\sin\theta_r \geq 1, \tag{5.3}$$

where α_1 and α_2 are the P-wave velocities above and below the interface. Likewise, the transmitted angle of P-S wave for angles beyond the critical angle is expressed as:

$$\theta_t = \frac{\pi}{2} - i\cosh^{-1}\left(\frac{\beta_2}{\alpha_1}\sin\theta_r\right), \qquad \frac{\beta_2}{\alpha_1}\sin\theta_r \geq 1, \tag{5.4}$$

where β_2 is the S-wave velocity below the interface.

To ensure the validity of the Aki and Richards approximation based on Equations (5.3) and (5.4), I make a comparison of synthetic seismogram between the Zoeppritz formula and Aki and Richards approximation in two cases. In the first case (Figure 5.24), the average angle is approximated by the incident angle as $\theta = \theta_i$. This simplification suggested by Shuey (1985) may have been more commonly used in the industry. In the

other case (Figure 5.25), the average angle is calculated by Equations (5.1) and (5.3). Note that the synthetic seismograms are made by the convolution model.

In Figure 5.24, substantial differences between the Zoepprtiz formula and Aki and Richards approximation can be observed, not only around the Top Devonian interface, but also the shallower section. In contrast, in the synthetic seismogram based on Equation (5.3), the differences significantly become smaller. Likewise, for the P-S wave, the comparison of synthetic seismogram between the Zoeppritz and Aki and Richards in the two cases are presented by Figures 5.26 and 5.27, showing similar results as the P-P wave. Thus, it can be concluded that using the complex number for the transmitted angle in the case beyond the critical angle is valid in the Aki and Richards approximation.

But, it is important that there are still substantial errors at around the Top Devonian in large angle range (Figures 5.25 and 5.27). My inversion method requires preparation of the same angle range at all time sampling, implying that I cannot partially remove the unreliable data. Thus, to practically solve this problem, I manually adjust the standard deviation. I make a polygon enclosing the unreliable data and set larger standard deviation within the polygon. Figure 5.28 shows the modified standard deviation of the data. The area within the polygon has a standard deviation of 375, which is 5 times larger than the normal value. This treatment means that, at around the Top Devonian interface, the inversion practically uses only small angle data and that the large angle data with very low confidence does not practically affect the inversion result.

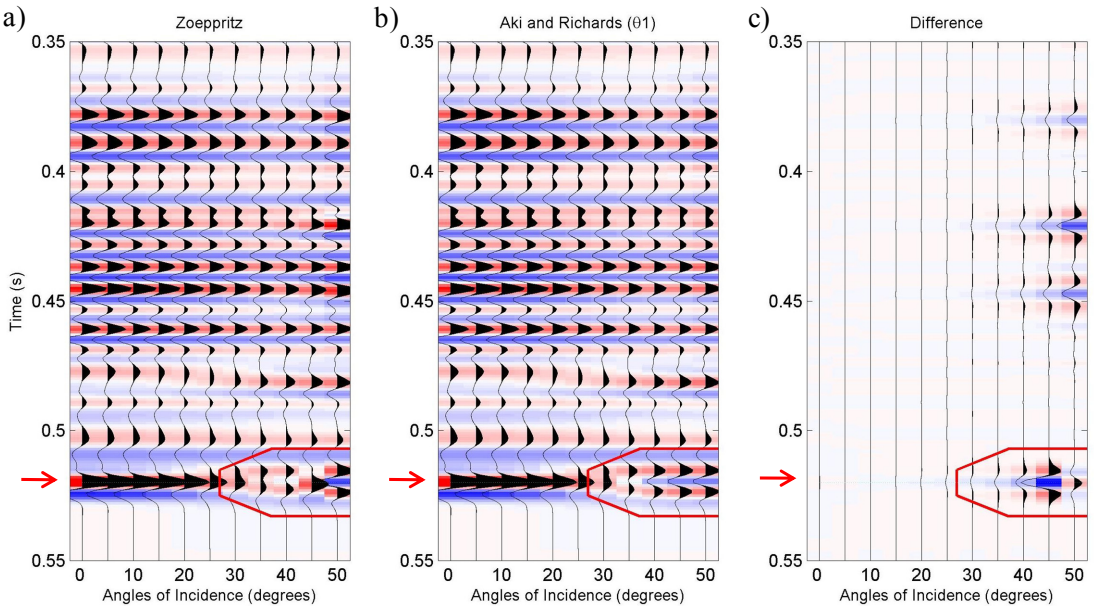

Figure 5.24. P-P Synthetic seismogram based on (a) Zoeppritz equation, (b) Aki and Richards approximation with incident angle ($\theta = \theta_i$), and (c) the difference between (a) and (b). The red arrows represent the Top Devonian interface.

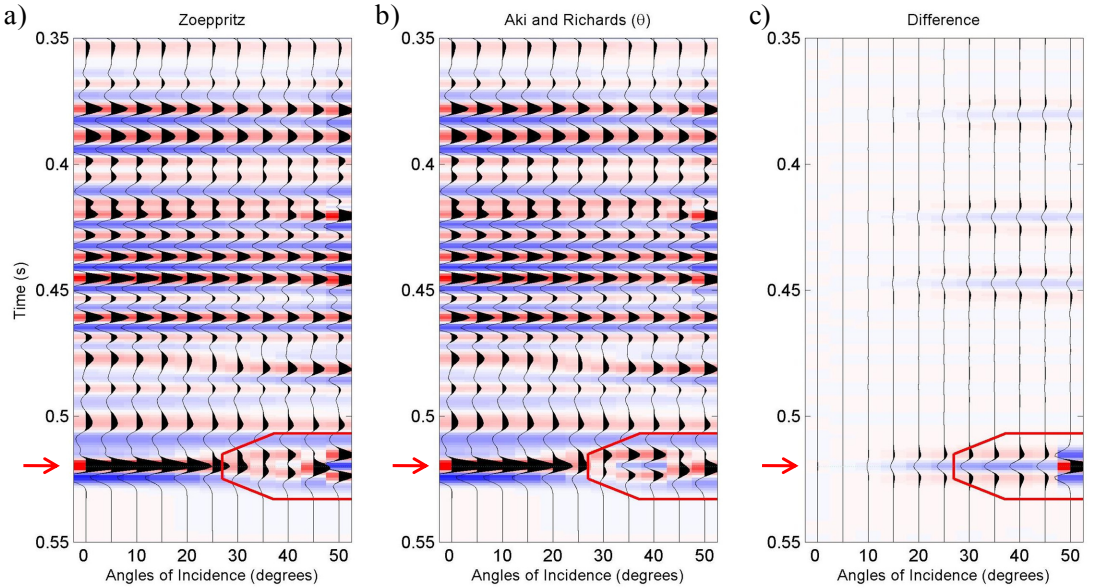

Figure 5.25. P-P Synthetic seismogram bansed on (a) Zoeppritz equation, (b) Aki and Richards approximation with Equations (5.1) and (5.3), and (c) the difference between (a) and (b). The red arrows represent the Top Devonian interface.

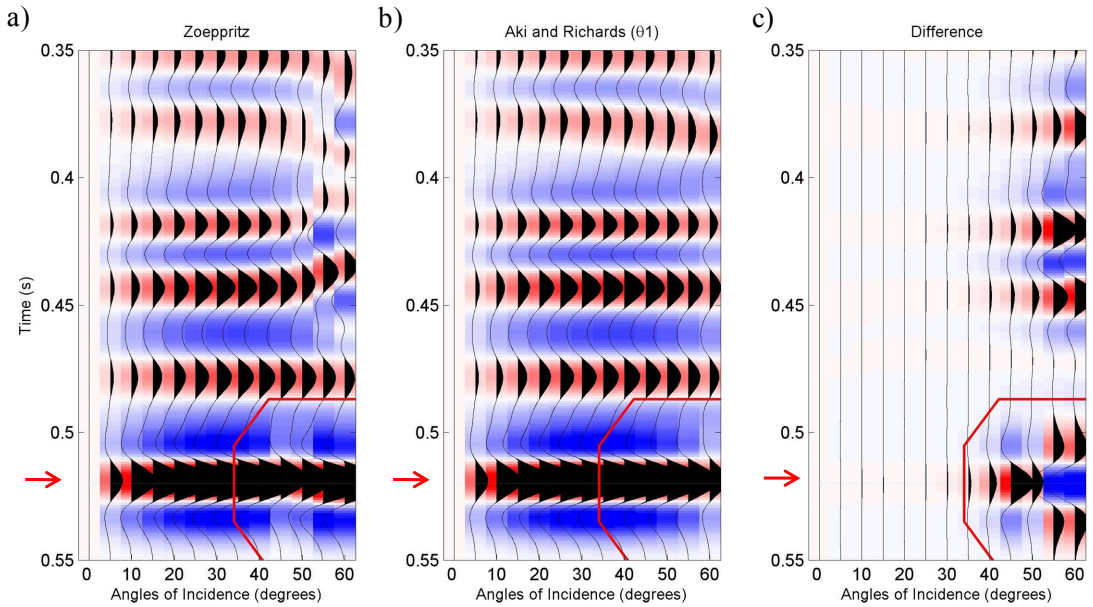

Figure 5.26. P-S Synthetic seismogram based on (a) Zoeppritz equation, (b) Aki and Richards approximation with incident angle ($\theta = \theta_i$), and (c) the difference between (a) and (b). The red arrows represent the Top Devonian interface.

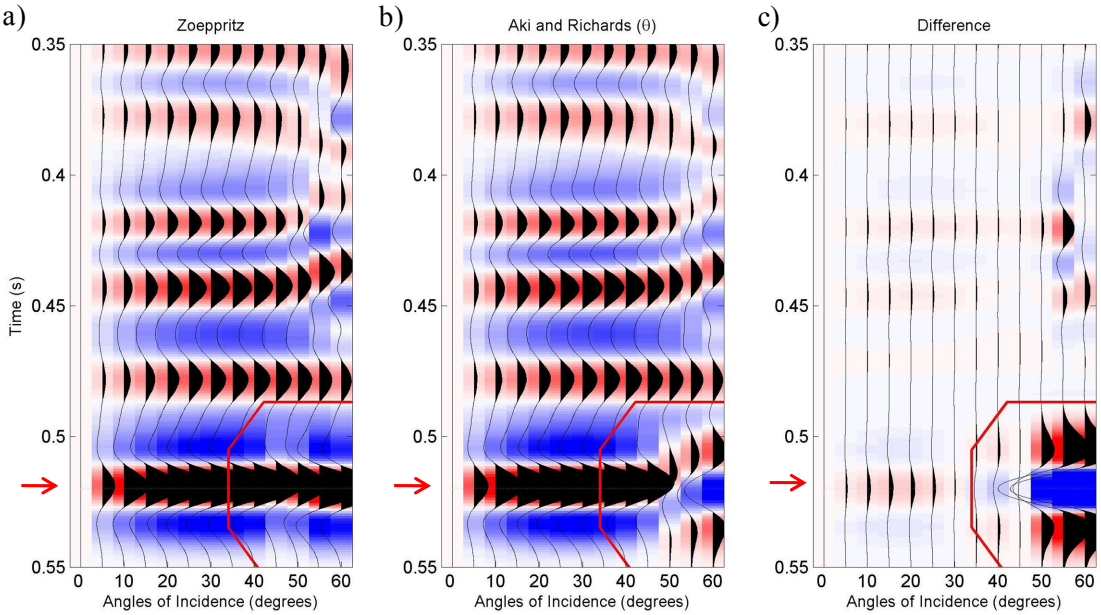

Figure 5.27. P-S Synthetic seismogram bansed on (a) Zoeppritz equation, (b) Aki and Richards approximation with Equations (5.2) and (5.4), and (c) the difference between (a) and (b). The red arrows represent the Top Devonian interface.

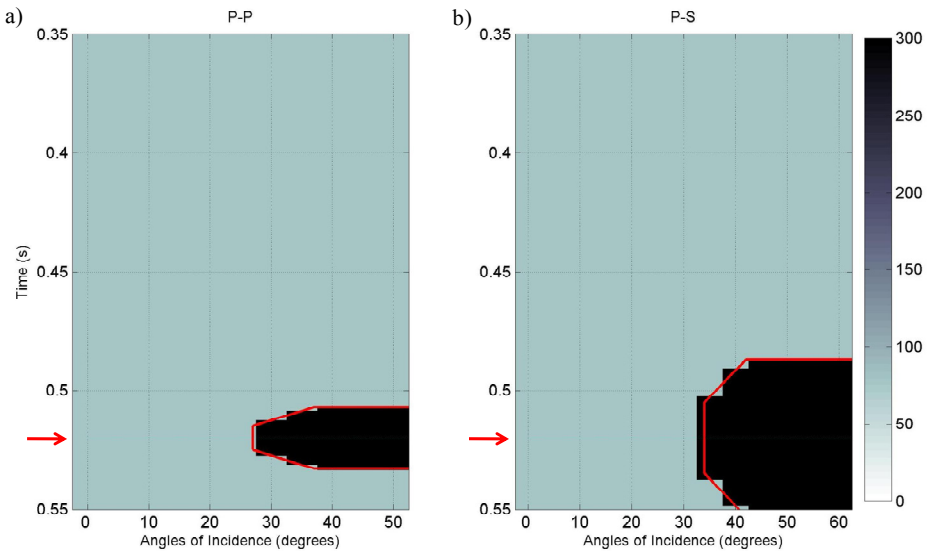

Figure 5.28. The standard deviation for (a) P-P and (b) P-S wave data. The red arrows represent the Top Devonian interface.

5.6 Inversion Result

The P- and S-wave velocities and density are inverted from the seismic data by using the developed method. Figures 5.29, 5.30, and 5.31 show the inversion result in the well position for the joint, P-P only, and P-S only inversions, respectively. The black and red solid curves represent the well log and inversion result, respectively. Furthermore, the black and red dot curves represent the prior and posterior prediction intervals of 95%, respectively. In this location, the reservoir layer is approximately from 478 to 521 ms, in which low values in the well log density indicate the reservoir clean sands. It is noted that the well log curves are applied with a low-pass filter (200 Hz) to match the frequency content with that of the inversion results.

The P-S inversion results have lower frequency content compared to that of the joint and P-P only inversions. However, it follows the trend of the well log curve pretty well over all. In contrast, the joint and P-P only inversions seem to have similar results with each other. But, if one looks carefully at the results, substantial differences are recognized; for example, the joint inversion gives better correlation with the well log at around 415 ms and 490 ms in density estimation. Tables 5.1 and 5.2 show the RMS error and correlation coefficient between the inversion results and the well log. For the comparison, the values of the prior mean model are shown in the tables. It is obvious that the joint inversion gives us the superior result in the density and P-wave velocity, compared to the P-P only inversion. For example, the RMS error and correlation coefficient of the joint inversion in the density estimation are 75 and 0.533, while these values of the P-P only inversions are 77 and 0.509. The improvement is not significant, but still substantial.

The joint inversion results of Inline 322 are shown in Figure 5.32. The well logs are plotted for comparison and show good agreement with the inversion results over all. The density section shows the lateral variations, which is consistent with the general geological interpretation in the previous studies.

As shown by Figure 4.1, the density has an almost linear relationship with the Vshale. Thus, assuming that density lower than 2,150 kg/m^3 corresponds to the reservoir clean sands, I estimate the total thickness of the clean sands within the reservoir layer (Figure 5.33). It is noted that unit of the thickness is two-way traveltime (ms). The thickness map shows that there is north-south trend; thin in the north and thick in the south. Furthermore,

at the southwest corner in the study area, thick clean sands are observed. These results could improve our geological interpretation.

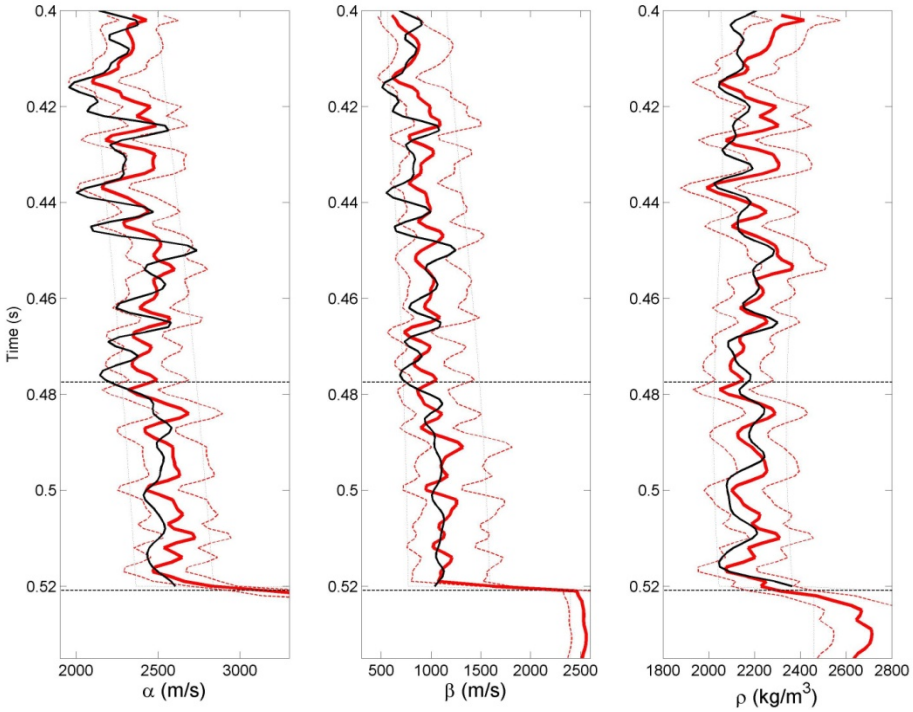

Figure 5.29. Results of P-P and P-S joint inversion in the well position. The black and red solid curves represent the well log and inversion result, respectively. The black and red dot curves represent the prior and posterior prediction intervals of 95%, respectively.

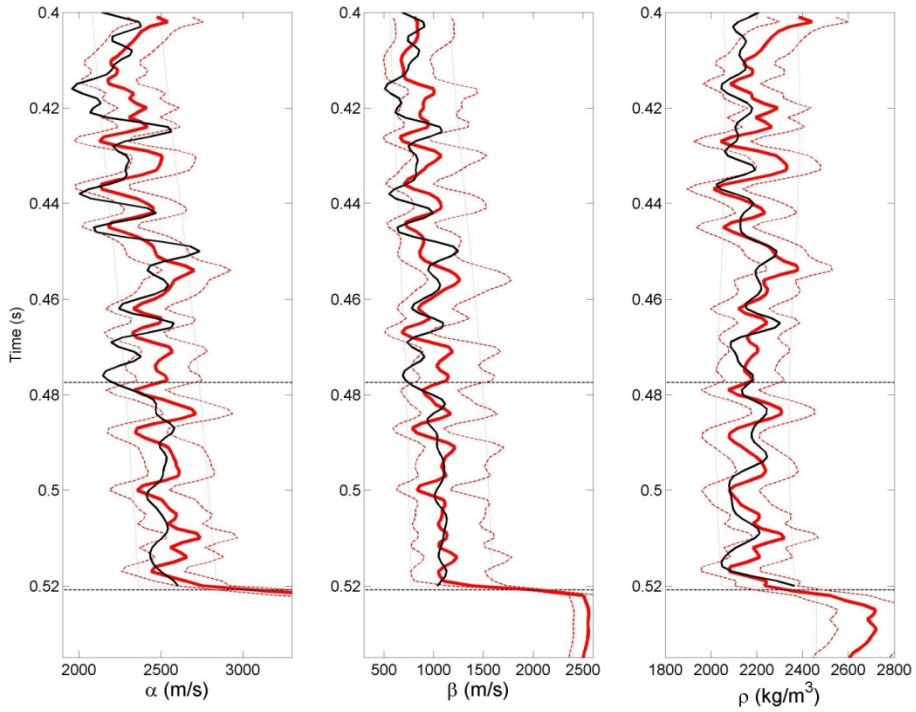

Figure 5.30. Results of P-P only inversion in the well position.

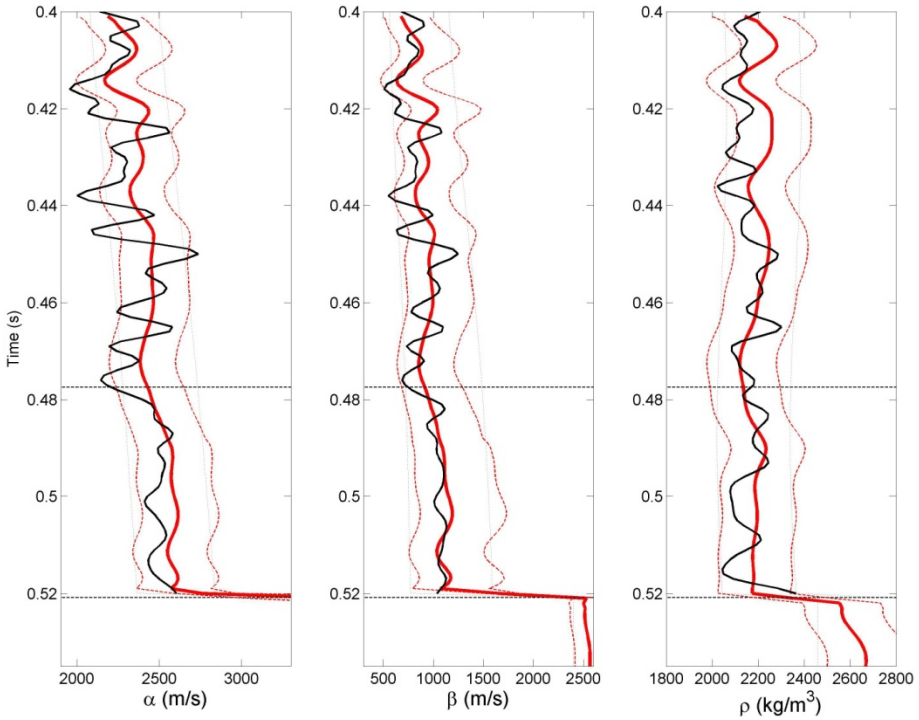

Figure 5.31. Results of P-S only inversion in the well position.

Table 5.1. RMS error of the inversion result and prior mean model with the well logs for two cases; whole interval and only reservoir interval.

	Whole Interval			Reservoir Interval		
	α (m/s)	β (m/s)	ρ (kg/m^3)	α (m/s)	β (m/s)	ρ (kg/m^3)
Joint	183	233	92	154	251	75
P-P only	194	228	96	153	196	77
P-S only	205	223	90	184	245	80
Prior Mean Model	253	219	93	293	227	88

Table 5.2. Correlation coefficient of the inversion result and prior mean model with the well logs for two cases; whole interval and only reservoir interval.

	Whole Interval			Reservoir Interval		
	α	β	ρ	α	β	ρ
Joint	0.618	0.420	0.443	0.478	0.266	0.533
P-P only	0.540	0.371	0.392	0.374	0.263	0.509
P-S only	0.488	0.449	0.193	0.443	0.300	0.294
Prior Mean Model	0.349	0.416	0.145	0.333	0.259	0.357

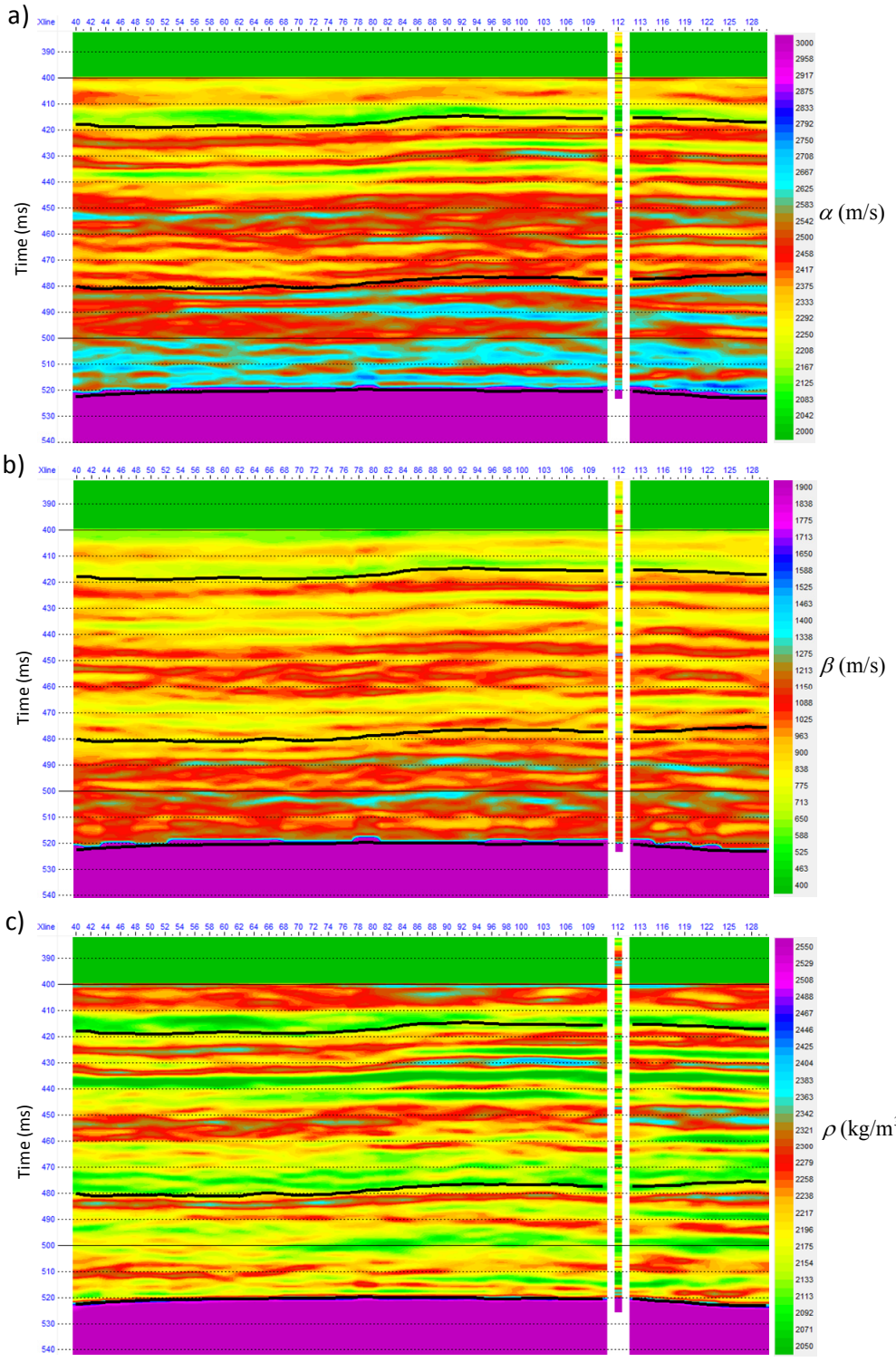

Figure 5.32. Joint inversion result and well log at Inline of 332 for (a) P-wave velocity, (b) S-wave velocity, and (c) density.

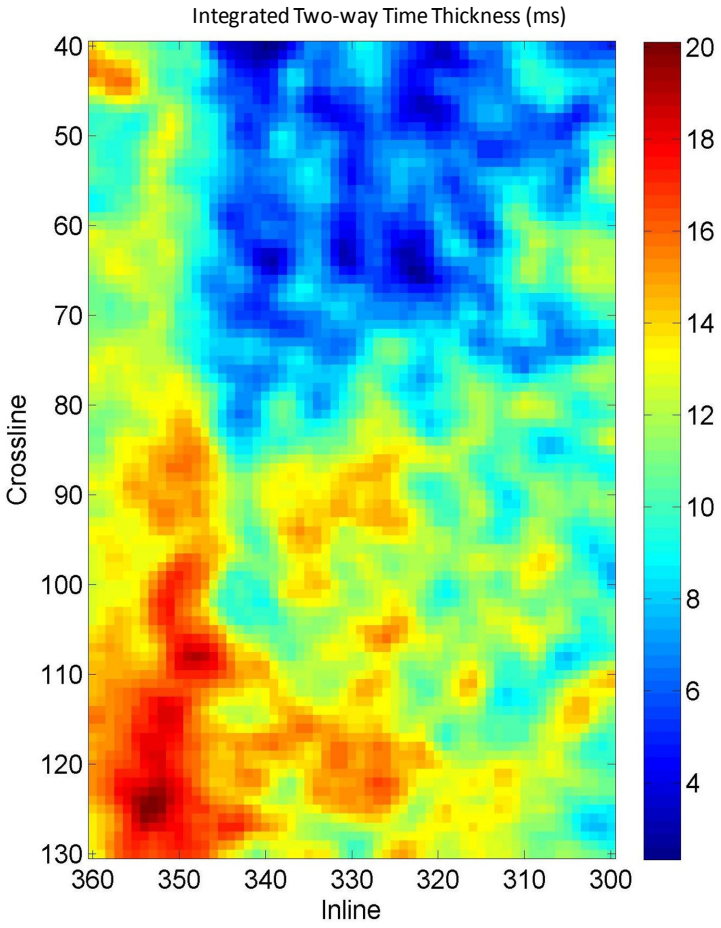

Figure 5.33. Integrated two-way time thickness of lower density than 2,150 kg/m^3 within the reservoir layer.

5.7 Summary

The developed P-P and P-S joint AVO inversion was applied to the Hangingstone oilfield. The seismic data conditioning and correlation between the P-P and P-S waves are two of the most key elements in the joint inversion. I carefully performed these processes and successfully obtained the fully processed data. The implementation of the Bayesian inversion using the data suggested that the joint inversion gives us superior results compared to the P-P only inversion. Furthermore, it is suggested that not only P- and S-

wave velocities but also density can be estimated by the joint inversion. I successfully created distribution map of the reservoir sands from the joint inversion result.

Chapter 6 - Time-Lapse AVO Inversion

- Methodology and Synthetic Test

6.1 Introduction

Time-lapse seismic analysis provides us understand of fluid movement and pressure change due to the production activity by extracting seismic response differences between the baseline and repeat surveys. There are many time-lapse seismic studies in heavy-oil reservoirs (e.g., Issac, 1996; Sun, 1999; Nakayama et al., 2008). They made interpretation of the steam distribution by using amplitude anomalies or travel-time differences. As the technique has become mature, emphasis on more quantitative interpretation of the time-lapse seismic data has increased. The time-lapse seismic inversion is one of the quantitative interpretation techniques. Since the time-lapse seismic inversion is still a challenging task, many workflows have been proposed (e.g., Sarkar et al., 2003; Lafet et al., 2005; Lafet et al., 2009; Toinet et al., 2010). They are mainly categorized into four groups (Lafet et al., 2009): 1) baseline and repeat survey data are separately inverted to elastic properties. The changes of the elastic properties are then obtained from differences in the two inversion results, 2) baseline data are firstly inverted to elastic properties, which are subsequently used as the initial model in the inversion of repeat data. The inversion results are then differenced to obtain the elastic property changes (e.g., Lafet et al., 2005), 3) seismic amplitude differences between the two surveys are directly inverted to the elastic property changes (e.g., Sarkar et al., 2003; Buland and Ouair, 2006), and 4) global inversion methods where all seismic data from baseline and repeat surveys are

simultaneously inverted using the global optimization technique (e.g., Lafet et al., 2009; Toinet et al., 2010).

Sarkar et al. (2003) tested the above first three workflows (1, 2, and 3) with synthetic data. They reported that the third one gives us the best result, because the first one is very sensitive to the non-uniqueness problem of the inversion process and the second one requires more complicated processes than third one. Moreover, the fourth one is a novel workflow which simultaneously achieves time alignment correction in the inversion process. However, since the workflow uses the global optimization technique such as the simulated annealing (e.g., Lafet et al., 2009), it is an expensive process from a computation time point of view. In contrast, since the third workflow is based on a linearized inversion, it is more robust and faster process, compared to the fourth one, although it requires the vertical alignment correction before the implementation.

Buland and Ouair (2006) proposed a method which uses the Bayesian theorem in the third workflow. They regard elastic property changes as model parameters and obtain the posterior distribution, which are consistent with both the prior information and seismic data in statistical sense. I take a similar approach as Buland and Ouair (2006). But, I use both baseline and repeat survey data, instead of using only the differences, and simultaneously obtain elastic properties at the baseline survey and the changes between the two surveys along with the uncertainties. Although Buland and Ouair (2006) assume the same wavelet in the two surveys, it is not unusual that time-lapse seismic data have different frequency bands between them. My method allows us to use individual wavelets in each seismic data. Furthermore, it can be extended to multicomponent seismic data.

In this chapter, I will describe the new method of the time-lapse AVO inversion. The developed method will be tested with synthetic data. The implementation of the method with the Hangingstone oilfield will be presented in the following chapter.

6.2 Formalization of Time-Lapse Seismic AVO Inversion

To make a formulation of the time-lapse seismic AVO inversion, one starts with P-P wave reflection coefficients in the baseline and repeat surveys for a single interface. As discussed in Chapter 4, they are expressed based on the Aki and Richards' AVO approximation [Equations (4.10) and (4.11)] as:

$$\begin{aligned} R_{PP1}(\theta) &= a_\alpha(\theta)L_{\alpha 1} + a_\beta(\theta,\gamma_1)L_{\beta 1} + a_\rho(\theta,\gamma_1)L_{\rho 1}, \\ R_{PP2}(\theta) &= a_\alpha(\theta)L_{\alpha 2} + a_\beta(\theta,\gamma_2)L_{\beta 2} + a_\rho(\theta,\gamma_2)L_{\rho 2}, \end{aligned} \tag{6.1}$$

where the subscripts 1 and 2 represent the baseline and repeat surveys, respectively; $R_{PP}(\theta)$ is the corresponding reflection coefficient at the incident angle θ; L_α, L_β, and L_ρ are the corresponding P- and S-wave velocities and density reflectivities at the interface; a_α, a_β, and a_ρ are the P-P wave AVO coefficients defined by (4.11); and γ is the corresponding Vs/Vp.

The repeat survey reflectivities (L_2) are decomposed to two terms; the baseline reflectivities (L_1) and the changes between the two surveys (ΔL) as:

$$\begin{aligned} L_{\alpha 2} &= L_{\alpha 1} + \Delta L_\alpha, \\ L_{\beta 2} &= L_{\beta 1} + \Delta L_\beta, \\ L_{\rho 2} &= L_{\rho 1} + \Delta L_\rho. \end{aligned} \tag{6.2}$$

By substituting (6.2) into (6.1), one obtains:

$$
\begin{aligned}
R_{PP1}(\theta) &= a_{\alpha 1}(\theta)L_{\alpha 1} + a_{\beta 1}(\theta)L_{\beta 1} + a_{\rho 1}(\theta)L_{\rho 1}, \\
R_{PP2}(\theta) &= a_{\alpha 2}(\theta)L_{\alpha 1} + a_{\beta 2}(\theta)L_{\beta 1} + a_{\rho 2}(\theta)L_{\rho 1} \\
&\quad + a_{\alpha 2}(\theta)\Delta L_{\alpha} + a_{\beta 2}(\theta)\Delta L_{\beta} + a_{\rho 2}(\theta)\Delta L_{\rho}.
\end{aligned} \tag{6.3}
$$

It is noted that γ in parentheses of the AVO coefficients is omitted to obtain simple expressions. When Equation (6.3) is expressed in a matrix form, one obtains:

$$
\begin{bmatrix} R_{PP1}(\theta) \\ R_{PP2}(\theta) \end{bmatrix} = \begin{bmatrix} a_{\alpha 1}(\theta) & a_{\beta 1}(\theta) & a_{\rho 1}(\theta) & 0 & 0 & 0 \\ a_{\alpha 2}(\theta) & a_{\beta 2}(\theta) & a_{\rho 2}(\theta) & a_{\alpha 2}(\theta) & a_{\beta 2}(\theta) & a_{\rho 2}(\theta) \end{bmatrix} \begin{bmatrix} L_{\alpha 1} \\ L_{\beta 1} \\ L_{\rho 1} \\ \Delta L_{\alpha} \\ \Delta L_{\beta} \\ \Delta L_{\rho} \end{bmatrix}. \tag{6.4}
$$

Furthermore, when we have an angle gather with m and n different incident angles for the baseline and repeat data, respectively, a linear system of $m + n$ linear equations with 6 unknown parameters is obtained as:

$$
\begin{bmatrix} R_{PP1}(\theta_1) \\ \vdots \\ R_{PP1}(\theta_m) \\ R_{PP2}(\theta_1) \\ \vdots \\ R_{PP2}(\theta_n) \end{bmatrix} = \begin{bmatrix} a_{\alpha 1}(\theta_1) & a_{\beta 1}(\theta_1) & a_{\rho 1}(\theta_1) & 0 & 0 & 0 \\ \vdots & \vdots & \vdots & \vdots & \vdots & \vdots \\ a_{\alpha 1}(\theta_m) & a_{\beta 1}(\theta_m) & a_{\rho 1}(\theta_m) & 0 & 0 & 0 \\ a_{\alpha 2}(\theta_1) & a_{\beta 2}(\theta_1) & a_{\rho 2}(\theta_1) & a_{\alpha 2}(\theta_1) & a_{\beta 2}(\theta_1) & a_{\rho 2}(\theta_1) \\ \vdots & \vdots & \vdots & \vdots & \vdots & \vdots \\ a_{\alpha 2}(\theta_n) & a_{\beta 2}(\theta_n) & a_{\rho 2}(\theta_n) & a_{\alpha 2}(\theta_n) & a_{\beta 2}(\theta_n) & a_{\rho 2}(\theta_n) \end{bmatrix} \begin{bmatrix} L_{\alpha 1} \\ L_{\beta 1} \\ L_{\rho 1} \\ \Delta L_{\alpha} \\ \Delta L_{\beta} \\ \Delta L_{\rho} \end{bmatrix}. \tag{6.5}
$$

The rows from first to m^{th} correspond to the baseline data while the remaining rows correspond to the repeat data.

Next, the single-interface formulas will be extended to a case with time-continuous data. In the same way as Chapter 4, if the small reflection coefficient approximation is satisfied (Stolt and Weglein, 1985), the time-continuous reflectivities are approximated as:

$$
\begin{aligned}
L_{\alpha 1}(t) &\approx \frac{\partial}{\partial t}\ln\alpha_1(t),\\
L_{\beta 1}(t) &\approx \frac{\partial}{\partial t}\ln\beta_1(t),\\
L_{\rho 1}(t) &\approx \frac{\partial}{\partial t}\ln\rho_1(t).
\end{aligned}
\tag{6.6}
$$

Furthermore, the reflectivity changes are expressed as:

$$
\begin{aligned}
\Delta L_{\alpha}(t) &\approx \frac{\partial}{\partial t}\left(\Delta\ln\alpha(t)\right),\\
\Delta L_{\beta}(t) &\approx \frac{\partial}{\partial t}\left(\Delta\ln\beta(t)\right),\\
\Delta L_{\rho}(t) &\approx \frac{\partial}{\partial t}\left(\Delta\ln\rho(t)\right),
\end{aligned}
\tag{6.7}
$$

where

$$
\begin{aligned}
\Delta\ln\alpha(\mathrm{t}) &= \ln\alpha_2(t)-\ln\alpha_1(t),\\
\Delta\ln\beta(t) &= \ln\beta_2(t)-\ln\beta_1(t),\\
\Delta\ln\rho(t) &= \ln\rho_2(t)-\ln\rho_1(t).
\end{aligned}
\tag{6.8}
$$

Using (6.5), (6.6), (6.7) and (6.8), the time-continuous reflection coefficients are obtained as:

$$
\begin{bmatrix}
\mathbf{R}_{\mathbf{PP}1}(\theta_1)\\ \vdots\\ \mathbf{R}_{\mathbf{PP}1}(\theta_m)\\ \mathbf{R}_{\mathbf{PP}2}(\theta_1)\\ \vdots\\ \mathbf{R}_{\mathbf{PP}2}(\theta_n)
\end{bmatrix}
=
\begin{bmatrix}
\mathbf{a}_{\alpha 1}(\theta_1) & \mathbf{a}_{\beta 1}(\theta_1) & \mathbf{a}_{\rho 1}(\theta_1) & 0 & 0 & 0\\
\vdots & \vdots & \vdots & \vdots & \vdots & \vdots\\
\mathbf{a}_{\alpha 1}(\theta_m) & \mathbf{a}_{\beta 1}(\theta_m) & \mathbf{a}_{\rho 1}(\theta_m) & 0 & 0 & 0\\
\mathbf{a}_{\alpha 2}(\theta_1) & \mathbf{a}_{\beta 2}(\theta_1) & \mathbf{a}_{\rho 2}(\theta_1) & \mathbf{a}_{\alpha 2}(\theta_1) & \mathbf{a}_{\beta 2}(\theta_1) & \mathbf{a}_{\rho 2}(\theta_1)\\
\vdots & \vdots & \vdots & \vdots & \vdots & \vdots\\
\mathbf{a}_{\alpha 2}(\theta_n) & \mathbf{a}_{\beta 2}(\theta_n) & \mathbf{a}_{\rho 2}(\theta_n) & \mathbf{a}_{\alpha 2}(\theta_n) & \mathbf{a}_{\beta 2}(\theta_n) & \mathbf{a}_{\rho 2}(\theta_n)
\end{bmatrix}
\times
\begin{bmatrix}
\mathbf{dt} & 0 & \cdots & & 0\\
0 & \mathbf{dt} & & & \\
 & & \mathbf{dt} & & \vdots\\
\vdots & & & \mathbf{dt} & \\
 & & & & \mathbf{dt} \quad 0\\
0 & & \cdots & & 0 \quad \mathbf{dt}
\end{bmatrix}
\begin{bmatrix}
\ln\boldsymbol{\alpha}_1\\ \ln\boldsymbol{\beta}_1\\ \ln\boldsymbol{\rho}_1\\ \Delta\ln\boldsymbol{\alpha}\\ \Delta\ln\boldsymbol{\beta}\\ \Delta\ln\boldsymbol{\rho}
\end{bmatrix}.
\tag{6.9}
$$

When one writes as:

$$\mathbf{R} = \begin{bmatrix} \mathbf{R}_{\mathbf{PP1}}(\theta_1) \\ \vdots \\ \mathbf{R}_{\mathbf{PP1}}(\theta_m) \\ \mathbf{R}_{\mathbf{PP2}}(\theta_1) \\ \vdots \\ \mathbf{R}_{\mathbf{PP2}}(\theta_n) \end{bmatrix}, \tag{6.10}$$

$$\mathbf{A} = \begin{bmatrix} \mathbf{a}_{\boldsymbol{\alpha}\mathbf{1}}(\theta_1) & \mathbf{a}_{\boldsymbol{\beta}\mathbf{1}}(\theta_1) & \mathbf{a}_{\boldsymbol{\rho}\mathbf{1}}(\theta_1) & 0 & 0 & 0 \\ \vdots & \vdots & \vdots & \vdots & \vdots & \vdots \\ \mathbf{a}_{\boldsymbol{\alpha}\mathbf{1}}(\theta_m) & \mathbf{a}_{\boldsymbol{\beta}\mathbf{1}}(\theta_m) & \mathbf{a}_{\boldsymbol{\rho}\mathbf{1}}(\theta_m) & 0 & 0 & 0 \\ \mathbf{a}_{\boldsymbol{\alpha}\mathbf{2}}(\theta_1) & \mathbf{a}_{\boldsymbol{\beta}\mathbf{2}}(\theta_1) & \mathbf{a}_{\boldsymbol{\rho}\mathbf{2}}(\theta_1) & \mathbf{a}_{\boldsymbol{\alpha}\mathbf{2}}(\theta_1) & \mathbf{a}_{\boldsymbol{\beta}\mathbf{2}}(\theta_1) & \mathbf{a}_{\boldsymbol{\rho}\mathbf{2}}(\theta_1) \\ \vdots & \vdots & \vdots & \vdots & \vdots & \vdots \\ \mathbf{a}_{\boldsymbol{\alpha}\mathbf{2}}(\theta_n) & \mathbf{a}_{\boldsymbol{\beta}\mathbf{2}}(\theta_n) & \mathbf{a}_{\boldsymbol{\rho}\mathbf{2}}(\theta_n) & \mathbf{a}_{\boldsymbol{\alpha}\mathbf{2}}(\theta_n) & \mathbf{a}_{\boldsymbol{\beta}\mathbf{2}}(\theta_n) & \mathbf{a}_{\boldsymbol{\rho}\mathbf{2}}(\theta_n) \end{bmatrix}, \tag{6.11}$$

$$\mathbf{D} = \begin{bmatrix} \mathbf{dt} & 0 & \cdots & & 0 \\ 0 & \mathbf{dt} & & & \\ & & \mathbf{dt} & & \vdots \\ \vdots & & & \mathbf{dt} & \\ & & & & \mathbf{dt} \quad 0 \\ 0 & & \cdots & & 0 \quad \mathbf{dt} \end{bmatrix}, \tag{6.12}$$

and

$$\mathbf{m} = \begin{bmatrix} \ln\boldsymbol{\alpha}_\mathbf{1} & \ln\boldsymbol{\beta}_\mathbf{1} & \ln\boldsymbol{\rho}_1 & \Delta\ln\boldsymbol{\alpha} & \Delta\ln\boldsymbol{\beta} & \Delta\ln\boldsymbol{\rho} \end{bmatrix}^T, \tag{6.13}$$

Equation (6.7) is expressed in a simple form as:

$$\mathbf{R} = \mathbf{ADm}, \tag{6.14}$$

where each element ($\mathbf{R}_{\mathbf{pp1}}$, $\mathbf{R}_{\mathbf{pp2}}$, $\mathbf{a}_{\boldsymbol{\alpha}}$, $\mathbf{a}_{\boldsymbol{\beta}}$, and $\mathbf{a}_{\boldsymbol{\rho}}$) in the matrix **A** and **R** is a $l \times l$ diagonal matrix containing the corresponding time continuous values, l is the number of data samplings, and **dt** is an element of the time derivative operator, which is defined by (4.14).

Furthermore, when one convolves the time-continuous reflection coefficients with the associated wavelets, a formula of the time-lapse seismic AVO inversion is obtained as:

$$\mathbf{d} = \mathbf{Gm}, \tag{6.15}$$

where **d** is noise-free observation data and is expressed as:

$$\mathbf{d} = \left[\mathbf{d}_{\mathbf{pp1}}(\theta_1) \quad \cdots \quad \mathbf{d}_{\mathbf{pp1}}(\theta_m) \quad \mathbf{d}_{\mathbf{pp2}}(\theta_1) \quad \cdots \quad \mathbf{d}_{\mathbf{pp2}}(\theta_n)\right]^T. \tag{6.16}$$

G is the forward modeling operator and is expressed as:

$$\mathbf{G} = \mathbf{WAD}. \tag{6.17}$$

In addition, **W** is the wavelet matrix and has the following form:

$$\mathbf{W} = \begin{bmatrix} \mathbf{W}_1(\theta_1) & & & & & \\ & \ddots & & & & \\ & & \mathbf{W}_1(\theta_m) & & & \\ & & & \mathbf{W}_2(\theta_1) & & \\ & & & & \ddots & \\ & & & & & \mathbf{W}_2(\theta_n) \end{bmatrix}, \tag{6.18}$$

where $\mathbf{W}_1(\theta_i)$ and $\mathbf{W}_2(\theta_i)$ are the associated wavelet at the incident angle θ_i in the baseline and repeat data, respectively, and have a similar form of Equation (4.23).

Moreover, extending the formula to multicomponent data can only be attained by modifying the matrixes **d**, **W**, and **A**. For example, in the case of P-S wave data which is additionally available at the repeat survey, the matrix **A** has the form:

$$\mathbf{A}=\begin{bmatrix} \mathbf{a}_{\alpha 1}(\theta_1) & \mathbf{a}_{\beta 1}(\theta_1) & \mathbf{a}_{\rho 1}(\theta_1) & 0 & 0 & 0 \\ \vdots & \vdots & \vdots & \vdots & \vdots & \vdots \\ \mathbf{a}_{\alpha 1}(\theta_m) & \mathbf{a}_{\beta 1}(\theta_m) & \mathbf{a}_{\rho 1}(\theta_m) & 0 & 0 & 0 \\ \mathbf{a}_{\alpha 2}(\theta_1) & \mathbf{a}_{\beta 2}(\theta_1) & \mathbf{a}_{\rho 2}(\theta_1) & \mathbf{a}_{\alpha 2}(\theta_1) & \mathbf{a}_{\beta 2}(\theta_1) & \mathbf{a}_{\rho 2}(\theta_1) \\ \vdots & \vdots & \vdots & \vdots & \vdots & \vdots \\ \mathbf{a}_{\alpha 2}(\theta_n) & \mathbf{a}_{\beta 2}(\theta_n) & \mathbf{a}_{\rho 2}(\theta_n) & \mathbf{a}_{\alpha 2}(\theta_n) & \mathbf{a}_{\beta 2}(\theta_n) & \mathbf{a}_{\rho 2}(\theta_n) \\ 0 & \mathbf{b}_{\beta 2}(\theta_1) & \mathbf{b}_{\rho 2}(\theta_1) & 0 & \mathbf{b}_{\beta 2}(\theta_1) & \mathbf{b}_{\rho 2}(\theta_1) \\ \vdots & \vdots & \vdots & \vdots & \vdots & \vdots \\ 0 & \mathbf{b}_{\beta 2}(\theta_q) & \mathbf{b}_{\rho 2}(\theta_q) & 0 & \mathbf{b}_{\beta 2}(\theta_q) & \mathbf{b}_{\rho 2}(\theta_q) \end{bmatrix}, \tag{6-19}$$

where $\mathbf{b}_\beta$ and $\mathbf{b}_\rho$ is a diagonal matrix containing the time-continuous values of the P-S wave coefficients of the AVO approximation, as defined by (4.11). The P-S wave is assumed to be an angle gather with q different incident angles.

Furthermore, in the case of P-S wave data which is available at both the surveys, the matrix **A** has the form:

$$\mathbf{A}=\begin{bmatrix} \mathbf{a}_{\alpha 1}(\theta_1) & \mathbf{a}_{\beta 1}(\theta_1) & \mathbf{a}_{\rho 1}(\theta_1) & 0 & 0 & 0 \\ \vdots & \vdots & \vdots & \vdots & \vdots & \vdots \\ \mathbf{a}_{\alpha 1}(\theta_m) & \mathbf{a}_{\beta 1}(\theta_m) & \mathbf{a}_{\rho 1}(\theta_m) & 0 & 0 & 0 \\ \mathbf{a}_{\alpha 2}(\theta_1) & \mathbf{a}_{\beta 2}(\theta_1) & \mathbf{a}_{\rho 2}(\theta_1) & \mathbf{a}_{\alpha 2}(\theta_1) & \mathbf{a}_{\beta 2}(\theta_1) & \mathbf{a}_{\rho 2}(\theta_1) \\ \vdots & \vdots & \vdots & \vdots & \vdots & \vdots \\ \mathbf{a}_{\alpha 2}(\theta_n) & \mathbf{a}_{\beta 2}(\theta_n) & \mathbf{a}_{\rho 2}(\theta_n) & \mathbf{a}_{\alpha 2}(\theta_n) & \mathbf{a}_{\beta 2}(\theta_n) & \mathbf{a}_{\rho 2}(\theta_n) \\ 0 & \mathbf{b}_{\beta 1}(\theta_1) & \mathbf{b}_{\rho 1}(\theta_1) & 0 & 0 & 0 \\ \vdots & \vdots & \vdots & \vdots & \vdots & \vdots \\ 0 & \mathbf{b}_{\beta 1}(\theta_p) & \mathbf{b}_{\rho 1}(\theta_p) & 0 & 0 & 0 \\ 0 & \mathbf{b}_{\beta 2}(\theta_1) & \mathbf{b}_{\rho 2}(\theta_1) & 0 & \mathbf{b}_{\beta 2}(\theta_1) & \mathbf{b}_{\rho 2}(\theta_1) \\ \vdots & \vdots & \vdots & \vdots & \vdots & \vdots \\ 0 & \mathbf{b}_{\beta 2}(\theta_q) & \mathbf{b}_{\rho 2}(\theta_q) & 0 & \mathbf{b}_{\beta 2}(\theta_q) & \mathbf{b}_{\rho 2}(\theta_q) \end{bmatrix}, \tag{6-20}$$

where the baseline P-S wave data is assumed to be an angle gather with p different incident angles.

Since Equation (6.15) has a linear form, the model parameters **m** can be solved in a least-square fashion (e.g., Menke, 1984; Tarantola, 1987). However, as I discussed in Chapter 4, the simple least-square method does not take into account individual variance and correlation of data noise and model parameters. The Bayesian inversion technique has advantages of handling the data noise, together with any available additional information, with a corresponding degree of confidence. Thus, I use the Bayesian inversion technique for finding the solution.

As I previously discussed, Buland and Ouair (2006) also used the Bayesian inversion technique to perform time-lapse acoustic impedance inversion. However, they used only the difference of time-lapse seismic data to obtain posterior distribution of the acoustic impedance change between the two surveys. In contrast, my method uses both the baseline and repeat data, instead of using only the difference, and simultaneously obtains the elastic properties at the baseline survey and the changes between the two surveys along with the associated uncertainties. It is a significant advantage to obtain the elastic properties at the baseline survey, which are consistent with both the survey data. The estimation is more robust to incoherent noise than that of the inversion only based on the baseline data. Furthermore, Buland and Ouair (2006) inherently assumed that the two surveys have the same parameters with each other in order to obtain the amplitude difference between them. However, it is not unusual that repeat data has a different frequency band from baseline data. My method allows us to use individual parameters. These points mainly differ from the previous study.

6.3 Synthetic Test

The developed method is tested with synthetic data. I use well A (Figure 3.19) to make the earth model.

6.3.1 Earth Model

The temperature observation data are not available in well A. Thus, I synthesize the temperature profile along with pore pressure and saturation. Figure 6.1 shows them; the blue and red curves represent the baseline and repeat surveys, respectively. The temperature profiles are drawn based on actual observation data in the neighbor wells, such as Figure 3.28. The pore pressure and saturation profiles are determined by the criteria that I described in Chapter 3. The interval from about 290 to 297 m corresponds to the core of the developed steam chamber, where heavy oil is largely replaced with the injected steam and the temperature is elevated over 200 °C.

Next, I use the established rock physics model to predict the velocities at the surface seismic frequency (100 Hz). Figure 6.2 shows the estimated P- and S-wave velocities along with the density in depth domain. The P-wave velocity and density show large decrease in the steam chamber. The S-wave velocity also shows substantial decrease, but the amount is smaller than the P-wave velocity. These changes are consistent with what I observed in Chapter 3 (see Figures 3.34 and 3.35).

The vertical mis-alignment between the two surveys should be corrected (see in Chapter 5.4). I regard the two-way traveltime of the P-P baseline data as a reference. Then, I map the other data onto the reference domain. Figure 6.3 shows the corrected data. It can be

observed that the repeat data are aligned with the baseline data (reference). Note that the time sampling is set to be 1 ms.

6.3.2 Prior Mean Model

The analysis time window mainly consists of three layers. The first layer is the overburden, in which shale is dominant. The second layer corresponds to the heavy-oil reservoir, in which elastic properties change due to the production. The last layer is well-consolidated carbonate rocks. The model parameters of each layer are defined individually (Figure 6.4). With the first and second layers, the baseline prior mean models ($\ln\alpha_1$, $\ln\beta_1$, and $\ln\rho_1$) are obtained by applying a low-passed filter of 7-12 Hz to the corresponding earth model. Also, the prior mean models of the elastic property changes ($\Delta\ln\alpha$, $\Delta\ln\beta$, and $\Delta\ln\rho$) in the second layer are obtained by applying the low-passed filter of 40-45 Hz to the corresponding earth models. The baseline prior mean models in the third layer are assumed to be constant; 8.61, 7.99, and 7.85 for $\ln\alpha_1$, $\ln\beta_1$, and $\ln\rho_1$, respectively. The first and third layers are assumed to have no change between the two surveys ($\Delta\ln\alpha = 0$, $\Delta\ln\beta = 0$, and $\Delta\ln\rho = 0$).

Differences between the earth model and the prior mean model are the model parameters to be solved in the inversion. Figure 6.5 and 6.6 show histograms of the model parameters and crossplots among them, respectively. It is suggested that the model parameters of the first layer are reasonably approximated by the Gaussian. In the second layer, although the amount of the measured data is not enough for the statistical analysis, the model parameters, except $\ln\rho$ and $\Delta\ln\rho$, seem to follow the Gaussian. Standard

deviation and correlation coefficient of the model parameters are determined by taking into account lateral heterogeneities (Table 6.1 and 6.2). These values are used to make the covariance matrix of the model parameters (Figure 6.7). Note that correlations among the model parameters, except the combinations which are shown in Table 6.2, are set to be zero.

Table 6.1 Standard deviation of the model parameters.

	1st layer			2nd layer						3rd layer		
Parameter	$\ln \alpha_1$ (m/s)	$\ln \beta_1$ (m/s)	$\ln \rho_1$ (kg/m^3)	$\ln \alpha_1$ (m/s)	$\ln \beta_1$ (m/s)	$\ln \rho_1$ (kg/m^3)	$\Delta \ln \alpha$ (m/s)	$\Delta \ln \beta$ (m/s)	$\Delta \ln \rho$ (kg/m^3)	$\ln \alpha_1$ (m/s)	$\ln \beta_1$ (m/s)	$\ln \rho_1$ (kg/m^3)
STD	0.045	0.185	0.037	0.045	0.129	0.048	0.099	0.031	0.034	0.099	0.031	0.034

Table 6.2 Correlation coefficient among the model parameters.

	1st layer			2nd layer						3rd layer		
Parameters	$\ln \alpha_1$ $\ln \beta_1$	$\ln \alpha_1$ $\ln \rho 1$	$\ln \beta_1$ $\ln \rho_1$	$\ln \alpha_1$ $\ln \beta_1$	$\ln \alpha_1$ $\ln \rho_1$	$\ln \beta_1$ $\ln \rho_1$	$\Delta \ln \alpha$ $\Delta \ln \beta$	$\Delta \ln \alpha$ $\Delta \ln \rho$	$\Delta \ln \beta$ $\Delta \ln \rho$	$\ln \alpha_1$ $\ln \beta_1$	$\ln \alpha_1$ $\ln \rho_1$	$\ln \beta_1$ $\ln \rho_1$
Correlation Coefficient	0.67	0.28	-0.09	0.67	0.28	-0.09	0.25	0.50	0.00	0.00	0.00	0.00

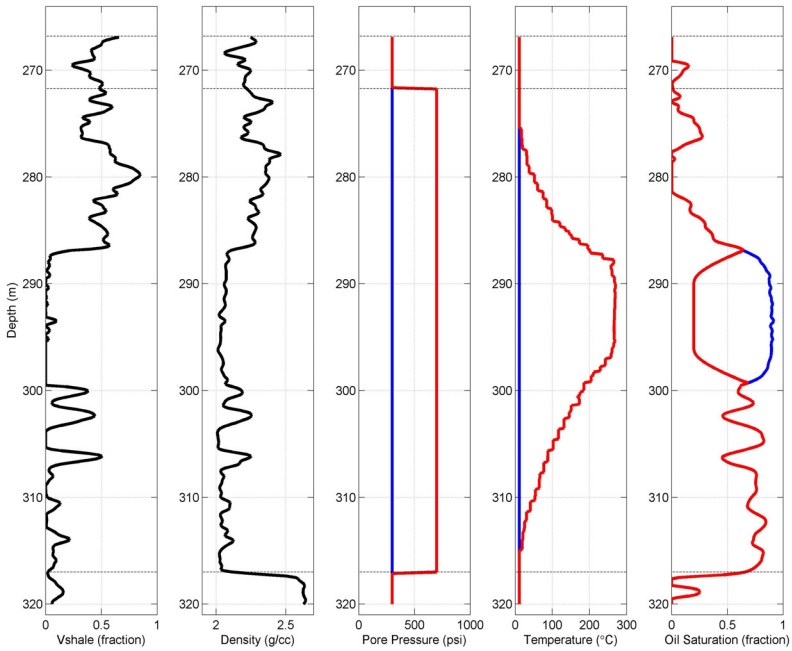

Figure 6.1. The synthesized pore pressure, temperature, and oil saturation. The blue and red curves represent the values before and after the steam injection, respectively.

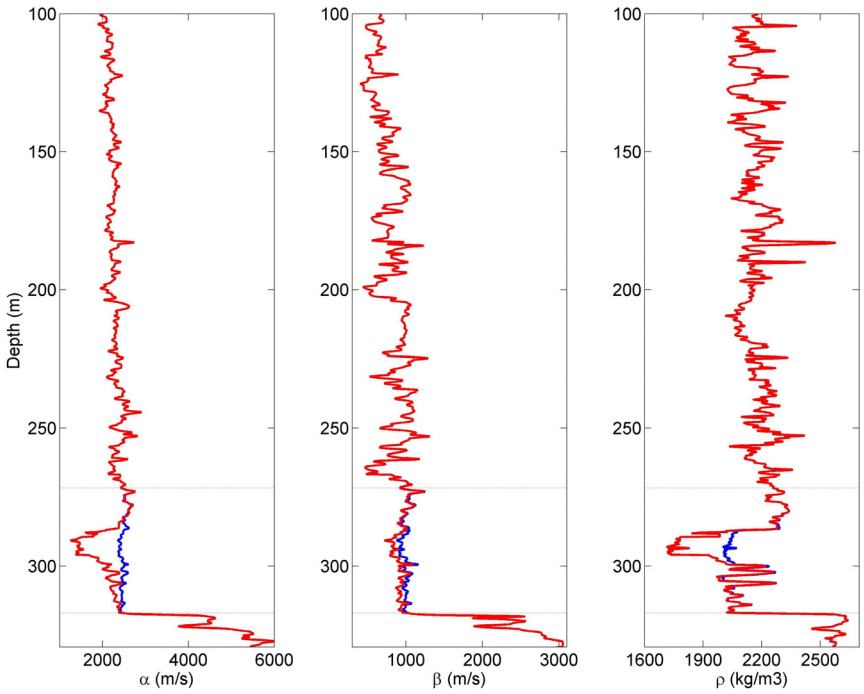

Figure 6.2. P- and S-wave velocities and density in depth domain. The blue and red curves represent the baseline and repeat data, respectively.

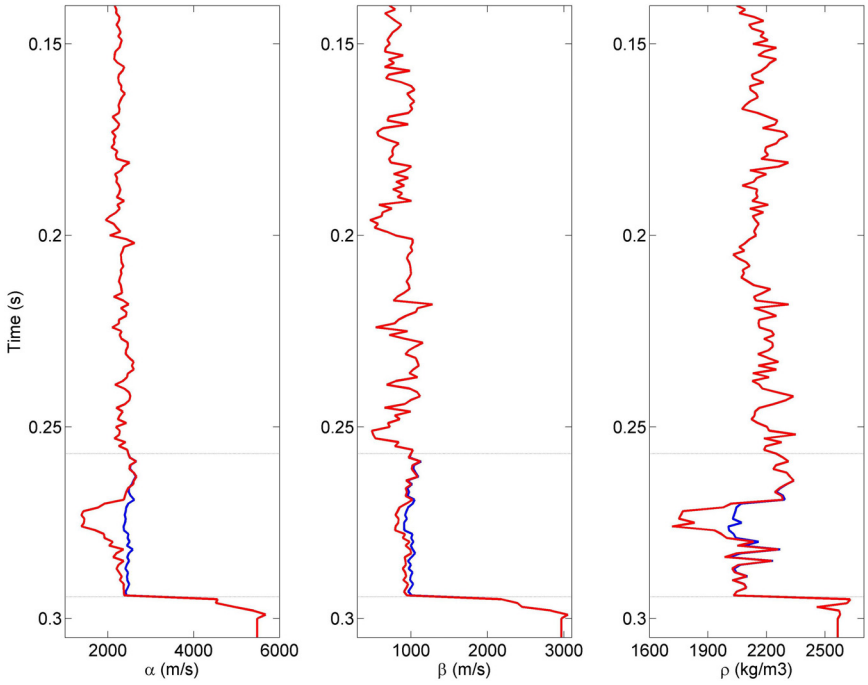

Figure 6.3. P- and S-wave velocities and density in the baseline tow-way time domain. The blue and red curves represent the baseline and repeat data, respectively.

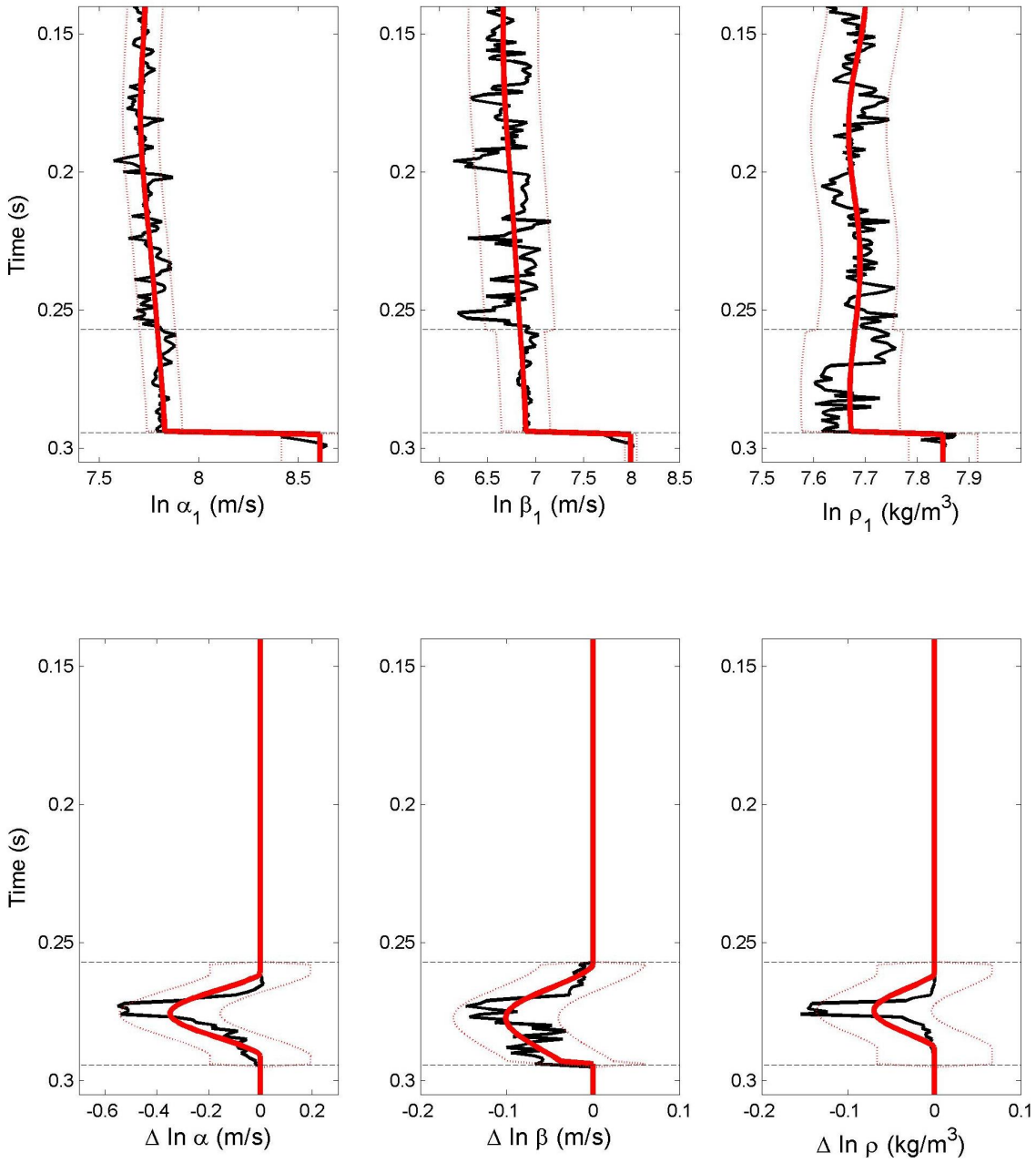

Figure 6.4. Prior mean models (red solid) and earth models (black solid). The red dot curves represent the prior prediction interval of 95 %.

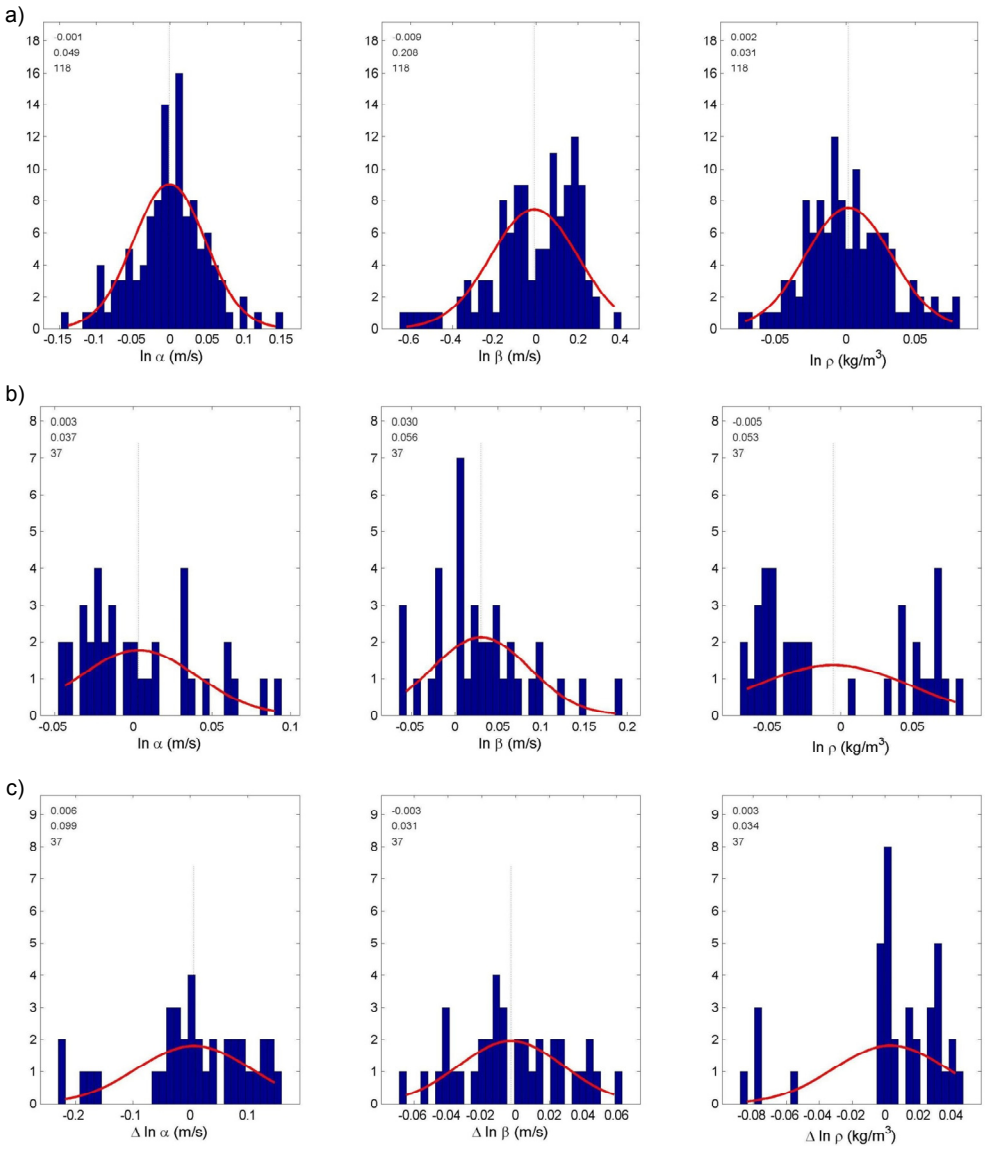

Figure 6.5. Histogram of the model parameter; (a) $\ln\alpha_1$, $\ln\beta_1$, and $\ln\rho_1$ of the first layer, (b) $\ln\alpha_1$, $\ln\beta_1$, and $\ln\rho_1$ of the second layer, and (c) $\Delta\ln\alpha$, $\Delta\ln\beta$, and $\Delta\ln\rho$ of the second layer. The first, second and third values at the upper left corner are the mean, standard deviation, and number of the data, respectively. The red curve is the fitted Gaussian distribution.

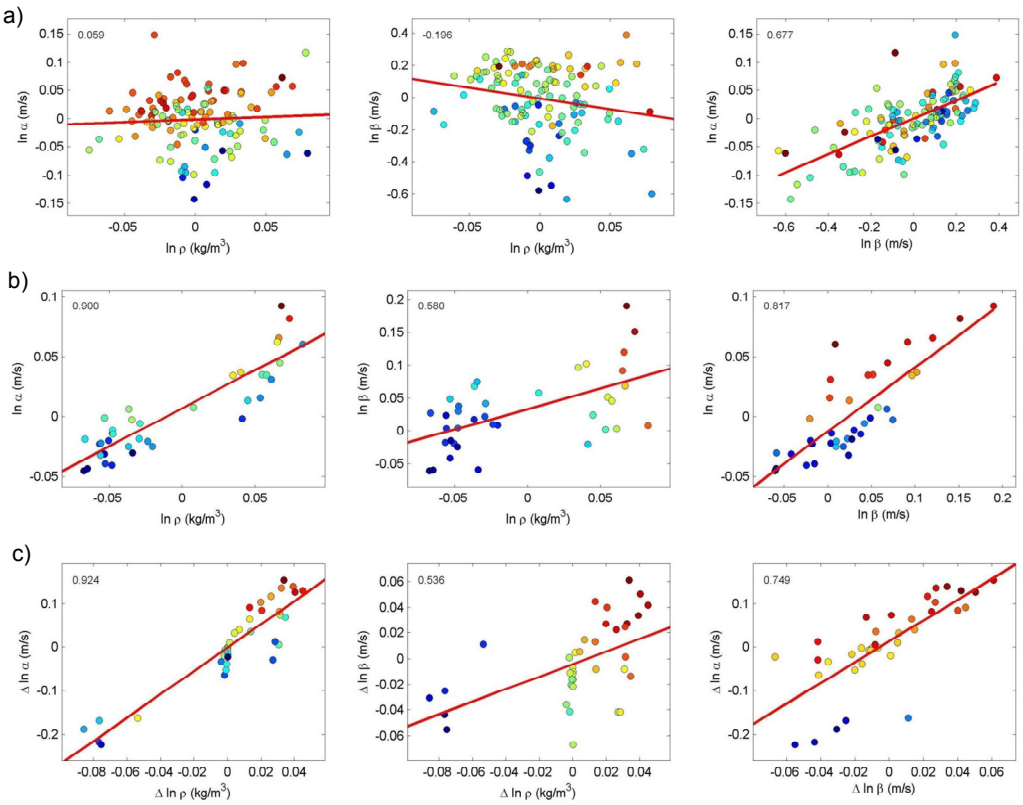

Figure 6.6. Crossplot (a) among $\ln\alpha_1$, $\ln\beta_1$, and $\ln\rho_1$ of the first layer, (b) among $\ln\alpha_1$, $\ln\beta_1$, and $\ln\rho_1$ of the second layer, and (c) among $\Delta\ln\alpha$, $\Delta\ln\beta$, and $\Delta\ln\rho$ of the second layer. The value at the upper left is the correlation coefficient between them. The red line represents the fitting curve determined in the least-square fashion.

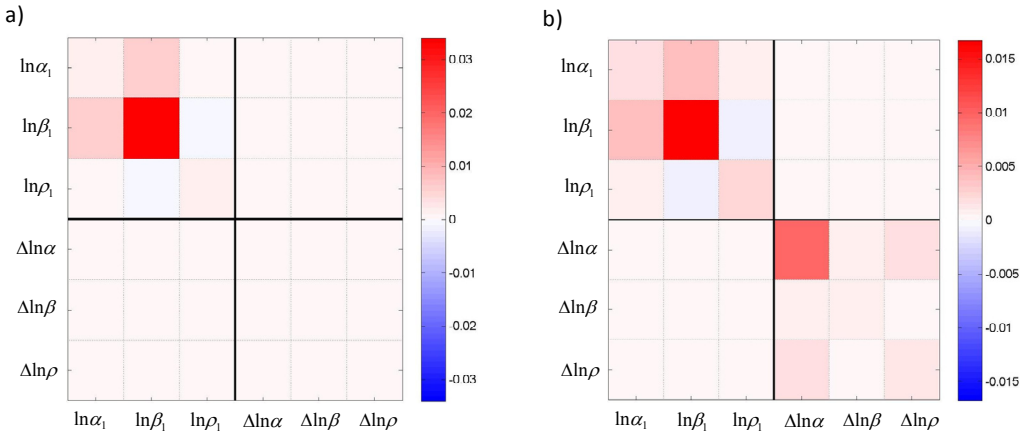

Figure 6.7. Covariance matrix of the model parameters for (a) the first layer and (b) second layer.

6.3.3 Seismic Forward Modeling

P-P and P-S angle gathers are synthesized by the convolution model along with the earth model, in which the reflection coefficients are calculated based on the Aki and Richards approximation, given by Equation (4.9) and (4.10). The required Vs/Vp is set to be a constant value of 0.372. The maximum incident angle and the sampling interval are set to be 50 degrees and 5 degrees. I use the Ricker wavelet and the dominant frequencies are assumed to be as:

P-P wave of the baseline data : 75 Hz

P-P wave of the repeat data : 100 Hz

P-S wave of the baseline data : 30 Hz

P-S wave of the repeat data : 45 Hz

Figure 6.8 shows the synthesized noise-free angle gathers. One can observe differences between the baseline and repeat data. In the P-P waves, significant difference is observed from around 260 ms to the end. The difference is associated with the properties changes due to the steam injection. Similarly, in the P-S wave, substantial differences are observed at the same interval, although the magnitude of the difference is smaller than that of the P-P wave. In addition, there are some differences in the overburden, which are associated with differences of the used wavelet.

In the test, I consider the two kinds of random noise in the same way as Chapter 4. I use the same standard deviation to obtain S/N ratio of 50, 5, 2, and 1 as:

P-P waves : $\sigma_1 = \sigma_2 = 0.00065,\ 0.0053,\ 0.015, \text{and}\ 0.028,$

P-S waves : $\sigma_1 = \sigma_2 = 0.00091,\ 0.0096,\ 0.024, \text{and}\ 0.048.$

The noise-contaminated data is obtained by adding random noise to the noise-free synthetic data.

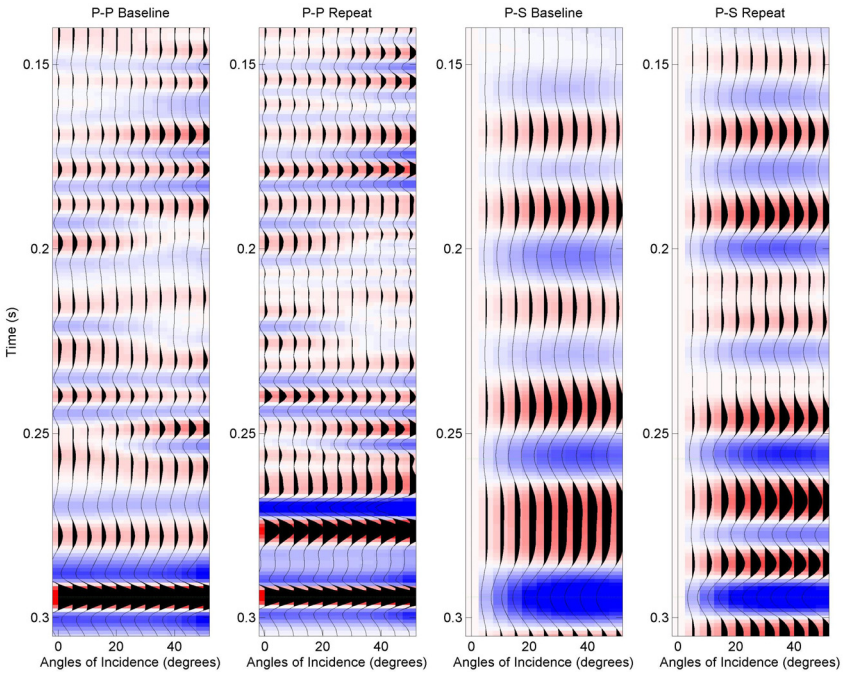

Figure 6.8. Noise-free synthetic angle gathers.

6.3.4 Inversion Result

Several combinations of P-P and P-S wave are possible. In this study, the following three cases are considered:

1. Baseline P-P wave / Repeat P-P wave (*PP / PP*)
2. Baseline P-P wave / Repeat P-P and P-S waves (*PP / PP + PS*)
3. Baseline P-P and P-S waves / Repeat P-P and P-S waves (*PP + PS / PP + PS*)

The *PP / PP + PS* case is mainly presented, because it corresponds to available seismic data in the Hangingstone oilfield. Figures 6.9, 6.10, 6.11, and 6.12 show the inversion results of the *PP / PP + PS* case with the S/N of 50, 5, 2, and 1, respectively. When the seismic data quality is close to the noise-free (S/N of 50), all model parameters are very well inverted. As the seismic data quality degrades, the correlation between the inversion result and the corresponding earth model becomes poorer. The deterioration is the most significant in the S-wave velocity change ($\Delta\beta$). At the S/N of 1, contribution from the seismic data to the $\Delta\beta$ determination is very subtle. In contrast, other model parameters, including $\Delta\alpha$ and $\Delta\rho$, are still reasonably inverted even at the poorest data quality (S/N of 1).

Figure 6.13 shows the summary of the synthetic test for all the cases. In the β_1 estimation, the *PP + PS / PP + PS* case gives us the best result among them. Furthermore, as the seismic data quality degrades, the difference between the *PP + PS / PP + PS* and the *PP / PP* cases becomes more significant. The result of the *PP / PP + PS* case is close to that of the *PP + PS / PP + PS* case, suggesting that adding the P-S wave at the repeat survey has an equivalent benefit in the β_1 estimation to that with the complete multicomponent time-lapse data (*PP + PS / PP + PS*). The α_1 estimation shows the similar trend as the β_1 estimation. As the data quality degrades, the *PP / PP + PS* and the *PP + PS / PP + PS* cases give us a better result than the *PP / PP* case. The better estimation is mainly due to the correlation between α_1 and β_1, which was set as a prior information. In the ρ_1 estimation, there is no substantial difference among them.

Moreover, in the $\Delta\alpha$ and $\Delta\rho$ estimations, there is a trend that contribution from the seismic data to the determination gradually decrease as the data quality degrades. The differences among the cases are virtually invisible. The $\Delta\beta$ estimation has larger error compared to that of $\Delta\alpha$ and $\Delta\rho$.

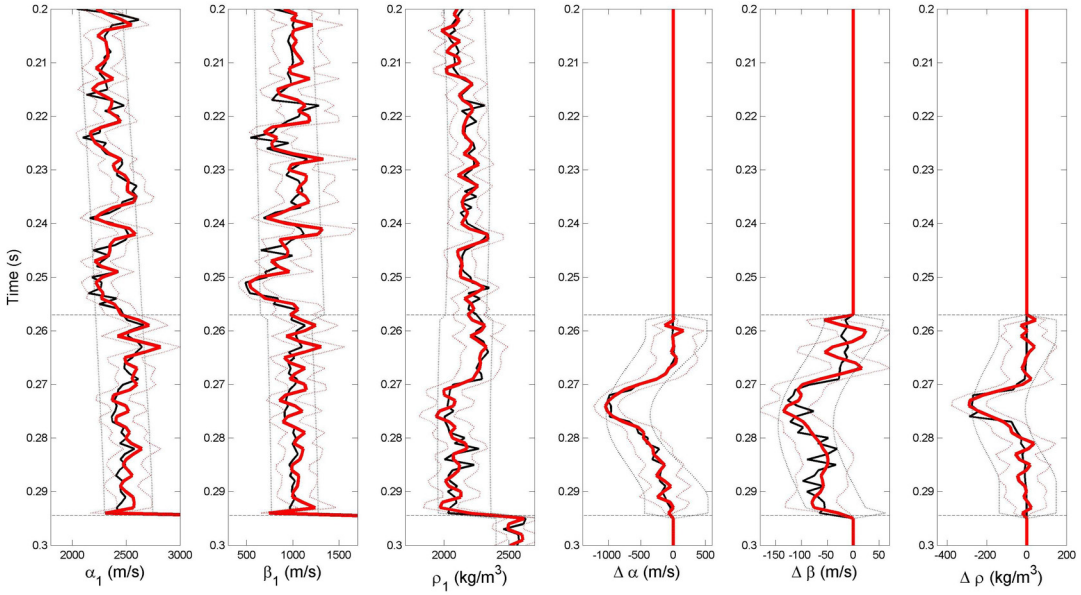

Figure 6.9. Inversion result at S/N ratio of 50.

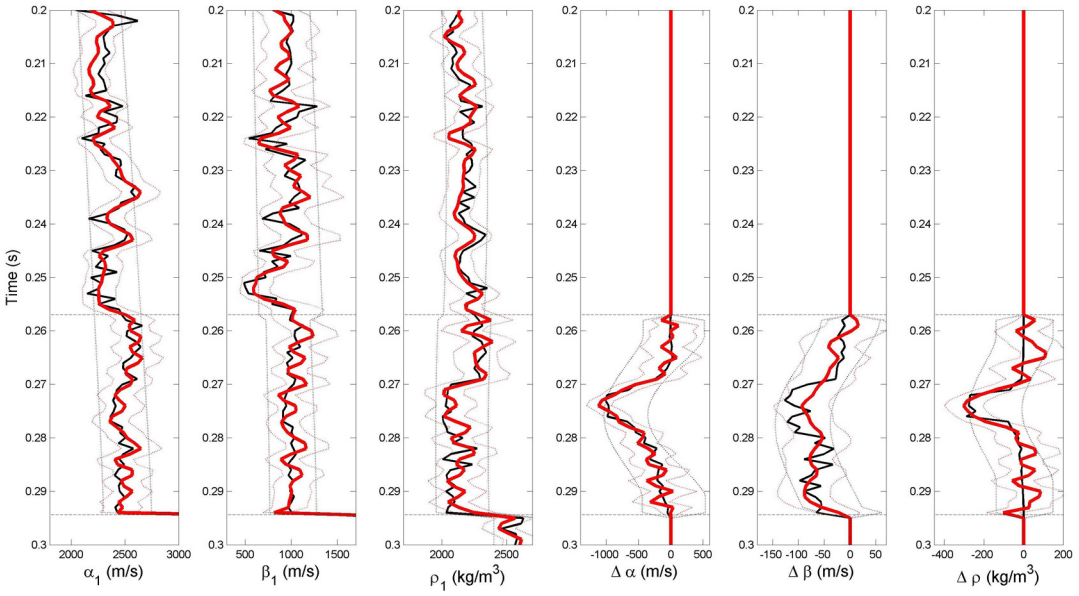

Figure 6.10. Inversion result at S/N ratio of 5.

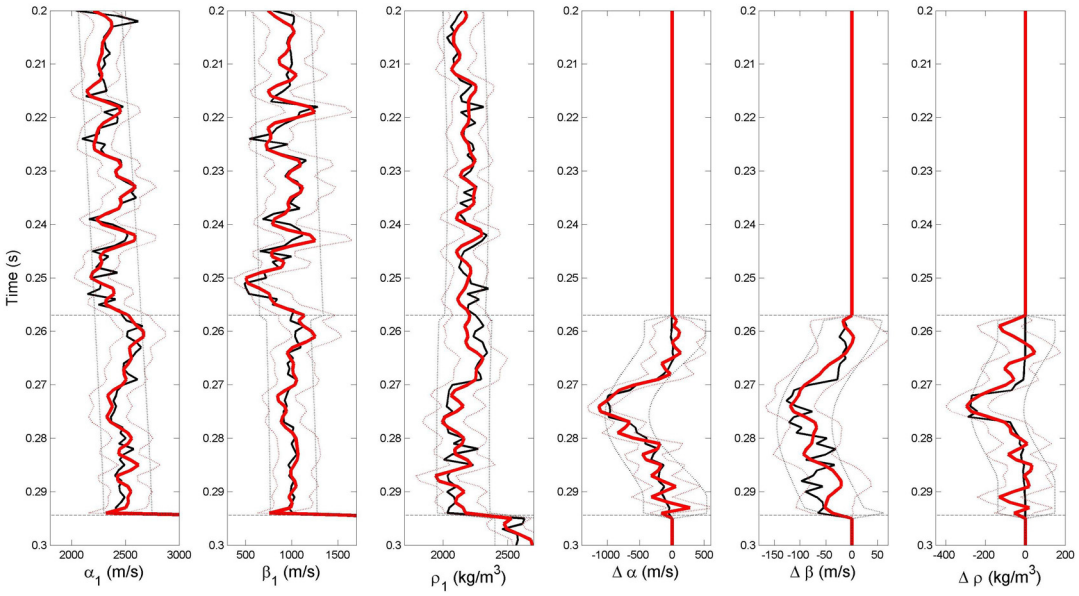

Figure 6.11. Inversion result at S/N ratio of 2.

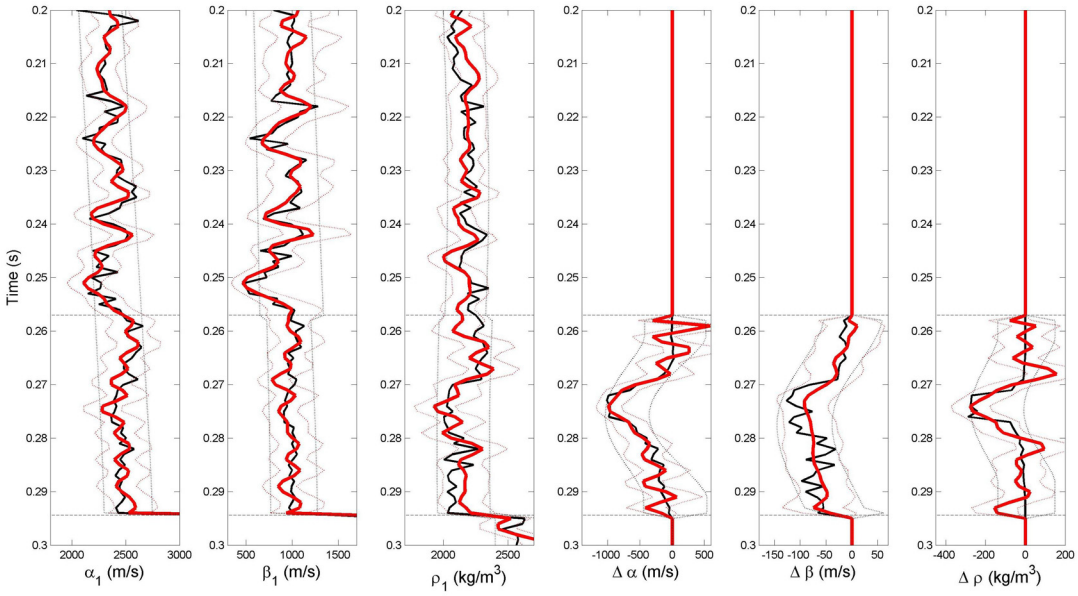

Figure 6.12. Inversion result at S/N ratio of 1.

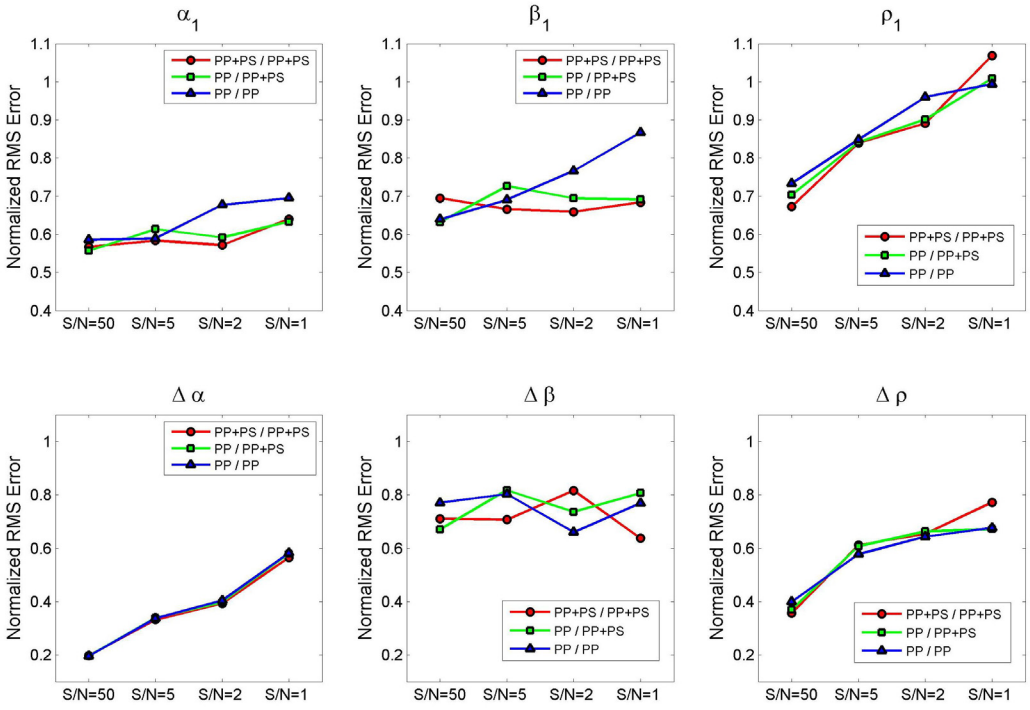

Figure 6.13. Normalized RMS error.

6.4 Summary

I have developed the time-lapse AVO inversion method based on the Bayesian theorem, in which all available seismic data can be used to obtain elastic properties, as well as the changes between baseline and repeat surveys. The inverted elastic properties and the changes are consistent with the seismic data and prior information. Furthermore, the method can be applied to incomplete time-lapse multicomponent seismic data, like the Hangingstone oilfield, in which PP data at baseline and PP & PS at monitor surveys are available.

I tested the method with the synthetic data. Major findings from the synthetic test are as follows:

1) All initial elastic properties (α_1, β_1, and ρ_1) and the P-wave velocity and density changes ($\Delta\alpha$ and $\Delta\rho$) are reasonably estimated. In contrast, there is only subtle contribution from the seismic data to estimation of the S-wave velocity change ($\Delta\beta$).
2) Compared to the normal P-P wave time-lapse seismic data, adding P-S wave data in the repeat survey yields better estimation in the S-wave velocity, as well as the P-wave velocity via the given correlation.

In the next chapter, I will apply this method to the Hangingstone oilfield.

Chapter 7 – Time-Lapse AVO Inversion

- Implementation with Field Data

7.1 Introduction

In the previous chapter, a time-lapse AVO inversion method based on the Bayesian inversion technique was developed. The method uses all available surface seismic data to simultaneously obtain the initial elastic properties (α_1, β_1, and ρ_1) and the changes ($\Delta\alpha$, $\Delta\beta$, and $\Delta\rho$) between the two surveys, along with the uncertainties. The synthetic tests suggested that the method is feasible for use in the Hangingstone oilfield. In this chapter, I apply the method to the field data. As discussed in Chapter 5, the data conditioning is one of the key elements in the AVO analysis. I carefully conducted the data processing. Furthermore, for the time-lapse AVO analysis, a reflection event of different surveys has to be aligned at the same vertical position. Thus, the P-P wave in the repeat survey is required to be mapped onto the corresponding baseline data. In addition, the P-S wave used in the inversion has to be correlated with the reference data. Also, it is important to build a proper prior mean model of the initial elastic properties and the change. In this chapter, these issues will be discussed in the implementation of the time-lapse AVO inversion.

7.2 Study Area

A small study area is selected for the implementation of the time-lapse AVO inversion (Figure 7.1). Although eight SAGD well pairs, injecting hot steam into the reservoir,

penetrate through the study area, they have different starting times of the steam injection (e.g., Tanaka et al., 2009; Table 7.1). Two SAGD well pairs, which are located in the middle of the study area, started the steam injection in February 2002, just after the baseline survey. Then, the steam injection was step-by-step extended to the southern and northern parts. The three SAGD well pairs in the northern part started the steam injection in August 2005, where the repeat survey was carried out only seven months after the steam injection commencement.

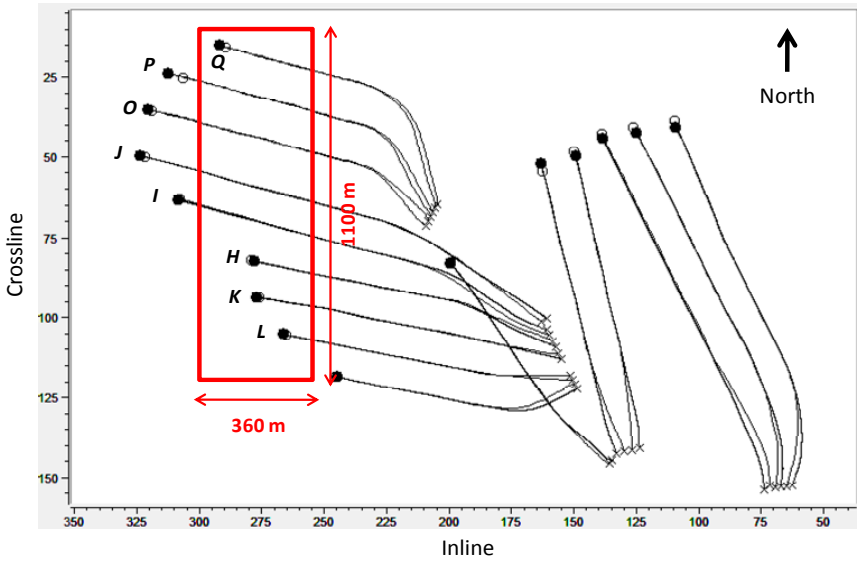

Figure 7.1. Study area (red rectangle) for the implementation of the time-lapse AVO inversion. The black solid lines represent the SAGD well paths.

There are two wells whose well logs are available for this study; wells B and C (see Figure 3.26 and 3.35). Well B is used for wavelet extraction, as well as construction of the prior mean model of the initial elastic properties, while well C is mainly used for a blind test of the inversion results. As discussed in Chapter 3, since direct measurement of the S-wave sonic log is not available in the wells, the S-wave velocity is predicted from

other well logs by using the established rock physics model. Furthermore, the P- and S-wave velocities and density at the repeat survey were predicted from the monitoring data of temperature. The predicted velocities and density are used in the inversion analysis.

Table 7.1. Steam injection start time for each well.

Well Name	Steam Injection Start
H, I	Feb. 2002
J, K	Aug. 2003
L	Jun. 2004
O, P, Q	Aug. 2005

7.3 Seismic Data Conditioning

After some parameters were optimized for each survey data, I followed the same data processing flow as Chapter 5. In this chapter, I present only the data before and after applying the data processing. Figure 7.2 and 7.3 shows the PSTM offset gathers and the processed angle gathers of the P-P wave in the baseline and repeat surveys, respectively. Furthermore, Figure 7.4 shows the PSTM offset gathers and the processed angle gathers of the P-S wave in the repeat survey. In the processed angle gathers of the three data, noise associated with Top Devonian, as well as random noise, has been suppressed and lateral continuities of reflection events have been improved. The P-P wave angle gathers from 5 to 50 degrees are used in the time-lapse AVO inversion. In contrast, the P-S wave angle gathers from 5 to 60 degrees are used.

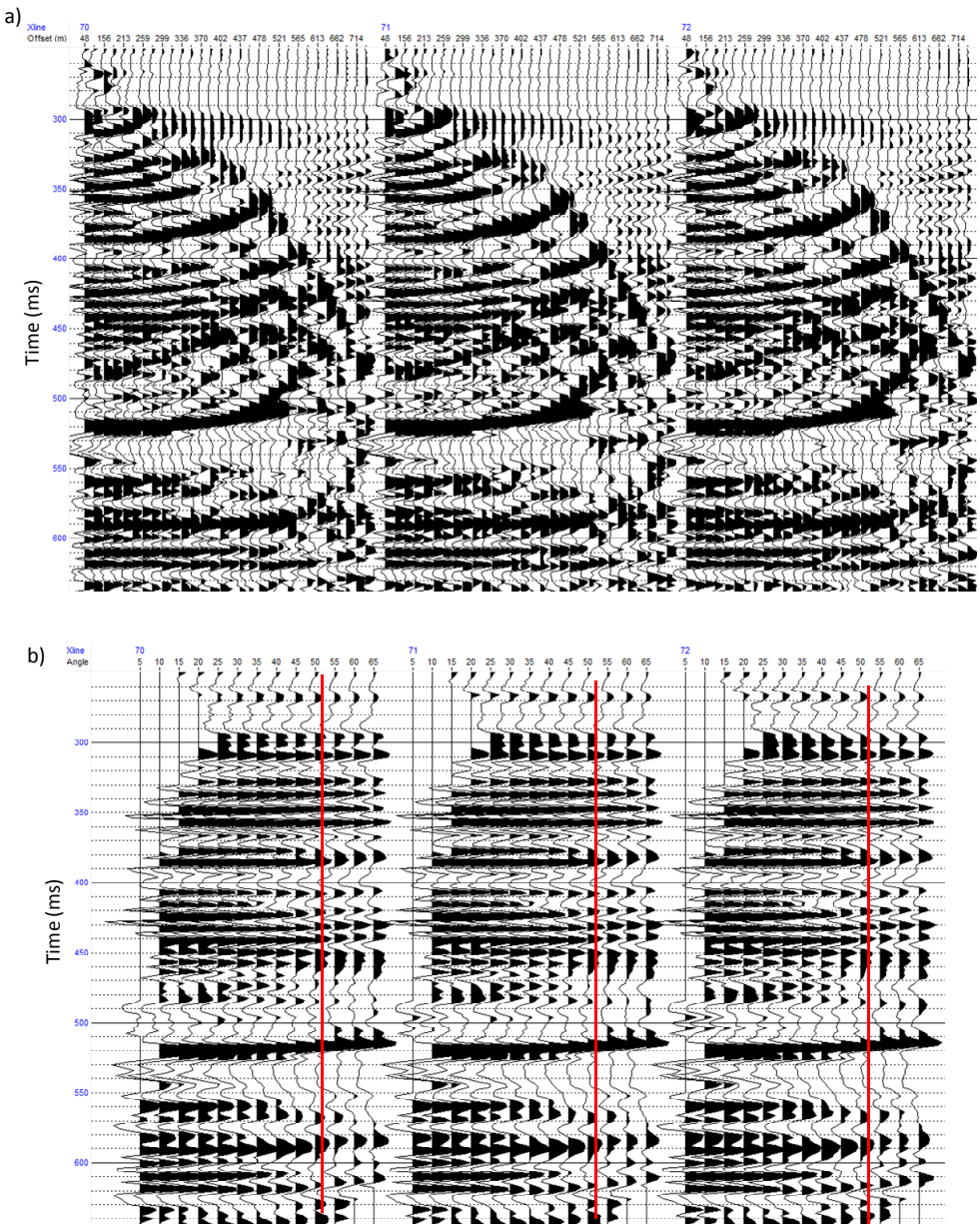

Figure 7.2. P-P wave PSTM CMP gathers in the baseline survey; (a) the offset and (b) processed angle gathers. The red curves represent the mute line.

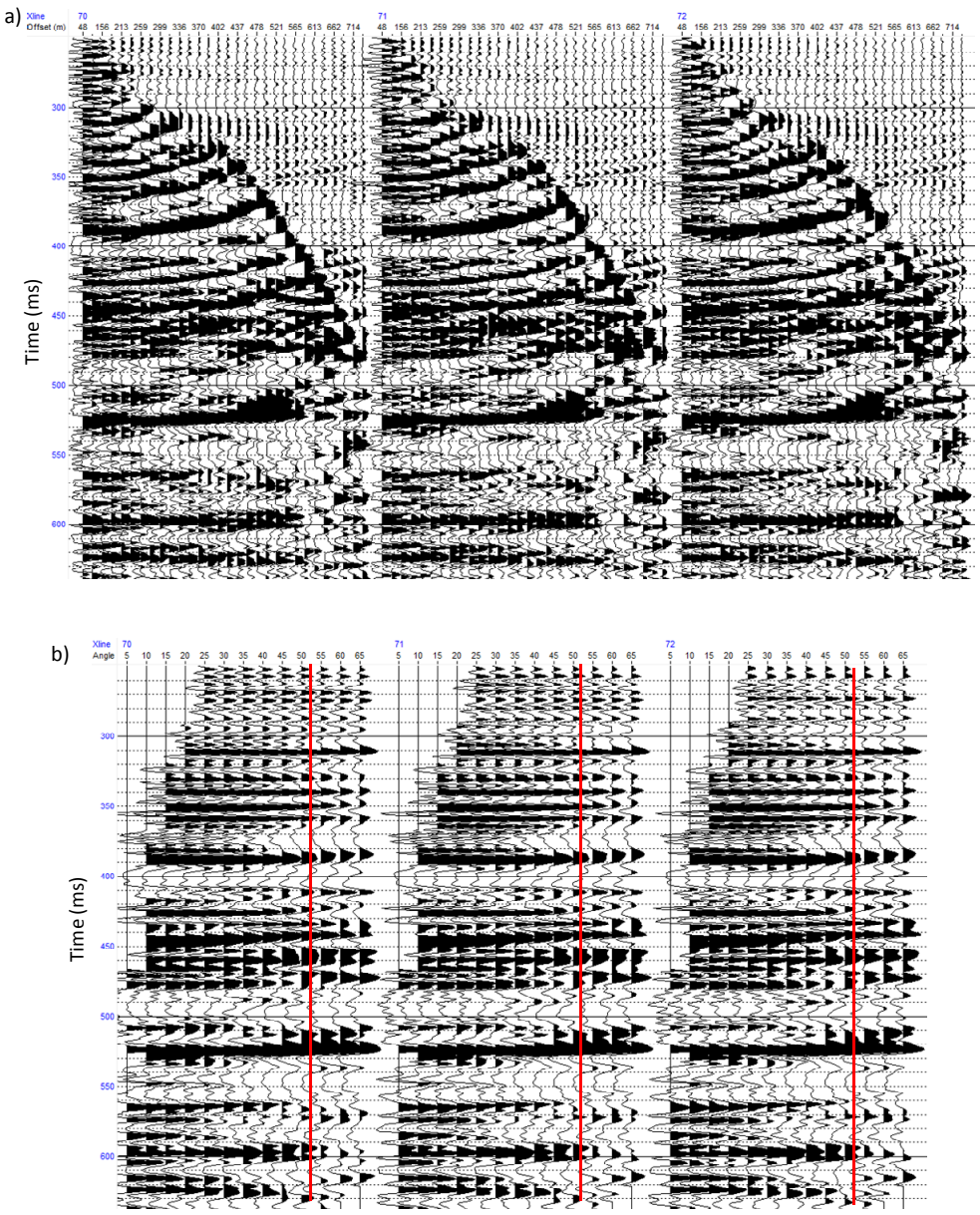

Figure 7.3. P-P wave PSTM CMP gathers in the repeat survey; (a) the offset and (b) processed angle gathers. The red curves represent the mute line.

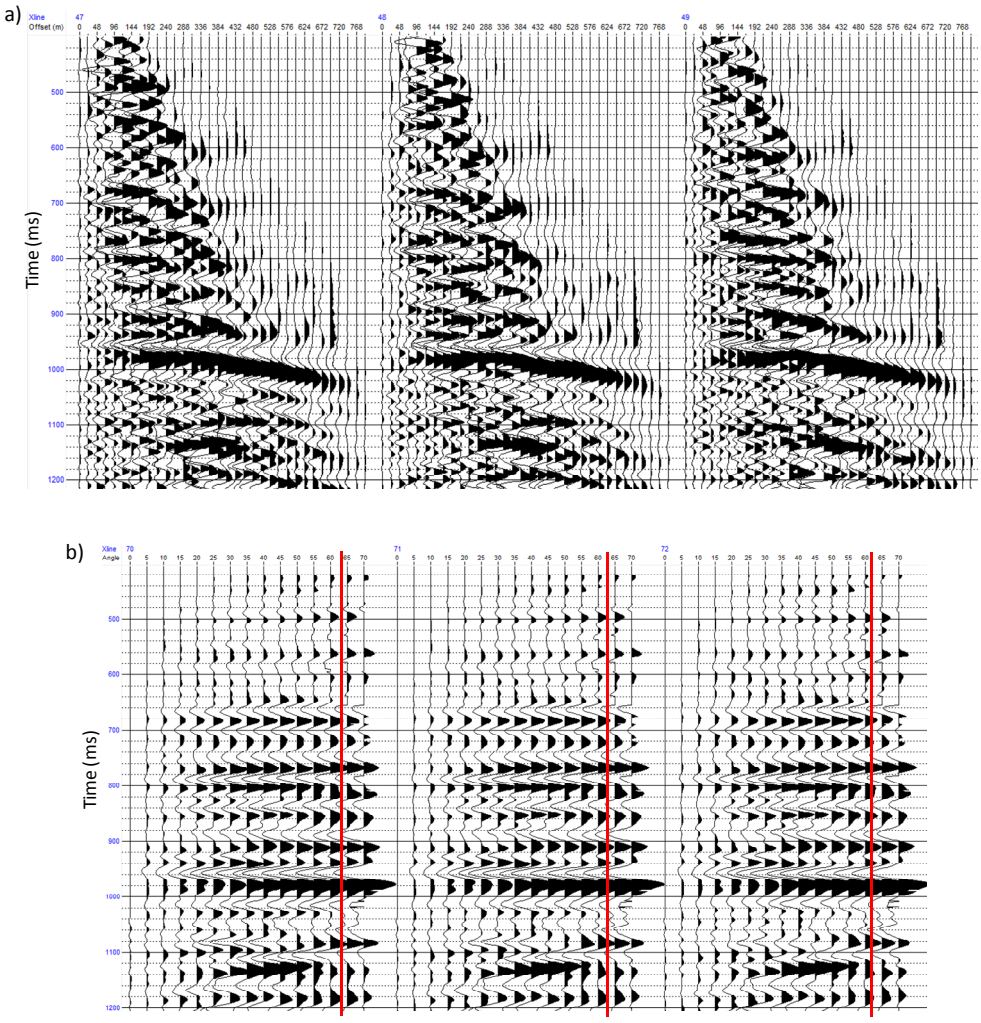

Figure 7.4. P-S wave PSTM CCP gathers in the repeat survey; (a) the offset and (b) processed angle gathers. The red curves represent the mute line.

7.4 Vertical Mis-alignment Correction

For the implementation of the linearized AVO inversion, a reflection event of different surveys has to be aligned at the same vertical time or depth position. The steam injection induces elastic property changes in the reservoir, leading to P-P reflection events from within and underneath the reservoir which have different travel times between the baseline and repeat surveys. Also, P-P and P-S waves naturally have different travel

times. Thus, we need to correct the vertical mis-alignment. In this study, I regard the baseline P-P wave data as a reference and map the repeat P-P and P-S data onto the reference. I assume the reflection events to be correctly positioned laterally in the migrated images so that the differences can be explained by vertical transformations only.

7.4.1 P-P Wave in the Repeat Survey

I first performed the alignment correction analysis by using the PSTM full-stacked data, instead of the angle gathers, to obtain the time-shift value at each bin. The time shift describes the change of coordinates necessary to map the repeat survey onto the baseline survey. Then, I use the time-shift volume to map the P-P wave angle gathers in the repeat survey onto the corresponding baseline data.

Figure 7.5 shows the PSTM full-stacked data in the baseline and repeat surveys. Although they are over all consistent with each other, the repeat data has higher frequency contents compared to the baseline data. Figure 7.6 shows the amplitude spectrums. The baseline data has maximum frequency of about 150 Hz. In contrast, the repeat data shows broader frequency band; the maximum frequency is up to 250 Hz.

To match the frequency band between the two surveys, I applied the global shaping filter to the repeat data in the same way as Nakayama et al. (2008). I use the Wiener-Levinson algorithm (Yilmaz, 2001) to design a local shaping filter at each bin. In the areas where the S/N is poor and there are direct influences associated with the steam injection, the correlation coefficient between the baseline and repeat data is low. To exclude these areas, I set the threshold of the correlation coefficient (0.70). Using only the traces which have a

higher correlation coefficient than the threshold, I determine the global shaping filter by averaging the local filters. Figure 7.7 shows the global shaping filter. Figure 7.8 shows the comparison between the baseline and repeat data after applying the global shaping filter. In the filtered repeat data, higher frequency contents than 170 Hz have been suppressed. The amplitude spectrum of the repeat data is virtually equivalent to the baseline data (Figure 7.9). It is obvious that the similarity of trace between the two surveys is significantly improved.

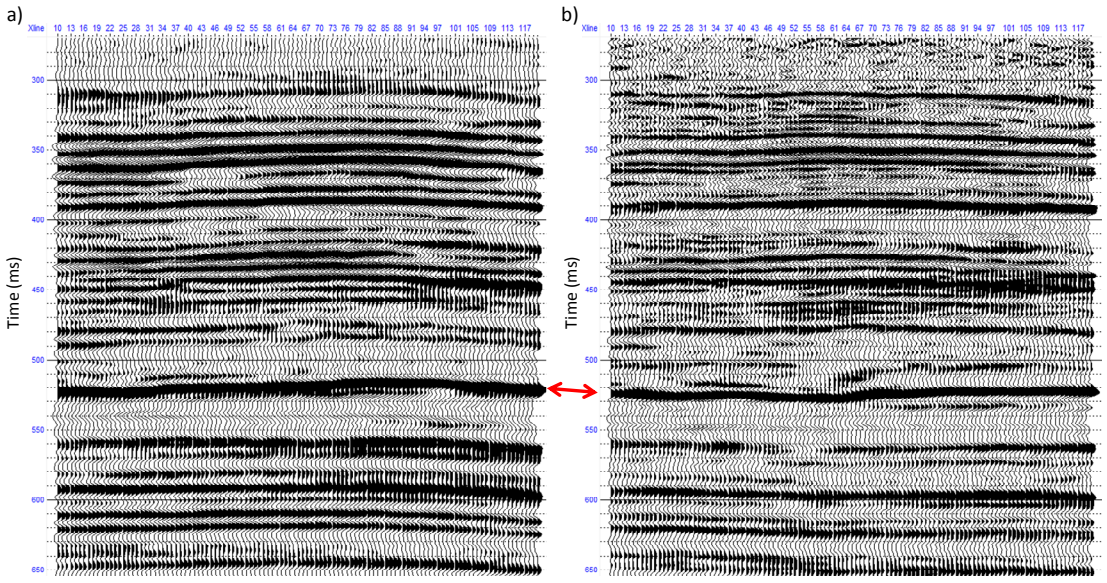

Figure 7.5. P-P full stack section; (a) the baseline and (b) repeat surveys. The red arrow represents the reflection event from Top Devonian interface.

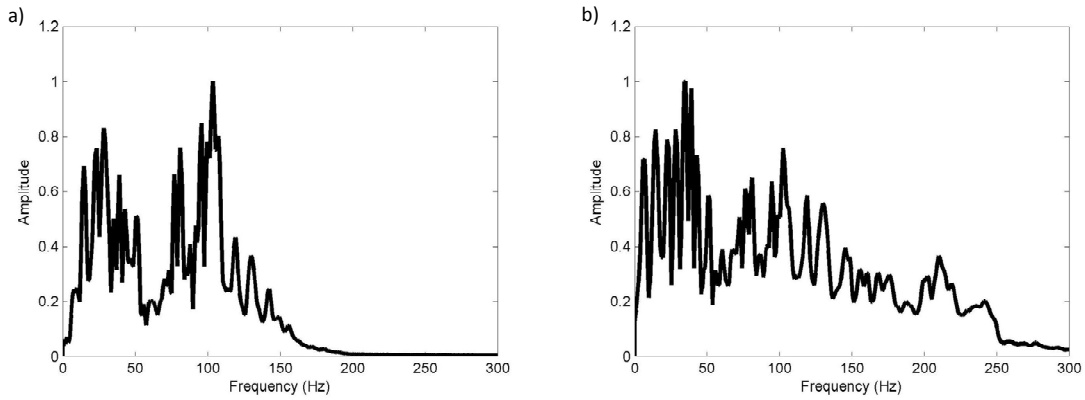

Figure 7.6. Amplitude spectrum; (a) the baseline and (b) repeat data.

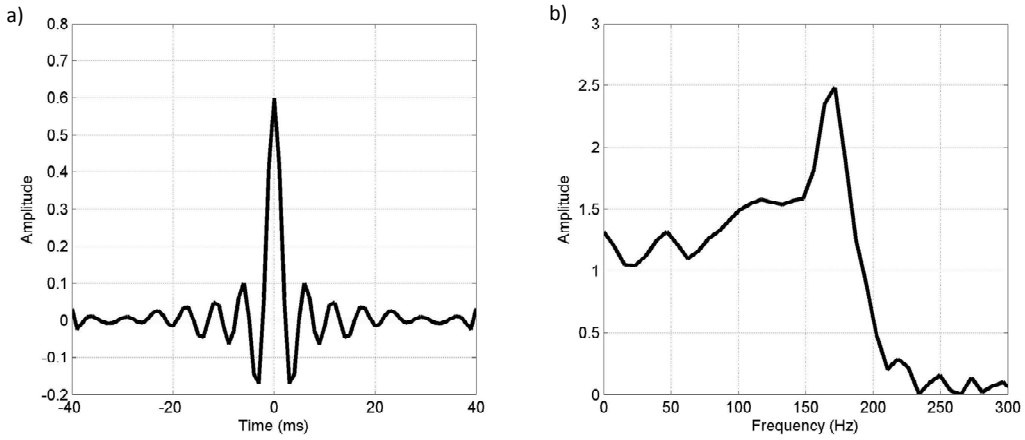

Figure 7.7. The global shaping filter; (a) time and (b) frequency domains.

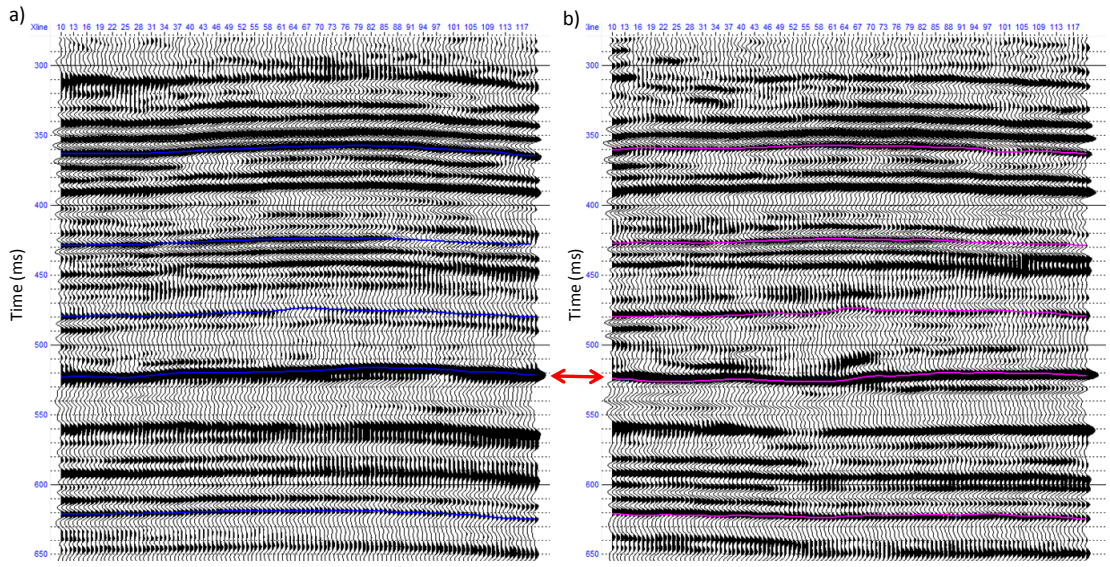

Figure 7.8. P-P full stack section after applying the shaping filter to the repeat data; (a) the baseline and (b) repeat surveys. The red arrow represents the reflection event from Top Devonian interface.

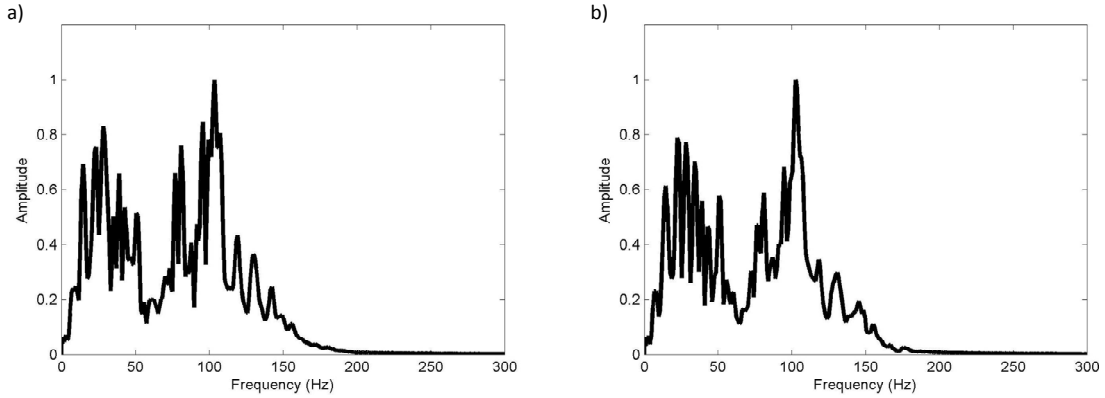

Figure 7.9. Amplitude spectrum after applying the shaping filter to the repeat data; (a) the baseline and (b) repeat data.

Next, I correct the mis-alignment associated with the steam injection. Some methods of the mis-alignment correction for time-lapse seismic analysis have been proposed (e.g., Eastwood, et al., 1998; Rickett and Lumley, 2001; Williamson, et al., 2007; Fomel and Jin, 2009; Hale, 2009). I used the warping technique based on a local cross-correlation. In

the process, I calculate local cross-correlations between the surveys and pick the maxima to obtain the cross-correlation coefficient and time-shift volumes. Figure 7.10 shows time section of the two volumes. In the time-shift section, large negative values are observed below around 500 ms, which are associated with the time-delay due to the steam injection. In contrast, in a shallower section than 500 ms, there is a patchy distribution of large time-shift values. Because the large time-shift of the patchy distribution corresponds to areas with low cross-correlation coefficients (Figure 7.10a), they are unreliable. Thus, I create a crossplot between the time-shift and correlation coefficient volumes (Figure 7.11) and manually make a polygon to remove the spurious data which have a large time-shift and low correlation coefficient. Figure 7.12a shows the time-shift volume after removing these data. Furthermore, I apply smoothing and interpolation to the volume and obtain a smoothed time-shift volume (Figure 7.12b). Figure 7.13 shows the time-shift volume superimposed with the repeat P-P wave amplitude data.

Figure 7.14 shows the baseline and repeat seismic sections after applying the time-shift. To make effects of the time-shift more visible, two sets of picked horizons are superimposed in the repeat section; one is horizons picked on the baseline data (blue horizons), and the other is horizons picked on the repeat data before applying the time-shift (magenta horizons). It can be observed that the time-shifted repeat data are consistent with the blue horizons, which means the time-shift correction was correctly performed. There are substantial differences between the blue and magenta Top Devonian horizons. Figure 7.15 shows the time differences. They are interpreted to be

caused by P-wave velocity decrease within the reservoir due to the SAGD production. The map is consistent with the previous study of Nakayama et al. (2008).

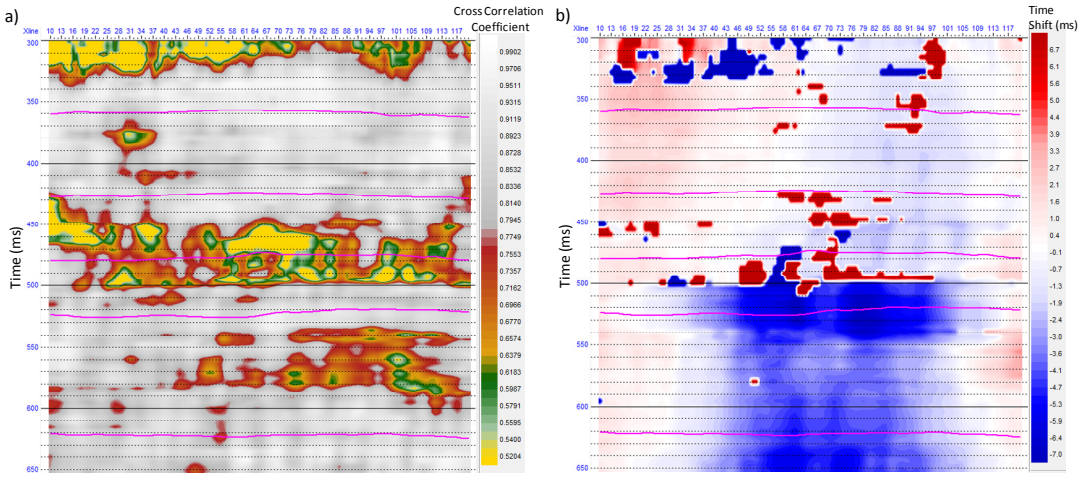

Figure 7.10. Local cross-correlation analysis; (a) the correlation coefficient and (b) time-shift sections.

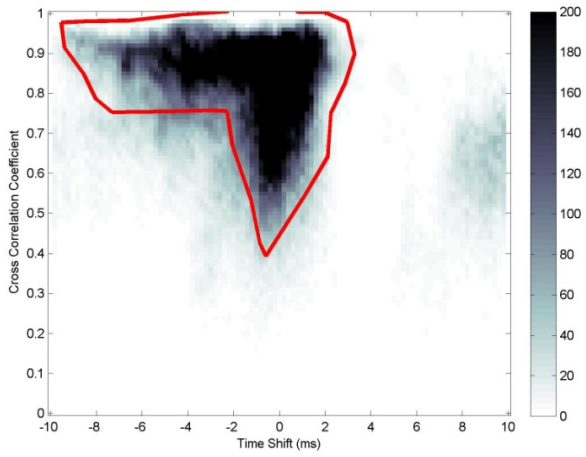

Figure 7.11. Cross plot between the time shift and correlation coefficient volumes. The color represent the data density.

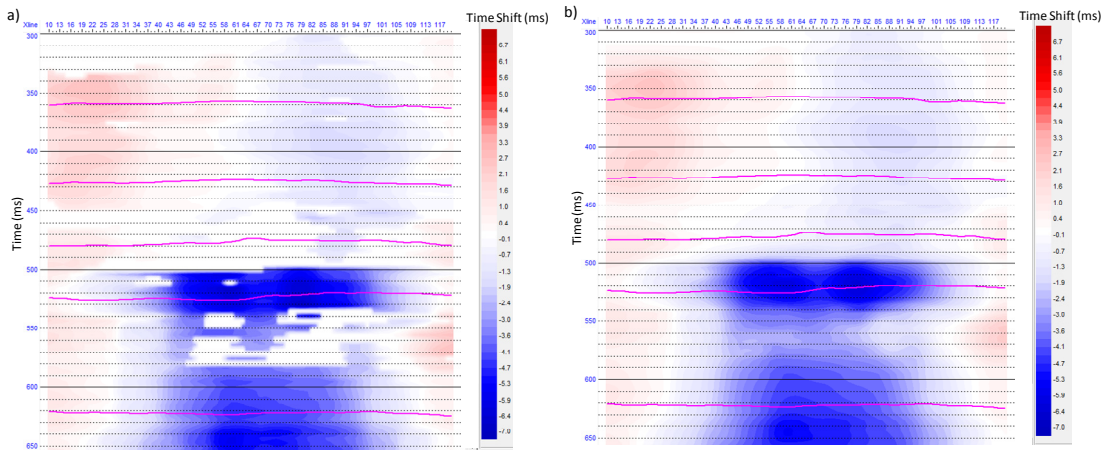

Figure 7.12. The time-shift sections; (a) after removing points with low correlation coefficient and large time-shift and (b) furthermore applying smoothing and interpolation.

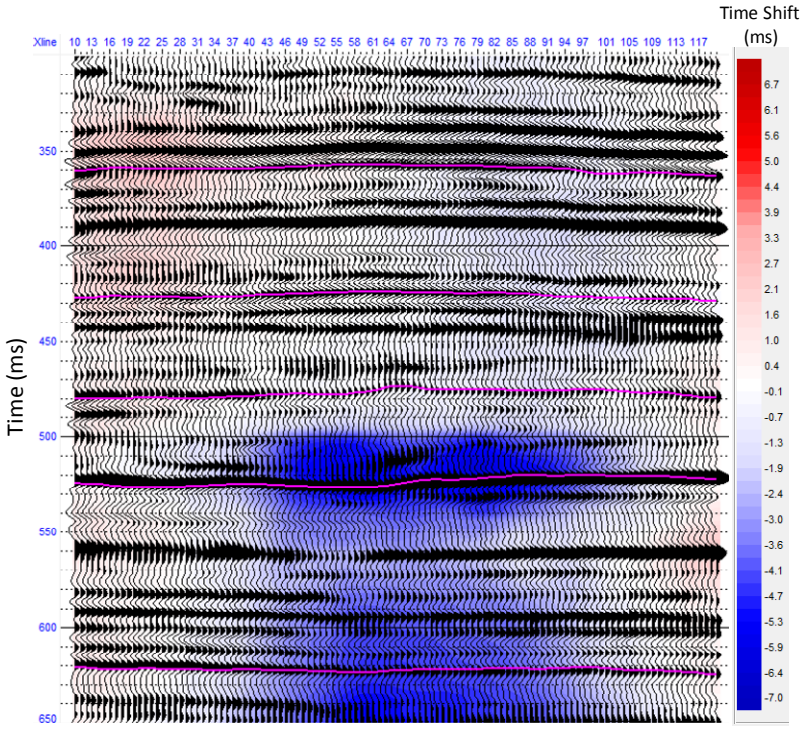

Figure 7.13. The final time-shift volume with the repeat P-P wave amplitude.

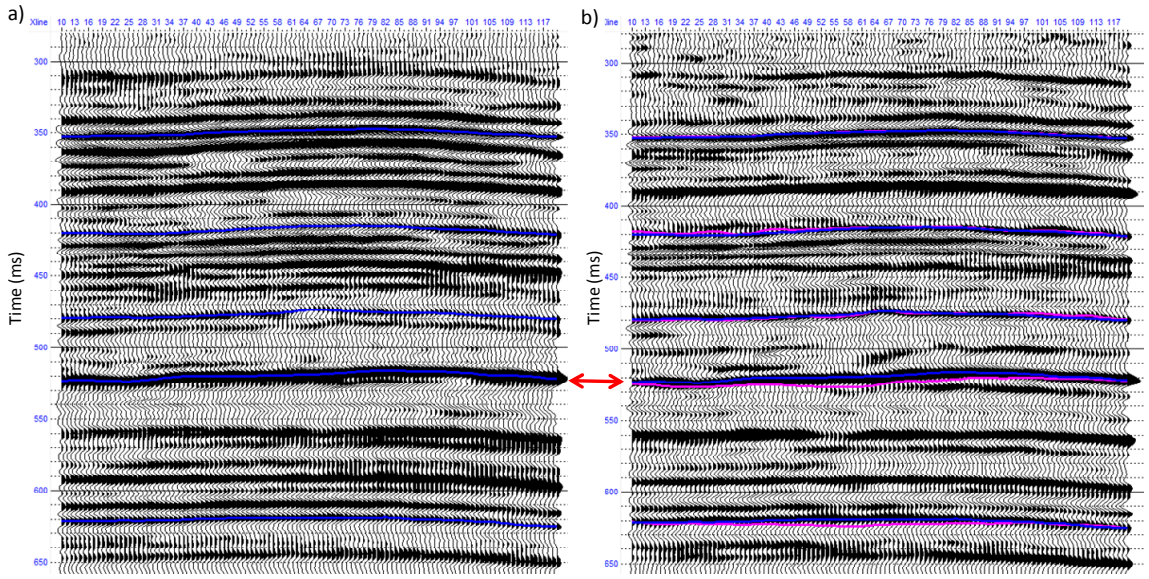

Figure 7.14. Time sections; (a) the baseline data and (b) repeat data applied with the time-shift.

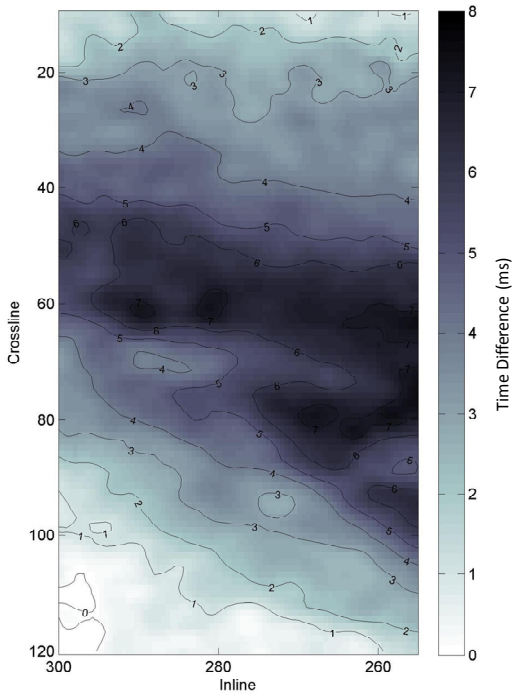

Figure 7.15. Time difference of Top Devonian between the baseline and repeat surveys.

7.5 P-S Wave in the Repeat Survey

The P-S wave is also required to be mapped onto the P-P baseline data. As discussed in Chapter 5, there is a significant difference of frequency band in the P-P and P-S waves. Thus, I use the horizon matching technique, instead of the warping technique, to correct the vertical mis-alignment. I chose the same five seismic horizons as Chapter 5. Figure 7.16 shows the P-P and P-S wave seismic sections before the horizon matching. The compression of the P-S time scale corresponds to constant Vp/Vs of 2.33. Note that the P-P wave data was applied with a low-passed filter (60 Hz) to match the frequency band with the P-S wave. Figure 7.17 shows the same sections but after the horizon matching. The P-S wave data is well correlated with the P-P wave data.

Thus, the P-P and P-S angle gathers in the repeat survey are ready to be mapped onto the P-P baseline data. Figure 7.18 shows the angle gathers applied with the vertical mis-alignment correction, which enables one to directly compare the AVO responses among them.

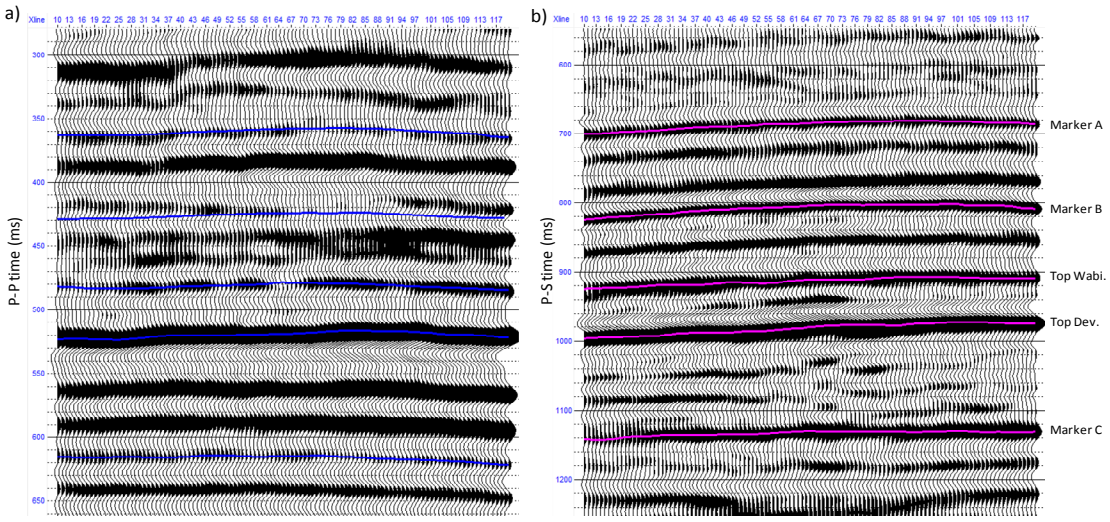

Figure 7.16. (a) P-P and (b) P-S sections with the picked seismic events. The compressing of the P-S time scale corresponds to constant Vp/Vs of 2.33.

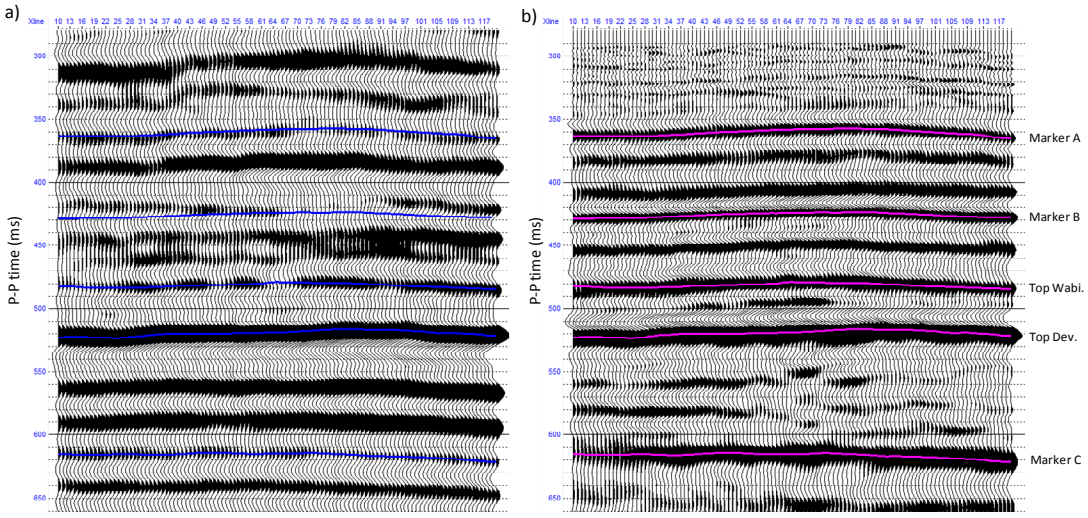

Figure 7.17. (a) P-P and (b) P-S sections after the horizon matching. Note that the P-S section is converted to the P-P time domain.

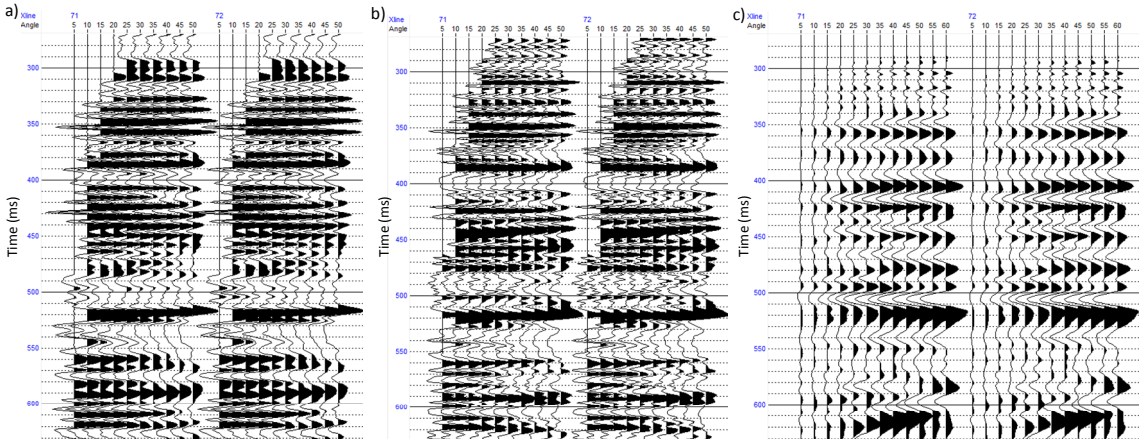

Figure 7.18. Angle gathers after the vertical mis-alignment correction; (a) the baseline P-P, (b) repeat P-P, and (c) repeat P-S data.

7.5 Implementation of Bayesian Inversion

7.5.1 Wavelet Extraction

In the same way as Chapter 5, I extracted near, mid, and far wavelets from each survey data. Figures 7.19, 7.20, and 7.21 show the wavelets for the P-P baseline, P-P repeat, and P-S repeat data, respectively. Note that the P-P and P-S repeat wavelets are extracted from the volume which had been mapped onto the baseline P-P data.

As I previously discussed, there are substantial difference of the frequency band between the baseline P-P and repeat P-P data. The baseline data is band-limited; the maximum frequency is about 150 Hz. In contrast, wavelets of the repeat survey are closer to a pulse. These differences are mainly due to the difference of the receiver type between the two surveys (Nakayama et al., 2008); analog geophone arrays were used in the baseline survey and three-component digital sensors were used in the repeat survey. Buland and Ouair (2006) used the Bayesian inversion technique to perform time-lapse acoustic

impedance inversion. However, their method intrinsically assumes that the baseline and repeat surveys have the same wavelet, unlike this data. In contrast, my method allows us to use individual wavelets. This is a significant advantage because the higher frequency contents in the repeat survey data are expected to help us to delineate smaller-scale heterogeneities.

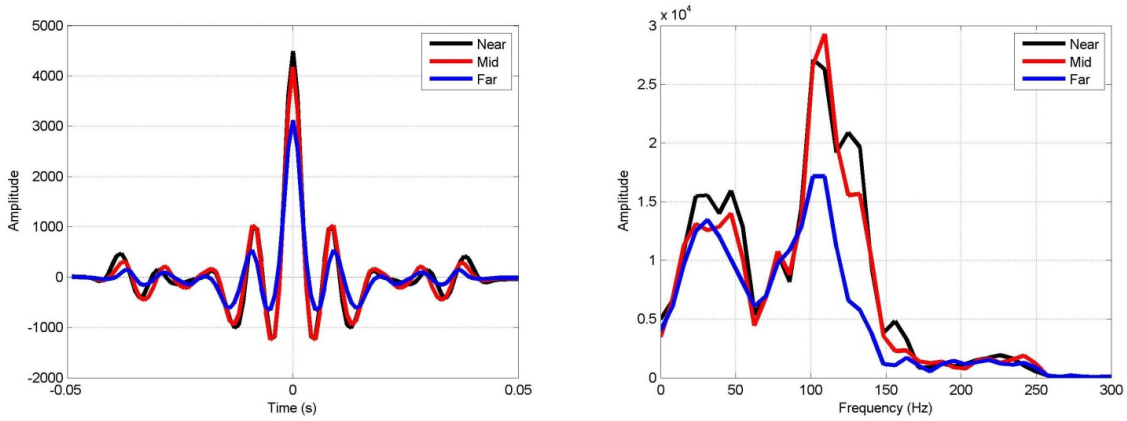

Figure 7.19. Extracted wavelets from the P-P wave data in the baseline survey.

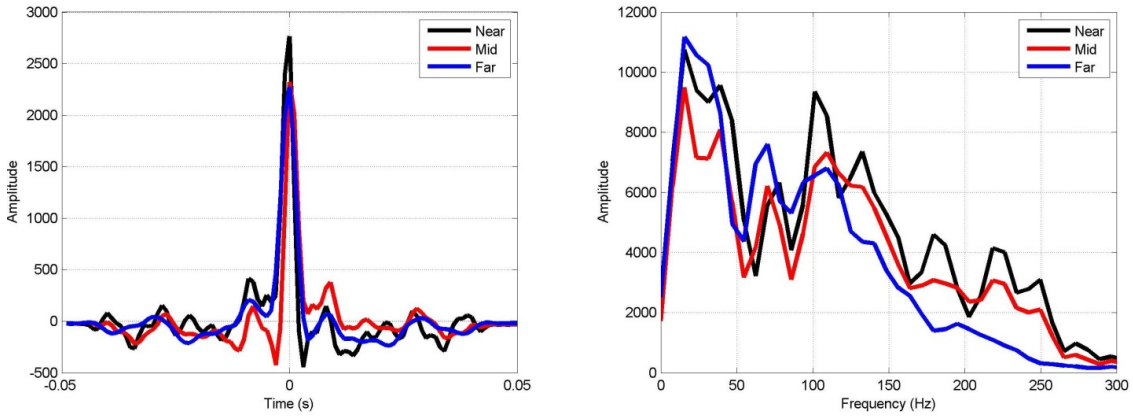

Figure 7.20. Extracted wavelets from the P-P wave data in the repeat survey.

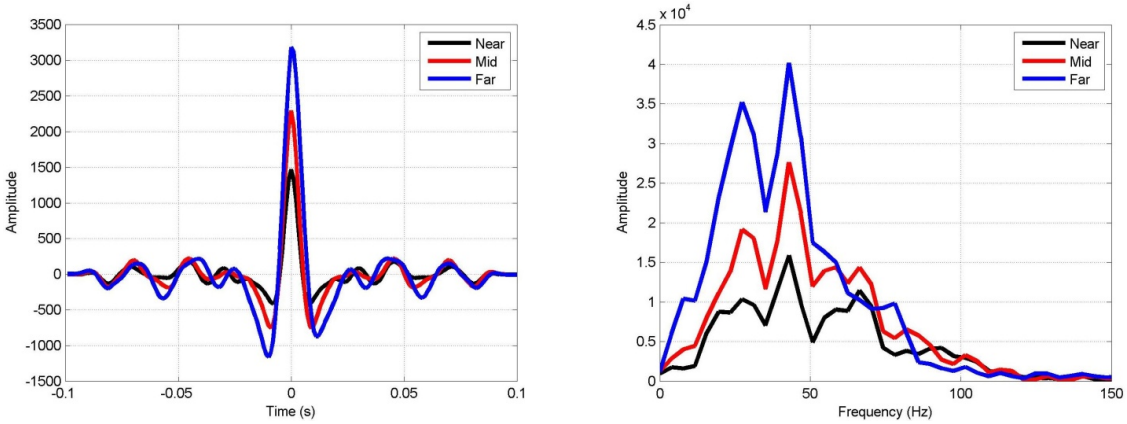

Figure 7.21. Extracted wavelets from the P-S wave data in the repeat survey.

7.5.2 Prior Mean Model

In the time-lapse AVO inversion, the model parameter consists of initial elastic properties (α_1, β_1, and ρ_1) and the changes ($\Delta\alpha$, $\Delta\beta$, and $\Delta\rho$) between the two surveys. For the initial elastic properties, I create the prior mean model in the same way as Chapter 5. The models have vertically smoothed variations above the Top Devonian interface and have constant value (α = 4,500 m/s, β = 2,550 m/s, and $\rho = 2{,}630$ kg/m^3) in the lower carbonate layer (Figure 7.22).

The elastic property changes ($\Delta\alpha$, $\Delta\beta$, and $\Delta\rho$) are expected to have larger lateral variations. Since there are only limited wells available in the study area, it is desirable to use additional information, such as the reservoir simulation model, for the construction of the prior mean model. I alternatively use the time-shift volume obtained in the cross-correlation analysis along with the rock physics model. I took the following procedure:

1. A P-wave velocity change ($\Delta\alpha$) volume is derived from the time-shift volume along with the initial P-wave velocity (α_1) volume.
2. An approximate relationship between $\Delta\alpha$ - $\Delta\beta$ and $\Delta\alpha$ - $\Delta\rho$ are obtained based on the rock physics analysis.
3. Convert the $\Delta\alpha$ volume to $\Delta\beta$ and $\Delta\rho$ volumes by using the approximate relationships.

After taking a vertical derivative of the time-shift volume, the P-wave velocity change is calculated as:

$$\Delta\alpha = \frac{\alpha_1 T_0}{T_0 - \Delta T} - \alpha_1 = \frac{\alpha_1 \Delta T}{T_0 - \Delta T}, \tag{7.1}$$

where T_0 and ΔT are the time sampling interval (ms) and vertical derivative of the time shift (ms); α_1 and $\Delta\alpha$ are the initial P-wave velocity (m/s) and the change between the two surveys (m/s), respectively. Figure 7.23a and 7.23b are the time-shift volume and the corresponding vertical derivative, respectively. In addition, Figure 7.23c is the P-wave velocity change calculated by Equation (7.1). One observes that there are substantial P-wave velocity decreases within the reservoir; the maximum decrease is up to 830 m/s. In addition, one observes substantial P-wave velocity increases in the lower carbonate layer as well as the overburden. The large P-wave velocity increases in the carbonate layer may be an artificial phenomenon associated with the data processing and/or cross-correlation analysis. Also, the initial P-wave velocity (α_1) in the carbonate layer is much faster than that of the reservoir so the velocity change has the similar magnitude as the reservoir,

although the corresponding time-shift is relatively smaller. Thus, I assume that there is no P-wave velocity change above and underneath the reservoir (Figure 7.24a).

Next, the relationships between $\Delta\alpha$ - $\Delta\beta$ and $\Delta\alpha$ - $\Delta\rho$ are obtained by using the P- and S-wave velocity changes in Figures 3.38 along with the density change in Figure 3.37, which are the sequential changes caused by steam injection. I assume that the curve of shaly sands is representative in the study area. I calculate the changes from the initial properties (α_1 = 2,459 m/s, β_1 = 923 m/s, and ρ_1=2,307 kg/m^3) at each step and make cross plots (Figure 7.25). The S-wave velocity continues to decrease at large rate in the steps from 1 to 7. However, after step 10, the S-wave velocity does not largely decrease. In contrast, the density continuously decreases, except for the first pressure changes, as the step increases. Using the relationships between $\Delta\alpha$ - $\Delta\beta$ and $\Delta\alpha$ - $\Delta\rho$, the $\Delta\alpha$ volume is converted to $\Delta\beta$ and $\Delta\rho$ volumes (Figure 7.24b and 7.24c), which are the prior mean model.

For the standard deviation and correlation coefficient of the initial elastic properties, I use the same values from Chapter 5 as follows:

1) Layer above Top Devonian:

Standard deviation : $\sigma_\alpha = 0.0454$, $\sigma_\beta = 0.1848$, and $\sigma_\rho = 0.0372$

Correlation coefficient: $\upsilon_{\alpha\beta} = 0.67$, $\upsilon_{\alpha\rho} = 0.28$, and $\upsilon_{\beta\rho} = -0.09$

2) Lower carbonate layer:

Standard deviation : $\sigma_\alpha = 0.099$, $\sigma_\beta = 0.031$, and $\sigma_\rho = 0.034$

Correlation coefficient: $\upsilon_{\alpha\beta} = 0$, $\upsilon_{\alpha\rho} = 0$, and $\upsilon_{\beta\rho} = 0$

For the elastic property changes in the reservoir, I set the following values from the rock physics analysis along with inversion sensitivity tests:

Standard deviation : $\sigma_{\alpha} = 0.0644$, $\sigma_{\beta} = 0.0202$, and $\sigma_{\rho} = 0.0221$

Correlation coefficient: $\upsilon_{\alpha\beta} = 0.25$, $\upsilon_{\alpha\rho} = 0.50$, and $\upsilon_{\beta\rho} = 0$

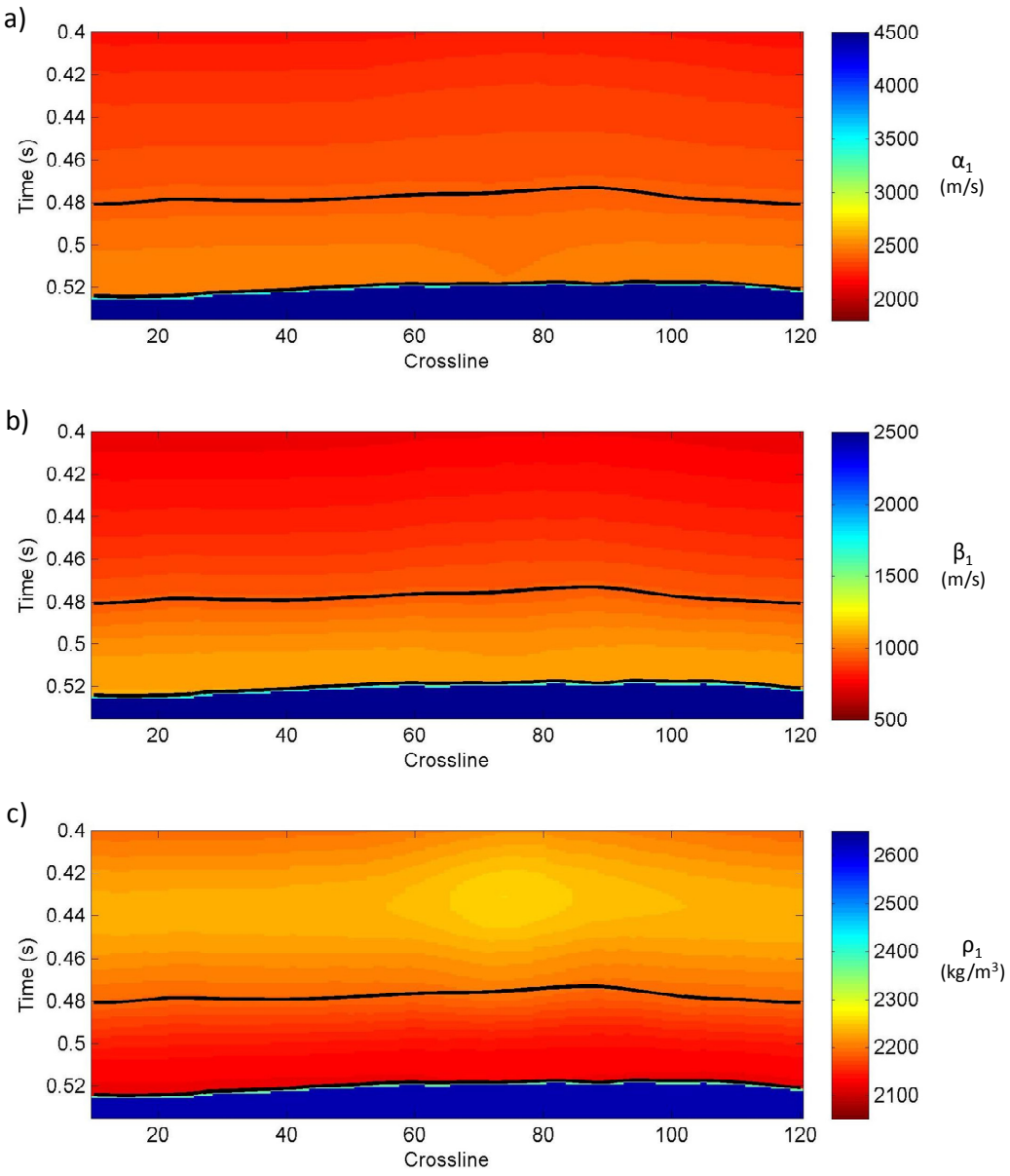

Figure 7.22. Prior mean model of the initial elastic properties; (a) P-wave velocity, (b) S-wave velocity and (c) density.

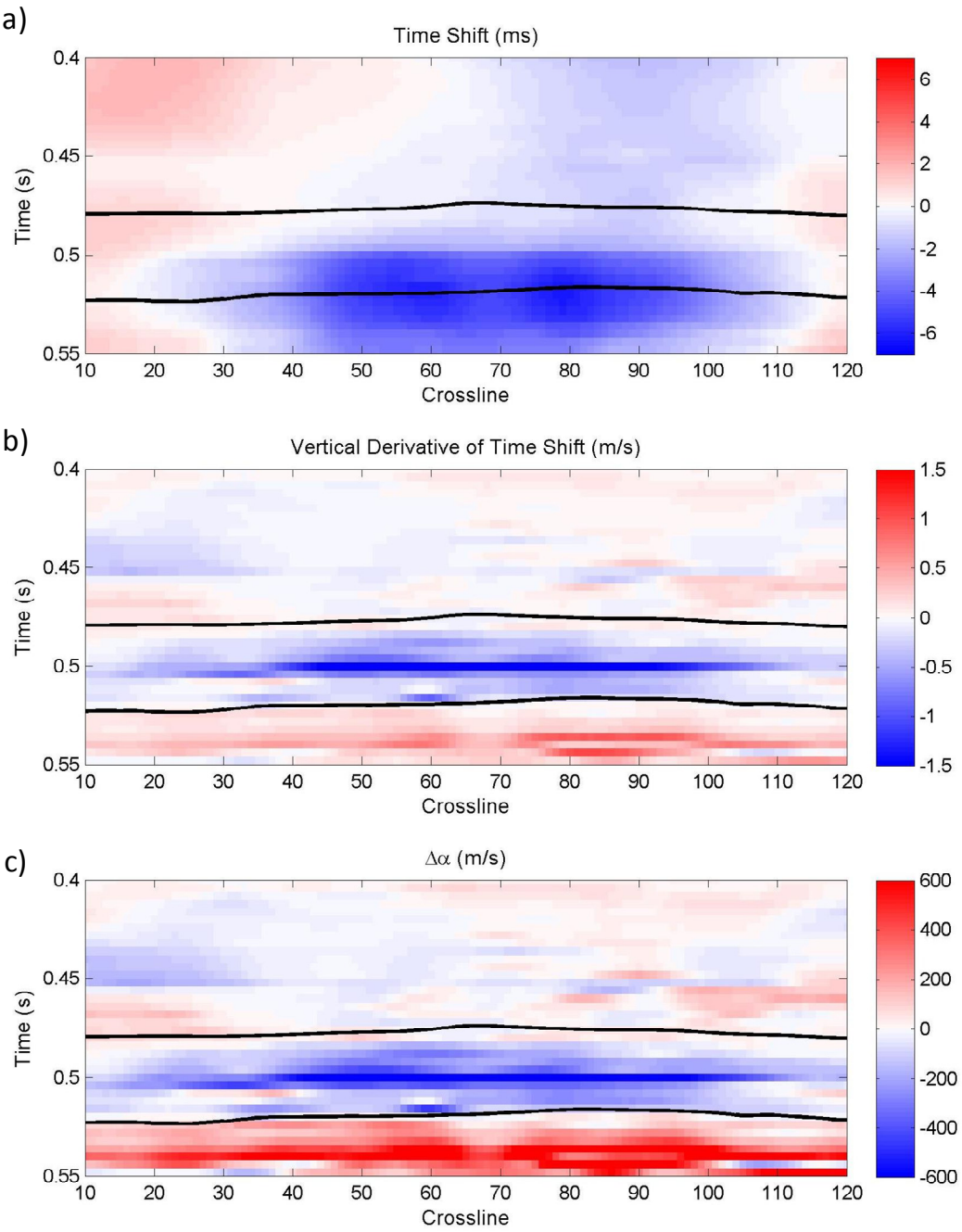

Figure 7.23. (a) The time-shift, (b) vertical derivative of the time-shift, and (c) P-wave velocity change.

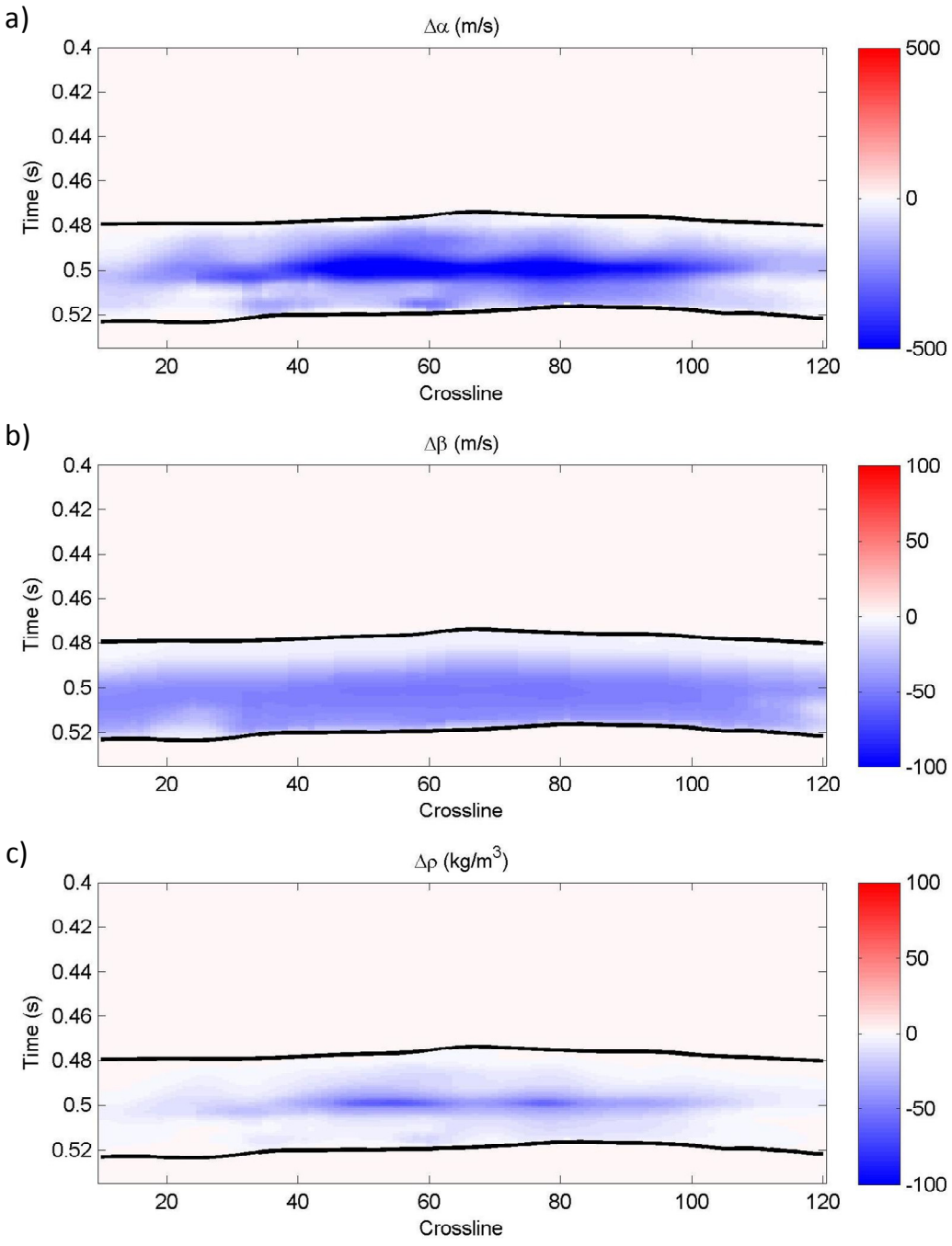

Figure 7.24. Prior mean model of the elastic property changes; (a) the P-wave velocity, (b) S-wave velocity, and (c) density changes.

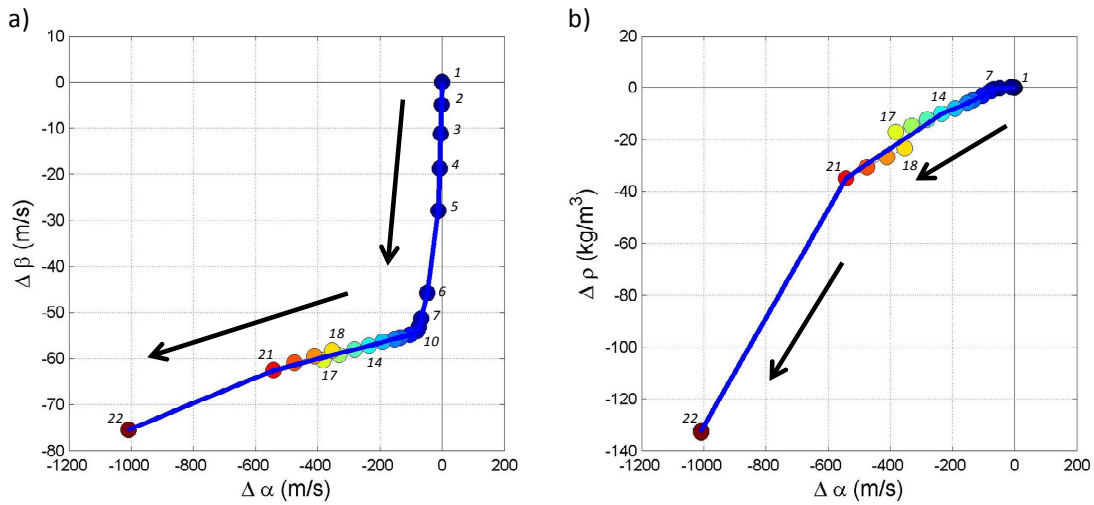

Figure 7.25. Cross plots of the elastic property changes; (a) between $\Delta\alpha$ and $\Delta\beta$ and (b) between $\Delta\alpha$ and $\Delta\rho$. The numbers represent the reservoir condition change, which is based on Figure 3.1.

7.6 Inversion Result and Steam Distribution

I applied the developed time-lapse AVO inversion method to the field data in three cases (Table 7.2). In the first case, all available 3D seismic data are used. This case is called *PP02+PP06+PS06*. In the second case, I use normal P-P time-lapse data (*PP02+PP06*). In the last case, only the baseline P-P data are used (*PP02*). The first two cases give us the inversion result for the initial elastic properties and the changes, while the last case gives us only the initial elastic properties.

Table 7.2 Data used in the inversion.

	P-P at Baseline Survey	P-P at Repeat Survey	P-S at Repeat Survey
PP02 + PP06 + PS06	Available	Available	Available
PP02 + PP06	Available	Available	Not Available
PP02	Available	Not Available	Not Available

Figures 7.26, 7.27, and 7.28 show the inversion results in the well position (well C) for the three cases. The black and red solid curves represent the well log and inversion result, respectively. Furthermore, the black and red dot curves represent the prior and posterior prediction intervals of 95%, respectively. In this location, the reservoir layer is approximately from 476 to 518 ms. The interval from about 500 to 510 ms corresponds to the core of the developed steam chamber. It is noted that the well log curves are resampled with 1 ms.

In the *PP02+PP06+PS06*, the initial elastic properties (α_1, β_1, and ρ_1) are well inverted over all. The P- and S-wave velocities have better agreement with the well logs than the density. If one carefully looks at the density profiles, the inversion result deviates from the well log from around 505 ms to the reservoir bottom. Since this deviation is also observed in *PP02* (Figure 7.28), as well as *PP02+PP06* (Figure 7.27), the error may be associated with the baseline P-P wave data. In contrast, the inversion result of the P- and S-wave velocity changes ($\Delta\alpha$ and $\Delta\beta$) has a good agreement with the well log over all. However, the large decrease in the density at around 504 ms, where a steam phase changes from liquid to vapor, is not retrieved by the inversion.

If one makes a comparison among the three cases, the inversion result of *PP02+PP06+PS06* in the initial S-wave velocity has a better agreement with the well log compared to the other cases. It can be considered that the repeat P-S wave data contributes to determination of the initial S-wave velocity. Also, *PP02+PP06+PS06* gives us a superior result in the initial P-wave velocity estimation. The better estimation in the initial P-wave velocity is mainly due to the correlation between P- and S-wave velocities, which has been set as prior information. In contrast, there is no substantial difference in the density estimation between *PP02+PP06+PS06* and *PP02+PP06*. Also, in the estimation of the elastic property changes, there is no substantial difference between them.

Tables 7.3 and 7.4 show the RMS error and correlation coefficient between the inversion results and the well logs, respectively. It is obvious that *PP02+PP06+PS06* gives us the superior result in the S-wave velocity estimation, compared to the other two cases. For example, the RMS error and correlation coefficient of the *PP02+PP06+PS06* in the S-wave velocity estimation are 177 and 0.484, while these values of *PP02+PP06* are 200 and 0.338, respectively. In addition, *PP02+PP06* has a better result in the P-wave and density estimations compared to *PP02*. These results lead to an interesting conclusion that estimation of initial elastic properties can be improved by using the repeat survey data along with the baseline data.

The inversion results of *PP02+PP06+PS06* of the inline passing through well C are shown in Figures 7.29 and 7.30. The well logs are superimposed for comparison and

show good agreement with the inversion results for all parameters except the density change.

I make a map of the maximum decrease of the P- and S-wave velocities by extracting the maximum magnitude from the $\Delta\alpha$ and $\Delta\beta$ volumes at each bin. Figure 7.31 and 7.32 show the P- and S-wave velocity change map, respectively. As I previously described, the SAGD well pairs, injecting hot steam into the reservoirs, have different starting time of the steam injection. The P-wave velocity change map shows significant decrease in the middle area, which is consistent with the interpretation based on the different starting times of the steam injection. In contrast, the S-wave velocity change map does not correlated well with it. For one of the reasons, it can be considered that S-wave velocity is not sensitive to temperature above 40 °C, as I discussed in Chapter 3.

Since the P-wave velocity is more sensitive to temperature compared to the S-wave velocity and density, the P-wave velocity change map is used to obtain a temperature map at the repeat survey. First, I make a cross plot between sequential changes of P-wave velocity and temperature due to the steam injection by using the rock physics analysis results (Figure 3.38). I use the curve of the clean sands. In the steps from 15 to 20, it is impossible to determine a single solution of the temperature from the P-wave velocity change. I assume that the interval can be approximated by a linear line because the P-wave velocity change is relatively small.

By using the approximate relationship between the P-wave velocity change and temperature, I obtain a temperature map at the repeat survey from the P-wave velocity change map. Figure 7.34 shows the temperature map, showing almost the whole area is

heated from the initial temperature of about 11˚C. Particularly, the temperature increase around the two SAGD well pairs (I and H) is significant; the maximum temperature is up to 242˚C. However, one observes some areas where the temperature increase do not coincide with the SAGD well path, including the SAGD well pair O. It may suggest irregular steam movement caused by the heterogeneities within the reservoir.

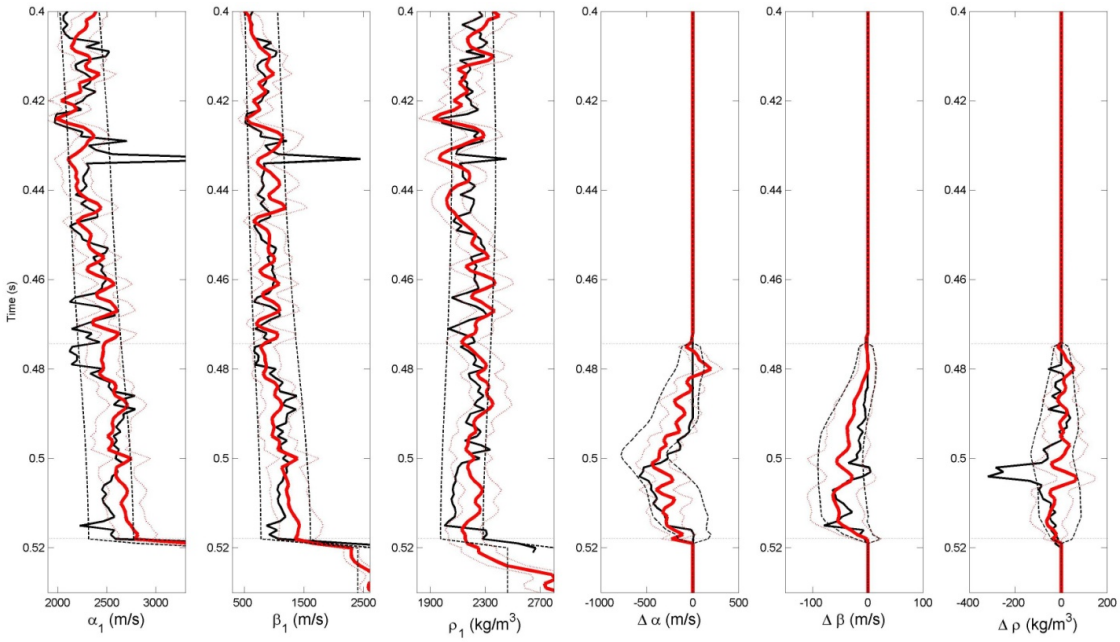

Figure 7.26. Inversion results of the *PP02+PP06+PS06* in the well position. The black and red solid curves represent the well log and inversion result, respectively. The black and red dot curves represent the prior and posterior prediction intervals of 95%, respectively.

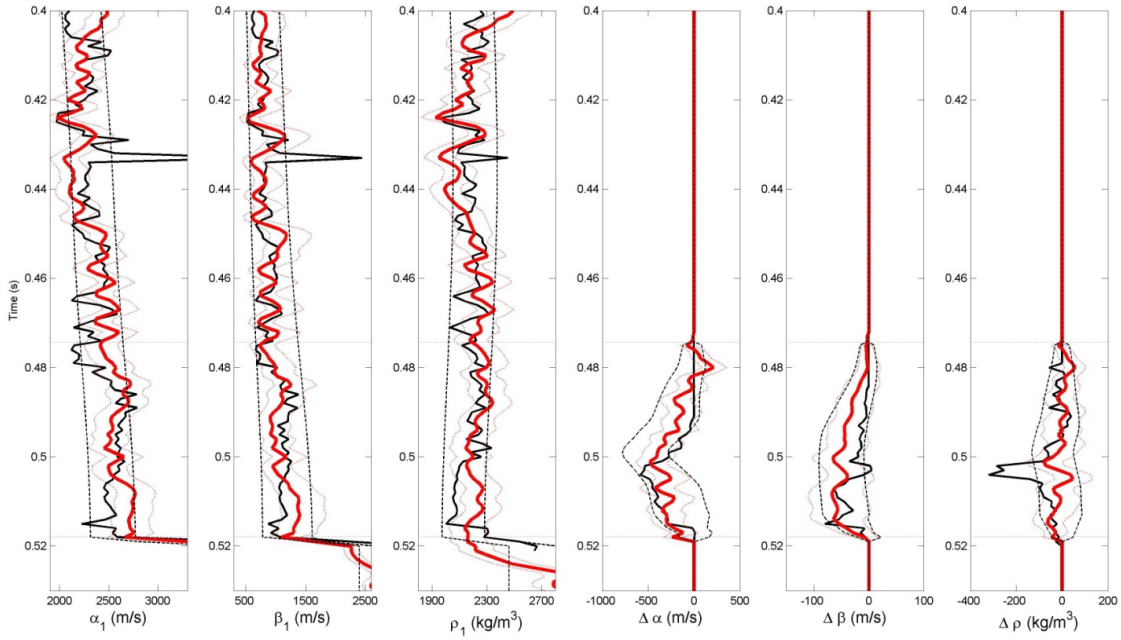

Figure 7.27. Inversion results of the *PP02+PP06* in the well position. The black and red solid curves represent the well log and inversion result, respectively. The black and red dot curves represent the prior and posterior prediction intervals of 95%, respectively.

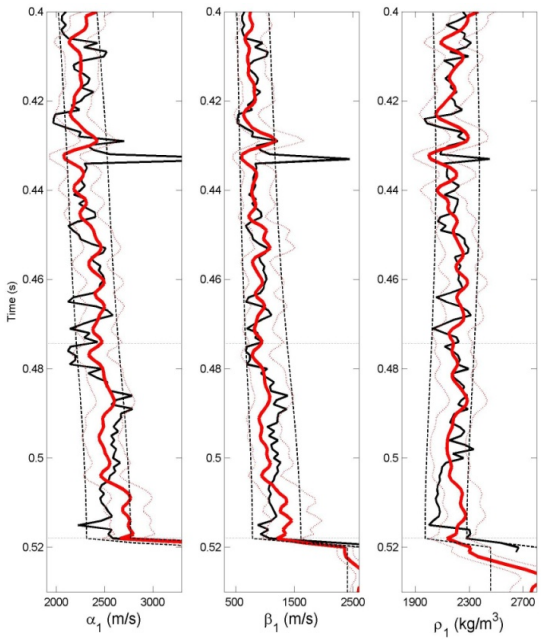

Figure 7.28. Inversion results of the *PP02* in the well position. The black and red solid curves represent the well log and inversion result, respectively. The black and red dot curves represent the prior and posterior prediction intervals of 95%, respectively.

Table 7.3. RMS error of inversion results and prior mean model with the well logs for the reservoir interval.

	α_1 (m/s)	β_1 (m/s)	ρ_1 (kg/m^3)	$\Delta\alpha$ (m/s)	$\Delta\beta$ (m/s)	$\Delta\rho$ (kg/m^3)
PP02 + PP06 + PS06	147	180	92	138	14	85
PP02 + PP06	171	204	92	139	15	78
PP02	178	204	104	-	-	-
Prior Mean Model	150	149	78	182	19	71

Table 7.4. Correlation coefficient of inversion results and prior mean model with the well logs for the reservoir interval.

	α_1	β_1	ρ_1	$\Delta\alpha$	$\Delta\beta$	$\Delta\rho$
PP02 + PP06 + PS06	0.431	0.463	0.247	0.717	0.766	-0.065
PP02 + PP06	0.235	0.318	0.222	0.723	0.740	0.153
PP02	0.209	0.261	-0.188	-	-	-
Prior Mean Model	0.409	0.489	0.568	0.485	0.539	0.426

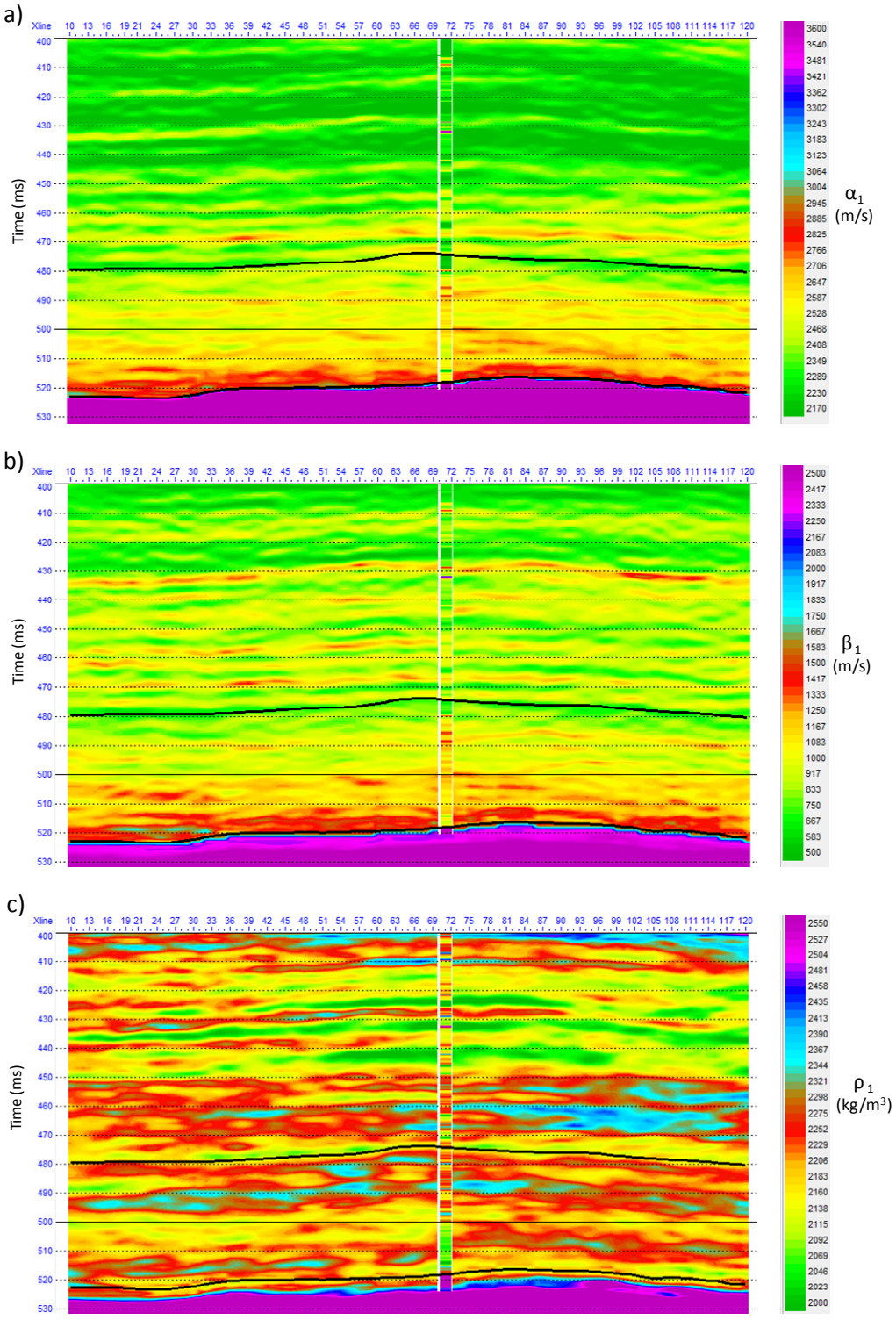

Figure 7.29. Inversion result of the *PP02+PP06+PS06* and well log for the initial elastic properties (α_1, β_1, and ρ_1).

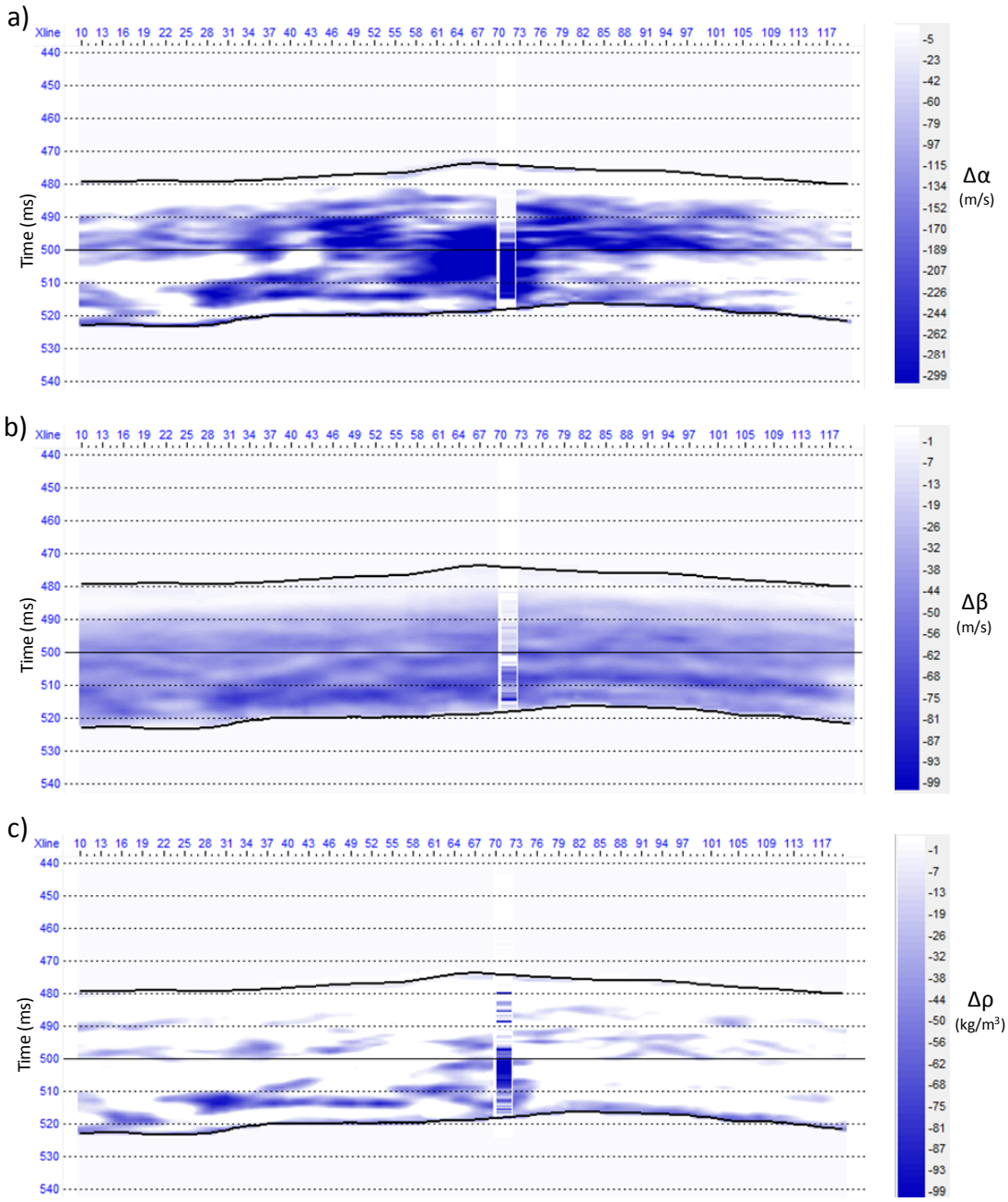

Figure 7.30. Inversion result of the *PP02+PP06+PS06* and well log for the elastic property changes ($\Delta\alpha$, $\Delta\beta$, and $\Delta\rho$).

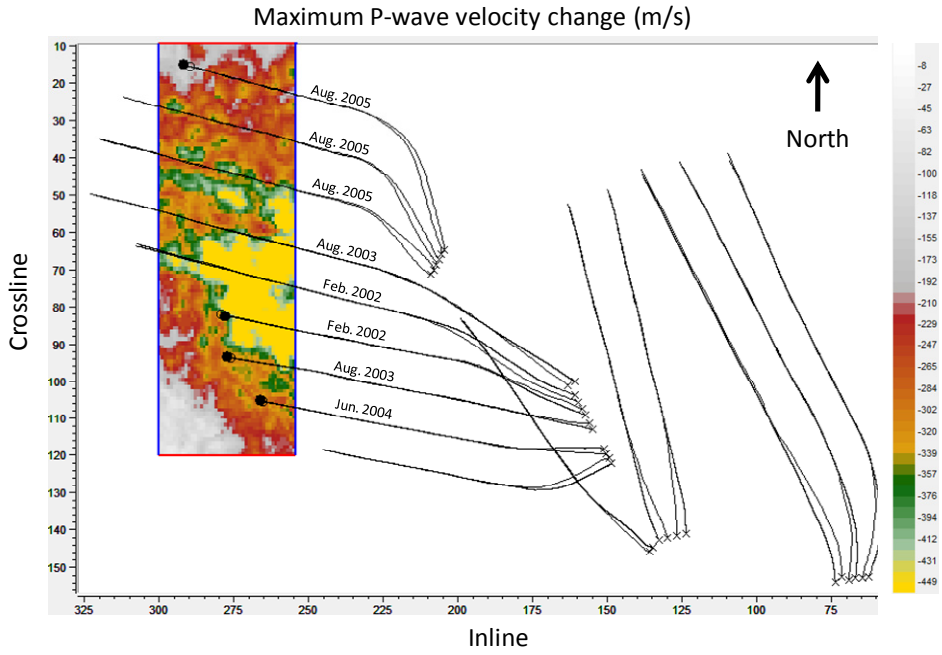

Figure 7.31. The maximum P-wave velocity decrease within the reservoir layer. The dates represent when the steam injection was started.

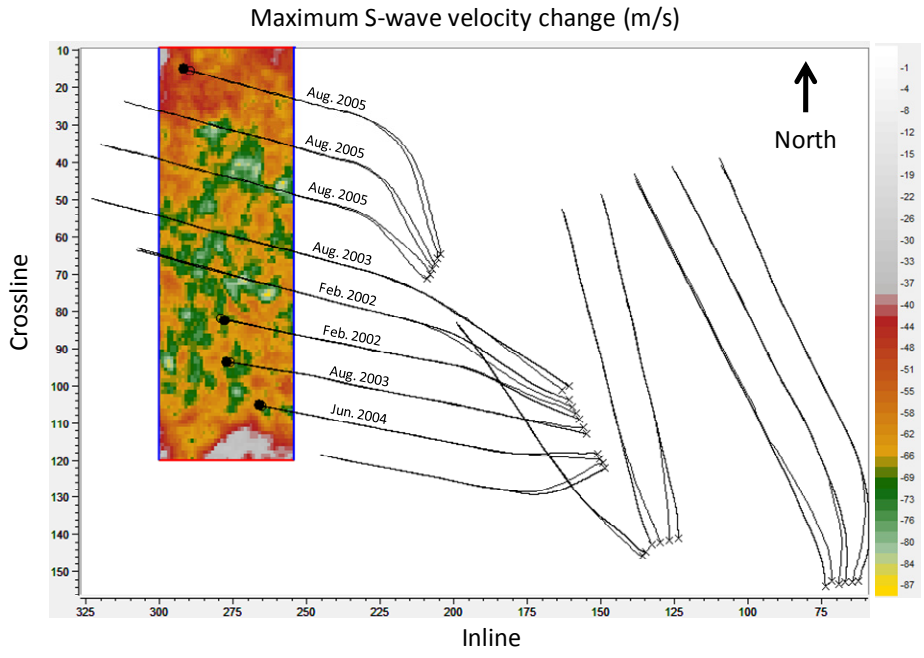

Figure 7.32. The maximum S-wave velocity decrease within the reservoir layer. The dates represent when the steam injection was started.

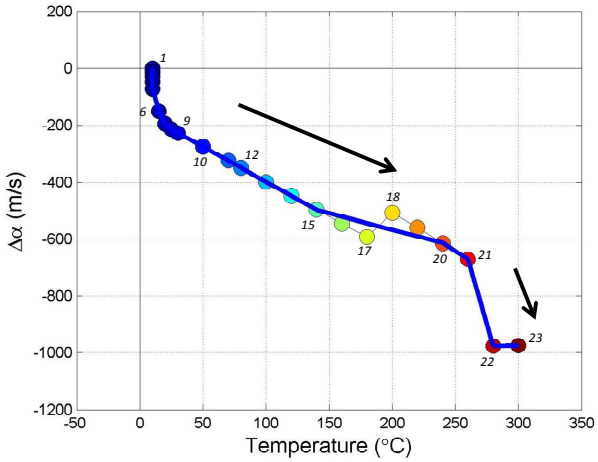

Figure 7.33. Relationship between temperature and P-wave velocity change. The numbers represent the reservoir condition change, which is based on Figure 3.1.

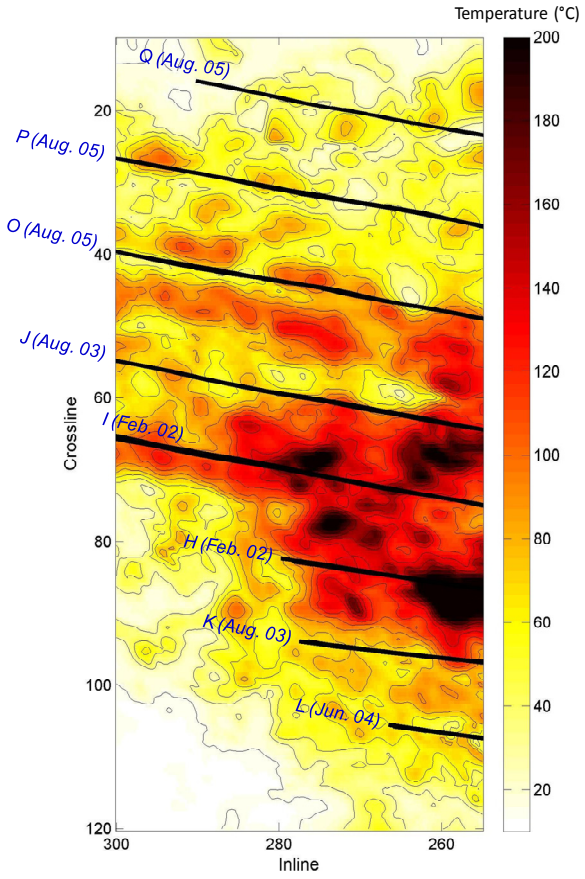

Figure 7.34. The temperature map at the repeat survey. The black solid curves represent the SAGD well path. The dates represent when the steam injection was started.

7.7 Summary

The developed time-lapse AVO inversion was applied to the Hangingstone oilfield. This method uses all available seismic data to simultaneously obtain the initial elastic properties (α_1, β_1, and ρ_1) and the changes ($\Delta\alpha$, $\Delta\beta$, and $\Delta\rho$) between the two surveys, along with the uncertainties. For the time-lapse AVO analysis, a reflection event of different surveys has to be aligned at the same vertical position. I used the warping technique to map the repeat P-P data onto the baseline P-P data. In contrast, the horizon matching technique was used for mapping the repeat P-S data onto the P-P wave data. I carefully created a prior mean model of the elastic properties and the changes. The implementation of the Bayesian inversion showed that the initial elastic properties and the P- and S-wave velocity changes ($\Delta\alpha$ and $\Delta\beta$) can be reasonably estimated. Also, it was suggested that estimation of initial elastic properties can be improved by additionally using the repeat data. Furthermore, it is suggested that adding P-S wave data yields a superior estimation in the initial S-wave velocity, as well as the P-wave velocity. From the inversion results along with the rock physics analysis result, I obtained a temperature map at the repeat survey. The temperature map is consistent with interpretation based on starting time of the steam injection. In addition, it may suggest inhomogeneous steam distribution.

Chapter 8 - Summary

The main goals of this dissertation are to establish an adequate rock physics model for poorly consolidated, heavy-oil saturated sands and to develop new methods of quantitative reservoir characterization and steam monitoring.

For quantitative interpretation of seismic data acquired in heavy-oil reservoirs, it is essential to precisely understand the relationship between seismic properties of the heavy-oil saturated rock (such as velocities and attenuation) and reservoir properties (such as temperature, pressure and fluid saturation). The most distinguished characteristic of heavy-oil saturated rock from a seismic point of view is the viscoelastic behavior which is due to extremely high viscosity of the heavy oil. Thus, I first explored temperature and pressure dependences of elastic properties of heavy oil. I used the ultrasonic velocity measurement data to investigate the bulk viscosity and its related bulk modulus of heavy oil. I compared the viscosity-induced bulk modulus with the corresponding shear modulus to obtain the relation between the bulk and shear viscosities. Furthermore, using the relationship along with the shear viscosity model, the temperature and frequency dependences of the moduli and velocities of the heavy oils were predicted. The predictions are virtually consistent with the ultrasonic measurement data. These analyses clearly show that the bulk viscosity of the heavy oils is larger than the corresponding shear viscosity. Thus, it is obvious that we should take into account effects of the bulk viscosity, as well as the shear viscosity, in the rock physics modeling of heavy-oil saturated rock.

Next, by taking into account the viscoelastic features of heavy oil, I established the rock physics model which can compute effective elastic properties for poorly consolidated, heavy-oil saturated sands. In the heavy-oil reservoir in the McMurray Formation, the grain-grain contacts are loose and the pores have high connectivity. It is important to correctly approximate interaction of the inclusions in the effective medium theory. I used Generalized Singular Approximation (GSA) method in the computation of effective elastic properties. The GSA method assumes that the whole effect of the interactions can be described only by the local interactions. The GSA method has no limitation on the volume concentration of the inclusions in the case of satisfying the assumption. This ability of the GSA method may be one of the reasons for successfully predicting effective properties for the poorly consolidated sands. The established model has a good agreement with the actual measurement data; the laboratory data, well logs, and the surface seismic data. Moreover, the elastic property changes caused by the steam injection were predicted. Also, by taking into account the viscoelastic features of heavy oil, the velocity dispersion and attenuation associated with the viscosities were estimated.

I investigated the relationship between lithology and the corresponding elastic properties in the Hangingstone oilfield and found that the contrast of P- and S-wave velocities between shale and reservoir at in-situ condition is small. On the other hand, bulk density has larger contrast between them, showing a more desired property for the reservoir delineation. Thus, I developed a method of P-P and P-S joint AVO inversion by extending the Bayesian inversion technique to the multicomponent seismic data. The method obtains density, as well as P- and S-wave velocities, which are consistent with the

seismic data along with the prior information. The prior information was based on the established rock physics model. The synthetic test confirmed that the developed joint inversion method gives us a more superior parameter estimation than the P-P only inversion. Furthermore, the developed method was applied to the Hangingstone oilfield. In the implementation, the seismic data conditioning and correlation between the P-P and P-S waves were carefully carried out. Finally, the reservoir sand thickness map was successfully obtained.

As the time-lapse seismic technique has become mature, emphasis on more quantitative interpretation of the time-lapse seismic data has increased. The time-lapse seismic inversion is one of the quantitative interpretation techniques. I developed the time-lapse AVO inversion method by extending the Bayesian inversion technique to time-lapse seismic data. The method simultaneously obtains elastic properties and the changes between two surveys, which are consistent with the all available seismic data with the rock physics knowledge. Furthermore, the method can be extended to the multicomponent time-lapse seismic data. After tests with synthetic data, the method was applied to the field data. I performed coupling between the baseline and repeat survey data. Finally, from the time-lapse AVO inversion results, the distribution map of the steam chamber was successfully obtained.

REFERENCES

Aki, K., and P. G. Richards, 1980, Quantitative seismology: Theory and methods: W. H. Freeman and Company.

Alberta Energy and Utilities Board, 2007, Alberta's energy reserves 2006 and supply/demand outlook 2007-2016, ST98-2007.

Alkhalifah, T., and I. Tsvankin, 1995, Velocity analysis for transversely isotropic media: Geophysics, **60**, 1550-1566.

Backus, G. E., 1962, Long-wave elastic anisotropy produced by horizontal layering: Journal of Geophysical Research, **67**, 4427-4440.

Barlow, A. J., and J. Lamb, 1959, The visco-elastic behavior of lubricating oils under cyclic shearing stress: Proceedings of the Royal Society of London. Series A, **253**, 52-69.

Barnett, D. M., 1972, The precise evaluation of derivatives of the anisotropic elastic Green's functions: Physical Status, Solidi B, **49**, 741-748.

Batzle, M., R. Hofmann, and D.-H. Han, 2006, Heavy oils-seismic properties: The Leading Edge, **25**, 750-757.

Bayuk, I. and E. M. Chesnokov, 1998, Correlation between elastic and transport properties of porous cracked anisotropic media: Journal of Physics and Chemistry of the Earth, **23**, 361-366.

Bayuk, I. O., and M. V. Rodkin, 1999, Modeling of a medium with hierarchic microcrack structure by the general singular approximation method: Physics of the Earth and Planetary Interiors, **114**, 15-24.

Bayuk, I. O., M. Ammerman, and E. M. Chesnokov, 2007, Elastic moduli of anisotropic clay: Geophysics, **72**, no. 5, D107-117.

Bayuk, I. O., M. Ammerman, and E. M. Chesnokov, 2008, Upscaling of elastic properties of anisotropic sedimentary rocks: Geophysical Journal International, **172**, 842-860.

Beggs, H. D., and J. R. Robinson, 1975, Estimating the viscosity of crude oil systems: Journal of Petroleum Technology, **27**, 1140-1141.

Behura, J., M. Batzle, R. Hofmann, and J. Dorgan, 2007, Heavy oils: Their shear story: Geophysics, **72**, no. 5, E175-E183.

Berryman, J. G., 1980, Long-wavelength propagation in composite elastic media II. Ellipsoidal inclusions: Journal of the Acoustical Society of America, **68**, 1980-1831.

Berryman, J. G., 1992, Single-scattering approximations for coefficients in Biot's equations of poroelasticity: Journal of the Acoustical Society of America, **91**, 551-571.

Biot, M. A., 1956, Theory of propagation of elastic waves in a fluid-saturated porous solid, 1, Low-frequency range: The Journal of the Acoustical Society of America, **28**, 168-178.

Brown, R., and J. Korringa, 1975, On the dependence of the elastic properties of a porous rock on the compressibility of the pore fluid: Geophysics, **40**, 608-616.

Buland, A., and H. Omre, 2003, Bayesian linearized AVO inversion: Geophysics, **68**, 185-198.

Buland, A., and Y. E. Ouair, 2006, Bayesian time-lapse inversion: Geophysics, **71**, no. 3, R43-R48.

Buryachenko, V., 2007, Micromechanics of heterogeneous materials: Springer.

Butler, R. M., 1991, Thermal recovery of oil and bitumen: Prentice Hall.

Castagna, J. P. M. L. Batzle, and R. L. Eastwood, 1985, Relationships between compressional-wave and shear-wave velocities in clastic slicate rocks: Geophysics, **50**, 571-581.

Castagna, J. P., 1993, AVO analysis - Tutorial and review, *in* Castagna, J. P. and M. M. Backus, eds., Offset-dependent reflectivity - Theory and practice of AVO analysis: SEG, 3-36.

Chesnokov, E. M., D. K. Tiwary, I. O. Bayuk, M. A. Sparkman, and R. L. Brown, 2009, Mathematical modeling of anisotropy of illite-rich shale: Geophysical Journal International, **178**, 1625-1648.

Christensen, R. M., 1982, Theory of viscoelasticiy: Academic Press Inc.

Ciz, R., and S. A. Shapiro, 2007, Generalization of Gassmann's equations for porous media saturated with a solid material: Geophysics, **72**, no.6, A75-A79.

Clark, V. A., B. R. Tittmann, and T. W. Spencer, 1980, Effect of volatiles on attenuation (Q^{-1}) and velocity in sedimentary rocks: Journal of Geophysical Research, **85**, 5190-5198.

Cole, K. S., and R. H. Cole, 1941, Dispersion and absorption in dielectric - I, alternating currents characteristics: Journal of Chemical Physics, **9**, 341-351.

Curtis, C., R. Kopper, E. Decoster, A. G. Garcia, C. Huggins, L. Knauer, M. Minner, N. Kupsch, L. M. Linares, H. Rough, and M. Waite, 2002, Heavy-oil reservoirs: Oilfield Review, **14**, 30-51.

Das, A., and M. Batzle, 2008, Modeling studies of heavy oil in between solid and fluid properties: The Leading Edge, **27**, 1116-1123.

Das, A., and M. Batzle, 2009, A combined effective medium approach for modeling the viscoelastic properties of heavy oil reservoirs: 79th Annual International Meeting, SEG, Expanded Abstracts, 2110-2114.

Davidson, D. W., and R. H. Cole, 1950, Dielectric relaxation in glycerine: Journal of Chemical Physics, **18**, 1417-1418.

Debye, P., 1929, Polar molecules: The Chemical Catalog Company, Inc.

DeGhetto, G., F. Paone, and M. Villa, 1995, Pressure-volume-temperature correlations for heavy and extra heavy oils: International Heavy Oil Symposium, SPE, 647-662.

Demirbag, E., C. Coruh, and J K. Costain, 1993, Inversion of P-wave AVO, *in* Castagna, J. P. and M. M. Backus, eds., Offset-dependent reflectivity - Theory and practice of AVO analysis: SEG, 287-302.

Downton, J. E., 2005, Seismic parameter estimation from AVO inversion: Ph.D. dissertation, University of Calgary.

Downton, J. E., and C. Ursenbach, 2006, A linearized amplitude variation with offset (AVO) inversion with supercritical angels: Geophysics, **71**, no. 5, E49-E55.

Duijndam, A. J. W., 1988a, Bayesian estimation in seismic inversion: Part I Principles: Geophysical Prospecting, **36**, 878-898.

Duijndam, A. J. W., 1988b, Bayesian estimation in seismic inversion: Part II Uncertainty analysis, Geophysical Prospecting, **36**, 899-918.

Dukhin, A. S., and P. J. Goetz, 2002, Ultrasound for characterizing colloids: Elsevier.

Dukhin, A. S., and P. J. Goetz, 2009, Bulk viscosity and compressibility measurement using acoustic spectroscopy: The Journal of Chemical Physics, **130**, 124519.

Dumitrescu, C. C., and L. Lines, 2007, Heavy oil reservoir characterization using Vp/Vs ratios from multicomponent data: 67th Conference and Technical Exhibition, EAGE, Extended Abstract, P301.

Dumitrescu, C. C., and L. Lines, 2009, Case study of a heavy oil reservoir interpretation using Vp/Vs ratio and other seismic attributes: 79th Annual International Meeting, SEG, Expanded Abstracts, 1765-1769.

Eastwood, J., 1993, Temperature-dependent propagation of P-waves and S-waves in Cold Lake oil sands: Comparison of theory and experiment: Geophysics, **58**, 863-872.

Eastwood, J., P. Lebel, A. Dilay, and S. Blakeslee, 1994, Seismic monitoring of steam-based recovery of bitumen: The Leading Edge, **13**, 242-251.

Eastwood, J. E., D. Johnston, X. Huang, K. Craft, and R. Workman, 1998, Processing for robust time-lapse seismic analysis: Gulf of Mexico example, Lena Field: 68th Annual International Meeting, SEG, Expanded Abstracts, 20-23.

Eshelby, D., 1957, The determination of the elastic field of an ellipsoidal inclusion, and related problems: Proceedings of the Royal Society of London: Series A. Mathematical and Physical Sciences, **241**, 376-396.

Ferry, J. D., 1980, Viscoelastic properties of polymers: John Wiley and Sons.

Fomel, S., M. Backus, K. Fouad, B. Hardage, and G. Winters, 2005, A multistep approach to multicomponent seismic image registration with application to a West Texas carbonate reservoir study: 75th Annual International Meeting, SEG, Expanded Abstracts, 1018-1021.

Fomel, S., and L. Jin, 2009, Time-lapse image registration using the local similarity attribute: Geophysics, **74**, no. 2, A7-A11.

Gaiser, J., 1996, Multicomponent Vp/Vs correlation analysis: Geophysics, **61**, 1137-1149.

Gardner, G. H. F., L. W. Gardner, and A. R. Gregory, 1974, Formation velocity and density-the diagnostic basics for stratigraphic traps: Geophysics, **39**, 770-780.

Garotta, R., 1985, Observation of shear waves and correlation with P events, *in* Dohr, G., eds., Seismic shear waves, Part B: Applications: Geophysical Press, **15B**, 1-86.

Gassmann, F., 1951, Über die elastizität poröser medien: Vierteljahresschrift der Naturforschenden Gesellschaft in Zurich, **96**, 1–23.

Graves, R. E., and B. M. Argrow, 1999, Bulk viscosity: Past to present: Journal of Thermophysics and Heat Transfer, **13**, 337-342.

Gurevich, B., K. Osypov, R. Ciz, and D. Makarynska, 2008, Modeling elastic wave velocities and attenuation in rocks saturated with heavy oil: Geophysics, **73**, no. 4, E115-E122.

Haase, A. B., and R. R. Stewart, 2010, Near-field seismic effects in a homogeneous medium and their removal in vertical seismic profile attenuation estimates: Geophysical Prospecting, **58**, 1023-1032.

Hale, D., 2009, A method for estimating apparent displacement vectors from time-lapse seismic images: Geophysics, **74**, no. 5, V99-V107.

Han, D.-H., A. Nur, and D. Morgan, 1986, Effects of porosity and clay content on wave velocities in sandstones: Geophysics, **51**, 2093-2107.

Han, D.-H., J. Liu, and M. Batzle, 2007a, Shear velocity as the function of frequency in heavy oils: 77th Annual International Meeting, SEG, Expanded Abstracts, 1716-1719.

Han, D.-H., H.-Z. Zhao, and Q. Yao, 2007b, Velocity of heavy oil sand: 77th Annual International Meeting, SEG, Expanded Abstracts, 1609-1613.

Han, D.-H., J. Liu, and M. Batzle, 2008, Seismic properties of heavy oils – Measured data: The Leading Edge, **27**, 1108-1115.

Han, D.-H., J. Liu, and M. Batzle, 2009, Viscosity model of heavy oil with calibration of shear velocity data: 79th Annual International Meeting, SEG, Expanded Abstracts, 2115-2119.

Hashin, Z., and S. Shtrikman, 1963, A variational approach to the elastic behavior of multiphase materials: Journal of the Mechanics and Physics of Solids, **11**, 127-140.

Haviliak, S. and S. Negami, 1967, A complex plane representation of dielectric and mechanical relaxation processes in some polymers: Polymer, **8**, 161-210.

Hein, F., and D. K. Cotterill, 2006, The Athabasca oil sands - a regional geological perspective, Fort McMurray area, Alberta, Canada: Natural Resources Research, **15**, 85-102.

Hinkle, A., 2007, Relation chemical and physical properties of heavy oils: M.S. thesis, Colorado School of Mines.

Hornby, B. E., L. M. Schwartz, and J. A. Hudson, 1994, Anisotropic effective medium modeling of the elastic properties of shales: Geophysics, **59**, 1570-1583.

Hossain, M. S., H.-Q. Zhang, L. Rhyne, and K. L. Greenhill, 2005, Assessment and development of heavy-oil viscosity correlations: SPE/PS-CIM/CHOA

International Thermal Operations and Heavy Oil Symposium, doi: 10.2118/97907-MS.

Issac, J. H., 1996, Seismic methods for heavy oil reservoir monitoring: Ph.D. dissertation, University of Calgary.

Jackson, D. D., M. Matsuura, 1985, A Bayesian approach to nonlinear inversion: Journal Geophysical Research, **90**, 581-591.

Jones, L. E. A., and H. F. Wang, 1981, Ultrasonic velocities in Cretaceous shales for the Williston Basin: Geophysics, **46**, 288-297.

Kalinin, V. A., and I. O. Bayuk, 1990, Effective elastic moduli of rocks at high pressure: Geophysical Journal, **9**, 257-269.

Kashihara, K., A. Takahashi, T. Tsuji, T. Torigoe, K. Hosokoshi, and K. Endo, 2010, Geostatistical reservoir modeling focusing on the effect of mudstone clasts on permeability for the steam-assisted gravity drainage process in the Athabasca oil sands, *in* S. Chopra, L. R. Lines, D. R. Schmitt, and M. L. Batzle, eds., Heavy oils: Reservoir characterization and production monitoring: SEG, 203-214.

Katahara, K. W., 1996, Clay minerals elastic properties: 66th Annual International Meeting, SEG, Expanded Abstracts, 1691-1694.

Kato, A. and S. Onozuka, 2007, Oil sands rock physics databook in Hangingstone field: Japan Oil, Gas and Metals National Corporation.

Kato, A., S. Onozuka, and T. Nakayama, 2008, Elastic property changes in a bitumen reservoir during steam injection: The Leading Edge, **27**, 1124-1131.

Kato, A., and D.-H. Han, 2009, Volume viscosity and it-induced bulk modulus of heavy oil: 71th Conference and Technical Exhibition, EAGE, Extended Abstract, Z023.

Kelvin, L., 1882, Note on the integration of the equations of equilibrium of an elastic solid, *in* Mathematical and Physical Papers 1: Cambridge University Press, 97-98.

Kennett, B. L. N., 1983, Seismic wave propagation in stratified media: Cambridge University Press.

Lafet, Y., P. Duboz, B. Deschizeaux, F. Lefeuvre, and C. Hubans, 2005, 4D stratigraphic inversion of the Girassol field - Towards a more quantitative approach, 67th Conference and Technical Exhibition, EAGE, Extended Abstract, C018.

Lafet, Y., B. Roure, P. M. Doyen, and H. Buran, 2009, Global 4-D seismic inversion and time-lapse fluid classification: 79th Annual International Meeting, SEG, Expanded Abstracts, 3830-3834.

Lai, W. M., D. Rubin, and E. Krempl, 1974, Introduction to continuum mechanics: Pergramon Press Inc.

Leurer, K. C., and J. Dvorkin, 2006, Viscoelasticity of precompacted unconsolidated sand with viscous cement: Geophysics, **71**, no. 2, T31-T40.

Lifshitz, I, M., and L. N. Rozenzweig, 1947, On the construction of the Green's tensor for the basic equation of the theory of elasticity of an anisotropic infinite medium: Journal of Experimental and Theoretical Physics, **17**, 7683-791.

Lines, L., Y. Zou, A. Zhang, K. Hall, B. Palmiere, C. Reine, P. Bessette, P. Cary, and D. Secord, 2005, Vp/Vs characterization of a heavy-oil reservoir: The Leading Edge, **24**, 1134-1136.

Litoviz, T. A., T. Lyon, and L. Peselnick, 1954, Ultrasonic relaxation and its relation to structure in viscous liquids: The Journal of the Acoustic Society of America, **26**, 566-576.

Litovitz, T. A., and C. M. Davis, 1964, Structural and shear relaxation in liquids, *in* W. P. Mason, eds., Physical Acoustics: Academic Press, 281-349.

Liu, J., 2006, Description of models used in the programs FLAG: 2006 annual meeting of Fluids/DHI consortium.

Liu, J. and D.-H. Han, 2007, Heavy oil velocities – new measurements and new models: 2007 annual meeting of Fluids/DHI consortium.

Macdonald, C., P. M. Davis, and D. D. Jackson, 1987, Inversion of reflection traveltimes and amplitudes: Geophysics, **52**, 606-617.

Macrides, C. G., and E. R. Kanasewich, 1987, Seismic attenuation and poisson's ratios in oil sands from crosshole measurements: Journal of the Canadian Society of Exploration Geophysicists, **23**, 46-55.

Makarynska, D., B. Gurevich, J. Behura, and M. Batzle, 2010, Fluid substitution in rocks saturated with viscoelastic fluids: Geophysics, **75**, no. 2, E115-E122.

Malbrunot, P., A. Boyer, E. Charles, and H. Abachi, 1983, Experimental bulk viscosities of argon, krypton, and xenon near their triple point: Physical Review A, **27**, 1523-1534.

Mase, G., 1970, Continuum mechanics: McGraw-Hill.

Mavko, G., and D. Jizba, 1991, Estimating grain-scale fluid effects on velocity dispersion in rocks: Geophysics, **56**, 1940-1949.

Mavko, G., T. Mukerji, and J. Dvorkin, 1998, The rock physics handbook: Cambridge University Press.

Menke, W., 1989, Geophysical data analysis: Discrete inverse theory: Academic Press.

Mindlin, R. D., 1949, Compliance of elastic bodies in contact: Journal of Applied Mechanics, **16**, 259-268.

Mura, T., 1982, Micromechanics of defects in solids: Springer.

Murphy, W. F., 1982, Effects of microstructure and pore fluids on the acoustic properties of granular sedimentary materials: Ph.D. dissertation, Stanford University.

Nakayama, T., A. Takahashi, L. Skinner, and A. Kato, 2008, Monitoring an oil-sands reservoir in northwest Alberta using time-lapse 3D seismic and 3D P-SV converted-wave data: The Leading Edge, **27**, 1158-1175.

Nickel, M., and L. Sonneland, 2004, Automated PS to PP event registration and estimation of a high-resolution Vp-Vs ratio volume: 74th Annual International Meeting, SEG, Expanded Abstracts, 869-872.

Norris, A., 1985, A differential scheme for the effective moduli of composites: Mechanics of Materials, **4**, 1-16.

Nur, A., C. Tosaya, and D. V. Thanh, 1984, Seismic monitoring of thermal enhanced oil recovery processes: 54th Annual International Meeting, SEG, Expanded Abstracts, 118-121.

Pan, Y. C., and T. W. Chou, 1976, Point force solution for an infinite transversely isotropic solid: Journal of Applied Mechanics, **43**, 608-612.

Phan, A.-V., L. J. Gray, and T. Kaplan, 2005, Residue approach for evaluating the 3D anisotropic elastic Green's function: multiple roots: Engineering Analysis with Boundary Elements, **29**, 570-576.

Prasad, M., M. Kopycinska, U. Rabe, and W. Arnold, 2002, Measurements of Youn's modulus of clay minerals using atomic force acoustic microscopy: Geophysical Research Letters, **29**, 1172-1175.

Quijada, M. F., 2009, Estimating elastic properties of sandstone reservoirs using well logs and seismic inversion: M.S. thesis, University of Calgary.

Reine, C., M. Baan, and R. Clark, 2009, The robustness of seismic attenuation measurements using fixed - and variable-window time-frequency transforms: Geophysics, **74**, no. 2, WA123–WA135.

Rickett, J. E., and D. E. Lumley, 2001, Cross-equalization data processing for time-lapse seismic reservoir monitoring: A case study from the Gulf of Mexico: Geophysics, **66**, 1015-1025.

Rojas, M. A., 2010, Viscoelastic properties of heavy oil samples: Ph.D. dissertation, University of Houston.

Roy, B., P. Anno, and M. Gurch, 2008, Imaging oil-sand reservoir heterogeneities using wide-angel prestack seismic inversion: The Leading Edge, **27**, 1192-1201.

Sarkar, S., W. P. Gouveia, and D. H. Johnston, 2003, On the inversion of time-lapse seismic data: 73th Annual International meeting, SEG, Expanded Abstracts, 1489-1492.

Sayers, C. M., 1994, The elastic anisotropy of shale: Journal of Geophysical Research, **99**, 767-774.

Sayers, C. M., 2005, Seismic anisotropy of shales: Geophysical Prospecting, **53**, 667-676.

Schmitt, D. R., 1999, Seismic attributes for monitoring of a shallow heated heavy oil reservoir: A case study: Geophysics, **64**, 368-377.

Sharkov, E. A., 2003, Passive microwave remote sensing of the earth: Springer.

Sheng, P., 1990, Effective medium theory of sedimentary rocks: Physical Review B, **41**, 4507-4512.

Shermergor, T. D., 1977, Theory of elasticity of microinhomogeneous media: Nauka (in Russian).

Song, J. H., 1986. Measurement of the visco-elasticity of Daqing crude oils: Oilfield Surf. Facil., **5**, 12– 21 (in Chinese).

Soubotcheva, N., and R. R. Stewart, 2006, Predicting lithology and porosity at the Pikes Peak heavy oilfield, Saskatchewan suing 3C seismic data and well logs: CSEG Recorder, 35-39.

Stewart, R. R., 1990, Joint P and P-SV inversion: The CREWES Research Report, **3**, 112-115.

Stewart, R. R., J. E. Gaiser, R. J. Brown, D. C. Lawton, 2002, Converted-wave seismic exploration: Methods: Geophysics, **67**, 1348-1363.

Stokes, G. G., 1845, On the theories of the internal friction of fluids in motion, and of the equilibrium and motion of elastic solids: Trans. Cambridge Phil. Soc. 8, 287.

Stolt, R. H., and A. B. Weglein, 1985, Migration and inversion of seismic data: Geophysics, **50**, 2458-2472.

Sun, Z., 1999, Seismic methods for heavy oil reservoir monitoring and characterization: Ph.D. dissertation, University of Calgary.

Synge, J. L., 1957, The hypercircle in mathematical physics: Cambridge University Press.

Takahashi, A., 2010, Oil-sands reservoir characterization for optimization of field development, *in* S. Chopra, L. R. Lines, D. R. Schmitt, and M. L. Batzle, eds., Heavy oils: Reservoir characterization and production monitoring: SEG, 227-234.

Tanaka, M, K. Endo, and S. Onozuka, 2009, Estimation of steam chamber extent using 4D seismic: Journal of Canadian Petroleum Technology, **49**, 1-6.

Tarantola, A., 1987, Inverse problem theory: Elservier Science.

Tasköprülü, N. S., A. J. Barlow, and J. Lamb, 1961, Ultrasonic and visco-elastic relaxation in a lubricating oil: The Journal of the Acoustical Society of America, **33**, 278-285.

Temkin, S., 2001, Elements of acoustics: John Wiley and Sons.

Ting, T. C. T., and V. G. Lee, 1997, The three-dimensional elastostatic Green's function for general anisotropic linear elastic solids: The Quarterly Journal of Mechanics and Applied Mathematics, **50**, 407-426.

Toinet, S., S. Maultzsh, V. Souvannavong, and O. Colnard, 2010, 4D pre-stack inversion workflow integrating reservoir model control and lithology supervised classification: 72th EAGE Conference and Exhibition, A027.

Vanorio, T., M. Prasad, and A. Nur, 2003, Elastic properties of dry clay mineral aggregates, suspensions and sandstones: Geophysical Journal International, **155**, 319-326.

Veire, H. H., and M. Landrø, 2006, Simultaneous inversion of PP and PS seismic data: Geophysics, **71**, no. 3, R1-R10.

Vo-Thanh, D., 1995, Influence of fluid chemistry on shear-wave attenuation and velocity in sedimentary rocks: Geophysical Journal International, **121**, 737-749.

Wagner, W., and A. Kruse, 1998, Properties of water and steam: Springer.

Walton, K., 1987, The effective elastic moduli of a random packing of spheres: Journal of the Mechanics and Physics of Solids, **35**, 213-226.

Wang, C.-Y., 1997, Elastic fields produced by a point source in solids of general anisotropy: Journal of Engineering Mathematics, **32**, 41-52.

Wang, S., Y. Huang, and F. Civan, 2006, Experimental and theoretical investigation of the Zaoyuan field heavy oil flow through porous media: Journal of Petroleum Science and Engineering, **50**, 83-101.

Williamson, P. R., A. J. Cherrett, and P. A. Sexton, 2007, A new approach to warping for quantitative time-lapse characterization: 69th Conference and Technical Exhibition, EAGE, Extended Abstract, P064.

Willis, J., 1977, Bounds and self-consistent estimates for the overall properties of anisotropic composites, Journal of the Mechanics and Physics of Solids, **25**, 185-202.

Wolf, K., T. Mukerji, and G. Mavko, 2006, Attenuation and velocity dispersion modeling of bitumen saturated sand: 76th Annual International meeting, SEG, Expanded Abstracts, 1993-1997.

Xu, C., and R. R. Stewart, 2006a, Estimating seismic attenuation (Q) from VSP data: CSEG RECORDER, **31**, 57-61.

Xu, C., and R. R. Stewart, 2006b, Delineating a sand channel using 3C-3D seismic data and well logs: Ross Lake heavy oilfield, Saskatchewan: CSEG Recorder, **31**, 87-89.

Xu, Y., and S. Chopra, 2008, Deterministic mapping of reservoir heterogeneity in Athabasca oil sands using surface seismic data: The Leading Edge, **27**, 1186-1191.

Yilmaz, O., 2001, Seismic data processing: SEG.

Appendix A – Static Green's Tensor

A-1. Static Green's Tensor

A basic procedure for the determination of effective elastic characterizations of micro-inhomogeneous and macroanisotropic media is based on a calculation of the static Green's tensor. For isotropic materials, Green's tensor and the derivatives are in simple analytical form and can be found in several studies (e.g., Kelvin, 1882; Mura, 1982). But in the case of a general anisotropic material, Green's tensor is basically difficult to obtain (e.g., Lifshitz and Rozenzwig, 1947; Synge, 1957; Ting and Lee, 1997). In this Appendix, I describe the method of calculating Green's tensor and the derivatives in the general anisotropic material, based on Cauchy's residual theory.

As Buryachenko (2007) reported, one starts from the equilibrium equation:

$$\frac{\partial \sigma_{ij}}{\partial x_j} = -f_i \,, \tag{A-1}$$

where σ_{ij} and f_i are a stress tensor and density of distribution of volume forces, respectively. By applying Hooke's law into (A-1) and replacing the strain by the displacement u_k, one obtains:

$$\frac{\partial}{\partial x_j} C_{ijkl} \frac{\partial}{\partial x_j} u_k = -f_i \,, \tag{A-2}$$

where C_{ijkl} is an elastic stiffness tensor. For a homogenous medium, (A-2) is rewritten in the operator form:

$$L_{ik} u_k = -f_i \,, \tag{A-3}$$

where

$$L_{ik} = \nabla_j C_{ijkl} \nabla_l . \tag{A-4}$$

The solution of the equilibrium equation is obtained as:

$$u_i(\mathbf{r}) = G_{il} * f_l = \int G_{il}(\mathbf{r} - \mathbf{r_1}) f(\mathbf{r_1}) d\mathbf{r_1}, \tag{A-5}$$

where $G_{il}(\mathbf{r})$ is the static Green's tensor. By substituting (A-5) into the equilibrium equation (A-3), one obtains:

$$L_{il} G_{lj}(\mathbf{r}) = -\delta_{ij} \delta(\mathbf{r}) \tag{A-6}$$

where $\delta(\mathbf{r})$ is the Dirac delta function and δ_{ij} is the Kronecker tensor. (A-5) gives us an intuition of the physical meaning of Green's tensor; $G_{il}(\mathbf{r}\text{-}\mathbf{r_1})$ determines the j component of the displacement vector $u(\mathbf{r})$ arising from the unit force directed along the axis $\boldsymbol{r_l}$ and applied at the location of $\boldsymbol{r_1}$. By applying the Fourier transform into (A-6), the expression in the **k** domain is obtained:

$$C_{ijmn} k_j k_n G_{ml}(\mathbf{k}) = \delta_{il} . \tag{A-7}$$

This transform formally reduces the solution to the linear algebraic system. When the Christoffel matrix is expressed by $\Gamma_{im} = C_{ijmn} k_j k_n$, (A-7) is rewritten as:

$$\Gamma_{im} G_{ml} = \delta_{il} . \tag{A-8}$$

Thus, the Green's tensor in the **k** domain is explicitly expressed as:

$$G_{ml}(\mathbf{k}) = (\Gamma^{-1})_{ml} = \frac{\Gamma_{ml}^{adj}}{\det|\Gamma_{ml}|}, \tag{A-9}$$

where Γ_{ml}^{adj} and $\det|\Gamma_{ml}|$ are the cofactor and determinant of the Christoffel tensor Γ_{ml}. By applying the inverse Fourier transform to (A-9), the static Green's tensor in the coordinate domain is obtained as:

$$G_{ml}(\mathbf{r}) = \frac{1}{(2\pi)^3} \int_{-\infty}^{\infty} \frac{\Gamma_{ml}^{adj}(\mathbf{k})}{\det|\Gamma(\mathbf{k})|} e^{i\mathbf{k}\cdot\mathbf{r}} d\mathbf{k} \,. \tag{A-10}$$

Unit vectors $\bar{\mathbf{k}}$ and $\bar{\mathbf{r}}$ are introduced as:

$$\begin{aligned} \bar{\mathbf{k}} &= \mathbf{k} / k, \\ \bar{\mathbf{r}} &= \mathbf{r} / r. \end{aligned} \tag{A-11}$$

Thus, the volume element $d\mathbf{k}$ is expressed as:

$$d\mathbf{k} = k^2 dk dS(\bar{\mathbf{k}}) \,, \tag{A-12}$$

where dS is the surface element on the unit sphere in the $\mathbf{k}$ domain which is centered at the origin of the coordinates. Since $\mathbf{\Gamma}^{adj}$ and $\det|\mathbf{\Gamma}|$ are the homogeneous polynomials with the fourth and sixth order, they can be expressed as:

$$\begin{aligned} \Gamma^{adj}(\mathbf{k}) &= k^4 \Gamma^{adj}(\bar{\mathbf{k}}), \\ \det|\Gamma(\mathbf{k})| &= k^6 \det|\Gamma(\bar{\mathbf{k}})|. \end{aligned} \tag{A-13}$$

Thus, (A-10) is rewritten as:

$$G_{ml}(\mathbf{r}) = \frac{1}{(2\pi)^3} \int_{0}^{\infty} dk \int_{S} \frac{\Gamma_{ml}^{adj}(\bar{\mathbf{k}})}{\det|\Gamma(\bar{\mathbf{k}})|} e^{ikr\bar{\mathbf{k}}\cdot\bar{\mathbf{r}}} dS \,. \tag{A-14}$$

When $\mathbf{k}$ in (A-14) is replaced by $-\mathbf{k}$ as a new variable, one obtains:

$$G_{ml}(\mathbf{r}) = \frac{1}{(2\pi)^3} \int_{-\infty}^{\infty} \frac{\Gamma_{ml}^{adj}(\mathbf{k})}{\det|\Gamma(\mathbf{k})|} e^{-i\mathbf{k}\cdot\mathbf{r}} d\mathbf{k}. \tag{A-15}$$

Then, taking the same procedures from (A-12) to (A-14), one obtains:

$$G_{ml}(\mathbf{r}) = \frac{1}{(2\pi)^3} \int_{-\infty}^{0} dk \int_{S} \frac{\Gamma_{ml}^{adj}(\bar{\mathbf{k}})}{\det|\Gamma(\bar{\mathbf{k}})|} e^{ikr\bar{\mathbf{k}}\cdot\bar{\mathbf{r}}} dS. \tag{A-16}$$

By adding (A-14) and (A-16), one obtains:

$$G_{ml}(\mathbf{r}) = \frac{(2\pi)^{-3}}{2} \int_{-\infty}^{\infty} dk \int_S \frac{\Gamma_{ml}^{adj}(\bar{\mathbf{k}})}{\det\left|\Gamma(\bar{\mathbf{k}})\right|} e^{ikr\bar{\mathbf{k}}\cdot\bar{\mathbf{r}}} dS. \tag{A-17}$$

The integral with respect to k in (A-17) is expressed by Dirac's delta function as:

$$\int_{-\infty}^{+\infty} \exp(ikr\bar{\mathbf{k}}\cdot\bar{\mathbf{r}})dk = 2\pi\delta\left(r\bar{\mathbf{k}}\cdot\bar{\mathbf{r}}\right). \tag{A-18}$$

Thus, (A-17) can be presented in the form of the surface integral over the surface of the unit sphere S in the **k** domain:

$$G_{ml}(\mathbf{r}) = \frac{1}{8\pi^2} \int_S \delta(r\bar{\mathbf{k}}\cdot\bar{\mathbf{r}}) \frac{\Gamma^{adj}(\bar{\mathbf{k}})}{\det\left|\Gamma(\bar{\mathbf{k}})\right|} dS(\bar{\mathbf{k}}). \tag{A-19}$$

By denoting the angle between $\bar{\mathbf{k}}$ and $\bar{\mathbf{r}}$ by Θ (Figure A-1), one obtains:

$$\begin{aligned} &\bar{\mathbf{k}}\cdot\bar{\mathbf{r}} = \cos\Theta, \\ &d\left(\bar{\mathbf{k}}\cdot\bar{\mathbf{r}}\right) = -\sin\Theta\, d\Theta, \\ &dS(\bar{\mathbf{k}}) = \sin\Theta d\Theta d\gamma_1 = -d(\bar{\mathbf{k}}\cdot\bar{\mathbf{r}})d\gamma_1, \end{aligned} \tag{A-20}$$

where γ_1 is defined on the plane perpendicular to ***x*** and the starting line for measuring γ_1 can be arbitrary.

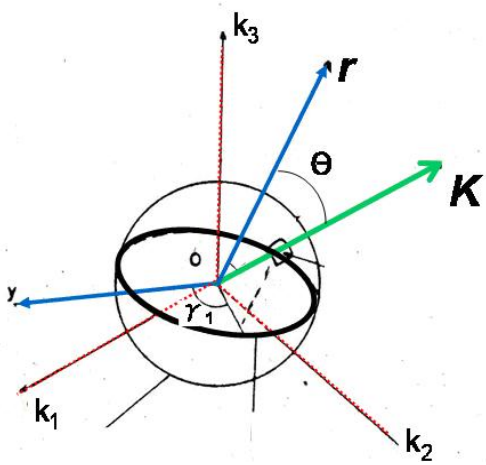

Figure A-1. Geometry relation (after Mura, 1982).

By using the following property of Dirac's delta function as:

$$\int_{-\infty}^{+\infty} \delta(r\bar{\mathbf{k}}\cdot\bar{\mathbf{r}})d(\bar{\mathbf{k}}\cdot\bar{\mathbf{r}}) = 1/r, \tag{A-21}$$

(A-19) can be presented in the form of the counter integral along the intersection between the unit sphere and the plane orthogonal to the vector **r** as:

$$G_{im}(\mathbf{r}) = \frac{1}{8\pi^2 r}\oint_{\bar{\gamma}_1} \frac{\Gamma^{adj}(\bar{\mathbf{k}})}{\det\left|\Gamma(\bar{\mathbf{k}})\right|} d\gamma_1(\bar{\mathbf{k}}). \tag{A-22}$$

The integral in (A-22) can be analytically solved for only isotropic and transversely isotropic mediums; Kelvin (1882) for isotropic case and Pan and Chou (1976) for transversely isotropic case. For an arbitrary anisotropic medium, the integral should be solved numerically. Two methods have been commonly used; the numerical quadrature method and Cauchy's theory of residues.

Since the integral has no singular point, it can be directly solved by a general numerical quadrature, such as the Romberg integration (e.g., Barnett, 1972). However, since the numerical calculation using the Romberg integration requires extensive computation time, it might be practically unfeasible in a complicated system. In contrast, the calculation based on Cauchy's theory only requires to numerically find roots of the denominator ($\det\left|\Gamma(\bar{\mathbf{k}})\right| = 0$) of integrand in (A-22). In order to apply Cauchy's theory, (A-22) should be rearranged to the appropriate form.

The coordinate vector is expressed by the spherical coordinate system as:

$$\bar{\mathbf{r}} = \begin{bmatrix} \sin\varphi\cos\theta \\ \sin\varphi\sin\theta \\ \cos\varphi \end{bmatrix}. \tag{A-23}$$

Then, two fixed orthogonal unit vectors (***a*** and ***b***) in the perpendicular plane are introduced as:

$$\mathbf{a} = \begin{bmatrix} \sin\theta \\ -\cos\theta \\ 0 \end{bmatrix},$$

$$\mathbf{b} = \begin{bmatrix} \cos\varphi\cos\theta \\ \cos\varphi\sin\theta \\ -\sin\varphi \end{bmatrix}. \tag{A-24}$$

The vector $\bar{\mathbf{k}}$ can be expressed by a new parameter t with the vectors, ***a*** and ***b***, as:

$$\bar{\mathbf{k}} = \cos t \cdot \mathbf{a} + \sin t \cdot \mathbf{b}\,. \tag{A-25}$$

The integral in (A-22) can be expressed with respect to t as:

$$\begin{aligned} G_{im}(r) &= \frac{1}{8\pi^2 r} I(\theta,\varphi), \\ I(\theta,\varphi) &= \int_0^{2\pi} \frac{\Gamma^{adj}(\bar{\mathbf{k}}(t))}{\det\left|\Gamma(\bar{\mathbf{k}}(t))\right|} dt. \end{aligned} \tag{A-26}$$

Furthermore, a new parameter Z is introduced as:

$$Z = \tan(t)\,. \tag{A-27}$$

The vector $\bar{\mathbf{k}}$ is expressed as:

$$\bar{\mathbf{k}} = \cos(t)\mathbf{S}(Z), \tag{A-28}$$

$$\mathbf{S}(Z) = \begin{bmatrix} \sin(\theta) + Z\cos(\theta)\cos(\varphi) \\ -\cos(\theta) + Z\sin(\theta)\cos(\varphi) \\ -Z\sin(\varphi) \end{bmatrix}. \tag{A-29}$$

The integral in (A-26) is rearranged in the following form:

$$I(\theta,\varphi)=2\int_{-\infty}^{\infty}\frac{\cos^4(t)\,\Gamma^{adj}(\mathbf{S}(Z))}{\cos^6(t)\,\det\left|\Gamma(\mathbf{S}(Z))\right|}\left(\cos^2(t)\,dZ\right)=2\int_{-\infty}^{\infty}\frac{\Gamma^{adj}(Z)}{\det\left|\Gamma(Z)\right|}dZ, \tag{A-30}$$

where the factor of 2 appears because changes of Z convert range from -∞ to +∞ twice in the interval of t. Because a polynomial with order N has N roots, the denominator of integrand in (A-30) has three roots λ_n satisfying as:

$$\det\left|\Gamma(\lambda_n)\right|=0 \text{ and } \operatorname{Im}\lambda_n>0\,. \tag{A-31}$$

Thus, (A-30) finally has the form which can be applied by Cauchy's theory. Using Cauchy's theory, one obtains:

$$\begin{aligned} I(\theta,\varphi)&=2\int_{-\infty}^{\infty}\frac{\Gamma^{adj}(Z)}{\det\left|\Gamma(Z)\right|}dZ=4\pi i\sum_{n=1}^{3}\operatorname{Re}s(\lambda_n),\\ \operatorname{Re}s(\lambda_n)&=\frac{1}{(m-1)!}\left[\frac{d^{m-1}}{dZ^{m-1}}\left\{(Z-\lambda_n)^m\,\frac{\Gamma^{adj}(Z)}{\det\left|\Gamma(Z)\right|}\right\}\right]_{Z=\lambda_n}, \end{aligned} \tag{A-32}$$

where m is the number of the multiple roots; one for simple root, two for double roots, and three for triple roots, respectively. It is noted that if a system has multiple roots, the expanded form of (A-32) becomes more complicated than that of the simple root (e.g., Wang, 1997; Phan et al., 2005). In order to obtain Green's tensor, it is only required to numerically find the roots.

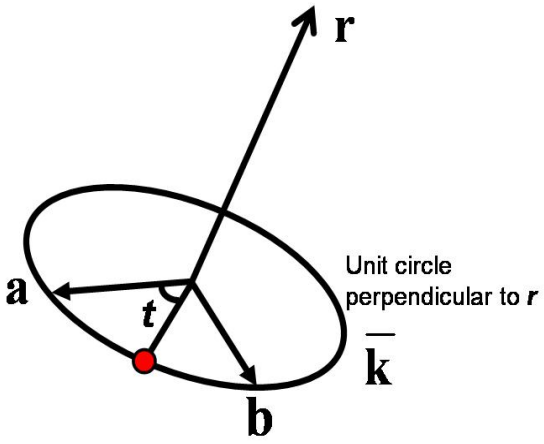

Figure A-2. The vectors **r**, **a**, **b**, and **k**.

A-2. Derivatives of Static Green's Tensor

The first derivative of the static Green's tensor $G(r,\theta,\varphi)$ with respect to x_k is expressed as:

$$\frac{\partial G_{ij}}{\partial x_k} = \frac{\partial G_{ij}}{\partial r}\frac{\partial r}{\partial x_k} + \frac{\partial G_{ij}}{\partial \theta}\frac{\partial \theta}{\partial x_k} + \frac{\partial G_{ij}}{\partial \varphi}\frac{\partial \varphi}{\partial x_k}. \tag{A-33}$$

Through definition of the variables, the partial differentiations with respect to x are as:

$$\begin{aligned}
&\frac{\partial r}{\partial x_i} = \frac{x_i}{r}, \\
&\frac{\partial \theta}{\partial x_1} = -\frac{\sin\theta}{r\sin\varphi}, \quad \frac{\partial \theta}{\partial x_2} = \frac{\cos\theta}{r\sin\varphi}, \quad \frac{\partial \theta}{\partial x_3} = 0, \\
&\frac{\partial \varphi}{\partial x_1} = \frac{\cos\varphi\cos\theta}{r}, \quad \frac{\partial \varphi}{\partial x_2} = \frac{\cos\varphi\sin\theta}{r}, \quad \frac{\partial \varphi}{\partial x_3} = -\frac{\sin\varphi}{r}.
\end{aligned} \tag{A-34}$$

The partial differentiation with respect to r is simple expressed as:

$$\frac{\partial G_{ij}}{\partial r} = -\frac{G_{ij}}{r}. \tag{A-35}$$

The partial differentiation of G_{ij} with respect to θ and φ has the same form with each other. By expressing $\alpha = \theta$ or $\alpha = \varphi$, the partial differentiation with respect to α has the form:

$$\frac{\partial G_{ij}}{\partial \alpha} = \frac{1}{4\pi^2 r}\int_{-\infty}^{\infty} \frac{d}{d\alpha}\left\{\frac{P_{ij}(Z)}{Q(Z)}\right\} dZ = \frac{1}{4\pi^2 r}\int_{-\infty}^{\infty} \frac{P_{ij,\alpha}(Z)Q(Z) - P_{ij}(Z)Q_{,\alpha}(Z)}{Q^2(Z)} dZ, \quad \text{(A-36)}$$

where $P_{ij}(Z) = \Gamma_{ij}^{adj}(Z)$ and $Q(Z) = \det|\Gamma(Z)|$. Applying Cauchy's theory, (A-36) is expressed as:

$$\begin{aligned} &\frac{\partial G_{ij}}{\partial \alpha} = \frac{1}{4\pi^2 r} \cdot 2\pi i \sum_{n=1}^{3} \mathrm{Re}\, s(\lambda_n), \\ &\mathrm{Re}\, s(\lambda_n) = \left[\frac{d}{dZ}\left\{(Z-\lambda_n)^2 \frac{P_{ij,\alpha}(Z)Q(Z) - P_{ij}(Z)Q_{,\alpha}(Z)}{Q^2(Z)}\right\}\right]_{Z=\lambda_n}, \end{aligned} \quad \text{(A-37)}$$

where λ_n is the root of $P_{ij}(Z)$. Thus, the first derivative of the static Green's tensor can be calculated. Moreover, following the same way, the higher order derivates can be evaluated by using the following relationship:

$$\frac{\partial^2 G_{ij}}{\partial x_k \partial x_l} = \frac{\partial G_{ij,k}}{\partial r}\frac{\partial r}{\partial x_l} + \frac{\partial G_{ij,k}}{\partial \theta}\frac{\partial \theta}{\partial x_l} + \frac{\partial G_{ij,k}}{\partial \varphi}\frac{\partial \varphi}{\partial x_l}. \quad \text{(A-38)}$$